INFLUENCE OF METAL IONS ON FORMATION OF SILICO-ALUMINOPHOSPHATE GEOPOLYMER

WANG YANSHUAI

PhD

The Hong Kong Polytechnic University

2018

The Hong Kong Polytechnic University

Department of Civil and Environmental Engineering

Influence of Metal Ions on Formation of Silico-aluminophosphate Geopolymer

WANG Yanshuai

A thesis submitted in partial fulfilment of the requirements for the degree of Doctor of Philosophy

July 2018

CERTIFICATE OF ORIGINALITY

I hereby declare that this thesis is my own work and that, to the best of my knowledge and belief, it reproduces no material previously published or written, nor material that has been accepted for the award of any other degree or diploma, except where due acknowledgement has been made in the text.

________________________(Signed)
WANG Yanshuai (Name of student)

To my family and friends

for their supports

ABSTRACT

Portland cement as the most widely used construction material plays a significant role on the global urbanization. However, numerous crises (e.g., environmental issues) coming with this progress have been emerging. Geopolymer cement (or chemically-activated cement [CAC] defined by other researchers) is an attractive alternate to the traditional Portland cement because such a type of cement can be calcination-free and derived through chemical reactions (e.g., gels formation and geopolymerization) between industrial by-products or natural minerals (i.e., aluminosilicate precursors) and activating solutions (e.g., alkali-silica or phosphate).

This thesis focuses on the influences of metal ions on the microstructural modification during the formation of silico-aluminophosphate geopolymer. An in-depth understanding of the material formation mechanism is believed to be a key to tailor this type of geopolymer to meet specific performance requirements in different engineering applications.

The study mainly involves four dimensions: (1) Synthesis of silico-aluminophosphate geopolymer based on a theoretical Si-Al-P ratio which is supported by a hypothetical molecular structure; (2) Improvement of the workability and setting time of silico-aluminophosphate geopolymer by incorporating aluminate species into the phosphate activator; (3) Use of dead-burnt magnesia-doped aluminosilicate precursor to induce acid-base reaction during the geopolymerization for improving the early age performance of silico-aluminophosphate geopolymer; (4) Use of high-calcium coal fly ash as the calcium donor during geopolymerization to acquire the castable silico-aluminophosphate geopolymer with high early strength.

Aluminum-incorporated phosphate activation and magnesium/calcium-doped aluminosilicate precursors (e.g., dead-burnt magnesia and high-calcium coal fly ash) were extensively studied and found to be effective to modify both the fresh and hardened properties of silico-aluminophosphate geopolymer. The knowledge arisen from the thesis has facilitated a solid basis for a wide range of engineering applications of this new category of geopolymer cement.

PUBLICATIONS DURING PH.D STUDY

Journal Papers published:

[1] **Wang, Y. S.**, & Dai, J. G.* (2017). X-ray computed tomography for pore-related characterization and simulation of cement mortar matrix. *NDT & E International*, *86*, 28-35.

[2] **Wang, Y. S.**, & Dai, J. G.* (2017). Use of magnesia sand for optimal design of high performance magnesium potassium phosphate cement mortar. *Construction and Building Materials*, *153*, 385-392.

[3] **Wang, Y. S.**, Dai, J. G.*, Ding, Z., & Xu, W. T. (2017). Phosphate-based geopolymer: Formation mechanism and thermal stability. *Materials Letters*, *190*, 209-212.

[4] **Wang, Y. S.**, Dai, J. G.*, Wang, L., Tsang, D. C.*, & Poon, C. S. (2018). Influence of lead on stabilization/solidification by ordinary Portland cement and magnesium phosphate cement. *Chemosphere*, *190*, 90-96.

[5] **Wang, Y. S.**, Provis, J. L.*, & Dai, J. G.* (2018). Role of soluble aluminum species in the activating solution for synthesis of silico-aluminophosphate geopolymers. *Cement Concrete & Composites*, 93, 186-195.

[6] Liu, Y. L., **Wang, Y. S.***, Fang, G., Alrefaei, Y., Dong, B., & Xing, F. (2018). A preliminary study on capsule-based self-healing grouting materials for grouted splice sleeve connection. *Construction and Building Materials*, *170*, 418-423.

[7] Xu, W. T., Dai, J. G.*, Ding, Z., & **Wang, Y. S.** (2017). Polyphosphate-modified calcium aluminate cement under normal and elevated temperatures: Phase evolution, microstructure, and mechanical properties. *Ceramics International*, *43*(17), 15525-15536.

[8] Wang, L., Iris, K. M., Tsang, D. C.*, Li, S., Li, J. S., Poon, C. S., **Wang, Y.**

S., & Dai, J. G. (2017). Transforming wood waste into water-resistant magnesia-phosphate cement particleboard modified by alumina and red mud. *Journal of Cleaner Production*, *168*, 452-462.

Journal Papers to be submitted:

[1] **Wang, Y. S.**, & Dai, J. G.* (2018). Early properties of silico-aluminophosphate geopolymer promoted by acid-base reaction: effect of dead-burnt magnesia. *Journal of the European Ceramic Society* (to be submitted).

[2] **Wang, Y. S.**, Provis, J. L.*, & Dai, J. G.* (2018). Utilization of coal fly ash in silico-aluminophosphate geopolymer. *Cement Concrete & Research* (to be submitted).

Conference papers/abstracts:

[1] **Wang, Y. S**. & Dai, J.G.* (2017). Role of soluble aluminum species in activating solution of phosphate-based geopolymer. The 3rd International Conference on Chemically Activated Materials, 8-11 August, Gold Coast, Australia,.

[2] **Wang, Y. S**. & Dai, J.G.* (2018). Al-incorporated phosphate activator to improve workability of phosphate-based geopolymer. The 4th International Symposium on Design, Performance and Use of Self-consolidating Concrete, 10-13 May, Changsha, Hunan, China.

ACKNOWLEDGEMENTS

Over the past three years when I was devoted to my Ph.D study at the Hong Kong Polytechnic University, I have received the direct or/and indirect consideration, help, support and encouragement from many individuals. Here, I hope to use the limited space to give my appreciations and blessings to these people.

First and foremost, I definitely express my sincere gratitude to my supervisor, Prof. Jian-Guo Dai, for taking me into a real academic world through his patient enlightenment and guidance. Prof. Dai's meticulous attitude, strong responsibility, and professional demeanor are perfectly embodied in countless face-to-face communications and distance discussions with him, which greatly benefited me during my Ph.D study, even in the future work and life. I am truly fortunate to have the opportunity to study and work with Prof. Dai.

I would also like to thank Prof. John L. Provis at the University of Sheffield (UK) for his hospitality and supervision during my visiting his research group for three months. His profound knowledge system, clear mind map, and humorous teaching way heavily deepen my understanding in geopolymer, especially the impressive interpretation on the geopolymer chemistry and the terminology of alkali-aluminosilicate geopolymer and silico-aluminophosphate geopolymer. Besides, his comments on aluminophosphate zeolite and NMR technology are indispensable in my thesis.

I wish to thank the colleagues and friends at PolyU, including the technicians, Mr. K.H. Wong (concrete lab) and Mr. W.S. Lam (water analysis lab), and our research group members, Dr. X. Xue, Dr. Y. Liu, Dr. Y. Ding, Mr. P. Dong, Mr.

J.Q. Huang, Mr. K.D. Peng, Mr. B.J. Tao, Mr. D. Guo, Mr. S. Kumar, Mr. X. Yang, Mr. K.Q. Yu and other visitors who are in Prof. Dai's research group, for their suggestions, collaborations and assistance. In addition, my appreciations should be presented to the staff at University Research Facility in Materials Characterization and Device Fabrication (UMF) for their technical training and supports.

Special thanks are given to one of our research group members, Mr. Y. Alrefaei, for refining and polishing the language in my thesis, and to my roommate, Mr. R. Chen, for accompanying at playtime.

Significantly, my love and appreciation will be dedicated to my family for their never-failing care, encouragement and support during my long journey of study.

Finally, the financial support from the Hong Kong Polytechnic University through Ph.D studentship is greatly appreciated.

CONTENTS

CHAPTER 6 SILICO-ALUMINOPHOSPHATE GEOPOLYMER IMPROVED BY DEAD-BURNT MAGNESIA 129

LIST OF FIGURES

CHAPTER 1

CHAPTER 2

CHAPTER 3

CHAPTER 4

CHAPTER 5

CHAPTER 6

CHAPTER 7

LIST OF TABLES

CHAPTER 2

CHAPTER 3

CHAPTER 4

CHAPTER 5

CHAPTER 6

CHAPTER 7

LIST OF ABBREVIATIONS

3D	three-dimension
AAM	alkali-activated material
ABC	acid-base cement
BSE	backscattered electron
CAM	chemically activated material
C-A-S-H	calcium-aluminate-silicate-hydrogen
CBPC	chemically bonded phosphate ceramic
CFA	coal fly ash
CFBC	circulating fluidized bed combustion
C-H	calcium-hydroxide
CP	cross polarization
CPC	calcium phosphate cement
C-P-H	calcium-phosphate-hydrate
C-S-H	calcium-silicate-hydrate
DBM	dead-burnt magnesia
DCPD	dicalcium phosphate dehydrate
DTA	differential thermal analysis
EDXS	energy dispersive X-ray spectroscopy
FBC	fluidized bed combustion
GGBS	granulated ground blast-furnace slag
HA	hydroxyapatite
HCFA	high-calcium coal fly ash
ITZ	interfacial transition zone
LCA	life cycle assessment
LCFA	low-calcium coal fly ash
LOI	loss on ignition

MAP	monoaluminum phosphate
MAS	magic angle spinning
MIP	mercury intrusion porosimetry
MK	metakaolin
MPC	magnesium phosphate cement
N-A-S-H	sodium-aluminate-silicate-hydrate
NMR	nuclear magnetic resonance
OPA	orthophosphoric acid
OPC	ordinary Portland cement
PCC	pulverized coal combustion
SAED	selected area electron diffraction
S-A-P	silicate-aluminate-phosphate
SCM	supplementary cementitious material
SEM	scanning electron microscopy
SF	silica fume
TEM	transmission electron microscope
TG	thermogravimetry
TGA	thermogravimetric analysis
w/s	water-to-solid
XRD	X-ray diffraction
XRF	X-ray fluorescence

This page is intentionally left blank

CHAPTER 1 MOTIVATIONS AND OBJECTIVES

1.1 Background

The invention of Portland cement tremendously meets the requirements for global housing and infrastructure since the middle of the 19th century (Shi et al., 2011). The annual amount of contemporary cement production all over the world has reached 2.8 billion tons, which is conservatively anticipated to increase to around 4 billion tons per year by 2050 if no alternative of cement comes out (Schneider et al., 2011; Worrell et al., 2001). The major needs from developing countries (e.g., China, India and some African and Asian countries or regions) account for more than 85% of total cement productions (Xu et al., 2014). Without external processing, the fresh Portland cement slurry can be transformed into a rigid 'stone' at room temperature. The produced binding phases adhere sands and gravels together to prop up modern city clusters. More importantly, civil engineers can arbitrarily tailor these rigid 'stones' according to the size, shape and structure requirements. Plus the architects' art design, a diverse city with public transportations, communities and skyscrapers has been gradually built. Thus, the social economy closely hinges on the cement industry (Dumez and Jeunemaǐtre, 1998).

Nevertheless, the cement industry is facing huge challenges because the intensive mineral resources, energy consuming and carbon footprints discharged during cement production are heavily aggressive towards the environment (Mahasenan et al., 2003; Rehan and Nehdi, 2005). The raw materials of cement clinker production are mainly composed by limestone, clay or its natural mixtures, which are almost non-renewable resources (Puertas et al., 2008; Schneider et al., 2011). The manufacture process of cement consists essentially of grinding these raw materials in certain proportions and burning in a cement kiln. In the meantime, high temperature calcination supported by a vast of fuels can fabricate the cement clinker with high activity; however carbon oxides are emitted from the ingredient dissolution, fuels combustion and power generation during this process (Worrell et al., 2001). The whole cement production contributes to nearly 10% of total anthropogenic carbon oxide emissions. The chase for dealing with energy saving or mitigation technique never gives up. Recently, the application of energy conservation techniques (e.g., benchmarking and energy saving tool) (Hasanbeigi et al., 2010) and assessment model (bottom-up energy conservation supply curves) (Worrel et al., 2000) has been substantially raised to improve the energy efficiency and carbon discharge during cement production. However, approximately 50-60% of carbon dioxides released from the decarbonation of limestone during Portland cement production failed to be reduced by improving energy efficiency (Damtoft et al., 2008).

1.2 Motivations of Research

The enthusiasm for the eco-friendly alternatives of construction materials to replace the energy-consuming ordinary Portland cement (OPC) has been motivated for several decades (Vizcaíno-Andrés et al., 2015). Currently, partial replacement of OPC with supplementary cementitious materials (SCMs) including industrial and natural aluminosilicate sources has been widely implemented in construction applications (Lothenbach et al., 2011) to reduce the cement usage, namely, decreasing mineral resources, energy and carbon output of cement production. Besides, the secondary hydration induced by the reaction between the SCMs and extra calcium species (i.e., pozzolanic reaction) can improve the strength and durability of cement matrix (Toutanji et al., 2004). On the other hand, geopolymer cement as a calcination-free binder has gained great interests from researchers and engineers recently. Just like Portland cement, the geopolymer cement enables the assembly of fine and coarse aggregates to be geopolymer mortar or concrete for construction (Aleem and Arumairaj, 2012; Ding et al., 2016). This alternative cement is titled as a low-carbon and low-energy construction material (Duxson et al., 2007; McLellan et al., 2011; Turner and Collins, 2013).

The geopolymer coined by Davidovits is defined as an amorphous or semi-crystalline three dimensional aluminosilicate structure, whose synthesis usually requires hostile pH condition and thermal curing (Davidovits, 1991). The geopolymerization mainly highlights the chemical process of aluminates and silicates, including bonds breaking (decomposition reaction) and remaking (polymerization reaction). The alkali-activated material (AAM) has started to receive attention since 1908 (Provis and van Deventer, 2014), which was explained as a traditional cement-like material formed by the reaction between an aluminosilicate precursor and an alkaline activator, such as the alkali-activated slag cement. The high reactivity of granulated ground blast-furnace slag (GGBS) in alkaline condition enables the production of the calcium-aluminate-silicate-hydrogen (C-A-S-H) gel, or the calcium-silicate-hydrate (C-S-H) gel in case of the low involvement of aluminate (Wang et al., 1995). However, Davidovits argued that the alkali activation process of the GGBS is hydration process instead of geopolymerization (Davidovits, 2011).

Recently, the term of chemically activated material (CAM) was proposed to describe the aluminosilicate sources that can be transformed into a cementitious matrix using some chemical solutions (e.g., alkali-silicate and phosphate solution)

(The 1st, 2nd and 3rd International conference on chemically activated materials, 2010 in Jinan, 2014 in Changsha and 2017 in Gold Coast). ‘Chemically activated materials’ may be more accurate from the scientific point of view, while ‘geopolymer’ seems to be more attractive to engineers because of its concision. In this thesis, the binders primarily prepared by aluminosilicate materials and some activating solutions are all termed as modern geopolymer for the convenient circulation in engineering application. Thus, geopolymer is classified into two categories according to the activation approach: alkali-aluminosilicate geopolymer and silico-aluminophosphate geopolymer. The alkali-aluminosilicate geopolymer includes the calcium-mixed aluminosilicate precursor (e.g., alkali-activated GGBS binder), low-impurity aluminosilicate precursor (e.g., alkali-activated low-calcium coal fly ash [LCFA] or metakaolin [MK] binder) or their blends (e.g., alkali-activated GGBS/LCFA blends). The silico-aluminophosphate geopolymer denotes that the (metal-mixed) aluminosilicate source is activated by the acid phosphate or other phosphate solutions. The terminology evolution regarding the geopolymer is depicted in Fig.1.1.

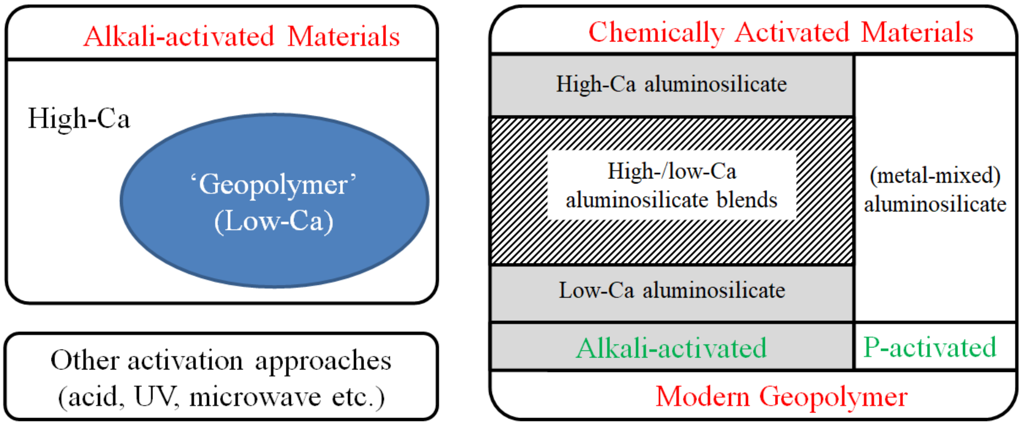

(a) Traditional geopolymer (b) Modern geopolymer

Fig. 1.1 Terminology developments and summary of the geopolymer

The silico-aluminophosphate geopolymer as a new type of geopolymer is paid little attention. It is believed that the mission of alkali-aluminosilicate geopolymer (i.e., alkali-activated material) is to take over Portland cement on a large scale application (Lecomte et al., 2006), while the silico-aluminophosphate geopolymer (i.e., phosphate-activated material) acts as a supplement to geopolymer for a functional material in construction or special engineering applications. This motivates researchers to explore the formation process of the silico-aluminophosphate geopolymer to obtain an optimum mix design for specific engineering requirements.

1.3 Objectives of Research

Recently, most of the existing studies on geopolymer are concentrated on the matrix prepared by the alkali-activated approach in terms of chemistry, mechanical behaviors and durability (Provis and van Deventer, 2009; Pacheco-Torgal et al., 2014). Some modified alkali-based geopolymers have been commercially branded for infrastructure projects, such as PYRAMENT cement (Davidovits, 2011). However, a new family of geopolymer activated by phosphates or phosphoric acid is barely given attention. The objectives of this thesis are to fill in the knowledge gaps in the geopolymer field by conducting an in-depth study about the influences of different metal ions on the formation of silico-aluminophosphate geopolymer from a fresh geopolymer paste to a harden geopolymer matrix. Microstructure evolution and phase change caused by the doped metal species to enhance the macroscopic performance are mainly studied for potential applications (e.g., refractory materials, low dielectric ceramics, acidic binder for heavy metal remediation, and 3D printing materials) (Luz et al., 2015; Cui et al., 2011; Wuana and Okieimen, 2011; Inzana et al., 2014). Thus, there are specific sub-objectives explicated as follow:

- To elaborate the terminology and classification of geopolymer in terms of synthesis mechanism and model, activation approach, and phase composition and form;
- To pinpoint formation process of the silico-aluminophosphate geopolymer without acceleration conditions, i.e., geopolymerization of silicate, aluminate and phosphate species;
- To develop the aluminum-incorporated phosphate activating solution to facilitate a rapid sol/gel transition that improves the rheological properties, setting time and early strength of the silico-aluminophosphate geopolymer paste.
- To synthesize a ‘hybrid’ silico-aluminophosphate geopolymer by doping dead-burnt magnesia into aluminosilicate precursor. Early properties of the ‘hybrid’ geopolymer are greatly enhanced.
- To utilize the CFAs in silico-aluminophosphate geopolymer. Acid-base or/and hydrolysis reaction between the alkaline calcium source in CFA and the acidic phosphate source in activator is induced, following the phosphate activation of glassy aluminosilicate phase within CFA particles.

1.4 Framework of Thesis

The research is stated from eight subsequent chapters to expatiate the role of the metal ions and their influences on the formation of the silico-aluminophosphate geopolymer. The thesis framework on silico-aluminophosphate geopolymer is illustrated in Fig. 1.2.

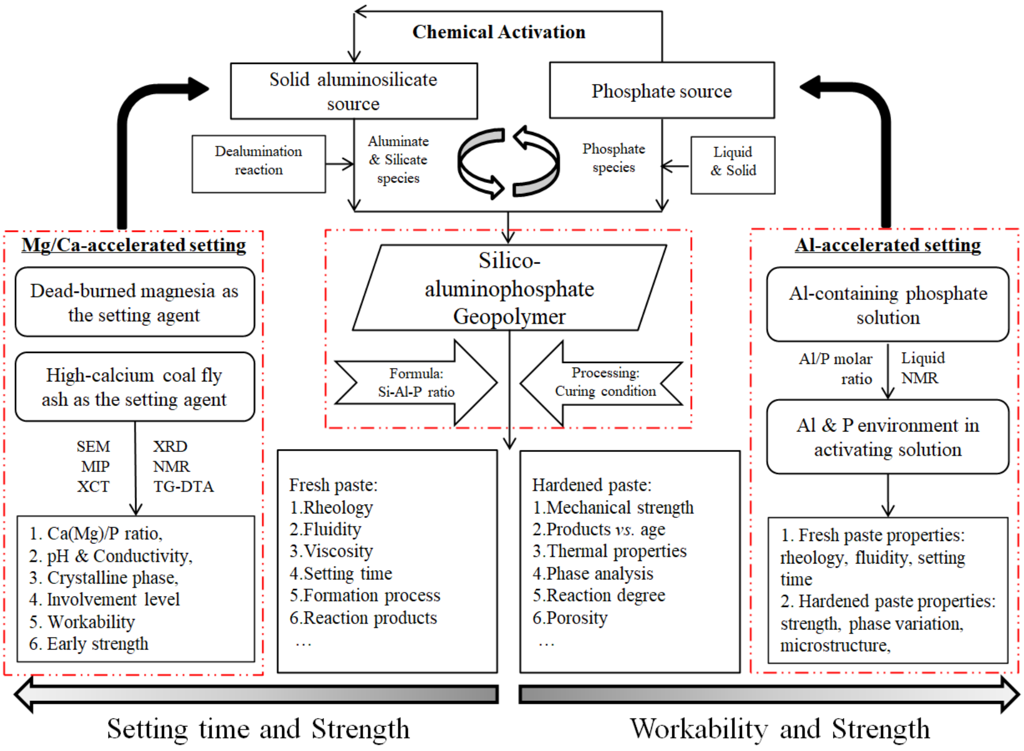

Fig. 1.2 Framework of research on silico-aluminophosphate geopolymer

Chapter 1 encompasses the motivations, objectives and framework of this research.

Chapter 2 presents a state-of-the-art review about the silico-aluminophosphate geopolymer in terms of terminology, classification, formation models, mechanisms, metal ions-induced phosphate chemistry, environmental impacts, performance, durability, and potential applications. The alkali-aluminosilicate geopolymer is referred throughout.

Chapter 3 provides information regarding the raw materials and characterization technologies used in this research. Their grades, sources, physical and chemical properties of solid and liquid materials are detailed. The methods for preparing phosphate activators in terms of pH variation and molar ratio are described in this chapter. The technical details to characterize the raw materials and silico-aluminophosphate geopolymer products are introduced as well.

Chapter 4 elaborates the formation mechanism and thermal properties of the silico-aluminophosphate geopolymer without extra acceleration conditions. This chapter is manly based on the published paper "Wang, Y. S., Dai, J. G., Ding, Z., & Xu, W. T. (2017). Phosphate-based geopolymer: Formation mechanism and thermal stability. *Materials Letters*, *190*, 209-212". The high purity metakaolin, silica fume and solid monoaluminum phosphate act as prime materials to prepare the silico-aluminophosphate geopolymer with three different Si:Al:P molar ratios. One with Si:Al:P molar ratio of 1:1:1 is designed according to theoretical molecular structure, as well as two geopolymers with silicate-deficient (0.49:1:1) and aluminate-deficient (1:0.18:1) molecular structures.

Chapter 5 discusses the improved workability and setting time of the fresh silico-aluminophosphate geopolymer by incorporating aluminum species into phosphate activator. The activating solutions with three Al/P molar ratios were prepared by adjusting the mix proportion of liquid monoaluminum phosphate and orthophosphoric acid. This chapter is manly based on the published paper "Wang, Y. S., Provis, J. L., & Dai, J. G. (2018). Role of soluble aluminum species in the activating solution for synthesis of silico-aluminophosphate geopolymers. *Cement Concrete & Composites*, 93, 186-195."

Chapter 6 proposes a silico-aluminophosphate geopolymer enhanced by dead-burnt magnesia (DBM). Introducing the DBM aims to create an acid-base reaction to improve the early properties of the silico-aluminophosphate geopolymer.

Chapter 7 utilizes the CFA as calcium and aluminosilicate donors for preparing silico-aluminophosphate geopolymer. Many studies indicated that using high calcium CFA to synthesis the alkali-aluminosilicate geopolymer at room temperature is a challenge. In silico-aluminophosphate geopolymer, partial replacement of aluminosilicate precursor by high-calcium CFA can provide the calcium source, which possibly enhances the properties of the geopolymer due to the physical and chemical actions of CFA particles.

Chapter 8 gives main conclusions and directions for further work in the field of silico-aluminophosphate geopolymer.

1.5 References

Aleem, M. A., & Arumairaj, P. D. (2012). Geopolymer concrete - A review. *International Journal of Engineering Sciences & Emerging Technologies*, 1(2), 118-22.

Cui, X. M., Liu, L. P., He, Y., Chen, J. Y., & Zhou, J. (2011). A novel aluminosilicate geopolymer material with low dielectric loss. *Materials Chemistry and Physics*, 130(1-2), 1-4.

Damtoft, J. S., Lukasik, J., Herfort, D., Sorrentino, D., & Gartner, E. M. (2008). Sustainable development and climate change initiatives. *Cement and Concrete Research*, 38(2), 115-127.

Davidovits, J. (1991). Geopolymers: inorganic polymeric new materials. *Journal of Thermal Analysis and Calorimetry*, 37(8), 1633-1656.

Davidovits, J. (2011). *Geopolymer: chemistry & applications*, 3rd edition. Geopolymer Institute, Saint-Quentin.

Ding, Y., Dai, J. G., & Shi, C. J. (2016). Mechanical properties of alkali-activated concrete: a state-of-the-art review. *Construction and Building Materials*, 127, 68-79.

Dumez, H., & Jeunemaǐtre, A. (1998). The unlikely encounter between economics and a market: the case of the cement industry. *The Sociological*

Review, 46(S1), 222-243.

Duxson, P., Provis, J. L., Lukey, G. C., & van Deventer, J. S. J. (2007). The role of inorganic polymer technology in the development of ‘green concrete’. *Cement and Concrete Research*, 37(12), 1590-1597.

Hasanbeigi, A., Price, L., Lu, H., & Lan, W. (2010). Analysis of energy-efficiency opportunities for the cement industry in Shandong Province, China: A case study of 16 cement plants. *Energy*, 35(8), 3461-3473.

Inzana, J. A., Olvera, D., Fuller, S. M., Kelly, J. P., Graeve, O. A., Schwarz, E. M., Kates, S. L., & Awad, H. A. (2014). 3D printing of composite calcium phosphate and collagen scaffolds for bone regeneration. *Biomaterials*, 35(13), 4026-4034.

Lecomte, I., Henrist, C., Liegeois, M., Maseri, F., Rulmont, A., & Cloots, R. (2006). (Micro)-structural comparison between geopolymers, alkali-activated slag cement and Portland cement. *Journal of the European Ceramic Society*, 26(16), 3789-3797.

Lothenbach, B., Scrivener, K., & Hooton, R. D. (2011). Supplementary cementitious materials. *Cement and Concrete Research*, 41(12), 1244-1256.

Luz, A. P., Gomes, D. T., & Pandolfelli, V. C. (2015). High-alumina phosphate-bonded refractory castables: $Al(OH)_3$ sources and their effects. *Ceramics International*, 41(7), 9041-9050.

Mahasenan, N., Smith, S., & Humphreys, K. (2003). The Cement Industry and Global Climate Change: Current and Potential Future Cement Industry CO_2 Emissions. In *Greenhouse Gas Control Technologies 6th International Conference* (pp. 995-1000).

McLellan, B. C., Williams, R. P., Lay, J., Van Riessen, A., & Corder, G. D. (2011). Costs and carbon emissions for geopolymer pastes in comparison to ordinary portland cement. *Journal of Cleaner Production*, 19(9-10), 1080-1090.

Pacheco-Torgal, F., Labrincha, J., & Leonelli C. (Eds.). (2014). *Handbook of alkali-activated cements, mortars and concretes*. Elsevier.

Provis, J. L., & van Deventer, J. S. J. (Eds.). (2009). *Geopolymers: structures, processing, properties and industrial applications*. Elsevier.

Provis, J. L. & van Deventer, J. S. J. (Eds.). (2014). *Alkali-activated materials: state-of-the-art report*, RILEM TC 224-AAM. RILEM/Springer, Dordrecht.

Puertas, F., García-Díaz, I., Barba, A., Gazulla, M. F., Palacios, M., Gómez, M. P., & Martínez-Ramírez, S. (2008). Ceramic wastes as alternative raw materials for Portland cement clinker production. *Cement and Concrete Composites*, 30(9), 798-805.

Rehan, R., & Nehdi, M. (2005). Carbon dioxide emissions and climate change: policy implications for the cement industry. *Environmental Science & Policy*, 8(2), 105-114.

Schneider, M., Romer, M., Tschudin, M., & Bolio, H. (2011). Sustainable cement production—present and future. *Cement and Concrete Research*, 41(7), 642-650.

Shi, C., Jiménez, A. F., & Palomo, A. (2011). New cements for the 21st century: the pursuit of an alternative to Portland cement. *Cement and Concrete Research*, 41(7), 750-763.

Toutanji, H., Delatte, N., Aggoun, S., Duval, R., & Danson, A. (2004). Effect of supplementary cementitious materials on the compressive strength and durability of short-term cured concrete. *Cement and Concrete Research*, 34(2), 311-319.

Turner, L. K., & Collins, F. G. (2013). Carbon dioxide equivalent (CO_2-e) emissions: A comparison between geopolymer and OPC cement concrete. *Construction and Building Materials*, 43, 125-130.

Vizcaíno-Andrés, L. M., Sánchez-Berriel, S., Damas-Carrera, S., Pérez-Hernández, A., Scrivener, K. L., & Martirena-Hernández, J. F. (2015). Industrial trial to produce a low clinker, low carbon cement. *Materiales de*

Construcción, 65(317), 045.

Wang, S. D., Pu, X. C., Scrivener, K. L., & Pratt, P. L. (1995). Alkali-activated slag cement and concrete: a review of properties and problems. *Advances in Cement Research*, 7(27), 93-102.

Worrell, E., Martin, N., & Price, L. (2000). Potentials for energy efficiency improvement in the US cement industry. *Energy*, 25(12), 1189-1214.

Worrell, E., Price, L., Martin, N., Hendriks, C., & Meida, L. O. (2001). Carbon dioxide emissions from the global cement industry. *Annual Review of Energy and the Environment*, 26(1), 303-329.

Wuana, R. A., & Okieimen, F. E. (2011). Heavy metals in contaminated soils: a review of sources, chemistry, risks and best available strategies for remediation. *Isrn Ecology*, 2011.

Xu, J. H., Fleiter, T., Fan, Y., & Eichhammer, W. (2014). CO_2 emissions reduction potential in China's cement industry compared to IEA's Cement Technology Roadmap up to 2050. *Applied Energy*, 130, 592-602.

CHAPTER 2 COMPARATIVE REVIEWS ON TWO TYPES OF GEOPOLYMERS

Geopolymer as an attractive inorganic binder has received many concerns from civil, environmental and material researchers. This chapter mainly presents the state-of-the-art reviews on the silico-aluminophosphate geopolymer in terms of terminology and classification, formation model and mechanism, metal ions chemistry involved during geopolymerization, environmental impacts, and their current performance and durability. In addition, the multi-disciplinary potential applications of the silico-aluminophosphate geopolymer are also introduced after metal ions modification. The alkali-aluminosilicate geopolymer is referred throughout.

2.1 Background

Cement is usually described as a cohesive material that can set and bind other materials together (Taylar, 1997). Generally, when the cement encounters water, cement hydration takes place and generates cementitious hydrates. The chemical and physical evolutions in microstructures of the formed hydrates allow the cement matrix to achieve strength. These developments always proceed as a function of time, but also are influenced by the servicing environment of the cement matrix. According to the cement setting mechanism, cement can be classified into three categories: hydraulic cement, condensation cement and acid-base cement (Wilson and Nicholson, 2005).

2.1.1 Cement classification

Hydraulic cement is the most commonly-used building material in the bulk construction applications. The setting process of hydraulic cement is characterized by two chemistries called the hydration and the precipitation. A typical representative of such cement group is the ordinary Portland cement (OPC), whose hydration products include four main components (Bullard et al., 2011): (1) tri-calcium silicate (C_3S, $3CaO \cdot SiO_2$), (2) di-calcium silicate (C_2S, $2CaO \cdot SiO_2$), (3) tri-calcium aluminate (C_3A, $3CaO \cdot Al_2O_3$) and (4) tetra-calcium ferroaluminate (C_4AF, $4CaO \cdot Al_2O_3 \cdot SiO_2$) (Neville, 2011). The term of ‘hydration’ is described as the chemical involvement of water to form the calcium silicate hydrate (C-S-H) gels, while ‘precipitation’ denotes the production of calcium hydroxide (C-H) and hydrogarnet (C_3AH_6). The main reactions of cement hydration are shown below (Eq. 2.1-2.4):

$$Clinker + Water \Rightarrow Gel + Precipitate \tag{2.1}$$

$$C_3S + H_2O \Rightarrow C - S - H + C - H \tag{2.2}$$

$$C_2S + H_2O \Rightarrow C - S - H + C - H \tag{2.3}$$

$$C_3A + H_2O \Rightarrow C_3AH_6 \tag{2.4}$$

The formation process of condensation cement is mainly based on a condensation polymerization, where the loss of water is due to the condensation of two hydroxyl groups (shown in Eq. 2.5) (Davidovits, 2011). Water acts as a mixing medium and evaporates eventually; however fast evaporation of water leads to dry-induced crack and shrinkage that degrades the mechanical performance and durability of the matrix. Therefore, high-humidity curing is usually imperative to yield a condensation cement matrix with moderate strength behavior. An example of the condensation cement is alkali-activated metakaolin (or low calcium coal fly ash) cement. The catalysis of hydroxide ion facilitates the disintegration of aluminosilicate precursor to form isolated aluminate (IV) and silicate (IV) species (De Jong et al., 1983). The setting stemmed from the condensation of aluminates and silicates along with their elevating concentrations (Provis et al, 2015). The condensation process reforms the high-connectivity gels with chain or ring network structures. This process is conceptually displayed in Eq. 2.6.

$$P - OH + HO - Q \xRightarrow{\substack{catalysis \\ \text{‘}activation\text{’}}} P - O - Q + H_2O \tag{2.5}$$

where, P and Q in Eq. 2.5 denote two different aluminate or/and silicate groups.

$$\equiv Si - OH + HO - Al \equiv \xRightarrow{high\ alkali} \equiv Si - O - Al \equiv + H_2O \tag{2.6}$$

As the name implied, the acid-base cement (ABC) chemistry primarily involves an acid-base reaction and some hydration/hydrolysis reactions (Wilson and Nicholson, 2005). As shown in Eq. 2.7, the release of cations from the metal oxides is the first step (hydrolysis reaction), where the hydration reactions enable the formation of aquo ions (hydration reaction in Eq. 2.8). The polyacids generated by the acidic salt or acid react with the oxide-formed aquo ions. The acid-base reaction is described in Eq. 2.9. The whole conversion from sols to gels is exothermic and rapid, and the resulting products are gel-like phases with good crystallinity and excellent adhesive property. Magnesium potassium phosphate cement (MKPC) is a typical ABC (Ma et al., 2014; Wang and Dai, 2017). The occurrence of MKPC is a through-solution chemical reaction (Eq. 2.10) undergoing the dissolution of MgO and KH_2PO_4 to the crystallization of hexahydrate, $MgKPO_4$ $6H_2O$ (Struvite-K). According to the standard enthalpies of formation of the reactants and resultant (shown under Eq. 2.10), this process is an exothermic reaction and theoretical reaction heat is 124 kJ/mol when 1 mol KH_2PO_4 is completely reacted with magnesia (Chau et al., 2011).

$$MO_{\frac{p}{2}} + \frac{p}{2}H_2O \Rightarrow M^{p+} + pOH^- \tag{2.7}$$

$$M^{p+} + qH_2O \Rightarrow [M(H_2O)_q]^{p+} \tag{2.8}$$

$$H_nPO_4^{-(3-n)} + [M(H_2O)_q]^{p+} \Rightarrow [M(H_nPO_4)]^{n+p-3} + qH_2O \tag{2.9}$$

$$MgO + KH_2PO_4 + 5H_2O \rightarrow MgKPO_4 \cdot 6H_2O \tag{2.10}$$

ΔH_f(kJ/mol) -602 -1568 -286 -3724 $\Delta H = -124$

2.1.2 Geopolymer cement

Geopolymer cement as a promising substitute for the conventional cement was poured into many attentions recently. Initially, geopolymer was strictly defined as the alkali-activated aluminosilicates without (or with little) impurity (e.g., metakaolin), and the dissolution and rearrangement of aluminate and silicate species under an alkaline environment are emphasized. Afterwards, the aluminosilicate precursor activated by phosphoric acid to generated phosphate-based geopolymer was proposed (Wagh, 2005). The catalytic process of un-doped aluminosilicate precursor transforming into geopolymer cement is assisted by extra energy (e.g., heat, ultraviolet, and microwave) or long curing periods depending on the reactivity of the aluminosilicate used (Agarwal, 2006). These special curing methods are acceptable in precast geopolymer products, yet very challenging to its in-situ construction and operation (Provis and Bernal, 2014). It is therefore imperative to introduce other chemical processes to induce a fast hardening mechanism of geopolymer at ambient temperature.

In alkali-activated systems, the calcium-containing solid aluminosilicate source (e.g., ground granulated blast-furnace slag [GGBS]) under high alkaline environment is habituated to form C-(A)-S-H gels rapidly (Li et al., 2010; Shi and Qian, 2000; Wang et al., 1994). This chemical product presents some features similar to hydraulic cement. In the meantime, soluble silicates (sometimes mixed with aluminates, Benavent et al., 2016) are generally mixed in the alkaline activating solution, with the same aim to obtain a rapid sol/gel transition. These actions equip the formed matrix with high excellence, inducing an alkali-aluminosilicate geopolymer ‘hybridized’ by hydraulic cement and condensation cement.

As a comparison, in phosphate-activated system, some solid agents (e.g., alkali metals) can be incorporated into the aluminosilicate source to induce an acid-base chemistry, which generally facilitates to form crystalline or amorphous phosphate phases (e.g., magnesium/calcium phosphate) during chemical process of the aluminosilicates (Wagh, 2016). Similarly, a ‘hybrid’ silico-aluminophosphate geopolymer (condensation cement and acid-base cement) is formed.

Currently, the aluminosilicate sources used for the geopolymer fabrication are prone to employ the industrial byproducts (e.g., CFA and GGBS) rather than the natural materials (e.g., MK) for environmental concerns. These industrial raw materials are often complex due to their diverse production technologies (Pacheco-Torgal et al., 2008; Yao et al., 2015; Xu and Shi, 2018). Thus, some 'impurities' (here, the impurities mean other components except aluminosilicate) in the byproducts will induce other chemistries during geopolymerization, and different activation conditions (e.g., acidic and alkaline) generate different chemical compositions, crystallinities and phases. Thus, according to acidic and alkaline activation conditions, the formation process of the impurity-contained geopolymer is illustrated in Fig. 2.1.

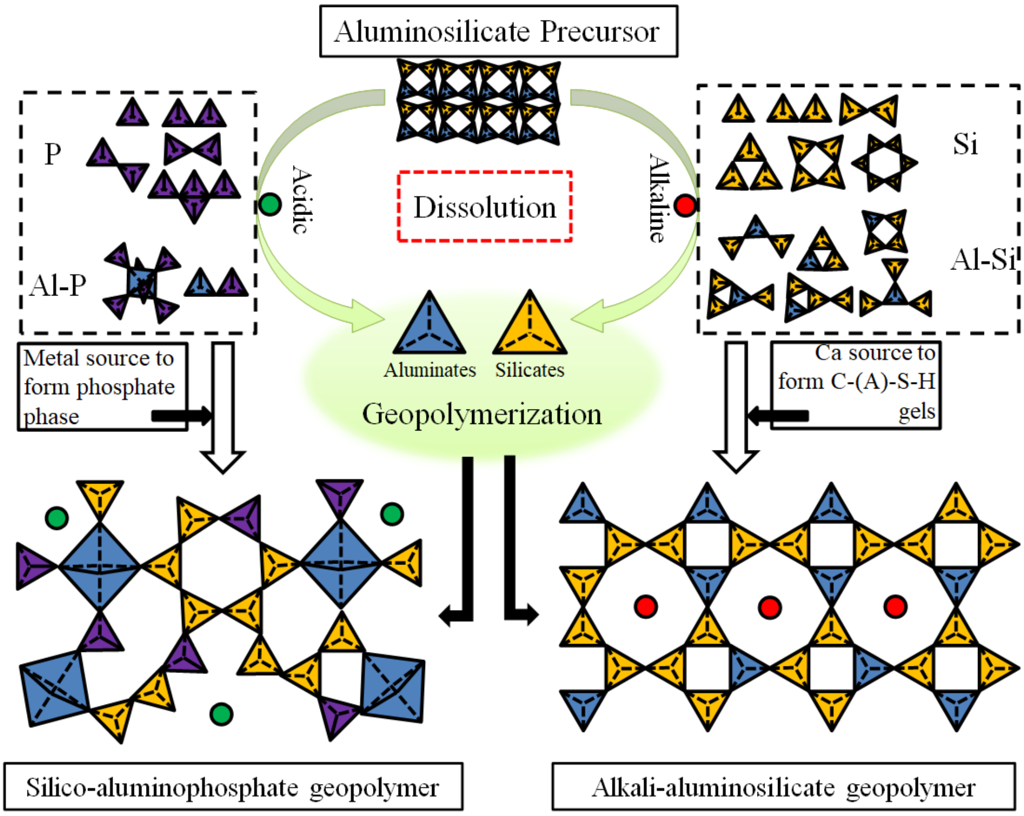

Fig. 2.1 Activation process of aluminosilicate sources under acidic and alkaline conditions to be geopolymer matrices

2.2 Terminology and Classification

The terminology of ‘Portland cement’ is internationally recognized as a commercial name. It was initially derived from the resemblance of the color and quality of the hardened cement to Portland stone (limestone rock) available in the Dorchester region in England (Neville, 2011). Although modern Portland cement is modified by some admixtures for multi-function, the term ‘Portland cement’ has been followed up to now.

The alkali-activated material (AAM) was widely concerned since 1908, which was explained as a traditional cement-like material formed by the reaction between an aluminosilicate precursor and an alkaline activator (Provis, 2014; Provis and Bernal, 2014). The tranquility was then broken by the term ‘geopolymer’ coined by Davidovits who inadvertently produced an inorganic polymer-like material with good fire-resistance (Davidovits, 2011). The initial ‘geopolymer’ was predominantly confined to the binder prepared by the aluminosilicate sources with marginal impurity. The term ‘geopolymer’ mainly highlighted the chemical behaviors of aluminate and silicate species, including bonds breaking (decomposition reaction) and remaking (polymerization reaction). The empiric formula of the initial geopolymer is shown in Eq. 2.11 (alkali-aluminosilicate geopolymer) and Eq. 2.12 (silico-aluminophosphate geopolymer) (Davidovits, 2011; Wagh, 2016; Cui et al., 2008).

$$M_n[-(SiO_2)_z - AlO_2]_n . mH_2O \qquad (2.11)$$

where n is the degree of geopolymerization, z is 1, 2 or 3, and M is an alkali cation (e.g., K or Na).

$$[-(\mathrm{Si} - \mathrm{O})_z - \mathrm{Al} - \mathrm{O} - \mathrm{P}]_n . mH_2O \qquad (2.12)$$

where n is the degree of geopolymerization.

Recently, the term of ‘chemically activated materials (CAMs)’ was also proposed to describe the aluminosilicate sources that can be formed into a cementitious matrix using some chemical solutions (e.g., alkali-silicate and phosphate solution). However, the term of geopolymer seems to be more attractive to (even widely-used by) engineers because of its concision. In this thesis, the binders primarily prepared by aluminosilicate materials and some activating solutions are all termed as geopolymer for the convenient circulation in academic, engineering and business communities, and it is classified two categories according to the activation approach: alkali-aluminosilicate geopolymer and silico-aluminophosphate geopolymer. The silico-aluminophosphate geopolymer is placed a significant emphasis in this thesis.

2.3 Formation Model and Mechanism of Geopolymer

2.3.1 Alkali-aluminosilicate geopolymer

As commonly explained, the three dimensional network of alkali-aluminosilicate geopolymer is configured with the negative $[AlO_4]^{5-}$ and $[SiO_4]^{4-}$ tetrahedrons and positive alkali metal ions (e.g., Na^+ or K^+) (Duxson et al., 2007; Buchwald et al., 2011). Recent researches have indicated that the hydroxyl free radicals ($\cdot OH$) released in the alkaline solutions catalyze to disintegrate the aluminosilicate precursor by breaking the bonds of Si-O-Si, Al-O-Si and Al-O-Al and to promote the reconstruction of the isolated aluminate and silicate anions by remaking the bonds of Si-O-Si, Al-O-Si and Al-O-Al (Feng et al., 2016). Thus, the tetrahedrons of silicon and aluminum are united together by oxygen bridges to form the high-connectivity chain or ring network structure. The negative charge given by tetra-coordinated aluminum is compensated by the alkali metal ions (Duxson et al., 2005; Xu et al., 2001; Provis et al., 2005a). However, the lower-silica gels in geopolymer matrix (e.g., a high molar ratio of Na_2O/SiO_2 in activating solution or a low molar ratio of Si/Al ratio in aluminosilicate source) tend to be formed into some loose particulate units (i.e., pseudo-zeolitic structure, mainly Q^4) rather than a continuous well-connected sodium-aluminate-silicate-hydrate (N-A-S-H) gel (Provis et al., 2005b; He et al., 2013b; Provis and Bernal, 2014). It was found that a reasonable content of silicate species in the activating solution could contribute to yielding a compact alkali-aluminosilicate geopolymer matrix with more continuous gels, especially when using solid aluminosilicate precursor with low Si/Al ratio.

As shown in Fig 2.2, the results from solid-state nuclear magnetic resonance (NMR) confirm the chemical environment of silicon and aluminum in the calcium-free geopolymer made by low-impurity aluminosilicate precursor. The higher intensity of the Q_4(4Al) (in Fig. 2.2a) and AlO_4 (in Fig. 2.2b) signals indicates that the tetra-coordinated silicate and aluminate species dominate in N-A-S-H gels formed in alkali-aluminosilicate geopolymer.

A low-calcium coal fly ash-based geopolymer activated by the alkaline solution was typically explained in Fig. 2.3, showing that the microstructure (Fig. 2.3a) and strength (Fig. 2.3b) development of the alkali-aluminosilicate geopolymer made by low-impurity aluminosilicate byproduct. The coal fly ash grains from one point to a large hole, until (almost) complete dissolution, are transformed to be a dense geopolymer matrix with useful strength (Fernández-Jiménez et al., 2005; Fernández-Jiménez et al., 2006). A three-stage corresponding relationship between microstructure evolution and geopolymerization is established to interpret the mechanical strength development in alkali-activated CFA-based geopolymer (Fernández-Jiménez et al., 2006). The first stage is the dissolution stage of the glassy aluminosilicate phase. As the matrix was not formed during this period, no mechanical property is observed. The second stage is the induction period, where massive metastable gels (denoted Gel 1) are formed and precipitated. Since the dissolution of silica is slower than that of alumina, Gel 1 is mainly enriched with reactive aluminum and associated with the initial setting of the paste. At this stage, the mechanical strength development is just initialized. The final stage is the silicon incorporation stage that described the transformation from Gel 1 to Gel 2. Reactive aluminum is embedded into the Si-rich gel to form Gel 2. After geopolymer matrix formation, when the content of Gel 1 is higher than that of Gel 2, the mechanical strength is lower. Conversely, the mechanical strength can achieve higher value in case of the content of Gel 2 outnumbering that of Gel 1.

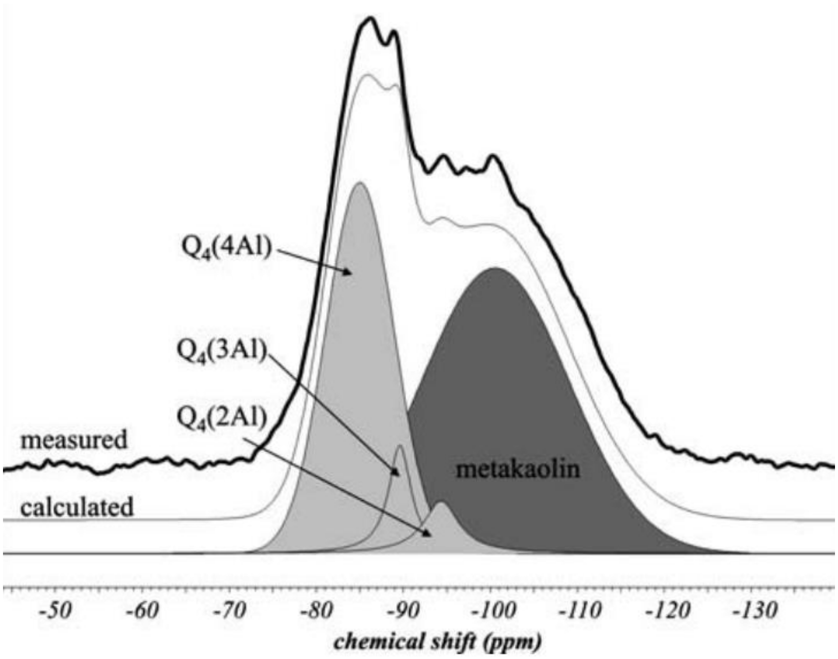

(a) ^{29}Si NMR spectrum

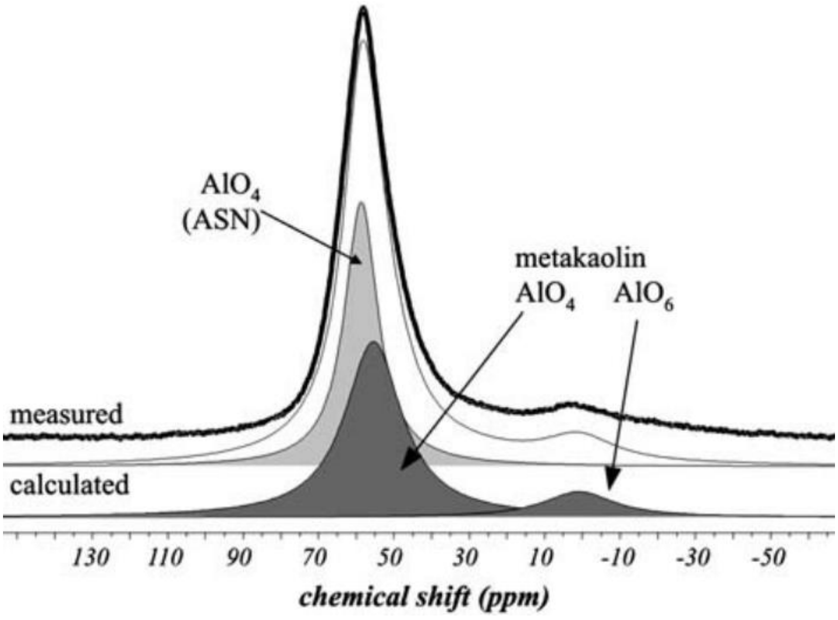

(b) ^{27}Al NMR spectrum

Fig. 2.2 Molecular structure and chemical environment of silicon and aluminum in calcium-free alkali-aluminosilicate geopolymer system confirmed by solid-state NMR (Buchwald et al., 2007). (Note: ASN in Fig. 2.2b means aluminosilicate network)

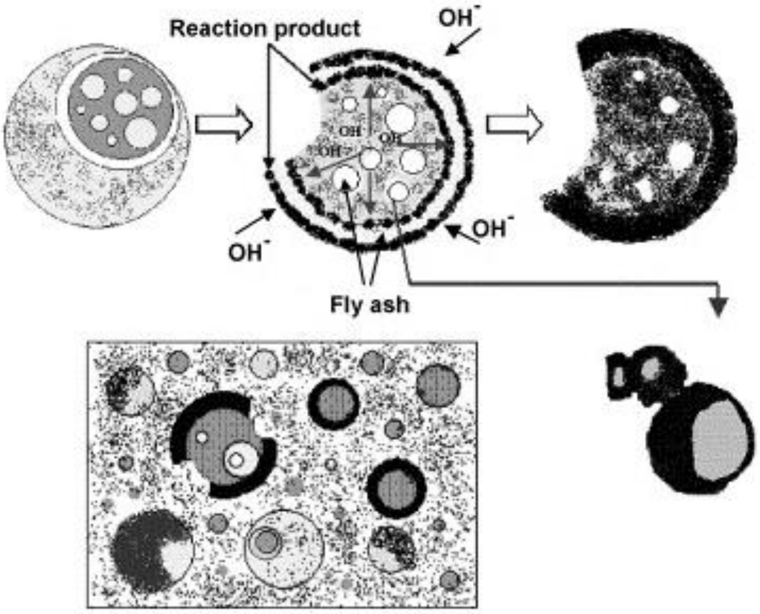

(a) Microstructure evolution

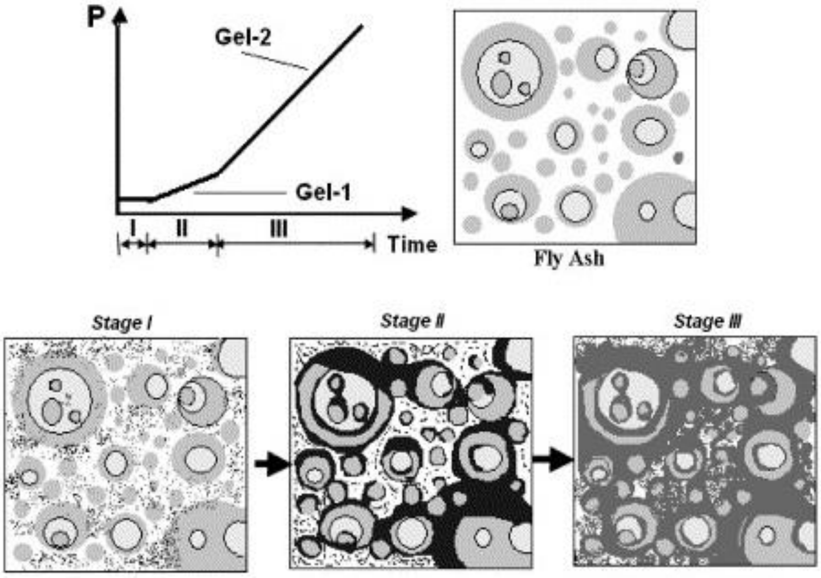

(b) Mechanical strength development

Fig. 2.3 A typical example of low-calcium CFA-based geopolymer

(Fernández-Jiménez et al., 2005)

2.3.2 Effect of 'impurity' in alkali-aluminosilicate geopolymer

Regarding the role of calcium in alkali-aluminosilicate geopolymer, it is usually claimed that the calcium aluminate silicate hydrate (C-A-S-H) gels with a tobermorite-like structure (mostly Q^2 and some Q^1) are generated (Richardson et al., 1994). Figure 2.4 shows an alkali-activated GGBS binder. The combined utilization of GGBS and low-calcium CFA can produce N-A-S-H and C-A-S-H gels, which are entangled together to form a compact geopolymer matrix. The molecular structure of C-A-S-H gels in high-calcium alkali-aluminosilicate geopolymer can be generalized as the Al-substituted C-S-H gel (Richardson et al., 1993; Brough et al., 2001; Lodeiro et al., 2010). The C-A-S-H gels have a Ca/Si ratio lower than that formed in Portland cement (Wang et al., 1995). This interpretation is similar to the feature of supplementary cementitious materials in OPC, where Si-rich SCMs improved the lower Ca/Si ratio and consume portlandite, while Al-rich SCMs promote the Al-uptake of hydration products (Lothenbach et al., 2011).

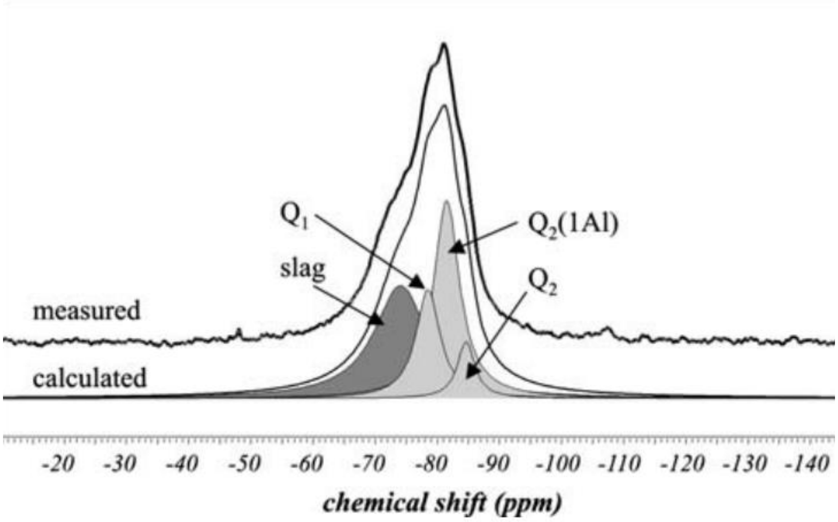

(a) ^{29}Si NMR spectrum

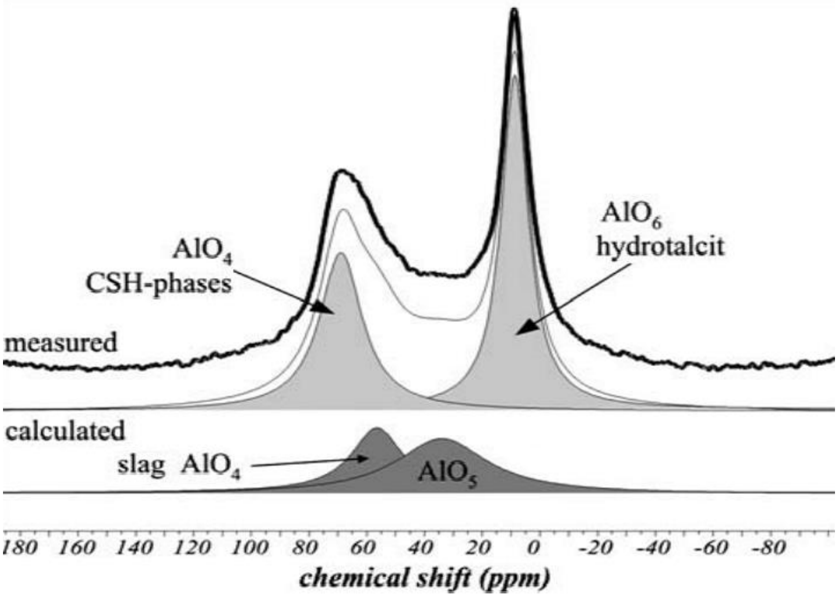

(b) ^{27}Al NMR spectrum

Fig. 2.4 Molecular structure and chemical environment of silicon and aluminum in high-calcium alkali-aluminosilicate geopolymer system confirmed by solid-state NMR (Buchwald et al., 2007)

Although the glassy aluminosilicate source with high calcium content in alkali environment easily generates C-A-S-H gels, the reactivity of calcium available in raw materials may be substantially different depending on its existence forms. The GGBS and high-calcium CFA have similar calcium and glassy aluminosilicate contents; however they behave differently in the alkali activation process. The high reactivity of GGBS is mainly attributed to the fast cooling technology (e.g., water quenching granulation), generating amorphous phases with the network-forming anions $[SiO_4]^{4-}$, $[AlO_4]^{5-}$ and $[MgO_4]^{6-}$, and network-modifying cations Ca^{2+} and Al^{3+} and Mg^{2+} (Garcia-Lodeiro et al., 2015). The existence of calcium species can lower the polymerization degree of silicon network, which can equip the slag with high pozzolanic activity. On the contrary, the high-calcium CFA particle usually forms crystalline phases (e.g., mullite and quartz), which present little or no cementitious properties by a slow cooling collection method. Therefore, the use of high-calcium CFA as a main raw material for the preparation of alkali-aluminosilicate geopolymer at room temperature is a great challenge.

In many studies on the durability and mechanical property studies of alkali-aluminosilicate geopolymer (Bernal et al., 2015; Bernal et al., 2016; Ismail et al., 2013; Ismail et al., 2014), the combination of GGBS and CFA as aluminosilicate precursors with a certain ratio (e.g., GGBS/CFA mass ratio of 1:3) can empirically meet the engineering requirements in a whole serve life. The incorporation of low-calcium source as a kind of supplementary of alumina and silica to high-calcium raw materials greatly affects the formation of the main binding gels (Bernal et al., 2016). The N-A-S-H type gels generated in low-calcium system exhibit a slower reaction compared to the C-A-S-H type gels in high-calcium system, but promote a highly cross-linked and compact product by extending the curing time (Bernal et al., 2016). In other words, the synergistic effect of the high and low-calcium aluminosilicate precursor is witnessed in the coexistence of these molecular structures, where the C-A-S-H gels ensure the early performances (e.g., setting time and early strength), and the N-A-S-H gels contribute to the long-term attributes (e.g., durability and strength development).

2.3.3 Silico-aluminophosphate geopolymer

Long history of Egyptian pyramids has well proven their reliability and durability for thousands of years. It was found that the surface of pyramid blocks was covered with a white/red coating which was complicated phosphate geopolymeric system made of crystalline hydroxyapatite and brushite embedded in a poly(sialate) matrix (Barsoum et al., 2006; Davidovits, 2011). The previous explorations (Kingery, 1950; Kingery, 1952; Tseitlin and Eltysheva, 1964; Tseitlin and Gubatenko, 1968) on aluminosilicate sources consolidated by phosphates or orthophosphoric acid for preparing refractory castables can be regarded as phosphate activation approach to aluminosilicate precursors, forming a silico-aluminophosphate geopolymer with excellent durability and high temperature resistance (Wagh, 2005). The formation process of such geopolymers occurs in acidic or low alkaline medium. The phosphate or phosphoric acid can be used as an activator to excite the aluminosilicate precursors, yielding the condensed poly(silicate-aluminate-phosphate) in geopolymer binder (Cao et al., 2005; Liu et al., 2010).

Regarding the molecular structure in the silico-aluminophosphate geopolymer, the $[AlO_4]^{5-}$, $[SiO_4]^{4-}$ and $[PO_4]^{3-}$ units act as basic blocks (He et al., 2013a). Compared with alkali-aluminosilicate geopolymer, the $[PO_4]^{3-}$ unit replaces the alkali metal ion as shown in Fig. 2.5. This model reveals that partial replacement of $[SiO_4]^{4-}$ unit by $[PO_4]^{3-}$ in the broken Si-O-Al bonds may occur in low polymeric network (Cui et al., 2011). Thus, the charge balance within the molecular structure can be achieved without the involvement of monovalent cations. Cao's interpretation showed that the updated Si-O-Al linkage (i.e., Al-O-P) can balance the charge due to the aluminum chemical shift ranging from octahedral or/and pentahedral coordination to a tetradentate form (Cao et al., 2005). However, many studies indicated that the hexa-coordinated aluminum dominates in the silico-aluminophosphate geopolymer (Davidovits, 2011; Louati et al., 2014; Louati et al., 2016).

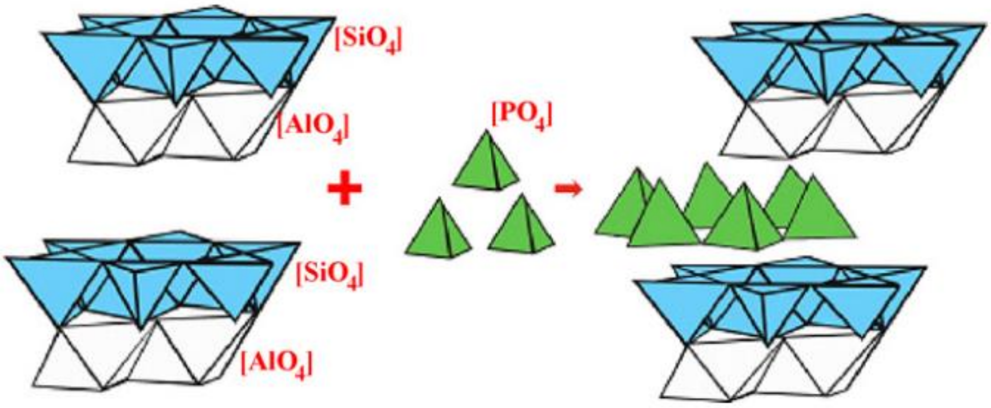

Fig. 2.5 Molecular structure model of silico-aluminophosphate geopolymer (Cui et al., 2011)

Since the model for microstructure evolution of silico-aluminophosphate geopolymer was barely reported according to our knowledge, some result-derived interpretations and hypotheses can be found in the literatures (Cui et al., 2008; Cui et al., 2011; Wagh, 2005; Duxson et al., 2007). Cui synthesized the silico-aluminophosphate geopolymer using pure Al_2O_3-$2SiO_2$ powders (synthesized in the lab) and phosphoric acid with a P/Si molar ratio of 1.2 (Cui et al., 2011). The XRD patterns showed no clear crystalline peak in phosphate activated geopolymers. Instead, a broad diffuse peak in the range of 15 ° to 40 ° (2θ) appeared in all the samples. The angle of diffraction peak was shifted from 22° (2θ) in calcined Al_2O_3-$2SiO_2$ powder to about 26 ° (2-theta) in geopolymers; however the diffraction intensity was marginally changed. It was claimed that the molecular structure and interlayer spacing were chemically shifted after geopolymerization in acid phosphorus environment compared with the raw Al_2O_3-$2SiO_2$ powders.

Besides, the natural aluminosilicate materials, e.g., Tunisian clay in Fig. 2.6a and metakaolin in Fig. 2.6b, activated by phosphate acid with various molar ratios of Si/P were investigated (Douiri et al., 2014; Louati et al., 2014). As shown in Fig. 2.6, a shift in the wide broad band from 18-30° (2θ) to 22-35° (2θ) in calcined clay and synthesized geopolymers was detected. Further, changes of the peak intensity were observed in some crystalline, e.g., aluminum phosphate ($AlPO_4$), augelite ($Al_2(PO_4)(OH)_3$) and monetite ($CaHPO_4$). These pattern differences between raw aluminosilicates and phosphate-activated aluminosilicates (i.e., silico-aluminophosphate geopolymer) can be attributed to the geopolymerization of the aluminosilicate precursors.

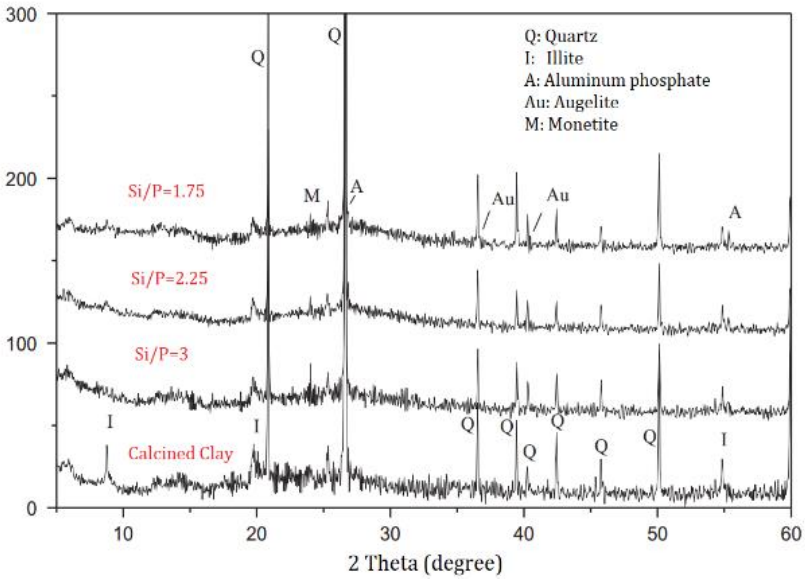

(a) Tunisian clay-based phosphate geopolymer

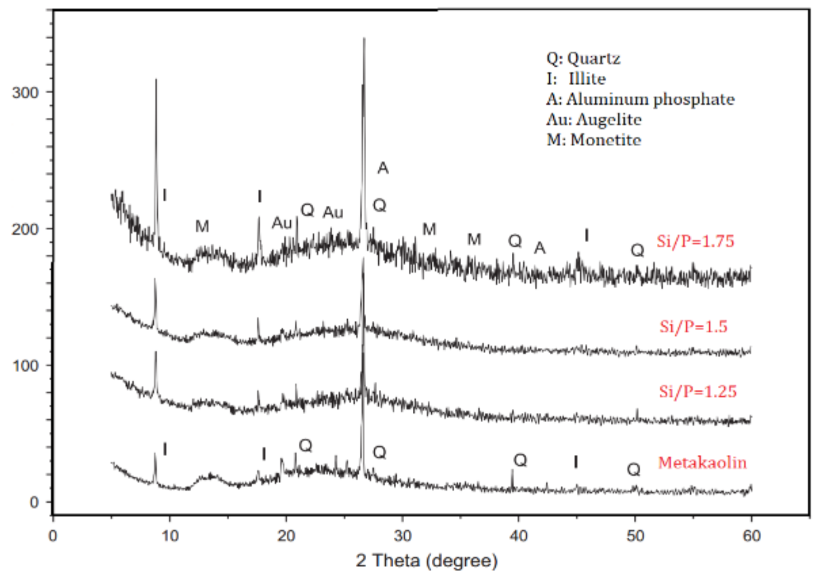

(b) Metakaolin-based phosphate geopolymer

Fig. 2.6 Shift of broad band and peak between aluminosilicate precursors and synthesized geopolymer with various molar ratio of Si/P (Douiri et al., 2014; Louati et al., 2014)

Perera also performed a thorough study on the comparison of metakaolin-based geopolymer activated by alkali and phosphate (Perera et al., 2008). Similar to Cui's observation (Cui et al., 2011), XRD results reveal that the silico-aluminophosphate geopolymer was amorphous. Perera further investigated these amorphous phases by the transmission electron microscope (TEM) equipped with energy dispersive X-ray spectroscopy (EDXS) and selected area electron diffraction (SAED). Figures 2.7a and 2.7b show the TEM image of phase structure in silico-aluminophosphate geopolymer and its SAED image, respectively. The element EDXS analysis revealed that the phase structure (Fig. 2.7a) contains Si, Al, P and O, while the SAED image exhibits some blurred rings and spots instead of crystal lattices, which supports the amorphous phase in silico-aluminophosphate geopolymer.

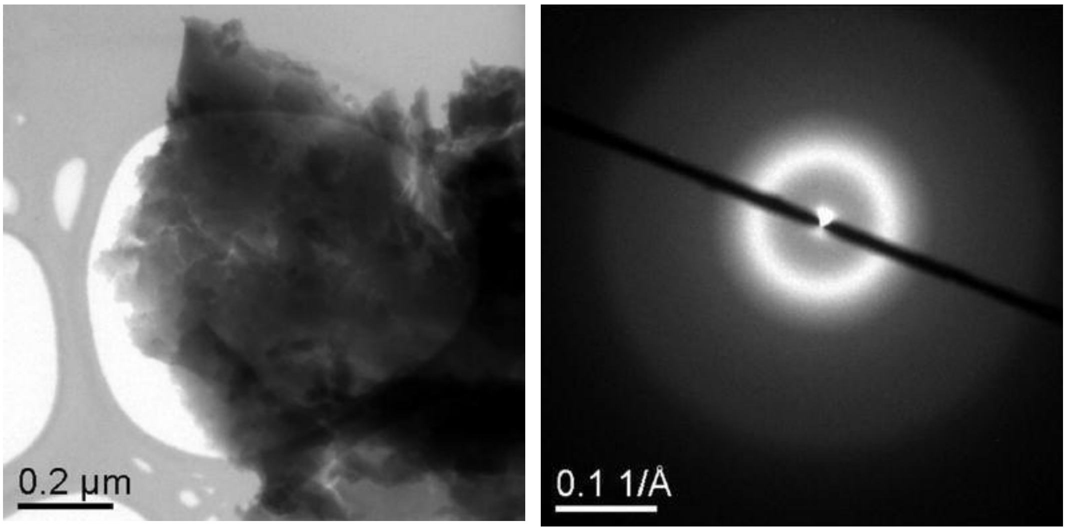

(a) TEM images (b) SAED images

Fig. 2.7 TEM and SAED images of the amorphous phases in silico-aluminophosphate geopolymer (Perera et al., 2008)

Furthermore magic angle spinning nuclear magnetic resonance (MAS-NMR) analysis was carried out on the silico-aluminophosphate geopolymer as shown in Fig. 2.8. A single $[PO_4]^{3-}$ resonance was observed at around -16 ppm, which can be deconvolved into two resonances (-4 ppm and -16 ppm) due to its asymmetric line shape. A cross polarization (CP) NMR was employed to enhance the dominance at -16 ppm. The ^{27}Al results indicated that the main chemical environment of aluminum in silico-aluminophosphate geopolymer was six-coordination (VI) as evidenced by the single resonance at an apparent shift of around -12 ppm. Thus, the phosphate activation promotes metakaolin to produce a mixed octahedral Al(VI) environment with both P and Si which influence the oxo-bridged second coordination sphere. This was mainly different from the alkali-aluminosilicate geopolymer, where Al(VI) was converted to tetrahedral sites. Three resonances (e.g., -91.8, -101.6 and -110.8 ppm) in ^{29}Si NMR curve were explained to describe Q^3, Q^4 (Al or P) and Q^4(Si) chemical environments, respectively. The intensity of Q^3 was lowest, which means that most of metakaolin was dissolved. Q^4 (Al or P) was assigned as the mixed environment of Si-Al-P phase in silico-aluminophosphate geopolymer, while Q^4(Si) was described as siliceous or Al-free portions (Cao et al., 2005) that might not fully connect to P phase.

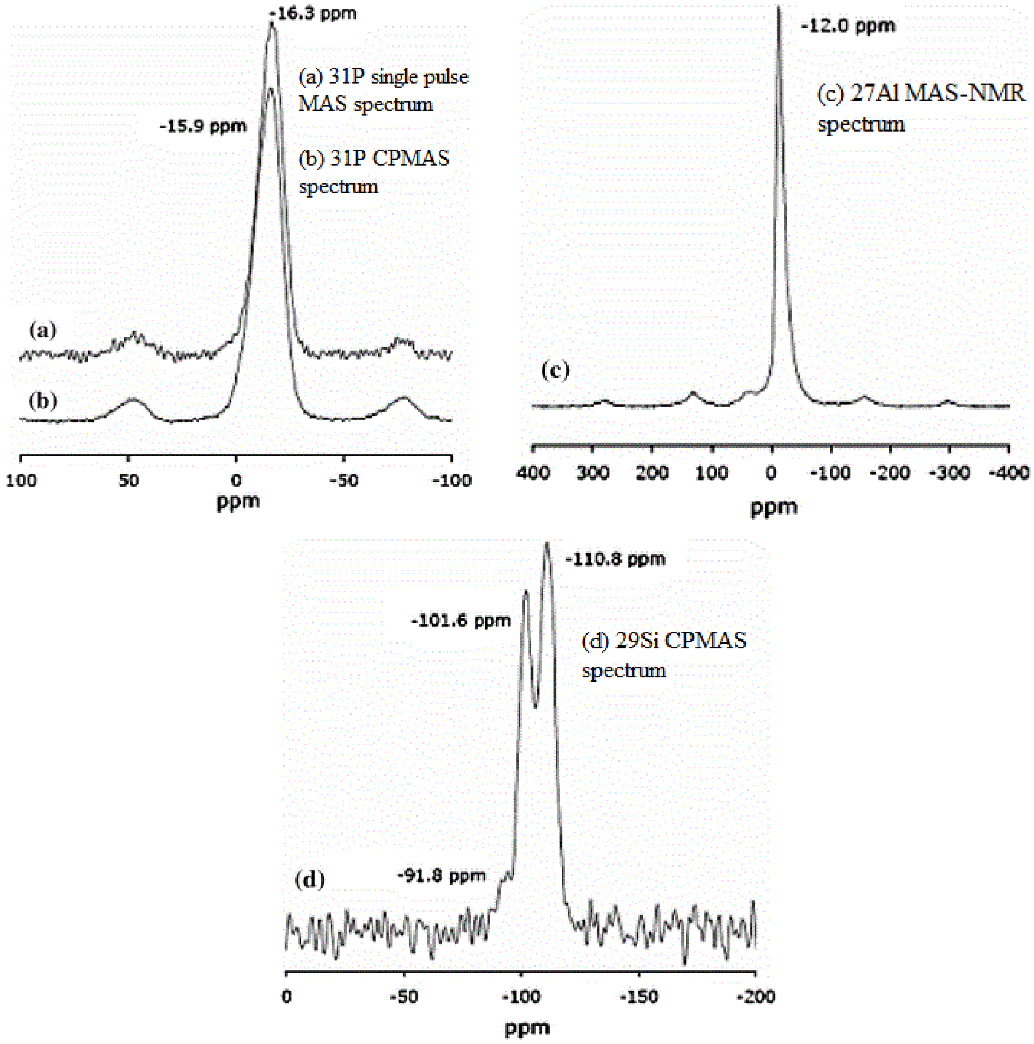

Fig. 2.8 MAS-NMR patterns of silico-aluminophosphate geopolymer (Perera et al., 2008)

2.3.4 Effect of 'impurity' in silico-aluminophosphate geopolymer

Incorporating setting agents (e.g., solid Mg/Ca source) into aluminosilicate precursors can induce a room-temperature-setting silico-aluminophosphate geopolymer matrix (Luz et al., 2015). In addition to geopolymerization, the acid-base reaction between the setting agents and phosphate species takes place, which can modify the early performance of this geopolymer. The chemistry of these setting agents is described below.

Phosphate cement is a general term that describes the phosphates as a main ingredient of cement (Walling and Provis, 2016). Since phosphate cement is usually a binder that hardens through acid-base and/or hydrolysis chemical reactions (usually generate crystalline phosphates as main products) at room temperature, it is also named as chemically bonded phosphate ceramic (CBPC) (Roy, 1987). CBPCs were discovered and developed as dental cements in the 19th century, and extended to construction field as patching materials for rapid rehabilitation of runway and bridge. The occurrence of CBPC experiences the dissolution of metal oxides and phosphates to form a crystalline structure with excellent adhesive and mechanical properties. It is expected that this chemistry can be introduced into silico-aluminophosphate geopolymer as a room temperature hardening mechanism, addressing its weak early properties.

The dissolution of metal oxides during CBPC formation is directly linked to the reaction rate and heat. However, the high violence reaction process between metal oxides and phosphate solution (e.g., rapid and exothermal) fails to form the well-crystallized phases, which may compromise the matrix strength. Dead-burnt metal sources processed by an ultra-high temperature (exceeding 1600 ℃) present a reduced reactivity (e.g., dead-burnt calcite and magnesia), which is suitable to enhance the early properties of silico-aluminophosphate geopolymer when mixed and matched with the aluminosilicate precursor.

Calcium phosphate cement (CPC) as a bioceramic has been applied in orthopedic industry due to its excellent bioactivity and biocompatibility (Chow, 2001; Ishikawa, 2014). The chemical process during the CPC setting reaction mainly involves three stages: dissolution, supersaturation and precipitation (Zhang et al., 2014). In the acid phosphate solution, the calcium donors slowly release the calcium ions, and react with (hydro)-phosphate groups to form a supersaturated solution (i.e., paste). When reaching the critical values (e.g., ions concentration and pH condition), new phase is nucleated, precipitated and grows as the continuous dissolution of calcium.

According to the composition of final products, the CPC includes apatite cement (β-tricalcium phosphate, $Ca_5(PO_4)_3(OH/Cl/F)$ or $Ca_3(PO_4)_2$) and brushite cement ($CaHPO_4 \cdot 2H_2O$) (Ishikawa, 2014). In general, the type of final products of the calcium phosphate cement is closely associated with the raw material (e.g., solubility and Ca/P ratio) and reaction conditions (e.g., pH value and hydrothermal environment). The chemical process involved in the CPC can be described as Eqs. (2.13, 2.14 and 2.15).

$$3Ca^{2+} + 2[H_nPO_4]^{n-3} \rightarrow Ca_3(PO_4)_2 + 2nH^+ \tag{2.13}$$

$$5Ca^{2+} + 3[H_nPO_4]^{n-3} + H_2O \rightarrow Ca_5(PO_4)_3(OH) + (3n+1)H^+ \tag{2.14}$$

$$Ca^{2+} + [H_nPO_4]^{n-3} + 2H_2O \rightarrow CaHPO_4.2H_2O + (n-1)H^+ \tag{2.15}$$

Fresh CPC is a castable paste, which provides an attraction for the bone defect reconstruction with minimum invasive surgery because it can be resorbed under physiological conditions after embedding into the body (Larsson and Bauer, 2002; Tamimi et al., 2012). Thus, the moldable properties of Ca-blended silico-aluminophosphate geopolymer extend its applications to three-dimension (3D) printing in civil engineering.

As one of the most typical CBPCs, magnesium phosphate cement (MPC) is widely used in civil engineering because of its excellent early performance. In the early stage, the MPC is fabricated with magnesia and phosphoric acid. The lower pH environment induces a rapid and highly exothermic reaction, where the reaction product is water-soluble magnesium dihydrogen phosphate ($Mg(H_2PO_4)_2.nH_2O$). Subsequently, attempts were made to use less acidic diphosphate (Sugama and Kukacka, 1983; Soudée and Péra, 2000). The employment of diphosphate and calcined magnesia further mitigates the reaction rate and heat during MPC formation. The diphosphates are soluble in water to create an acid environment, which facilitates the dissolution of magnesia. When concentration and pH are approaching ideal value, crystal generation and growth occurs in the supersaturated slurry (Chauhan et al., 2011). The general reaction of MPC is described in Eq. 2.16. The resulted phase is crystalline struvite or its analogues (e.g., struvite-K or struvite-Na) with 6-8 crystal waters (Chauhan et al., 2011; Chauhan et al., 2014). These hydrates have excellent cementitious and mechanical properties (Ding et al., 2012). Finch and Sharp also studied the reaction of mono-aluminum phosphate and magnesia in terms of molar ratio and final products, showing that the crystalline newberyite ($MgHPO_4.3H_2O$) appeard instead of struvite analogue in case of the Mg/P moral ratio of 4 (Finch and Sharp, 1989). The phosphate species may involve into the formation of amorphous phase as well.

$$MgO + XH_2PO_4 + nH_2O \rightarrow MgXPO_4 \cdot (n+1)H_2O \tag{2.16}$$

The characteristics of crystalline calcium/magnesium phosphate phases including their mineral name, chemical formula and main application fields are listed in Table 2.1. Apatite is mostly used in biomaterial for dental cement and mimic bone due to their good biocompatibility. Its variants can also be employed to immobilize the heavy metal pollutants (e.g., Pb, Cd, Zn, or Cr) by embedding them into the respective apatite minerals (e.g., Ca/Zn replacement) (Chen et al., 1997; Saxena and D'Souza, 2006). The final products containing struvite or its analogues are usually used as rapid repair materials in civil engineering due to its high mechanical performance and adhesive property.

Table 2.1 Specific crystalline products in calcium/magnesium phosphate cement

Mineral name		Chemical formula	Application
Ca series	Brushite/Monetite	$CaHPO_4 \cdot 2H_2O/CaHPO_4$	Biomaterial, Phosphor material, Waste treatment
	Hydroxyapatite (HAp)	$Ca_5(PO_4)_3 \cdot OH$	
	Chloroapatite (ClAp)	$Ca_5(PO_4)_3 \cdot Cl$	
	Fluoroapatite (FAp)	$Ca_5(PO_4)_3 \cdot F$	
Mg series	Struvite	$Mg(NH_4)PO_4 \cdot 6H_2O$	Building material, Waste encapsulation
	Struvite-K (Ceramicrete)	$MgKPO_4 \cdot 6H_2O$	
	Struvite-Na	$MgNaPO_4 \cdot 7H_2O$	
	Newberyite	$MgHPO_4 \cdot 3H_2O$	

2.3.5 Model comparison of alkali-aluminosilicate geopolymer and silico-aluminophosphate geopolymer

Alkali activation process of Ca sources (i.e., C-A-S-H gel formation) and acid-base reaction process of Ca/Mg and phosphate (i.e., amorphous or crystalline phosphates) can promote both the rapid setting at room and the strength upscaling by forming new phases. Their simplified synthesis models of the two 'hybrid' geopolymers are conceptualized in Fig. 2.9.

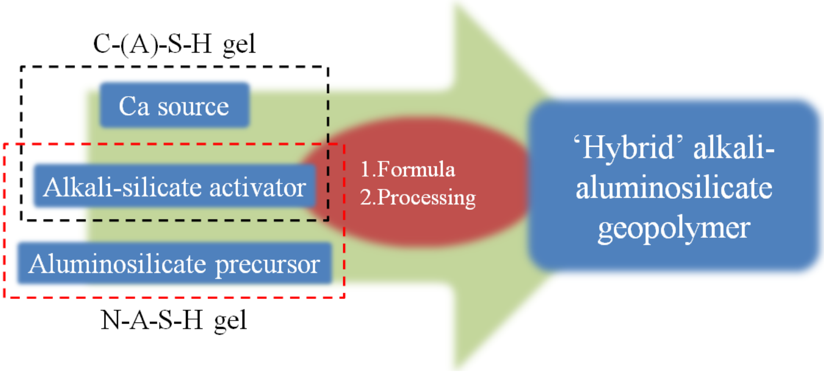

(a) 'Hybrid' alkali-aluminosilicate geopolymer

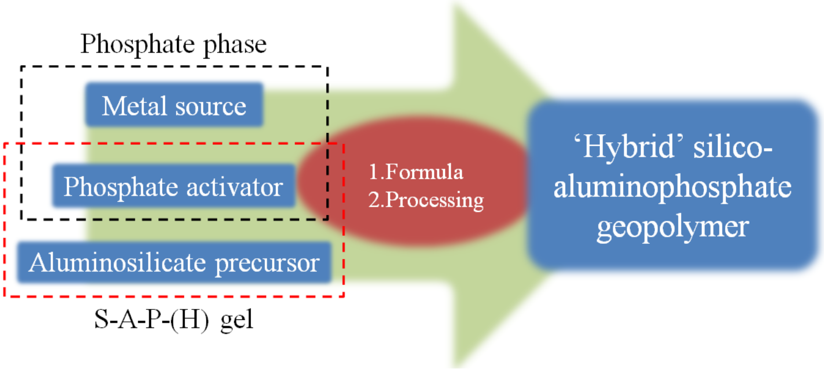

(b) 'Hybrid' silico-aluminophosphate geopolymer

Fig. 2.9 Simplified conceptual models of two 'hybrid' geopolymers

Thus, Figure 2.10 shows a comparative flow chart between the formation processes of alkali-aluminosilicate and silico-aluminophosphate geopolymers, where the key stages from the raw materials to geopolymer are outlined. The Ca-containing alkali-aluminosilicate geopolymer has been investigated for many years (as shown in Fig. 2.10a), including dissolution, speciation, gelation, reorganization and final polymerization (Duxson et al., 2007; van Deventer et al., 2007). The chemically-dissolved aluminosilicate precursors facilitate the formation of the C-(A)-S-H gels when encountering the free Ca species. This chemical process is relatively faster than that of N-A-S-H gels at ambient temperature. It is believed that the entanglement of the two gels (i.e., C-A-S-H and N-A-S-H gels) constitutes the final geopolymer.

As a comparison, the synthesis process of silico-aluminophosphate geopolymer with several milestones is simplified in Fig. 2.10b according to the combination of acid-base reaction and geopolymerization. However, the researches related to silico-aluminophosphate geopolymer are rare, so it should be noted that the synthesis process of this geopolymer is deduced according to the classical interpretations on phosphate cement and alkali-aluminosilciate geopolymer. The solation of phosphate species, including the dissolution and speciation of (hydro)-phosphate ions, is the first step during silico-aluminophosphate geopolymer formation (Perera et al., 2008). Thus, the acid-base reaction between Ca or Mg sources and (hydro)-phosphate ions is started before the dissolution of aluminosilicate precursors. The gelation and reorganization among aluminate, silicate and phosphate form S-A-P gels by the condensation processes. Final polymerization of these species gradually synthesizes a silico-aluminophosphate geopolymer matrix. Unlike alkali-aluminosilicate geopolymer, phosphate-bearing crystalline or amorphous phases may occur in some cases, when reasonable molar ratio and pH environment are provided (Guo et al., 2016; Wang et al., 2017).

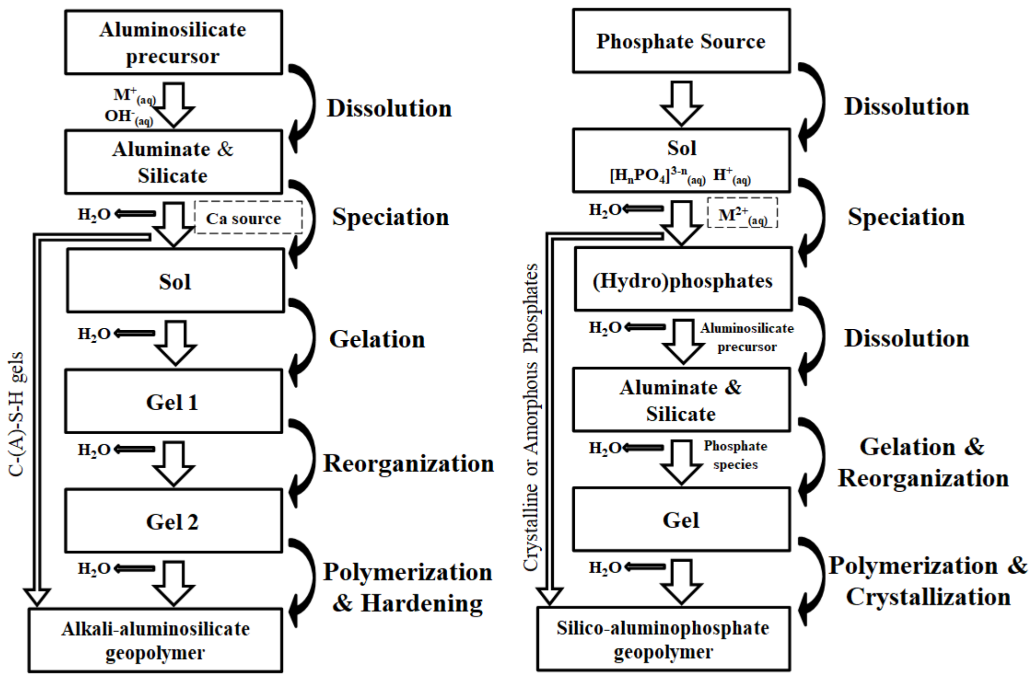

(a) alkali-aluminosilicate geopolymer (b) silico-aluminophosphate geopolymer

Fig. 2.10 Flow chart of conceptual formation process of alkali-aluminosilicate and silico-aluminophosphate geopolymer containing ‘impurities’

2.4 Environmental Impact

Due to a vast of mineral resource consumptions, intensive energy usage and high carbon emissions during the production of Portland cement, the geopolymer cement is strongly proposed to (partially) replace the Portland cement because it can be prepared using aluminosilicate-containing industrial wastes (e.g., coal fly ash) to achieve (even surpass) the Portland cement-like performance. Besides, the clinker-free attribute of geopolymer cement is entitled as energy-saving and carbon emission-reducing features. Geopolymers seemed to reduce the environmental issues of Portland cement, yet the published results on life cycle assessment (LCA) of the geopolymer binder aroused controversies (Davidovits, 2015; Habert et al., 2011; Turner and Collins, 2013; Yang et al., 2013). This difference lies in complex steps from cradle to construction site, such as components usage (local availability, mix proportion, thermal treatment etc.), mix and casting of the fresh geopolymer concrete. Besides, the LCA-based ISO standard used for an environmental burden of production system should include each product (Passuello et al., 2017; ISO 14040, 2016). The demand is how to define the environmental impact of aluminosilicate byproducts (e.g., CFA and GGBS) when compared with the OPC in terms of LCA. Recently, Habert's findings showed that the production of most standard types of the alkali-aluminosilicate geopolymer concrete just presents a slightly lower impact on the global warming compared to standard OPC concrete (Habert et al., 2011). Moreover, the production of the geopolymer concrete activated by a large amount of waste glass shows a higher environmental impact (except carbon footprint) than its counterpart (Fawer et al., 1999; Habert et al., 2011). If these raw materials are considered as the waste forms (e.g., in Europe) and counted out (EU, 2008), the geopolymer cement is indeed a groundbreaking solution for environmental issues caused by traditional cement industry (Habert and Ouellet-Plamondon, 2016). Regarding the silico-aluminophosphate geopolymer, there is barely clear research on the comparison to OPC in terms of LCA. It was just reported that the energy usage during the production of phosphate binder (mainly the phosphate products) accounted for about one-fourth energy consumed in Portland cement industry (Wagh, 2016).

When comparing the two types of geopolymer, the key point lies in the activating solution in terms of environmental impact. During the preparation of alkali-aluminosilicate geopolymer, it is necessary to use soluble sodium silicates to meet the performance requirements (e.g., mechanical properties, Ding et al., 2016) of geopolymer concrete, especially when aluminosilicate precursor with a lower ratio of Si/Al is employed (Krizan and Zivanovic, 2002). However, the silicate solutions are contentious due to its high cost and aggressiveness to the environment during production (e.g., intensive energy consumption and global warming potential) (Habert et al., 2011; Habert and Ouellet-Plamondon, 2016; Turner and Collins, 2013). In silico-aluminophosphate geopolymer, the phosphate solution is majorly manufactured by reaction between phosphate rock and sulfuric acid at less than 100 ℃ or ambient temperature. Thus, the environmental impact of phosphate solution is largely determined by the sulfuric acid production industry (Kongshaug, 1998). No or little emission (e.g., carbon dioxide) is linked to the raw materials in the modern sulfuric acid production industry, and the exothermic reactions involved in this production may generate a net energy export for other things (Wood, 2004). Emission standard of pollutants for sulfuric acid industry is severely implemented all over the world (China Emission Standard of Oollutants for Sulfuric Acid Industry, 2011; EU Best Available Techniques for Pollution Prevention and Control in the European Sulphuric Acid and Fertilizer Industries, 2000; US Guidelines for Limitation of Contact Sulfuric Acid Plant Emissions, 1971). As compared, the phosphate solution seems to be less demanding than the alkali-silicate solution in terms of the gas emission and energy expenditure.

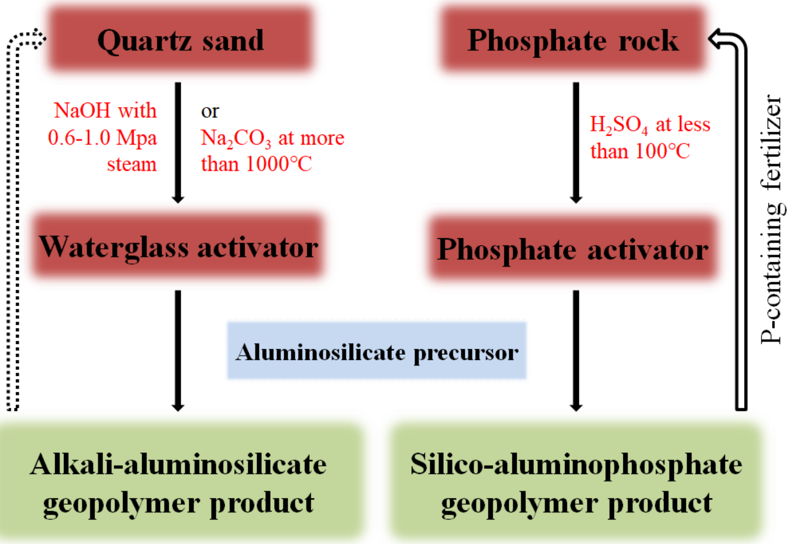

(a) Silicate (b) Phosphate

Fig. 2.11 Industrial ecology of activating solutions and geopolymer products

In addition to the carbon emission and energy consumption, the application of the silico-aluminophosphate geopolymer products may form a virtuous eco-system as the phosphorus available in this binder can be absorbed or extracted to be the P-containing fertilizers for crops after abandoning (Bartos et al., 1990; Raven and Loeppert, 1996; Salutsky and Sanborn, 1966). These biological and chemical actions may further form a mineral deposit (e.g., phosphate rock). Such an eco-friendly loop (shown in Fig. 2.11b) makes the phosphate-based products more ‘green’ and sustainable, which meets the concept of industrial ecology in the long run (Jelinski et al, 1992). Adversely, the alkali-silicate activators (varying modulus of sodium silicate) used for preparing the alkali-aluminosilicate geopolymer products are usually non-recyclable, as shown in Fig. 2.11a. Some researchers are exploring some waste-derived activators (e.g., silica fume and rice husk ash) to replace commercial silicate solutions for alkali-aluminosilicate geopolymer preparation (Bernal et al., 2012; He et al., 2013b; Nazari et al., 2011), which may reduce environment burden caused by water glass industry.

2.5 Performance, Durability, Cost and Accessibility

2.5.1 Compressive strength

In addition to the environmental advantages, geopolymer cement is a competitive alternate to OPC due to its excellent mechanical properties and durability. The mechanical strength reported in the published literatures widely varies because of the differences in raw materials (e.g., attribute and recipe), curing condition (e.g., temperature and moisture), and sample preparation technology (e.g., size and age). The 28 day compressive strengths of the geopolymer obtained from literature survey, including low- and high-calcium alkali-aluminosilicate geopolymer and silico-aluminophosphate geopolymer, is shown in Fig. 2.12 (Reddy et al., 2016; Wang et al., 2016). The statistics clearly shows that the compressive strength of the alkali-aluminosilicate geopolymer (i.e., 15-65 MPa for low-calcium series), especially the high-calcium series (i.e., alkali-activated GGBS, 70-110 MPa), significantly outperforms that of the silico-aluminophosphate geopolymer (i.e., 10-50 MPa). Ding et al. (2016) summarized the mechanical properties of alkali-aluminosilicate geopolymer concrete, revealing that compressive strength and elastic modulus can moderately meet the requirements of codes of practice for Portland cement concrete. Perera et al. (2008) synthesized (60 ℃ curing for 24 hour) a silico-aluminophosphate geopolymer material with relatively high compressive strength approaching 140 MPa, which is twofold that of alkali-aluminosilicate geopolymer. On the other hand, Wang et al. (2017) reported that the final setting times were more than 2 day and the compressive strength reached 31 MPa at 28 day for metakaolin-based geopolymer activated by a monoaluminum phosphate at room temperature curing. Guo et al. (2016) obtained the phosphate-based geopolymer using MK and disused phosphate liquid, which resulted in a compressive strength of 62-67 MPa when the matrix experienced a 7-day 60 ℃ curing. The activating effect of disused phosphate liquid exceeded that of phosphoric acid because of the presence of aluminum ions and thermal curing.

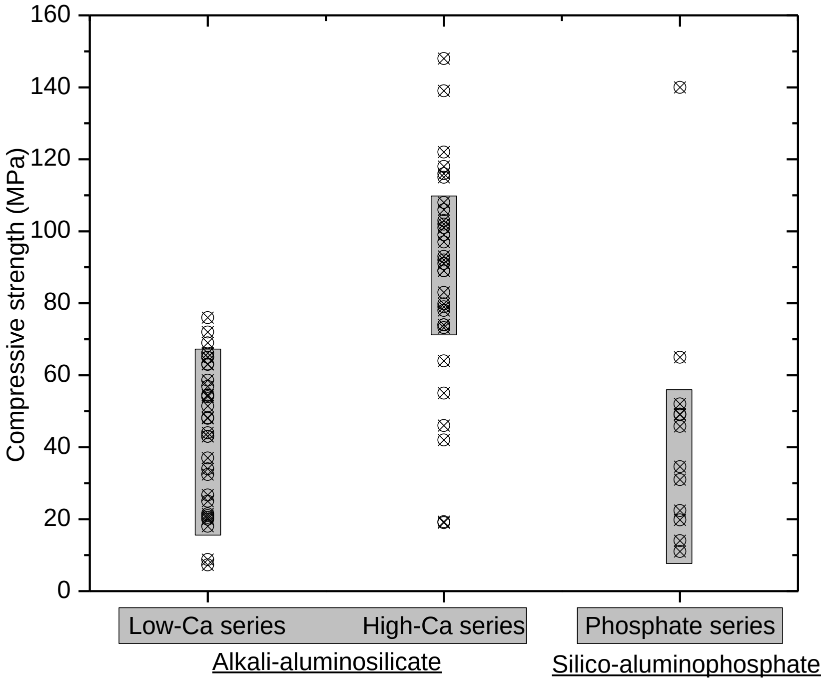

Fig. 2.12 Literature survey on compressive strength of the geopolymer cured at 28 day. It should be noted that the statistics ignore the attribute and recipe of raw materials and curing conditions used.

2.5.2 Thermal stability, dielectricity and efflorescence

The thermal stability and dielectric property of the silico-aluminophosphate geopolymer are noticeable as a small-scale or specifically-required functional material (e.g., fire-proof material and dielectric ceramics). MK-based geopolymer activated by phosphoric acid exhibited good thermal and volume stability (Liu et al., 2012). Phase transition (from aluminum hydrogen phosphate to berlinite) is observed when the geopolymer sample is subjected to elevated temperatures (900-1550 ℃). In the alkali-aluminosilicate geopolymer, the presence of calcium source could reduce the curing cost and increase the early strength as previously explained. The compressive strength of such hybrid geopolymer matrix was improved along with the increase of slag content (Guerrieri and Sanjayan, 2010). However, such practice lowers the ability of geopolymer to resist fire and high temperature (Buchwald et al., 2007). This could be due to the existence of the non-fire-resistant C-(A)-S-H gels. Cui et al. (2011) compared the dielectric loss of two types of geopolymers. It was found that the silico-aluminophosphate geopolymer holds a very low dielectric loss (around 0.01 for frequencies more than 300 MHz) at 300 ℃ dried for 2 hour. The dielectricity of alkali-aluminosilicate geopolymer is strongly dependable to the free metal ions and hydroxyl ions, which means the dielectric loss caused by ion transfer is changeable.

Besides, the efflorescence was also a serious issue but attracted limited attention (Allahverdi et al., 2015; Pacheco-Torgal et al., 2017). Efflorescence in alkali-aluminosilicate geopolymer is the result of the incomplete consumption of alkaline and/or soluble silicates which leads to form the sodium carbonate in the pores or on the surface of geopolymer matrix (as shown in Fig. 2.13), which may weaken the bond of sodium in geopolymer.

The efflorescence rate of alkali-aluminosilicate geopolymer is strongly activation-dependent (Zhang et al., 2014). In case of the same alkali content and curing temperature, NaOH-activated geopolymers show less and slower efflorescence than that activated by sodium silicate. Geopolymer with a high Na_2O/Al_2O_3 ratio can suffer from moderate efflorescence as well (Kani et al., 2012). Hydrothermal curing and CFA/GGBS-based geopolymers exhibited relatively lower efflorescence; however the slag addition appears to present a delaying rather than mitigating effect for efflorescence (Zhang et al., 2014). Kani stated that the alumina-rich admixtures can reduce the efflorescence (Kani et al., 2012). These actions on efflorescence resistance need economic and environmental costs. On the other hand, the acidic synthesis environment enables silico-aluminophosphate geopolymer to have a high resistance to efflorescence relative to the alkali-aluminosilicate geopolymer.

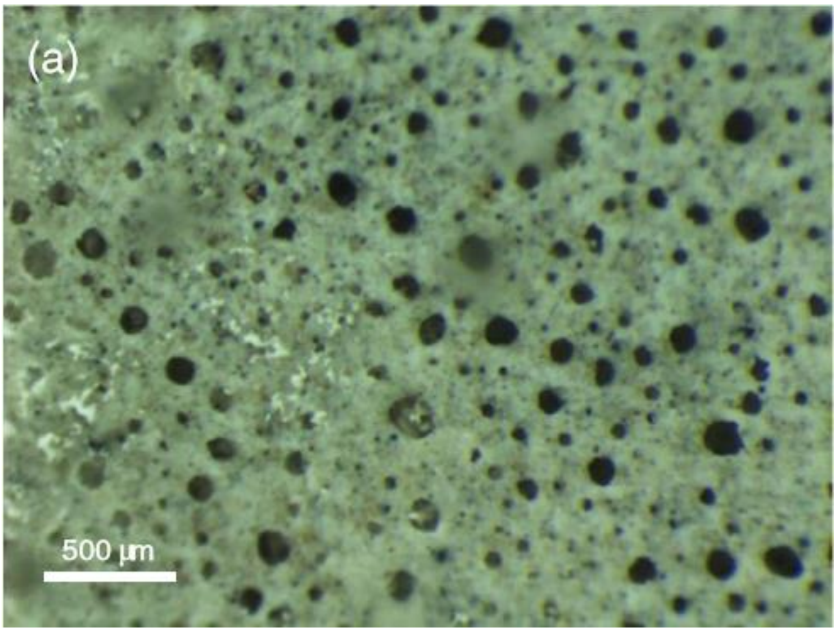

(a) 1 day

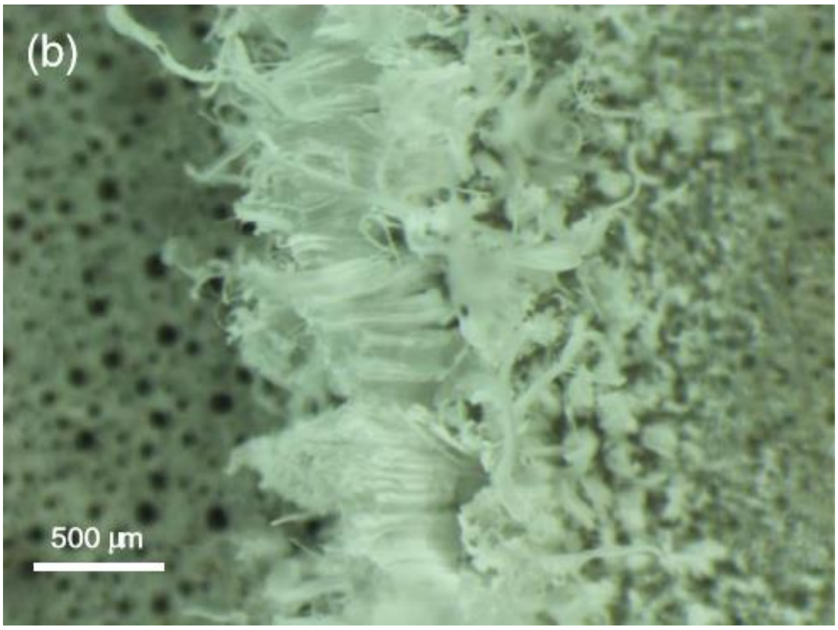

(b) 7 day

Fig. 2.13 Optical micrographs of the efflorescence products in the pores and on the surface of geopolymer matrix (Zhang et al., 2014)

2.5.3 Cost and availability

In addition to the performance comparison, their cost and availability are also crucial to the practical engineering. The quotations form regional supplier (Alibaba) indicates that the price of phosphate acid is more than 3 times higher compared to that of sodium silicate. The application cost determines that the silico-aluminophosphate geopolymer development is developing towards a functional material (e.g., as coating materials, fast-rapid materials, and 3D printing materials), while the mission of alkali-aluminosilicate geopolymer cement is to reduce the traditional cement consumption.

The major concern of raw material availability is the complexity of aluminosilicate sources, especially aluminosilicate-containing industrial byproducts. Fly ash as a typical aluminosilicate source for geopolymer preparation is an anthropogenic material with polymorphic, polycrystal, multi-component system (Blissett and Rowson, 2012). According to different regions, more than 316 individual minerals and 188 mineral groups in coal fly ash have been identified and characterized which may cause even more difference in non-crystalline phases and particle characteristics (Vassilev and Vassileva, 2005). The diversity of raw materials results in wide differences of geopolymer in mechanical properties, even when using the same formula. The geopolymer turns out to possessmulti-phase, multi-component and multi-morphology. Its performances are strongly dependable on the types of raw materials. Proper characterization, classification, and pretreatment to the aluminosilicates enabled to obtain a range of geopolymer products with tailored performance.

In order to achieve a high performance geopolymer matrix, the assessment indexes of aluminosilicate for preparing different geopolymers required before use consist of three aspects. (Agarwal, 2006; De Rojas et al., 1996; Luxán et al., 1989)

(1) Material characterization. The characterization indexes of aluminosilicates include their composition (oxide and phase) and physical features (particle size, specific gravity and surface and loss of ignition), which can greatly influence the performances of geopolymer products.

(2) Reactivity test. The reactivity of the aluminosilicate precursors is closely associated with their phases. The combined use of Rietveld analysis (Izumi and Ikeda, 2000) and PONKCS (partial or no known crystal structure (Scarlett and Madsen, 2006) prove to be useful for initial gauging of the crystalline and amorphous phase content. Glassy phase composition of some aluminosilicates can be captured by SEM-EDXS with multispectral image analysis, discerning between the inert crystalline and the reactive amorphous phases in case of similar elemental composition (Chancey et al., 2010; Durdziński et al., 2015). The participation degree of aluminosilicates in geopolymerization heavily determines the properties of geopolymer products.

(3) Performance enhancements. For unacceptable aluminosilicate sources, particle size reduction and mineral additions seem to be valid; however the thermal and chemical pretreatments can be more effective because these pretreatments increase the amorphous proportion and decreases the loss of ignition (Bentz et al., 2011; Handoo et al., 2002; Škvára et al., 2009).

2.6 Potential Applications

The silico-aluminophosphate geopolymer exhibits the polymer-like molecular structure, as well as the tailored features when other chemistries are involved in geopolymerization. Therefore, immense potential values in a wide range of research fields are being gradually developed.

2.6.1 Application in construction

One of the large scale applications of geopolymer (mainly alkali-aluminosilicate geopolymer cement) is in construction due to their good mechanical behaviors and durability. Some modified alkali-aluminosilicate geopolymer cement has been commercially branded for infrastructure projects, such as PYRAMENT cement (Davidovits, 2011). On the other hand, the silico-aluminophosphate geopolymer is being studied in labs through the synthesis reaction between phosphate and aluminosilicate from the perspective of chemistry. In a high volume content of CFA-blended phosphate binder, the coal fly ash is considered as a diluent or inert filler that modifies the aesthetics (e.g., change color and reduce porosity) to make it compatible to Portland cement as a rapid healant (Wang and Dai, 2017). Some reports indicated that the high mechanical strength is also attributable to the formation of secondary amorphous phase (e.g., phospho-siloxonate geopolymeric phases) (Gardner et al., 2015).

2.6.2 Application in waste management

The waste production is closely accompanied with the increase of population. In order to stop the contaminants from flowing into the food chain of human, some effective and low-cost amendments are applied to stabilize/solidify the hazardous or radioactive waste streams (Morrissey and Browne, 2004). According to the definition of stabilization/solidification (Conner, 1990), stabilization process emphasizes the chemical converting the contaminants into their insoluble, immobile or nontoxic forms without spillage, leakage and disintegration in a long time. While solidification is defined as the physical consolidating sludges, liquids or powders into a solid form so that they are not dispersible during transportation, long-term storage or disposal. Recently, alkali-aluminosilicate geopolymer binders are explored for the stabilization/solidification (S/S) remediation for heavy metals (Galiano et al., 2011). It is claimed that the heavy metals could be fixed in the molecular network during geopolymerization, possibly either chemically embedded into the structure for charge balance or physically trapped by the surrounding 3D network (Van Jaarsveld et al., 1997). In silico-aluminophosphate geopolymer, the phosphate ions also chemically combined with detrimental metal species to form highly insoluble phosphates (e.g. pyromorphite during Pb S/S) (Wang et al., 2018).

2.6.3 Application in biomaterials

Considering the biocompatibility, resorbability and customization of living body, the silico-aluminophosphate geopolymer with Ca-containing setting agent is an excellent candidate in bio-engineering. The tailor-made shape can be pre-prepared using 3D printing due to the good injection ability of these materials (Chia and Wu, 2015; Tamimi-Marino et al., 2007). Besides being used as the precast skeletal structure, silico-aluminophosphate geopolymer paste can be injected into the needed region in the biological body. The paste not only cements the adjacent tissues, but also is less intrusive compared to the implant of hardened biomaterial. Since the bone and tooth contain mainly calcium phosphate compounds, Ca-containing silico-aluminophosphate geopolymer provides necessary compositions to achieve better biocompatibility.

2.6.4 Application in 3D printing

3D printing, as an emerging technique, promises to rapidly manufacture products with spatially complex and precise distribution (Lim et al., 2012; Rengier et al., 2010; Bassoli et al., 2007). Such an attractive rapid prototyping (RP) is based on the additive manufacturing (AM), defined by the ASTM International as ‘the process of joining materials to make objects from 3D model data, usually layer upon layer’ (ASTM F2791-10). The customized imaging database (e.g., computed tomography scans) can be really visualized via the 3D printing system. Nevertheless, how to select appropriate materials with ideal rheology, setting time, temperature, strength and durability while meeting other special requirements, is a key issue. Recently, the 3D printing of biomaterials has been applied for surgical planning and prosthetics using the phosphate material, with the aim to realize the biocompatible and prefabricated solid implants with the patient-tailored shapes and features in various clinical situations. Another mega-scale application in civil engineering was the freeform construction, conceptualized by Buswell (Buswell et al., 2007; Buswell et al., 2008), which means ‘processes for integrated building components which demonstrate added value, functionality and capabilities over and above traditional methods of construction’. According to the requirements of printable materials, the ‘two-part’ geopolymer (aluminosilicate and activator) is also potentially applicable for ‘3D concrete printing’ (Xia and Sanjayan, 2016; Zhong et al., 2017).

2.7 Chapter Summary

This chapter provides a comprehensive review on the phosphate activation for aluminosilicate materials. According to the activation mode, this kind of material can be termed as silico-aluminophosphate geopolymer, for which extra promotion (e.g., thermal curing or setting agent) is usually needed to obtain reasonable engineering properties. The thermal curing is usually inappropriate for in-situ applications, while the incorporation of a setting agent induces an ambient-temperature setting mechanism for the geopolymer matrix because fast-setting chemistry is involved during the geopolymerization. Just like the formation of C-(A)-S-H gels in alkali-aluminosilicate geopolymer, the silico-aluminophosphate geopolymer can produce crystalline or amorphous phosphate phases during geopolymerization when metal ions are incorporated with the aluminosilicates. The different activation modes generate various potential values of these ‘hybrid’ geopolymers in a wide range of research fields. According to the performance, cost and accessibility, the alkali-aluminosilicate and silico-aluminophosphate geopolymers are mutually supplemented in terms of function and application fields.

2.8 References

Agarwal, S. K. (2006). Pozzolanic activity of various siliceous materials. *Cement and Concrete Research*, *36*(9), 1735-1739.

Allahverdi, A., Kani, E. N., Hossain, K. M. A., & Lachemi, M. (2015). Methods to control efflorescence in alkali-activated cement-based materials. In *Handbook of Alkali-Activated Cements, Mortars and Concretes* (pp. 463-483).

Barsoum, M. W., Ganguly, A., & Hug, G. (2006). Microstructural evidence of reconstituted limestone blocks in the Great Pyramids of Egypt. *Journal of the American Ceramic Society*, *89*(12), 3788-3796.

Bartos, J. M., Mullins, G. L., Sikora, F. J., & Copeland, J. P. (1991). Availability of phosphorus in the water-insoluble fraction of monoammonium phosphate fertilizers. *Soil Science Society of America Journal*, 55(2), 539-543.

Bassoli, E., Gatto, A., Iuliano, L., & Grazia Violante, M. (2007). 3D printing technique applied to rapid casting. *Rapid Prototyping Journal*, 13(3), 148-155.

Benavent, V., Steins, P., Sobrados, I., Sanz, J., Lambertin, D., Frizon, F., Rossignol, S., & Poulesquen, A. (2016). Impact of aluminum on the structure of geopolymers from the early stages to consolidated material. *Cement and Concrete Research*, 90, 27-35.

Bentz, D. P., Sato, T., De la Varga, I., & Weiss, W. J. (2012). Fine limestone additions to regulate setting in high volume fly ash mixtures. *Cement and Concrete Composites*, 34(1), 11-17.

Bernal, S. A., Rodríguez, E. D., De Gutiérrez, R. M., Provis, J. L., & Delvasto, S. (2012). Activation of metakaolin/slag blends using alkaline solutions based on chemically modified silica fume and rice husk ash. *Waste and Biomass Valorization*, 3(1), 99-108.

Bernal, S. A., Rodríguez, E. D., De Gutiérrez, R. M., & Provis, J. L. (2015). Performance at high temperature of alkali-activated slag pastes produced with silica fume and rice husk ash based activators. *Materiales de Construcción*, 65(318), 049.

Bernal, S. A., San Nicolas, R., van Deventer, J. S. J., & Provis, J. L. (2016). Alkali-activated slag cements produced with a blended sodium carbonate/sodium silicate activator. *Advances in Cement Research*, 28(4), 262-273.

Blissett, R. S., & Rowson, N. A. (2012). A review of the multi-component utilisation of coal fly ash. *Fuel*, 97, 1-23.

Brough, A. R., Katz, A., Sun, G. K., Struble, L. J., Kirkpatrick, R. J., & Young, J. F. (2001). Adiabatically cured, alkali-activated cement-based wasteforms containing high levels of fly ash: Formation of zeolites and Al-substituted CSH. *Cement and Concrete Research*, 31(10), 1437-1447.

Buchwald, A., Zellmann, H. D., & Kaps, C. (2011). Condensation of aluminosilicate gels—model system for geopolymer binders. *Journal of Non-Crystalline Solids*, 357(5), 1376-1382.

Buchwald, A., Hilbig, H., & Kaps, C. (2007). Alkali-activated metakaolin-slag blends—performance and structure in dependence of their composition. *Journal of Materials Science*, 42(9), 3024-3032.

Bullard, J. W., Jennings, H. M., Livingston, R. A., Nonat, A., Scherer, G. W., Schweitzer, J. S., Scrivener, K. L. & Thomas, J. J. (2011). Mechanisms of cement hydration. *Cement and Concrete Research*, 41(12), 1208-1223.

Buswell, R. A., Soar, R. C., Gibb, A. G., & Thorpe, A. (2007). Freeform construction: mega-scale rapid manufacturing for construction. *Automation in Construction*, 16(2), 224-231.

Buswell, R. A., Thorpe, A., Soar, R. C., & Gibb, A. G. (2008). Design, data and process issues for mega-scale rapid manufacturing machines used for construction. *Automation in Construction*, 17(8), 923-929.

Cao, D., Su, D., Lu, B., & Yang, Y. (2005). Synthesis and structure characterization of geopolymeric material based on metakaolinite and phosphoric acid. *Journal Chinese Ceramic Society*, 33, 1385-1389.

Chancey, R. T., Stutzman, P., Juenger, M. C., & Fowler, D. W. (2010). Comprehensive phase characterization of crystalline and amorphous phases of a Class F fly ash. *Cement and Concrete Research*, 40(1), 146-156.

Chau, C. K., Qiao, F., & Li, Z. (2011). Microstructure of magnesium potassium phosphate cement. *Construction and Building Materials*, 25(6), 2911-2917.

Chauhan, C. K., Vyas, P. M., & Joshi, M. J. (2011). Growth and characterization of Struvite-K crystals. *Crystal Research and Technology*, 46(2), 187-194.

Chauhan, C. K., & Joshi, M. J. (2014). Growth and characterization of struvite-Na crystals. *Journal of Crystal Growth*, 401, 221-226.

Chen, X., Wright, J. V., Conca, J. L., & Peurrung, L. M. (1997). Evaluation of heavy metal remediation using mineral apatite. *Water, Air, and Soil Pollution*, 98(1-2), 57-78.

Chia, H. N., & Wu, B. M. (2015). Recent advances in 3D printing of biomaterials. *Journal of Biological Engineering*, 9(1), 4.

Chow, L. C. (2001). *Calcium phosphate cements*. In Octacalcium Phosphate (Vol. 18, pp. 148-163). Karger Publishers.

Conner J R (1990). *Chemical fixation and solidification of hazardous wastes*. Van Nostrand Reinhold, New York, 692: f5

Cui, X. M., Zheng, G. J., Han, Y. C., Su, F., & Zhou, J. (2008). A study on electrical conductivity of chemosynthetic Al2O3–2SiO2 geoploymer materials. *Journal of Power Sources*, 184(2), 652-656.

Cui, X. M., Liu, L. P., He, Y., Chen, J. Y., & Zhou, J. (2011). A novel aluminosilicate geopolymer material with low dielectric loss. *Materials Chemistry and Physics*, 130(1-2), 1-4.

Davidovits J (1991). Geopolymers: Inorganic polymeric new materials. *Journal of Thermal Analysis*, 37: 1633–1656.

Davidovits J (2011). *Geopolymer: Chemistry & Application*. Institute Geopolymer, 3rd Edition.

De Jong, B. H. W. S., Schramm, C. M., & Parziale, V. E. (1983). Polymerization of silicate and aluminate tetrahedra in glasses, melts, and aqueous solutions—IV. Aluminum coordination in glasses and aqueous solutions and comments on the aluminum avoidance principle. *Geochimica et Cosmochimica Acta*, 47(7), 1223-1236.

De Rojas, M. S., & Frías, M. (1996). The pozzolanic activity of different materials, its influence on the hydration heat in mortars. *Cement and Concrete Research*, 26(2), 203-213.

Ding, Z., Dong, B., Xing, F., Han, N., & Li, Z. (2012). Cementing mechanism of potassium phosphate based magnesium phosphate cement. *Ceramics*

International, 38(8), 6281-6288.

Ding, Y., Dai, J. G., & Shi, C. J. (2016). Mechanical properties of alkali-activated concrete: a state-of-the-art review. *Construction and Building Materials*, 127, 68-79.

Douiri, H., Louati, S., Baklouti, S., Arous, M., & Fakhfakh, Z. (2014). Structural, thermal and dielectric properties of phosphoric acid-based geopolymers with different amounts of H_3PO_4. *Materials Letters*, 116, 9-12.

Durdziński, P. T., Dunant, C. F., Haha, M. B., & Scrivener, K. L. (2015). A new quantification method based on SEM-EDXS to assess fly ash composition and study the reaction of its individual components in hydrating cement paste. *Cement and Concrete Research*, 73, 111-122.

Duxson, P., Lukey, G. C., Separovic, F., & van Deventer, J. S. J. (2005). Effect of alkali cations on aluminum incorporation in geopolymeric gels. *Industrial & Engineering Chemistry Research*, 44(4), 832-839.

Duxson, P., Fernández-Jiménez, A., Provis, J. L., Lukey, G. C., Palomo, A., & van Deventer, J. S. J. (2007). Geopolymer technology: the current state of the art. *Journal of Materials Science*, 42(9), 2917-2933.

EU (2008). *Directive 2008/98/EC of the European Parliament and of the Council on waste and repealing certain Directives*. L312: 3-30

European Sulphuric Acid Association (2000). *Best Available Techniques for Pollution Prevention and Control in the European Sulphuric Acid and Fertilizer Industries*, Production of Sulphuric acid.

Fawer, M., Concannon, M., & Rieber, W. (1999). Life cycle inventories for the production of sodium silicates. *The International Journal of Life Cycle Assessment*, 4(4), 207.

Feng, G., Cheng, P., Yan, W., Boronat, M., Li, X., Su, J. H., Wang, J.,Corma, A., Xu, R. & Yu, J. (2016). Accelerated crystallization of zeolites via hydroxyl free radicals. *Science*, 351(6278), 1188-1191.

Fernández-Jiménez, A., Palomo, A., & Criado, M. (2005). Microstructure development of alkali-activated fly ash cement: a descriptive model. *Cement and Concrete Research*, 35(6), 1204-1209.

Fernández-Jiménez, A., Palomo, A., Sobrados, I., & Sanz, J. (2006). The role played by the reactive alumina content in the alkaline activation of fly ashes.

Microporous and Mesoporous Materials, 91(1-3), 111-119.

Finch, T., & Sharp, J. H. (1989). Chemical reactions between magnesia and aluminium orthophosphate to form magnesia-phosphate cements. *Journal of Materials Science*, 24(12), 4379-4386.

Galiano, Y. L., Pereira, C. F., & Vale, J. (2011). Stabilization/solidification of a municipal solid waste incineration residue using fly ash-based geopolymers. *Journal of Hazardous Materials*, 185(1), 373-381.

Garcia-Lodeiro, I., Palomo, A., & Fernández-Jiménez, A. (2015). An overview of the chemistry of alkali-activated cement-based binders. *In Handbook of alkali-activated cements, mortars and concretes* (pp. 19-47).

Gardner, L. J., Bernal, S. A., Walling, S. A., Corkhill, C. L., Provis, J. L., & Hyatt, N. C. (2015). Characterisation of magnesium potassium phosphate cements blended with fly ash and ground granulated blast furnace slag. *Cement and Concrete Research*, 74, 78-87.

Guerrieri, M., & Sanjayan, J. G. (2010). Behavior of combined fly ash/slag-based geopolymers when exposed to high temperatures. *Fire and Materials*, 34(4), 163-175.

Guo, C. M., Wang, K. T., Liu, M. Y., Li, X. H., & Cui, X. M. (2016). Preparation and characterization of acid-based geopolymer using metakaolin and disused polishing liquid. *Ceramics International*, 42(7), 9287-9291.

Habert, G., & Ouellet-Plamondon, C. (2016). Recent update on the environmental impact of geopolymers. *RILEM Technical Letters*, 1, 17-23.

Habert, G., De Lacaillerie, J. D. E., & Roussel, N. (2011). An environmental evaluation of geopolymer based concrete production: reviewing current research trends. *Journal of Cleaner Production*, 19(11), 1229-1238.

Handoo, S. K., Agarwal, S., & Agarwal, S. K. (2002). Physicochemical, mineralogical, and morphological characteristics of concrete exposed to elevated temperatures. *Cement and Concrete Research*, 32(7), 1009-1018.

He, Y., Cui, X. M., Liu, X. D., Wang, Y. P., Zhang, J., & Liu, K. (2013a). Preparation of self-supporting NaA zeolite membranes using geopolymers. *Journal of Membrane Science*, 447, 66-72.

He, J., Jie, Y., Zhang, J., Yu, Y., & Zhang, G. (2013b). Synthesis and characterization of red mud and rice husk ash-based geopolymer composites.

Cement and Concrete Composites, 37, 108-118.

Ishikawa, K. (2014). Calcium phosphate cement. In *Advances in Calcium Phosphate Biomaterials* (pp. 199-227). Springer, Berlin, Heidelberg.

Ismail, I., Bernal, S. A., Provis, J. L., San Nicolas, R., Brice, D. G., Kilcullen, A. R., Hamdan, S. & van Deventer, J. S. J. (2013). Influence of fly ash on the water and chloride permeability of alkali-activated slag mortars and concretes. *Construction and Building Materials*, 48, 1187-1201.

Ismail, I., Bernal, S. A., Provis, J. L., San Nicolas, R., Hamdan, S., & van Deventer, J. S. J. (2014). Modification of phase evolution in alkali-activated blast furnace slag by the incorporation of fly ash. *Cement and Concrete Composites*, 45, 125-135.

ISO 14040: 2006 (2006). Environmental Management-Life Cycle Assessment - Principles and Framework.

Izumi, F., Ikeda, T. (2000). A Rietveld-analysis programm RIETAN-98 and its applications to zeolites, *Materials Science Forum*. 321: 198-205

Jelinski, L. W., Graedel, T. E., Laudise, R. A., McCall, D. W., & Patel, C. K. (1992). Industrial ecology: concepts and approaches. *Proceedings of the National Academy of Sciences*, 89(3), 793-797.

Kani, E. N., Allahverdi, A., & Provis, J. L. (2012). Efflorescence control in geopolymer binders based on natural pozzolan. *Cement and Concrete Composites*, 34(1), 25-33.

Kingery, W. D. (1950). Fundamental study of phosphate bonding in refractories: I, literature review. *Journal of the American Ceramic Society*, 33(8), 239-241.

Kingery, W. D. (1952). Fundamental Study of Phosphate Bonding in Refractories: IV, Mortars Bonded with Monoaluminum and Monomagnesium Phosphate. *Journal of the American Ceramic Society*, 35(3), 61-63.

Kongshaug G. (1998). Energy consumption and greenhouse gas emissions in fertilizer production. *IFA Technical Conference*, Marrakech, Morocco, 28: 18.

Krizan, D., & Zivanovic, B. (2002). Effects of dosage and modulus of water glass on early hydration of alkali–slag cements. *Cement and Concrete Research*, 32(8), 1181-1188.

Larsson, S., & Bauer, T. W. (2002). Use of injectable calcium phosphate cement for fracture fixation: a review. *Clinical Orthopaedics and Related Research*, 395, 23-32.

Li, C., Sun, H., & Li, L. (2010). A review: The comparison between alkali-activated slag (Si+ Ca) and metakaolin (Si+ Al) cements. *Cement and Concrete Research*, 40(9), 1341-1349.

Lim, S., Buswell, R. A., Le, T. T., Austin, S. A., Gibb, A. G., & Thorpe, T. (2012). Developments in construction-scale additive manufacturing processes. *Automation in Construction*, 21, 262-268.

Liu, L. P., Cui, X. M., Qiu, S. H., Yu, J. L., Zhang L. (2010). Preparation of phosphoric acid-based porous geopolymers. *Applied Clay Science*, 50(4): 600-603.

Lodeiro, I. G., Fernández-Jimenez, A., Palomo, A., & Macphee, D. E. (2010). Effect on fresh CSH gels of the simultaneous addition of alkali and aluminium. *Cement and Concrete Research*, 40(1), 27-32.

Lothenbach, B., Scrivener, K., & Hooton, R. D. (2011). Supplementary cementitious materials. *Cement and Concrete Research*, 41(12), 1244-1256.

Louati, S., Hajjaji, W., Baklouti, S., & Samet, B. (2014). Structure and properties of new eco-material obtained by phosphoric acid attack of natural Tunisian clay. *Applied Clay Science*, 101, 60-67.

Louati, S., Baklouti, S., & Samet, B. (2016). Acid based geopolymerization kinetics: Effect of clay particle size. *Applied Clay Science*, 132, 571-578.

Luxán, M. D., Madruga, F., & Saavedra, J. (1989). Rapid evaluation of pozzolanic activity of natural products by conductivity measurement. *Cement and Concrete Research*, 19(1), 63-68.

Luz, A. P., Gomes, D. T., & Pandolfelli, V. C. (2015). High-alumina phosphate-bonded refractory castables: Al(OH)3 sources and their effects. *Ceramics International*, 41(7), 9041-9050.

Ministry of Environmental Protection (2011). Emission standard of pollutants for sulfuric acid industry, China.

Morrissey, A. J., & Browne, J. (2004). Waste management models and their application to sustainable waste management. *Waste Management*, 24(3), 297-308.

Nazari, A., Bagheri, A., & Riahi, S. (2011). Properties of geopolymer with seeded fly ash and rice husk bark ash. *Materials Science and Engineering: A*, 528(24), 7395-7401.

Neville, A. M. (2011). *Properties of Concrete* (Vol. 5). London: Longman.

Pacheco-Torgal, F., Abdollahnejad, Z., Miraldo, S., & Kheradmand, M. (2017). *Alkali-activated cement-based binders (AACBs) as durable and cost-competitive low-CO_2 binder materials: some shortcomings that need to be addressed* (pp. 195-216). Butterworth-Heinemann, Oxford, UK.

Pacheco-Torgal, F., Castro-Gomes, J., & Jalali, S. (2008). Alkali-activated binders: A review: Part 1. Historical background, terminology, reaction mechanisms and hydration products. *Construction and Building Materials*, 22(7), 1305-1314.

Passuello, A., Rodríguez, E. D., Hirt, E., Longhi, M., Bernal, S. A., Provis, J. L., & Kirchheim, A. P. (2017). Evaluation of the potential improvement in the environmental footprint of geopolymers using waste-derived activators. *Journal of Cleaner Production*, 166, 680-689.

Perera, D. S., Hanna, J. V., Davis, J., Blackford, M. G., Latella, B. A., Sasaki, Y., & Vance, E. R. (2008). Relative strengths of phosphoric acid-reacted and alkali-reacted metakaolin materials. *Journal of Materials Science*, 43(19), 6562-6566.

Provis, J. L. & van Deventer, J. S. J. (2014). *Alkali-activated materials: state-of-the-art report*, RILEM TC 224-AAM. RILEM/Springer, Dordrecht.

Provis, J. L. (2014). Geopolymers and other alkali activated materials: why, how, and what?. *Materials and Structures*, 47(1-2), 11-25.

Provis, J. L., & Bernal, S. A. (2014). Geopolymers and related alkali-activated materials. *Annual Review of Materials Research*, 44, 299-327.

Provis, J. L., Duxson, P., van Deventer, J. S. J., & Lukey, G. C. (2005a). The role of mathematical modelling and gel chemistry in advancing geopolymer technology. *Chemical Engineering Research and Design*, 83(7), 853-860.

Provis, J. L., Lukey, G. C., & van Deventer, J. S. J. (2005b). Do geopolymers actually contain nanocrystalline zeolites? A reexamination of existing results. *Chemistry of Materials*, 17(12), 3075-3085.

Provis, J. L., Palomo, A., & Shi, C. (2015). Advances in understanding alkali-activated materials. *Cement and Concrete Research*, 78, 110-125.

Raven, K. P., & Loeppert, R. H. (1997). Trace element composition of fertilizers and soil amendments. *Journal of Environmental Quality*, 26(2), 551-557.

Reddy, M. S., Dinakar, P., & Rao, B. H. (2016). A review of the influence of source material’s oxide composition on the compressive strength of geopolymer concrete. *Microporous and Mesoporous Materials*, 234, 12-23.140

Rengier, F., Mehndiratta, A., Von Tengg-Kobligk, H., Zechmann, C. M., Unterhinninghofen, R., Kauczor, H. U., & Giesel, F. L. (2010). 3D printing based on imaging data: review of medical applications. *International Journal of Computer Assisted Radiology and Surgery*, 5(4), 335-341.

Richardson, I. G., Brough, A. R., Brydson, R., Groves, G. W., & Dobson, C. M. (1993). Location of aluminum in substituted calcium silicate hydrate (C-S-H) gels as determined by 29Si and 27Al NMR and EELS. *Journal of the American Ceramic Society*, 76(9), 2285-2288.

Richardson, I. G., Brough, A. R., Groves, G. W., & Dobson, C. M. (1994). The characterization of hardened alkali-activated blast-furnace slag pastes and the nature of the calcium silicate hydrate (CSH) phase. *Cement and Concrete Research*, 24(5), 813-829.

Roy, D. M. (1987). New strong cement materials: chemically bonded ceramics. *Science*, 235(4789), 651-658.

Salutsky, M. L., & Sanborn, J. M. (1966). *U.S. Patent No. 3,285,731*. Washington, DC: U.S. Patent and Trademark Office.

Saxena, S., & D'Souza, S. F. (2006). Heavy metal pollution abatement using rock phosphate mineral. *Environment International*, 32(2), 199-202.

Scarlett, N. V., & Madsen, I. C. (2006). Quantification of phases with partial or no known crystal structures. *Powder Diffraction*, 21(4), 278-284.

Shi, C., & Qian, J. (2000). High performance cementing materials from industrial slags—a review. *Resources, Conservation and Recycling*, 29(3), 195-207.

Škvára, F., Kopecký, L., Myšková, L., Šmilauer, V., Alberovska, L., & Vinšová, L. (2009). Aluminosilicate polymers–influence of elevated temperatures, efflorescence. *Ceramics–Silikáty*, 53(4), 276-82.

Soudée, E., & Péra, J. (2000). Mechanism of setting reaction in magnesia-phosphate cements. *Cement and Concrete Research*, 30(2), 315-321.

Sugama, T., & Kukacka, L. E. (1983). Magnesium monophosphate cements derived from diammonium phosphate solutions. *Cement and Concrete Research*, 13(3), 407-416.

Tamimi, F., Sheikh, Z., & Barralet, J. (2012). Dicalcium phosphate cements: Brushite and monetite. *Acta Biomaterialia*, 8(2), 474-487.

Tamimi-Marino, F., Mastio, J., Rueda, C., Blanco, L., & López-Cabarcos, E. (2007). Increase of the final setting time of brushite cements by using chondroitin 4-sulfate and silica gel. *Journal of Materials Science: Materials in Medicine*, 18(6), 1195-1201.

Taylor, H. F. (1997). *Cement chemistry*. Thomas Telford.

Tseitlin, L. A., & Eltysheva, A. A. (1964). Aluminosilicate ramming bodies with a phosphate bond. *Refractories*, 5(7-8), 384-386.

Tseitlin, L. A., & Gubatenko, A. P. (1968). Phosphate-bonded aluminosili cate mortars. *Refractories*, 9(7-8), 506-508.

Turner, L. K., & Collins, F. G. (2013). Carbon dioxide equivalent (CO_2-e) emissions: A comparison between geopolymer and OPC cement concrete. *Construction and Building Materials*, 43, 125-130.

US Environmental Protection Agency (1971). *Guidelines for Limitation of Contact Sulfuric Acid Plant Emissions*.

van Deventer, J. S. J., Provis, J. L., Duxson, P., & Lukey, G. C. (2007). Reaction mechanisms in the geopolymeric conversion of inorganic waste to useful products. *Journal of Hazardous Materials*, 139(3), 506-513.

Van Jaarsveld, J. G. S., van Deventer, J. S. J., & Lorenzen, L. (1997). The potential use of geopolymeric materials to immobilise toxic metals: Part I. Theory and applications. *Minerals Engineering*, 10(7), 659-669.

Vassilev, S. V., & Vassileva, C. G. (2005). Methods for characterization of composition of fly ashes from coal-fired power stations: a critical overview. *Energy & Fuels*, 19(3), 1084-1098.

Wagh, A. S. (2005). Chemically bonded phosphate ceramics—a novel class of geopolymers. *Ceramic Transactions*, 165, 107-116.

Wagh, A. S. (2016). *Chemically bonded phosphate ceramics- Twenty-first century materials with diverse applications*. Elsevier Science.

Walling, S. A., & Provis, J. L. (2016). Magnesia-based cements: a journey of 150 years, and cements for the future?. *Chemical reviews*, 116(7), 4170-4204.

Wang, S. D., Scrivener, K. L., & Pratt, P. L. (1994). Factors affecting the strength of alkali-activated slag. *Cement and Concrete Research*, 24(6), 1033-1043.

Wang, S. D., & Scrivener, K. L. (1995). Hydration products of alkali activated slag cement. *Cement and Concrete Research*, 25(3), 561-571.

Wang, W. C., Wang, H. Y., & Tsai, H. C. (2016). Study on engineering properties of alkali-activated ladle furnace slag geopolymer. *Construction and Building Materials*, 123, 800-805.

Wang, Y. S., & Dai, J. G. (2017). Use of magnesia sand for optimal design of high performance magnesium potassium phosphate cement mortar. *Construction and Building Materials*, 153, 385-392.

Wang, Y. S., Dai, J. G., Ding, Z., & Xu, W. T. (2017). Phosphate-based geopolymer: Formation mechanism and thermal stability. *Materials Letters*, 190, 209-212.

Wang, Y. S., Dai, J. G., Wang, L., Tsang, D. C., & Poon, C. S. (2018). Influence of lead on stabilization/solidification by ordinary Portland cement and magnesium phosphate cement. *Chemosphere*, 190, 90-96.

Wilson, A. D., & Nicholson, J. W. (2005). *Acid-base cements: their biomedical and industrial applications*, 3rd Edition. Cambridge University Press.

Wood, S. W., & Cowie, A. (2004). A review of greenhouse gas emission factors for fertiliser production. *IEA Bioenergy Task 38*.

Xia, M., & Sanjayan, J. (2016). Method of formulating geopolymer for 3D printing for construction applications. *Materials & Design*, 110, 382-390.

Xu, H., van Deventer, J. S. J., & Lukey, G. C. (2001). Effect of alkali metals on the preferential geopolymerization of stilbite/kaolinite mixtures. *Industrial & Engineering Chemistry Research*, 40(17), 3749-3756.

Xu, G., & Shi, X. (2018). Characteristics and applications of fly ash as a sustainable construction material: A state-of-the-art review. *Resources, Conservation and Recycling*, 136, 95-109.

Yang, K. H., Song, J. K., & Song, K. I. (2013). Assessment of CO_2 reduction of alkali-activated concrete. *Journal of Cleaner Production*, 39, 265-272.

Yao, Z. T., Ji, X. S., Sarker, P. K., Tang, J. H., Ge, L. Q., Xia, M. S., & Xi, Y. Q. (2015). A comprehensive review on the applications of coal fly ash.

Earth-Science Reviews, 141, 105-121.

Zhang, J., Liu, W., Schnitzler, V., Tancret, F., & Bouler, J. M. (2014). Calcium phosphate cements for bone substitution: chemistry, handling and mechanical properties. *Acta Biomaterialia*, 10(3), 1035-1049.

Zhang, Z., Provis, J. L., Reid, A., & Wang, H. (2014). Fly ash-based geopolymers: the relationship between composition, pore structure and efflorescence. *Cement and Concrete Research*, 64, 30-41.

Zhong, J., Zhou, G. X., He, P. G., Yang, Z. H., & Jia, D. C. (2017). 3D printing strong and conductive geo-polymer nanocomposite structures modified by graphene oxide. *Carbon*, 117, 421-426.

This page is intentionally left blank

CHAPTER 3 MATERIALS AND METHODS

This chapter introduces the materials information used in this study, including solid materials (used as aluminosilicate precursor or metal sources) and liquid materials (used as phosphate activators or ions modifiers). The product characterization and performance assessment technologies are also described.

3.1 Solid Raw Materials

3.1.1 Metakaolin (MK)

Metakaolin [$2SiO_2 \cdot Al_2O_3$] is a product of the dehydroxylated clay mineral kaolinite [$Si_2O_5Al_2(OH)_4$] under high temperature calcination (Sperinck et al., 2011). The metakaolin comprises two Al-oxides: Si-O-Al(1O) (i.e., Al in 5-fold coordination) and Si-O-Al(2O) (i.e., Al in 4-fold coordination) (Sperinck et al., 2011; Davidovits, 2018). The kiln technology determines the desired chemical reactivity. These inherent features strongly attract much of the original research into the geopolymer chemistry, especially the alkali-aluminosilicate geopolymer (Wang et al., 2005; Bell et al., 2009; Sawant and Ghugal, 2015).

This study employs the metakaolin as the aluminosilicate precursor to synthesize the silico-aluminophosphate geopolymer (Douiri et al., 2016). The relatively pure aluminosilicates can simplify the geopolymer formation process, and suppress interference caused by other impurities (e.g., alkali metals and organics). Two commercial metakaolins were used in this research, whose chemical compositions, bulk density, loss on ignition and granularity information (average particle size and D_{50} particle size) are listed in Table 3.1. The MK1 and MK2 were supplied by Chaopai Kaolin Co., Ltd., and Jiaozuo City Yu-Kun Mining Co., Ltd., respectively. The MK1 was used in Chapter 5, Chapter 6 and Chapter 7, and MK2 was used in Chapter 4 only.

3.1.2 Silica fume (SF)

Silica fume as a high-purity and fine-particle cementitious material is widely used for fabricating ultra-high performance cement (UHPC) products (de Larrard and Sedran, 1994; Mazloom et al., 2004; Plank et al., 2009). It is also known as nano-silica, micro-silica or condensed silica fume (Maheswaran et al., 2013). The silica fume is an indusial byproduct during the manufacture of silicon and ferrosilicon alloys.

The advantages of silica fume lie in its extreme fineness, purity and reactivity. The average particle size of silica fume used in civil engineering ranges from 0.01 to 10 μm (Mehta & Monteiro, 2006; Siddique and Chahal, 2011; Quercia et al., 2013), while more than 90% silica is generally contained in silica fume according to chemical composition (XRF determination). The amorphous state and glass phase of silica entitle the silica fume with high reactivity (Yajun & Cahyadi, 2004). In traditional Portland cement (Mehta and Gjørv, 1982) and alkali-activated cement (Brew and MacKenzie, 2007; Prud'homme et al., 2010), silica fume has been successfully introduced as a pozzolan, for increasing particle packing density, reducing bleeding, improving cohesion, and thinning cement/aggregate interfacial transition zone (ITZ) (Neville, 2011).

In this research, the silica fume was provided by Guangzhou Gongshi Chemical Materials Co., Ltd. Its chemical compositions, bulk density, loss on ignition and granularity information (average particle size and D_{50} particle size) are displayed in Table 3.1. The silica fume as a silicate donor is used in Chapter 4, for synthesizing the silico-aluminophosphate geopolymers with theoretical and aluminum-deficient molecular structures.

3.1.3 Dead-burnt magnesia (DBM)

Commercially available magnesia is generally obtained, either by a dry route from the calcination of mined magnesite deposits or by a wet route from solutions of magnesium-bearing brines or seawater (Bhatti et al., 1984; Shand, 2006; Walling and Provis, 2016). The further treatment to the produced magnesia, by prolonging the residence time within calcining kiln and elevating calcination temperature, increases the crystallite size and reduces the reactivity and surface area (Eubank, 1951). The varying calcination time and temperature enable the magnesia to be applied for different purposes and scenarios. According to the calcination temperature, the magnesia can be divided into light-burnt magnesia (700-1000 ℃), hard-burnt magnesia (1000-1500 ℃) and dead-burnt magnesia (1500-2000 ℃) (Jin and Al-Tabbaa, 2014).

The dead-burnt magnesia is typically used in the refractories industry (Salomao et al., 2007) and magnesium phosphate cement preparation (Seehra et al., 1993), principally because of its high melting point and low reactivity, respectively. This research chooses the dead-burnt magnesia as the magnesium source, to induce a rapid reaction between magnesium and phosphate species in silico-aluminophosphate geopolymer. The dead-burnt magnesia was purchased from Jimei Refractory Co., Ltd., and Table 3.1 summarizes its chemical and physical information.

3.1.4 Low-calcium coal fly ash (LCFA)

Coal fly ash is a widely available byproduct of coal combustion in thermal power plants (Blissett and Rowson, 2012). Its similarity of chemical composition to natural pozzolan encourages the use of coal fly ash in conjunction with Portland cement. Depending on the upstream raw materials, quenching process and place of origin, the coal fly ash particles have a wide variance in composition, mineralogy and particle size, and inherent heterogeneity behaves distinguishing reactivity (Ilic et al., 2003).

Coal fly ash can be sub-divided into two categories according to ASTM C618: Class F, known as low-calcium coal fly ash, and Class C, known as high-calcium coal fly ash. The low-calcium coal fly ash is generally produced by pulverized anthracite or bituminous coal. These high calorific value coals can create a high temperature (1300-1700 ℃), facilitating to yield spherical CFA particles with high content of glassy or vitreous aluminosilicate phases and low content of impurities (e.g., calcium and sulfur) (Seames, 2003; Chindaprasirt and Rattanasak, 2010). Such low-calcium CFA has high pozzolanic activity and alkali activation reactivity (Fernández-Jiménez and Palomo, 2003), and is most widely used in geopolymer synthesis as a host material (Duxson and Provis, 2008) and Portland cement replacement as a supplementary cementitious material.

The low-calcium coal fly ash used in this study was produced by China Light and Power Co. Ltd. (Hong Kong), which is defined as directly-used ash in concrete production in accordance to BS3892: Part1: 1997. The chemical compositions, bulk density, loss on ignition and granularity information (average particle size and D_{50} particle size) of the low-calcium coal fly ash are shown in Table 3.1, while their microscopic morphologies obtained by scanning electron microscopy technology are demonstrated in Fig. 3.1. This coal fly ash as the aluminosilicate replacement was used in Chapter 7.

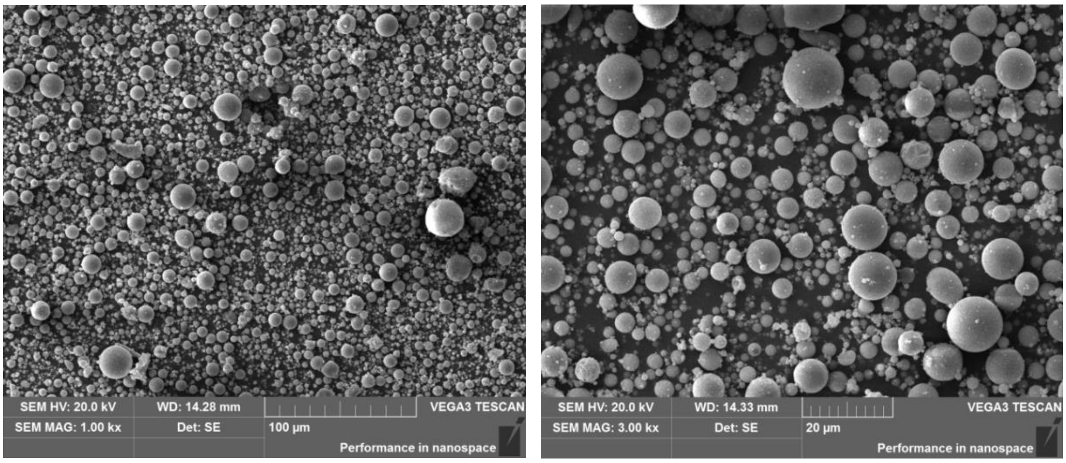

(a) 1000x (b) 3000x

Fig. 3.1 Microscopic morphologies of low-calcium coal fly ash

3.1.5 High-calcium coal fly ash (HCFA)

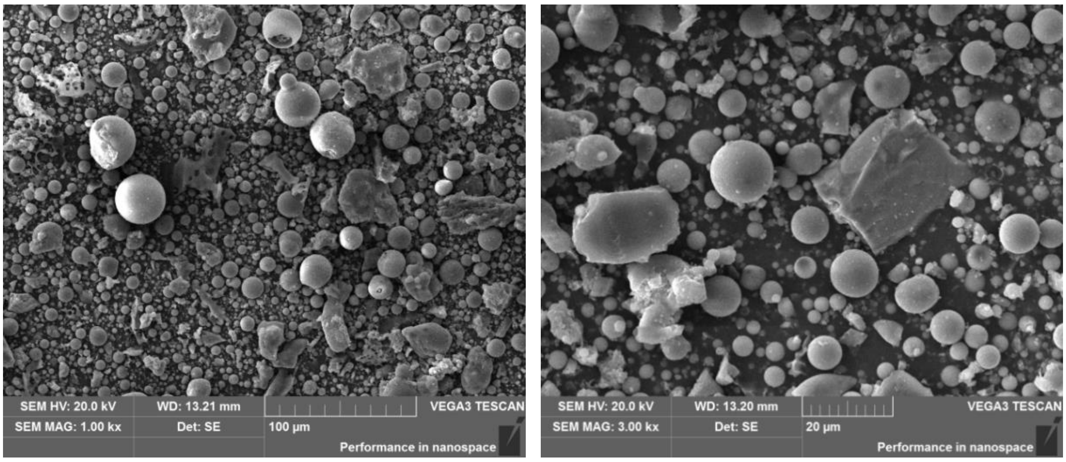

(a) 1000x (b) 3000x

Fig. 3.2 Microscopic morphologies of high-calcium coal fly ash

The high-calcium coal fly ash defined by ASTM C618 usually has the calcium contents of more than 10%, which is a result of lignite or other low-quality coal burning. Recently, fluidized bed combustion (FBC) technology as an advanced coal-combustion technology is proposed for high-efficiency energy utilization. This combustion process is considered green and clean from the view of gas and dust emission reduction. The desulfurizer (e.g., lime) is usually mixed with the coal in order to reduce sulfide discharge (Srivastava et al., 2004). Thus, such CFA particles produced during this process usually contain high contents of calcium and sulfur compounds. However, in alkaline environment the sulfur contained in such coal fly ash easily reacted with the activated calcium and alumina in cement, forming anhydrites and delayed ettringite crystals (Taylor et al., 2001), whose apparent solid volume expands by around 62% and 125%, respectively. Therefore, this coal fly ash needs to experience some treatments and modifications before use in construction in order to avoid premature distress in concrete (Hulett and Weinberger, 1980; Slavik et al., 2008; Chindaprasirt et al., 2010).

The high-calcium coal fly ash as the calcium donor was proposed to prepare silico-aluminophosphate geopolymer in Chapter 7. This coal fly ash is regarded as unqualified ash by China Light and Power Co. Ltd. (Hong Kong), and needs to be reprocessed in Green Island Cement Co. Ltd. The chemical compositions, bulk density, loss on ignition and granularity information (average particle size and D_{50} particle size) of the high-calcium coal fly ash are shown in Table 3.1. Besides, their microscopic morphologies obtained by scanning electron microscopy technology are demonstrated in Fig. 3.2.

Table 3.1 Chemical composition and physical properties of MKs, SF, DBM, LCFA and HCFA

Chemical composition [a]	MK-1	MK-2	SF	DBM	LCFA	HCFA
Aluminum oxide, Al_2O_3	46.8%	43.8%	-	-	31.2%	26.5%
Silicon oxide, SiO_2	51.1%	54.1%	94.6%	4.2%	44.5%	38.1%
Calcium oxide, CaO	0.2%	0.2%	0.8%	2.4%	5.3%	16.5%
Ferric oxide, Fe_2O_3	0.5%	0.8%	0.6%	3.2%	6.5%	8.5%
Magnesium oxide, MgO	-	0.1%	0.8%	88.9%	1.9%	1.2%
Sulfur trioxide, SO_3	0.2%	-	0.3%	-	3.3%	3.6%
Titanium dioxide, TiO_2	0.8%	0.2%	-	-	1.2%	1.7%
Sodium oxide, Na_2O	-	0.1%	0.5%	-	1.1%	0.6%
Potassium oxide, K_2O	-	0.6%	1.3%	-	1.3%	1.1%
Phosphorus pentoxide, P_2O_5	-	-	0.4%	-	0.2%	0.4
Others	0.4%	0	0.7%	1.3%	3.5%	1.8%
Bulk density (g/cm^3)	0.61	0.54	2.09	2.73	2.49	2.43
Loss on ignition [b]	4.1%	3.7%	2.9%	0.9%	3.8%	6.5%
Average particle size (µm) [c]	3.12	4.16	2.01	8.29	8.58	14.91
D_{50} particle size (µm) [c]	4.37	4.09	1.28	5.55	22.93	19.12

a. Chemical composition is determined by X-ray fluorescence (XRF) (Thermo Fisher Scientific), and elements are represented as oxides and normalized by wt. %.

b. Loss on ignition (LOI) is measured at 1050℃.

c. Average particle size and D_{50} particle size are measured by laser particle size analyzer (HELOS H3585).

3.2 Liquid Raw Materials

3.2.1 Orthophosphoric acid (OPA)

The orthophosphoric acid used in this research is a commercial product, purchased from Ajax Finechem Laboratory Chemicals. The mass concentration of the orthophosphoric acid is 85%.

3.2.2 Monoaluminum phosphate (MAP)

Monoaluminum phosphate is an industrial grade product with a nominal formula of $Al(H_2PO_4)_3$. The standard monoaluminum phosphate is the product of the complete reaction between orthophosphoric acid and aluminum hydroxide with a P/Al molar ratio of 3. However, the indusial grade monoaluminum phosphate usually contains other aluminum phosphates, e.g., $AlPO_4$ and $Al_2(HPO_4)_3$, leading to varying P/Al ratios (Finch and Sharp, 1989). Besides, the monoaluminum phosphate has solid and liquid forms. In this study, there are three types of monoaluminum phosphates used.

One used in Chapter 4 is solid monoaluminum phosphate powders, obtained from Zibo Hanye Industry Refractory Materials Sales Co., Ltd. The chemical composition of the solid monoaluminum phosphate is detected by X-ray fluorescence as P_2O_5 (78.6%), Al_2O_3 (20.4%) and Fe_2O_3 (0.8%). The calculated P/Al molar ratio of this monoaluminum phosphate is 2.77 because of the presence of aluminum phosphate (# 01-076-0232), which is discussed in Chapter 4.

A commercial liquid monoaluminum phosphate from Xianju Litian Chemical Co., Ltd. is applied in Chapter 5. The composition measurement result reveals that the P/Al molar ratio of this monoaluminum phosphate is 2.99, with a mass concentration of 61.3%.

In Chapters 6 and 7, the liquid monoaluminum phosphate is prepared in laboratory, by a hydrothermal reaction between the powdered aluminum hydroxide and the liquid orthophosphoric acid, resulting in an activating solution with a P/Al molar ratio of 3.0. Two different mass concentrations, i.e., 62.0% and 53.4%, are used in Chapter 6 and Chapter 7, respectively.

3.2.3 Phosphate activator preparation

The synthesis of silico-aluminophosphate geopolymer is mainly based the geopolymerization between the aluminosilicate precursor and the activating solution. In alkali-aluminosilicate geopolymer, the alkali-silico activator is generally prepared with a mixture of sodium hydroxide and sodium silicate, with a certain modulus (i.e., molar ratio of SiO_2/Na_2O). The ion molar ratio is critical to the performance of the formed geopolymer matrix. Similarly, the phosphate activator used in this research is prepared by different Al/P molar ratios.

As shown in Table 3.2, the mix proportions of phosphate activator with different Al/P ratios are adjusted by mixing commercial liquid monoaluminum phosphate and orthophosphoric acid. The initial pH increases with the content of aluminum, from 1.59 at Al/P of 0.05 to 1.73 at Al/P of 0.33. The change range is marginal. After 28 day standing, some white aluminum phosphate gels appear in the solutions with the Al/P ratios more than 0.3, possibly disabling the efficiency of phosphate activating solution. Therefore, the ready prepared phosphate solutions are used in all sub-studies.

Table 3.2 Mix proportions of phosphate activators through blending orthophosphoric acid with commercial liquid monoaluminum phosphate

No.[a]	Weight ratio		Al^{3+} ion concertation (mol/L)	Initial pH[b]	28 day pH[b]
	OPA	MAP			
Al/P=0.33	0	1	0.1	1.73	1.67
Al/P=0.30	0.08	1	0.1	1.69	1.54
Al/P=0.20	0.46	1	0.1	1.64	1.65
Al/P=0.10	1.61	1	0.1	1.62	1.71
Al/P=0.05	3.92	1	0.1	1.59	1.67

a. Al/P is the molar ratio of aluminum-to-phosphorus in final solution

b. pH measurement is at a temperature of 25 ℃.

The influences of Al/P ratio on the Al and P environment in phosphate activators are assessed by liquid-state nuclear magnetic resonance (NMR). The liquid-state ^{31}P and ^{27}Al NMR spectra of the phosphate activators with different Al/P molar ratios are shown in Fig. 3.3. The ^{31}P spectra for all activators (Fig. 3.3a), three distinct bands at 0 to -2.5 ppm, -8 to -9 ppm, and -12 to -14 ppm were detected, and attributed to Q^0, Q^1 and Q^2 phosphate structural units, respectively. The orthophosphate group (i.e., phosphoric acid molecules and ions) generates the phosphorus environment of Q^0, while the two clear signals resonated between -5 to -24 ppm are due to polyphosphates – either sites with P-O-P linkages, or Al complexed to phosphate-containing ligands (Chavda et al., 2015). It can be seen that using a small dosage of MAP to dilute the OPA for a resulting Al/P molar ratio of 0.05, the spectrum of its final solution is embodied by a sharp resonance peak at -0.5 ppm and two small resonances at -8 and -13 ppm. The sharp band is weakened with the increase of Al/P ratio, companied by enhancement of the small bands at -8 and -13 ppm. Similarly, the chemical shift of the ^{27}Al spectra at around -8 ppm (Fig. 3.3b), corresponding to a clear six-coordinated environment of aluminum (Samadi-Maybodi et al., 2009), slightly increases with the Al/P molar ratio. Thus, the range of these Al/P ratios (0.05-0.33) barely changes the chemical environmental of phosphorus and aluminum when the molar ratio of aluminum to phosphorus was less than 1.0 (Samadi-Maybodi et al., 2009).

As shown in Fig. 3.4, the liquid monoaluminum phosphate prepared in laboratory holds the similar aluminum and phosphorus chemical structure to the commercial product. More importantly, the desirable molar ratio and concentration of the phosphate activator with high accuracy and marginal impurity is more easily obtained in laboratory. Therefore, the studies in Chapters 6 and 7 for synthesis of Mg and Ca-accelerated silico-aluminophosphate geopolymer use the laboratory-prepared activators.

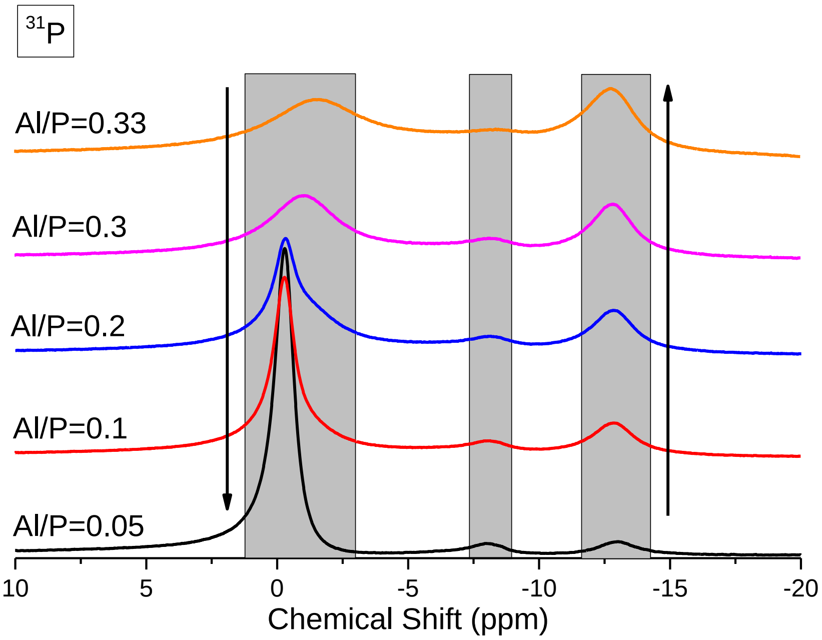

(a)

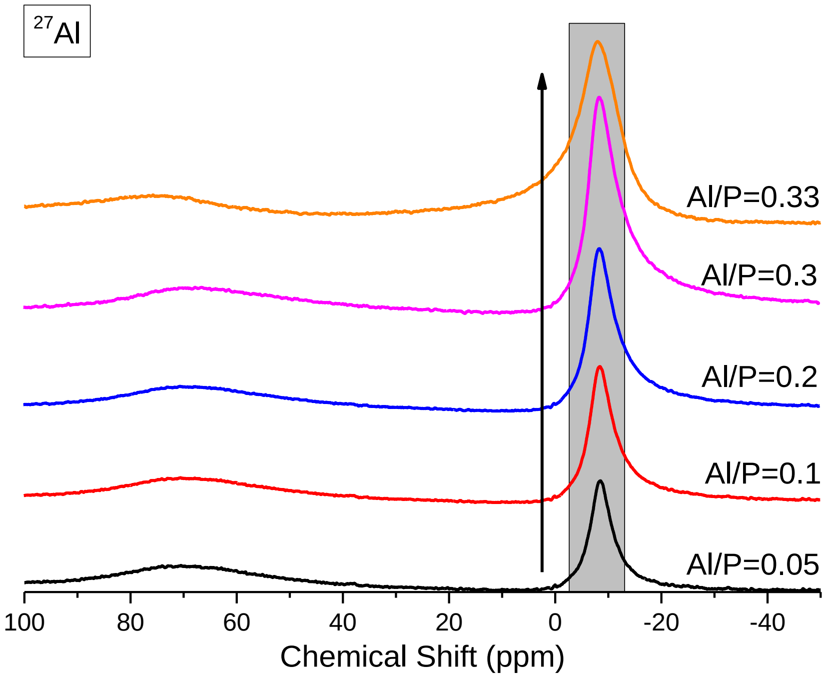

(b)

Fig. 3.3 Liquid-state ^{31}P and ^{27}Al NMR spectra of the phosphate activators with different Al/P ratios

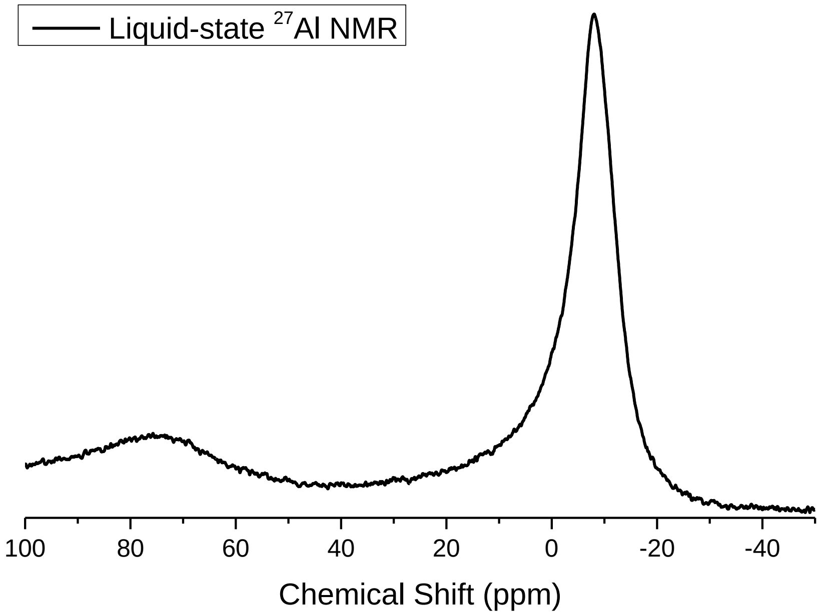

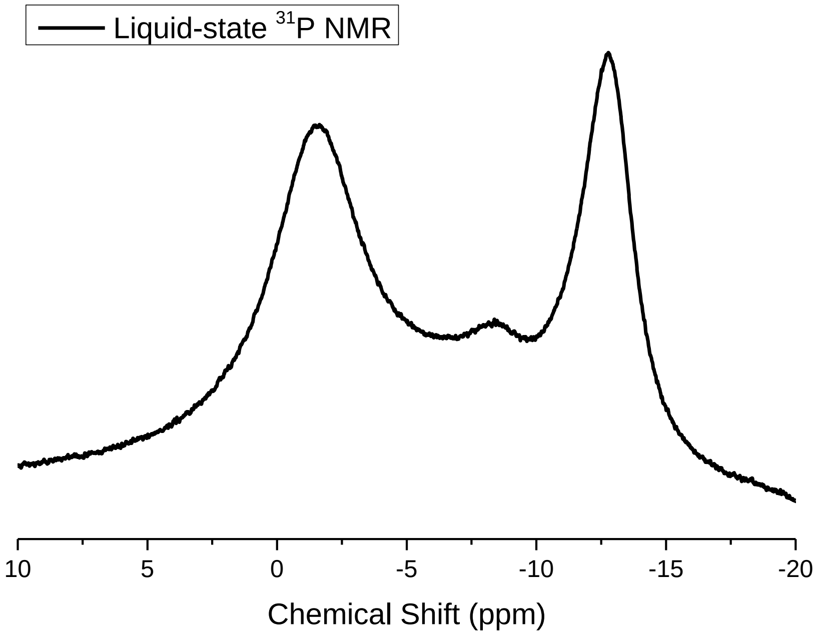

Fig. 3.4 Liquid-state ^{27}Al and ^{31}P NMR spectra of commercial liquid monoaluminum phosphate

3.3 Characterization and Assessment Methods

3.3.1 Rheology

The influence of aluminum species on the rheological properties of the fresh silico-aluminophospahte geopolymer was investigated by a rotational and oscillatory rheometer (Anton Paar MC302) equipped with a parallel-plate measuring system (maximum torque, 200 mN m). Previous researches on the rheological parameters of Portland cement (Chow et al., 1988) and alkali-aluminosilicate geopolymer cement (Poulesquen et al., 2011) are referred. The evolution of shear stress (Pa) and viscosity (Pa s) under shear rates ranging from 0.01 to 100 s^{-1} was measured in the fresh geopolymer pastes at a temperature of 25 °C. In Chapter 5, the solid volume fractions of the geopolymer pastes with the two H_2O/MK ratios (0.4 and 0.5) were about 0.78 and 0.70, respectively, to ensure that the paste displayed a yield stress.

3.3.2 X-ray diffraction (XRD)

Regardless of the activation approach, the alkali-alumnosilicate geopolymer and silico-aluminophosphate geopolymer are both X-ray amorphous, consistent with the poorly-ordered, ill-crystallized reaction products (e.g., N-A-S-H and S-A-P gels). When comparing the raw materials and the formed geopolymers, their X-ray diffraction results usually show some position shifts of hump assigned to glassy components, which are associated with the geopolymerization. Besides, the Mg/Ca-induced reactions explored in Chapter 6 and 7 produce some crystalline phosphate phases, which were identified by X-ray diffraction.

This study employs a Rigaku SmartLab X-ray diffractometer to identify the hump shift and crystalline phases. X-ray diffraction test was conducted under a 9 kW Cu-Kα radiation source (λ=1.5406 Å), with a step size of 0.02° and a count time of 5 s/step. The measurement range was from 5 to 85° (2θ), and characteristic range was selected according to the sample feature.

3.3.3 Scanning electron microscopy (SEM)

The microstructural features and elemental composition were characterized by scanning electron microscopy (TESCAN VEGA3) with energy-dispersive X-ray spectroscopy (Oxford INCA Energy 250). The backscattered electron (BSE) imaging is applied in Chapter 7. The applied acceleration voltage was 20 kV and the working distance ranged between 10 and 20 mm for a good focus. The dried geopolymer samples were solidified into transparent epoxy resin, leaving a typical surface by carbon/gold sputtering for investigation.

3.3.4 Thermogravimetric analysis (TGA)

Thermogravimetric analysis provides the information that the mass of the samples change over time as the temperature increase. The thermal decomposition and phase transitions of the silico-aluminophosphate geopolymers were studied by thermogravimetric analysis. The simultaneous thermal analysis (Thermo plus EVO2, Rigaku) was performed from 30 to 1100 ℃ with a heating rate of 10 ℃/min. The argon atmosphere as protective gas was applied throughout.

3.3.5 Magic angle spinning nuclear magnetic resonance (MAS-NMR)

Magic angle spinning nuclear magnetic resonance (MAS-NMR) spectroscopy, including liquid-state and solid-state, is a powerful technique that can provide element structural information for ion chemical environment in solutions and amorphous and poorly crystalline materials in hardened geopolymers. All the MAS-NMR spectra in this work were acquired on a Bruker AVANCE III 400 WB spectrometer (9.4 T) at 297 K.

The liquid-state ^{31}P and ^{27}Al NMR to explore the aluminum phosphate gels, solutions, and final powders is common in material science (Lookman et al., 1996; Lookman et al., 1997; Zhang et al., 2004; Damodaran et al., 2006). In this liquid-state NMR measurement, the spectrometer frequencies for ^{31}P and ^{27}Al nuclei were 202.47 and 130.33 MHz, respectively. The corresponding recycle delays applied were 6 and 5 s, with 90º pulse durations of 8 and 2 μs, respectively. The chemical shifts of ^{31}P were expressed in ppm relative to the orthophosphoric acid, and the ^{27}Al resonances were referenced to a 1.0 mol/L $AlCl_3$ solution.

The solid-state NMR has been widely used to investigate the chemistry of Portland cement and alkali-aluminosilicate geopolymer cement. For example, the reaction extent, the polymerization degree of the aluminum-silicate chains and the incorporation extent of Al into the C-S-H in low-calcium alkali-aluminosilicate geopolymer and high-calcium alkali-aluminosilicate geopolymer have been determined through ^{29}Si NMR (Wang and Scrivener, 2003; Buchwald et al., 2007). ^{27}Al NMR spectrum identifies the tetrahedral or octahedral coordinated Al environment, existed in C-(A)-S-H type gels in calcium-containing alkali-aluminosilicate geopolymers (Sun et al., 2006). ^{31}P NMR was also used to pinpoint the calcium-phosphate-hydrate (C-P-H) gels in calcium phosphate cement (Chavda et al., 2015).

In the solid-state ^{31}P and ^{27}Al NMR measurement of silico-aluminophosphate geopolymer, the dried and finely-powdered samples were packed in 4 mm zirconia rotors. For ^{27}Al, X channel was tuned to 104.3 MHz, with a spinning speed of 12 kHz and a pulse duration of 0.9 μs. A total of 2000 scans were recorded with 2s recycle delay for each sample. ^{31}P spectrum was conducted at 161.9 MHz, with a spinning speed of 12 kHz. The ^{31}P NMR measurement was conducted at a contact time of 2 ms. A total of 1000 scans were recorded with 5 s recycle delay for each sample. Chemical shifts of ^{27}Al and ^{31}P are benchmarked by the resonances of aluminum chloride solution (1.0 mol/L) and monoammonium phosphate solution (1.0 mol/L), respectively.

3.3.6 Other methods and standards

The macroscopic fluidity, setting time and compressive strength of all the silico-aluminophosphate geopolymer products were evaluated following ASTM C1437-15, ASTM C191-13 (or BS EN 196-3: 2005) and ASTM C109/C109M-16a, respectively. The pore information of the hardened geopolymers in Chapter 5 was obtained by mercury intrusion porosimetry (MIP). A geometrical model based on the Washburn equation, as shown in Eq. 3.1, was applied to determine the pore diameter.

$$D = -4\gamma \cos\theta / P \tag{3.1}$$

where, D (m) is the calculated pore diameter, γ (N/m) is the surface tension, θ (°) is the contact angle between mercury and pore wall, and P (Pa) is the applied pressure. The surface tension (γ) and contact angle (θ) selected in this study were 0.485 N/m and 140°, respectively. The applied pressure (P) ranged from 1 to 30,000 Psia (around 0.007-207 MPa)

Some methods for chemical analysis, e.g., pH and conductivity variation, are employed to monitor the ion evolution and chemistry of the DBM/MAP suspensions in Chapter 6.

3.4 **References**

Bell, J. L., Driemeyer, P. E., & Kriven, W. M. (2009). Formation of ceramics from metakaolin-based geopolymers. Part II: K-based geopolymer. *Journal of the American Ceramic Society*, *92*(3), 607-615.

Bhatti, A. S., Dollimore, D., & Dyer, A. (1984). Magnesia from seawater: a review. *Clay Mineral*, 19(5), 865.

Blissett, R. S., & Rowson, N. A. (2012). A review of the multi-component utilisation of coal fly ash. *Fuel*, 97, 1-23.

Brew, D. R. M., & MacKenzie, K. J. D. (2007). Geopolymer synthesis using silica fume and sodium aluminate. *Journal of Materials Science*, 42(11), 3990-3993.

Buchwald A, Hilbig H, Kaps C. Alkali-activated metakaolin-slag blends performance and structure in dependence of their composition. *Journal of Materials Science*, 2007, 42(9): 3024-3032.

Chavda, M. A., Bernal, S. A., Apperley, D. C., Kinoshita, H., & Provis, J. L. (2015). Identification of the hydrate gel phases present in phosphate-modified calcium aluminate binders. *Cement and Concrete Research*, 70, 21-28.

Chindaprasirt, P., Chareerat, T., Hatanaka, S., & Cao, T. (2010). High-strength geopolymer using fine high-calcium fly ash. *Journal of Materials in Civil Engineering*, 23(3), 264-270.

Chow, T. W., McIntire, L. V., Kunze, K. R., & Cooke, C. E. (1988). The rheological properties of cement slurries: Effects of vibration, hydration conditions, and additives. *SPE Production Engineering*, 3(04), 543-550.

Damodaran, K., Wiench, J. W., de Menezes, S. C., Lam, Y. L., Trébosc, J., Amoureux, J. P., & Pruski, M. (2006). Modification of H-ZSM-5 zeolites with phosphorus. 2. Interaction between phosphorus and aluminum studied by solid-state NMR spectroscopy. *Microporous and Mesoporous Materials*, 95(1-3), 296-305.

Davidovits, J. (2018, January). Geopolymers based on natural and synthetic metakaolin a critical review. In *Proceedings of the 41st International Conference on Advanced Ceramics and Composites (Vol. 614, p. 201)*. John Wiley & Sons.

de Larrard, F., & Sedran, T. (1994). Optimization of ultra-high-performance concrete by the use of a packing model. *Cement and Concrete Research*, 24(6), 997-1009.

Douiri, H., Kaddoussi, I., Baklouti, S., Arous, M., & Fakhfakh, Z. (2016). Water molecular dynamics of metakaolin and phosphoric acid-based geopolymers investigated by impedance spectroscopy and DSC/TGA. *Journal of Non-Crystalline Solids*, 445, 95-101.

Duxson, P., & Provis, J. L. (2008). Designing precursors for geopolymer cements. *Journal of the American Ceramic Society*, 91(12), 3864-3869

Eubank, W. R. (1951). Calcination studies of magnesium oxides. *Journal of the American Ceramic Society*, 34(8), 225-229.

Fernández-Jiménez, A., & Palomo, A. (2003). Characterisation of fly ashes. Potential reactivity as alkaline cements. *Fuel*, 82(18), 2259-2265.

Finch, T., & Sharp, J. H. (1989). Chemical reactions between magnesia and aluminium orthophosphate to form magnesia-phosphate cements. *Journal of Materials Science*, 24(12), 4379-4386.

Hulett, L. D., & Weinberger, A. J. (1980). Some etching studies of the microstructure and composition of large aluminosilicate particles in fly ash from coal-burning power plants. *Environmental Science & Technology*, 14(8), 965-970.

Ilic, M., Cheeseman, C., Sollars, C., & Knight, J. (2003). Mineralogy and microstructure of sintered lignite coal fly ash. *Fuel*, 82(3), 331-336.

Jin, F., & Al-Tabbaa, A. (2014). Characterisation of different commercial reactive magnesia. *Advances in Cement Research*, 26(2), 101-113.

Lookman, R., Geerts, H., Grobet, P., Merckx, R., & Vlassak, K. (1996). Phosphate speciation in excessively fertilized soil: a ^{31}P and ^{27}Al MAS NMR spectroscopy study. *European Journal of Soil Science*, 47(1), 125-130.

Lookman, R., Grobet, P., Merckx, R., & Van Riemsdijk, W. H. (1997). Application of ^{31}P and ^{27}Al MAS NMR for phosphate speciation studies in soil and aluminium hydroxides: promises and constraints. *Geoderma*, 80(3-4), 369-388.

Maheswaran, S., Bhuvaneshwari, B., Palani, G. S., Nagesh, R., & Kalaiselvam, S. (2013). An overview on the influence of nano silica in concrete and a research initiative. *Research Journal of Recent Sciences*, ISSN2277, 2502.

Mazloom, M., Ramezanianpour, A. A., & Brooks, J. J. (2004). Effect of silica fume on mechanical properties of high-strength concrete. *Cement and Concrete Composites*, 26(4), 347-357.

Mehta, P. K., & Monteiro, P. J. (1976). Concrete: microstructure, properties, and materials. 2006. *Utilization of Palm Oil Fuel Ash in Concrete: a review*.

Mehta, P. K., & Gjørv, O. E. (1982). Properties of portland cement concrete containing fly ash and condensed silica-fume. *Cement and Concrete Research*, 12(5), 587-595.

Neville, A. M. (2011). *Properties of Concrete* (Vol. 5). London: Longman.

Plank, J., Schroefl, C., Gruber, M., Lesti, M., & Sieber, R. (2009). Effectiveness of polycarboxylate superplasticizers in ultra-high strength concrete: the importance of PCE compatibility with silica fume. *Journal of Advanced Concrete Technology*, 7(1), 5-12.

Poulesquen, A., Frizon, F., & Lambertin, D. (2011). Rheological behavior of alkali-activated metakaolin during geopolymerization. *Journal of Non-Crystalline Solids*, 357(21), 3565-3571.

Prud'homme, E., Michaud, P., Joussein, E., Peyratout, C., Smith, A., Arrii-Clacens, S., & Rossignol, S. (2010). Silica fume as porogent agent in geo-materials at low temperature. *Journal of the European Ceramic Society*, 30(7), 1641-1648.

Quercia, G., Lazaro, A., Geus, J. W., & Brouwers, H. J. H. (2013). Characterization of morphology and texture of several amorphous nano-silica particles used in concrete. *Cement and Concrete Composites*, 44, 77-92.

Salomao, R., Bittencourt, L. R. M., & Pandolfelli, V. C. (2007). A novel approach for magnesia hydration assessment in refractory castables. *Ceramics International*, 33(5), 803-810.

Samadi-Maybodi, A., Nejad-Darzi, S. K. H., & Bijanzadeh, H. (2009). ^{31}P and ^{27}Al NMR studies of aqueous (2-hydroxyethyl) trimethylammonium solutions containing aluminum and phosphorus. *Spectrochimica Acta Part A: Molecular and Biomolecular Spectroscopy*, 72(2), 382-389.

Sawant, R. M., & Ghugal, Y. M. (2015). Recent trend: Use of metakaolin as admixture: A review. *American Journal of Engineering Research (AJER)*, 4(12), 08-14.

Seames, W. S. (2003). An initial study of the fine fragmentation fly ash particle mode generated during pulverized coal combustion. *Fuel Processing Technology*, 81(2), 109-125.

Seehra, S. S., Gupta, S., & Kumar, S. (1993). Rapid setting magnesium phosphate cement for quick repair of concrete pavements—characterisation and durability aspects. *Cement and Concrete Research*, 23(2), 254-266.

Shand, M. A. (2006). The Chemistry and Technology of Magnesia. *John Wiley & Sons*.

Siddique, R., & Chahal, N. (2011). Use of silicon and ferrosilicon industry by-products (silica fume) in cement paste and mortar. *Resources, Conservation and Recycling*, 55(8), 739-744.

Slavik, R., Bednarik, V., Vondruska, M., & Nemec, A. (2008). Preparation of geopolymer from fluidized bed combustion bottom ash. *Journal of Materials Processing Technology*, 200(1-3), 265-270.

Sperinck, S., Raiteri, P., Marks, N., & Wright, K. (2011). Dehydroxylation of kaolinite to metakaolin—a molecular dynamics study. *Journal of Materials Chemistry*, 21(7), 2118-2125.

Srivastava, R. K., Miller, C. A., Erickson, C., & Jambhekar, R. (2004). Emissions of sulfur trioxide from coal-fired power plants. *Journal of the Air & Waste Management Association*, 54(6), 750-762.

Sun, G. K., Young, J. F., & Kirkpatrick, R. J. (2006). The role of Al in C–S–H: NMR, XRD, and compositional results for precipitated samples. *Cement and Concrete Research*, 36(1), 18-29.

Taylor, H. F. W., Famy, C., & Scrivener, K. L. (2001). Delayed ettringite formation. *Cement and Concrete Research*, 31(5), 683-693.

Walling, S. A., & Provis, J. L. (2016). Magnesia-based cements: a journey of 150 years, and cements for the future?. *Chemical Reviews*, 116(7), 4170-4204.

Wang, S. D., & Scrivener, K. L. (2003). ^{29}Si and ^{27}Al NMR study of alkali-activated slag. *Cement and Concrete Research*, 33(5), 769-774.

Wang, H., Li, H., & Yan, F. (2005). Synthesis and mechanical properties of metakaolinite-based geopolymer. *Colloids and Surfaces A: Physicochemical and Engineering Aspects*, 268(1-3), 1-6.

Yajun, J., & Cahyadi, J. H. (2004). Simulation of silica fume blended cement hydration. *Materials and Structures*, 37(6), 397-404.

Zhang, L., & Eckert, H. (2004). Sol–gel synthesis of Al_2O_3–P_2O_5 glasses: mechanistic studies by solution and solid state NMR. *Journal of Materials Chemistry*, 14(10), 1605-1615.

This page is intentionally left blank

CHAPTER 4 FORMATION MECHANISM OF SILICO-ALUMINOPHOSPHATE GEOPOLYMER WITHOUT ACCELERATION CONDITIONS

Geopolymer cement is titled as a low carbon and eco-friendly construction material (Komnitsas, 2011). This chapter introduces a new family of geopolymer, i.e., silico-aluminophosphate geopolymer. Its formation mechanism and thermal stability of this type of geopolymer are mainly investigated. In this sub-study, three mixes of the silico-aluminophosphate geopolymer were synthesized at ambient temperature with different molar ratios of Si, Al and P, which were supplied by the raw materials of silica fume, metakaolin and solid monoaluminum phosphate. The geopolymer pastes with ideal, silicate-deficient and aluminate-deficient molecular structures were designed by the Si:Al:P molar ratios of 1:1:1, 0.49:1:1 and 1:0.18:1, respectively. No extra promotion for geopolymerization and setting acceleration was applied.

4.1 Introduction

This sub-study aims to figure out the formation mechanism and thermal stability of the silico-aluminophosphate geopolymer hardened at room temperature. The metakaolin (a product of kaolin calcined at 750 ℃) as an aluminosilicate precursor to provide silicate and aluminate species (Ilić, 2010), together with silica fume as a supplement of silicates, were applied to react with the monoaluminum phosphate that was chosen as aluminate and phosphate donors. It should be noted that no accelerating setting condition (e.g., through the addition of metal oxides or the use of high temperature curing) was adopted in the present work. Geopolymers with a theoretical molecular structure, a silicate-deficient molecular structure and an aluminate-deficient molecular structure are designed without the use of any accelerating setting condition (e.g., thermal curing or using setting agent) in this experiment, to facilitate a clear investigation into the formation mechanism of the synthesized silico-aluminophosphate geopolymer. Synthesis mechanism associated with phase distribution and transition, morphological features and compressive strength were significantly reported in this chapter.

4.2 Experimental Program

4.2.1 Materials

The solid monoaluminum phosphate used in this chapter is an industrial grade, and usually includes a mixture of different aluminum acid phosphates with varying P/Al ratio (e.g., $Al(H_2PO_4)_3$, $AlPO_4$ and $Al_2(HPO_4)_3$) (Finch and Sharp, 1989). Since the solid MAP is extremely hygroscopic and agglomerating in humid environment, it needs to be dry treatment and grinding before use. Metakaolin and undensified silica fume are commercially available products with nominal mean particle diameters of 3.5 μm and 2.0 μm respectively.

4.2.2 Mix design and sample preparation

In this work, the P/Al molar ratio of MAP and Si/Al molar ratio of MK measured were 2.77 and 0.765, respectively, according to the X-ray fluorescence element analysis. The mixture proportions of silico-aluminophosphate geopolymer pastes are presented in Table 4.1. The water-to-solid (*w/s*) of all the geopolymer pastes is kept as 0.25. Three geopolymer pastes with theoretical, silicate-deficient and aluminate-deficient molecular structures were designed by the Si: Al: P molar ratios of 1:1:1, 0.49:1:1 and 1:0.18:1, denoted as SAP, AP and SP, respectively.

As designed recipe, the silico-aluminophosphate geopolymer pastes were prepared by homogenizing the solid MAP, MK, SF and water by a mechanical mini-mixer. Before adding water, all the solids were dry mixed for 5 min. The fresh pastes were cast into 50 mm plastic cubic molds and compacted by a mechanical vibration table. The casted geopolymer pastes were wrapped up by a membrane to retain moisture in an environmental chamber with a temperature of 25℃ and a relative humidity of 50%. After 3 day, the relative humidity in the environmental chamber was adjusted to 95% to cure the demolded geopolymer matrices for further analysis at specified periods.

Table 4.1 Mixture proportions of silico-aluminophosphate geopolymer pastes

Series	Molar ratio of Si:Al:P	*w/s*	Components by weight ratio				Final setting time
			MAP	MK	SF	Water	(at 25±2 ℃)
SAP	1:1:1	0.25	1	0.591	0.283	0.469	47 h
AP	0.49:1:1	0.25	1	0.591	-	0.398	52 h
SP	1:0.18:1	0.25	1	-	0.554	0.389	108 h

a. The purities of MAP, MK and SF are 98.92%, 91.40% and 94.60%, respectively;
b. *w/s* is water-to-solid mass ratio, and the solid compositions consist of MAP, MK and SF;

4.2.3 Characterization methods

The compressive strength was determined from triplicate 50 mm cube specimens at a loading rate of 0.5 MPa/s after 7, 14 and 28 day curing. Micro-morphological features for the hardened pastes were characterized by scanning electron microscopy equipped with energy dispersive X-ray spectroscopy detector. The applied acceleration voltage is 20 kV and the working distance ranges between 10 and 15.0 mm for a good focus. The powder mineralogical compositions of raw materials and hardened geopolymer pastes were determined by a high resolution X-ray diffractometer using 9 kW Cu-K_α radiation source, ranging from 5 to 50° (2θ) with a scanning step of 0.02°. Simultaneous thermal analysis was employed to determine the thermal decomposition behavior of hardened pastes at a heating rate of 10 ℃/min with argon gas environment.

4.3 Results and Discussion

4.3.1 Compressive strength and setting time

The development of compressive strength of the above three series of hardened geopolymer pastes varied depending on the molar ratios of Si, Al and P, as displayed in Fig. 4.1. It is clear that the two series of SAP and AP geopolymers show the similar tendency from about 4 MPa at 7 day to around 30 MPa at 28 day. The gradual participation of silicon-containing phase during geopolymerization might render that the SAP geopolymer slightly outperformed the AP geopolymer in terms of the 28-day compressive strength. Regarding the SP geopolymer, it scarcely has the strength during the whole period although it can be hardened at 108 hour and always keeps the shape after the demolding. It was therefore concluded that the absence of aluminate building block in the SP geopolymer prevented the S-A-P molecular structure formation at room temperature (Louati et al., 2014).

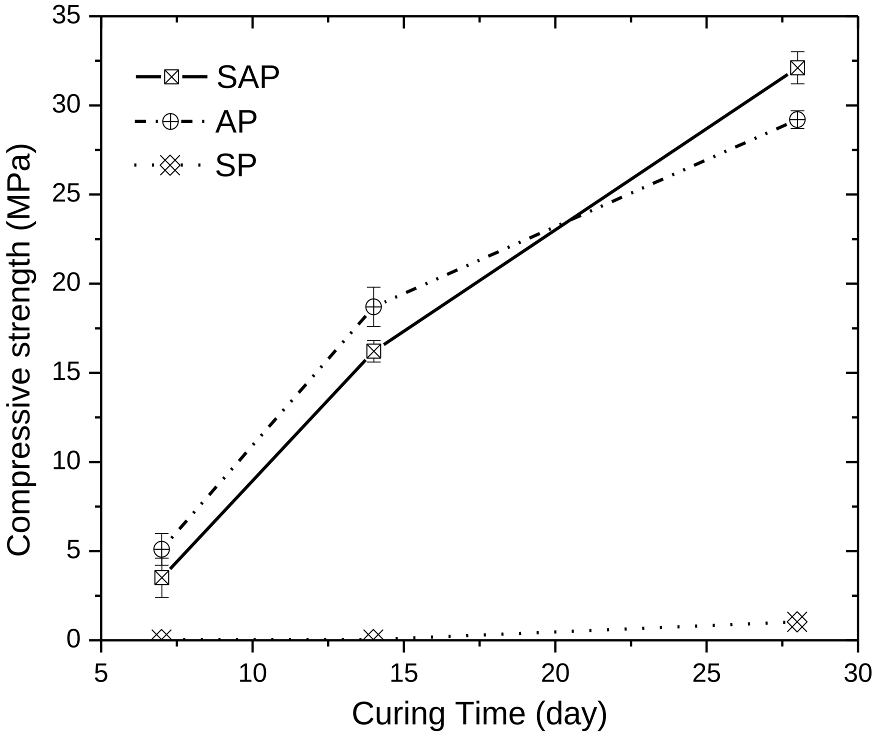

Fig. 4.1 Compressive strength development for three series of the hardened geopolymer pastes subjected to chamber curing

Despite achieving moderate strength, the setting time behaves poor in all geopolymers. Fig. 4.2 demonstrates the influences three Si:Al:P molar ratios on the setting time of the geopolymer pastes. When the solids encounter water in the early period, the dissolution of solid MAP creates an acidic environment, in which phosphate species attack the MK and SF particles. The setting of the geopolymer pastes stemmed from pH value increase, as the aluminum and phosphorus generally exist in the free state at a pH of less than 3 and they start to combine together to form an aluminophosphate gel in critical pH value (Petzet et al., 2011). Therefore, the long setting time in these geopolymer pastes might be a result of the slow dissolution of the solid MAP. The added water contents are difficult to control the pH value of the geopolymer paste.

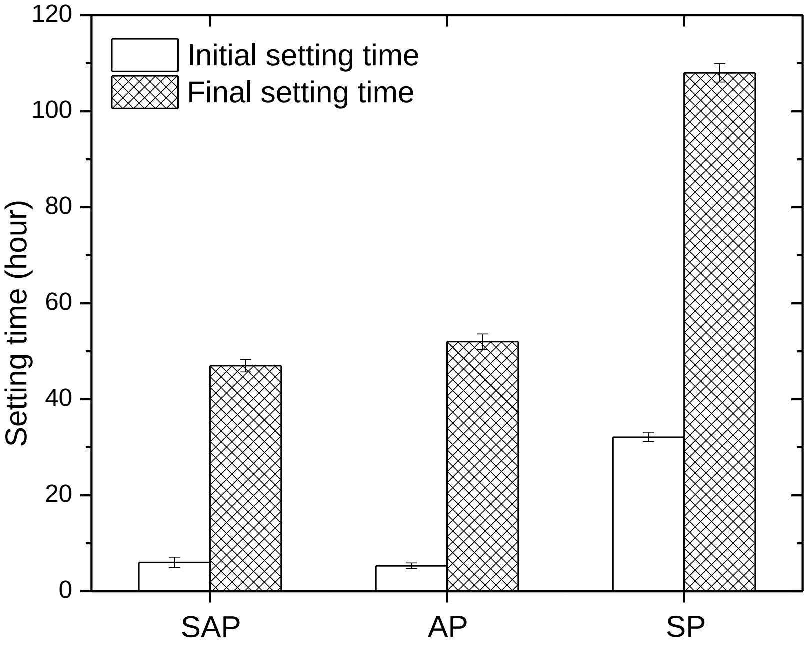

Fig. 4.2 Initial and final setting time of three series of the geopolymer pastes at room temperature

4.3.2 Mineralogical and morphological analysis

The diffractograms for raw materials (i.e., MAP, SF and MK), along with the hardened geopolymer pastes (i.e., AP, SAP, SP) at 28 day, are displayed in Fig. 4.3, indicating the well-defined reflections of crystalline phases. A broad diffuse scattering range $(20^\circ < 2\theta < 25^\circ)$ is identified in both silica fume and metakaolin, which was attributed to the amorphous aluminosilicate phase. Quartz and illite existed in the MK. Several intense peaks of MAP can be assigned to the polymorphic aluminophospahte, such as aluminum hydrogen phosphate (#00-044-0724) and aluminum phosphate (#01-076-0232). In the formed geopolymers, these crystalline phases were transformed into another type of aluminum hydrogen phosphate ($AlH_3(PO_4)_2$ $3H_2O$ #00-020-0010). The diffuse scattering range of aluminosilicate was disappeared and an amorphous aluminosilicophosphate ($SiO_2 \cdot Al_2O_3 \cdot P_2O_5 \cdot nH_2O$) was possibly formed.

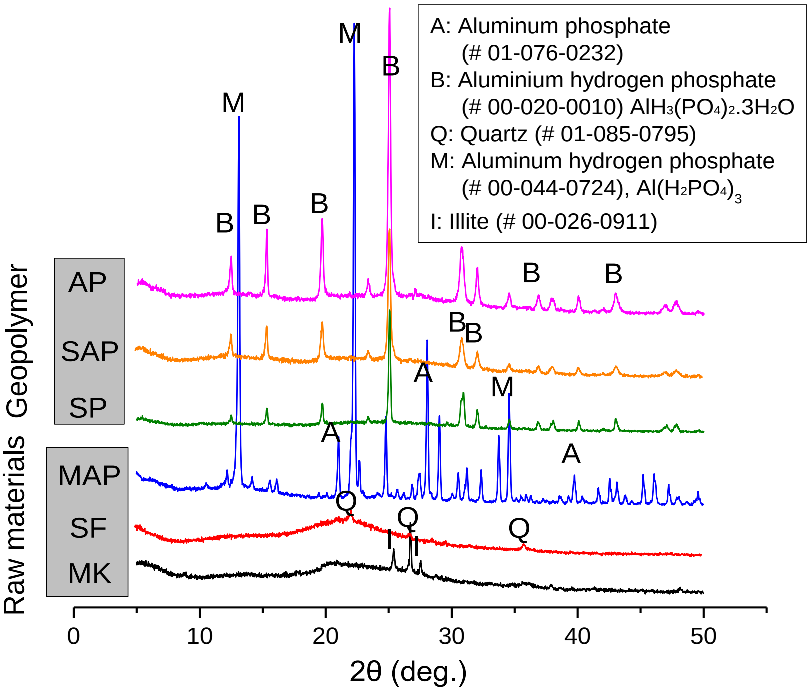

Fig. 4.3 X-ray diffraction patterns for three series of the hardened geopolymer pastes at 28 day chamber curing. The patterns of the raw materials are referred.

The micro-morphological features of the hardened SAP geopolymer pastes are showed in Fig. 4.4. The Fig. 4.4a displays the amorphous textures of the generated aluminosilicophosphate phase, indicating high-connectivity gels. Crystalline morphologies of $AlH_3(PO_4)_2 \cdot 3H_2O$ (identified by XRD patterns in Fig. 4.3) are found in Figs. 4.4 b and c, and enlarged in d. The EDXS analysis of amorphous aluminosilicophosphate and crystalline $AlH_3(PO_4)_2 \cdot 3H_2O$ shown in Fig. 4.5 further confirmed the phase identification results determined by XRD. It can be seen that the molar ratio of Si, Al and P at the point 1 (Fig. 4.4a) is approaching to 1:1:1, while this ratio become around 1:0:2 at the point 2 (Fig. 4.4b). These ratios around accord with the theoretical value of amorphous Si-Al-P gels and crystalline $AlH_3(PO_4)_2 \cdot 3H_2O$. Besides, it should be noted that the observed crystalline shape of $AlH_3(PO_4)_2 \cdot 3H_2O$ is different in Figs. 4.4 b and c. It may be because the habits $AlH_3(PO_4)_2 \cdot 3H_2O$ is associated with the molar ratio of silicon that participated in the formation of amorphous structures in silico-aluminophosphate geopolymer, and with the localized pH environment and raw materials features.

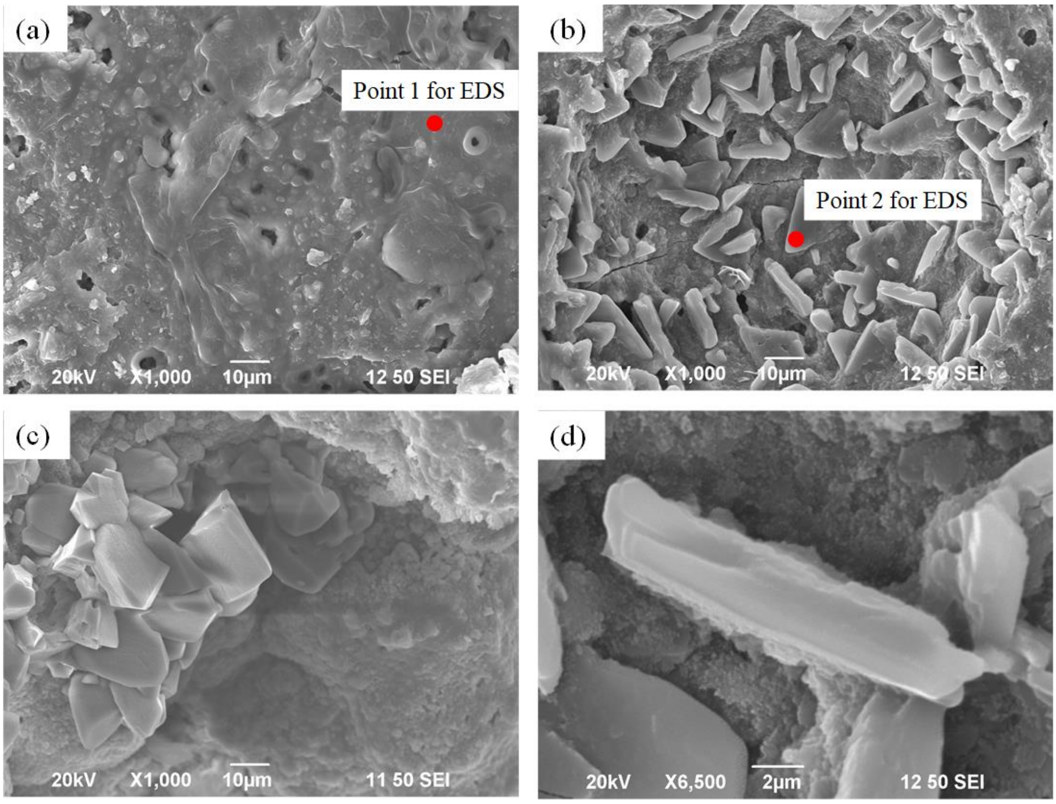

Fig. 4.4 Micro-morphological images for the hardened SAP geopolymer pastes after 28 day chamber curing

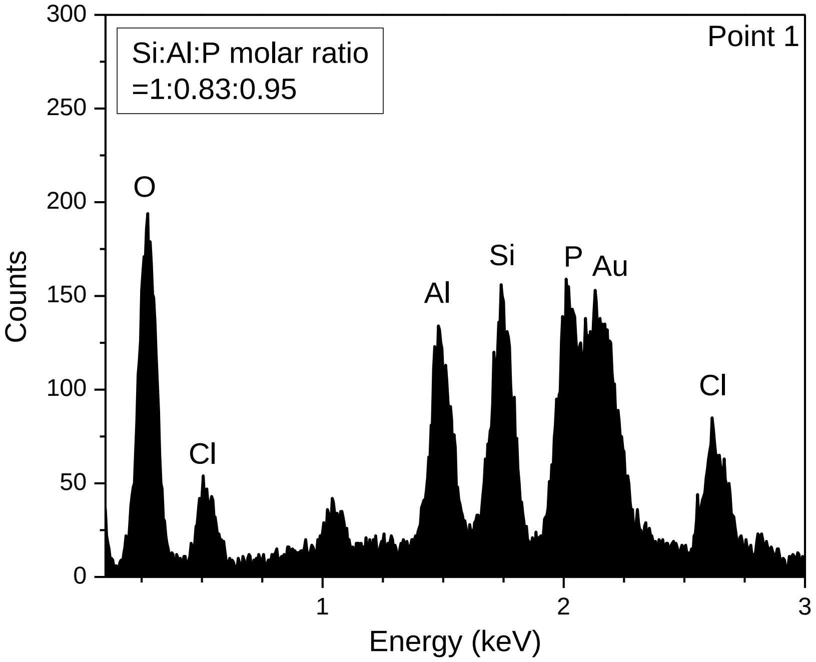

(a)

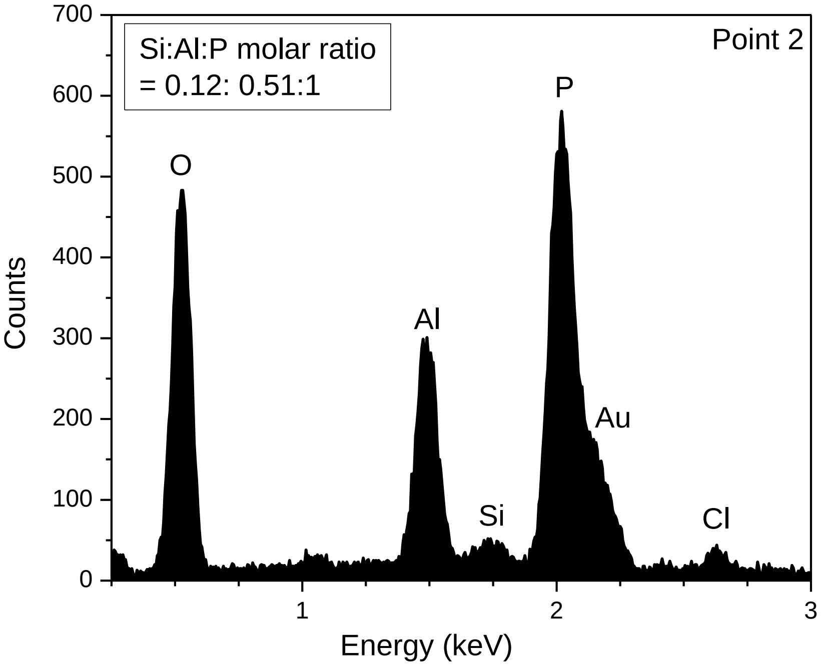

(b)

Fig. 4.5 EDXS analysis for the element compositions of phase in the hardened silico-aluminophosphate geopolymer pastes at 28 day

Similarly, the morphologies of the AP geopolymer are shown Fig. 4.6. However, its structure (Fig. 4.6a) seems to be slightly looser than that of the SAP geopolymer (Fig. 4.4). The numerous lump phases with low connectivity and isolation were observed in Fig. 4.6a, which coincides with their results of compressive strengths at 28 day. Regarding the crystalline phase in Figs. 4.6b and c, the crystalline growth direction presents great differences compared with the SAP geopolymer, although the elementary distribution of crystalline phase was identified as the Si:Al:P molar ratio of 0.09:0.56:1 (Fig. 4.6d), approximating the theoretical Al/P ratio of $AlH_3(PO_4)_2$ $3H_2O$. The silicate contents in silico-aluminophosphate may influence the crystal habits of aluminum phosphate.

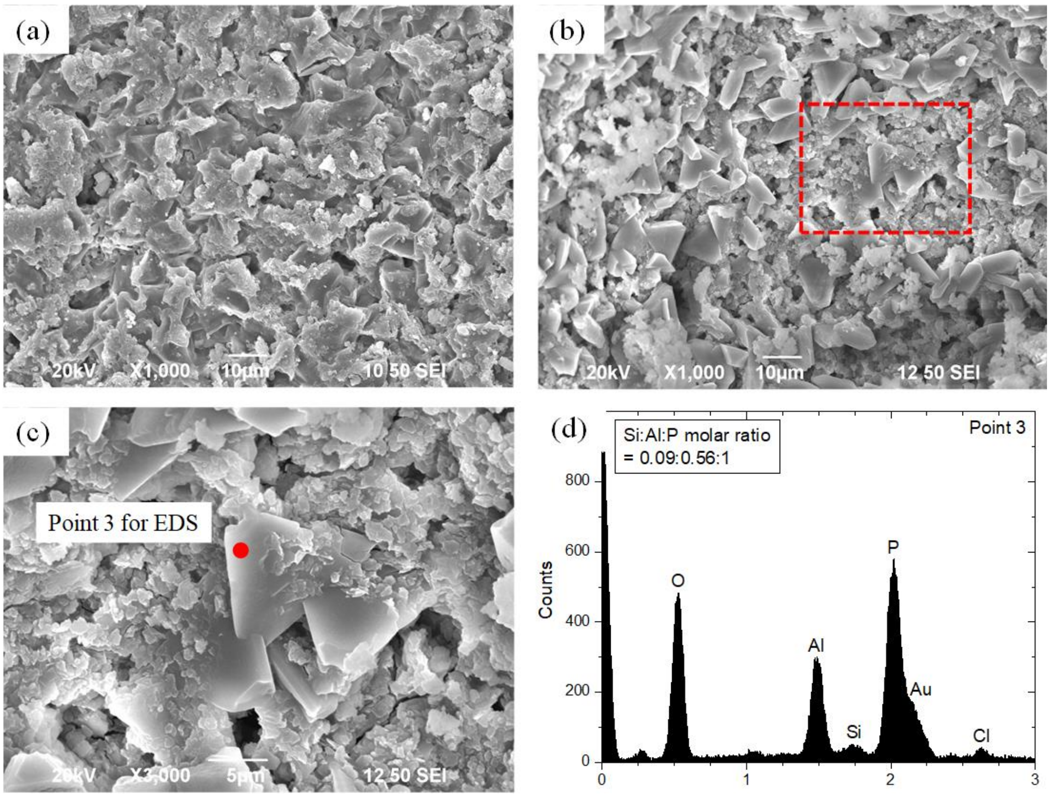

Fig. 4.6 Micro-morphological images for hardened AP geopolymer pastes at 28 day

4.3.3 Thermal properties of silico-aluminophosphate geopolymer

The thermal decomposition and transition of silico-aluminophosphate geopolymer at elevated temperatures (1000 ℃) are examined and the results are shown in Fig. 4.7. For all three series of silico-aluminophosphate geopolymers, a mass loss of approximately 15% occurred with a sharp endothermic peak between 100 and 125 ℃ due to dehydration. Another endothermic peak appeared at about 226 ℃, with a continued mass loss of around 4%, was attributable to the decomposition of $AlH_3(PO_4)_2\cdot 3H_2O$. From 250 to 1000 ℃, the mass almost remained unchanged. About 2.5% mass loss was recorded because of the dehydroxylation of hydroxyl groups.

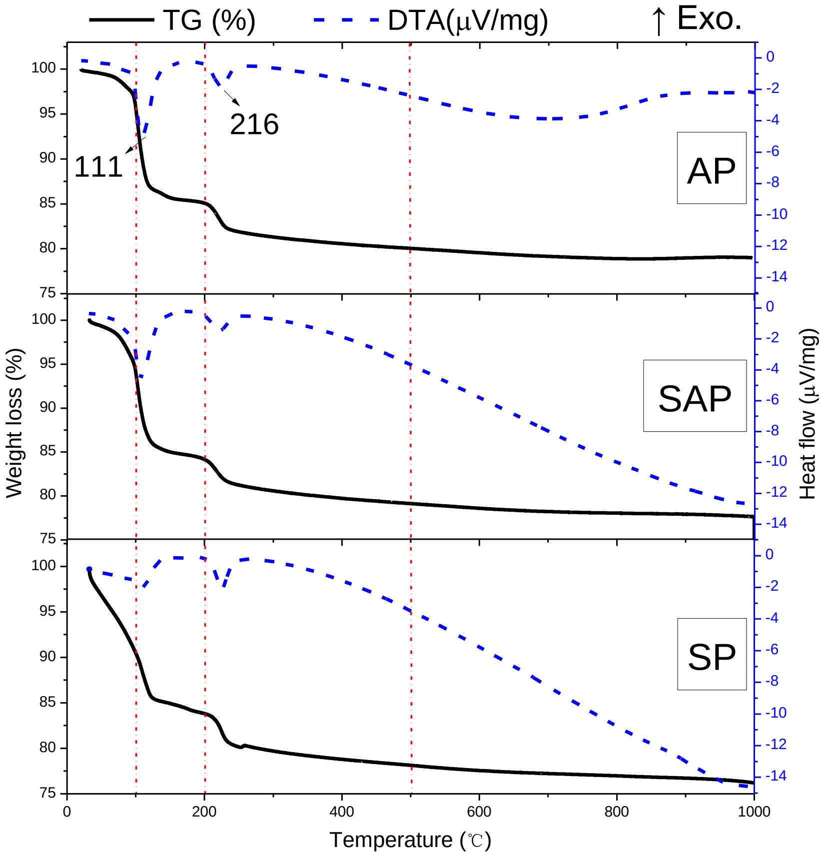

Fig. 4.7 TG-DTA thermograms of silico-aluminophosphate geopolymer subjected to elevated temperatures (from 30 to 1000 ℃)

TG-DTA curves recorded the weight loss of samples along with the temperature change, but barely manifested the phase transition during the process of the elevating temperature. In order to fill this gap, XDR patterns of these geopolymer samples subjected to 1 hour ageing at elevated temperatures (e.g., 200 and 500 ℃) were carried out. The thermal changes can be further confirmed by the X-ray diffractogram at elevated temperatures, as shown in Fig. 4.8. The onset temperature of crystalline phase, $AlH_3(PO_4)_2 \cdot 3H_2O$, was about 200 ℃, which can explain the partial disappearance of intense peaks when heating geopolymer pastes at 200 ℃ for 1 hour. When the temperature was elevated at 500 ℃, the intense peaks for $AlH_3(PO_4)_2 \cdot 3H_2O$ were gone completely, and some peaks assigned to silicon oxide (#01-076-0931) and berlinite (#00-010-0423) were identified (Prado-Herrero et al., 2010).

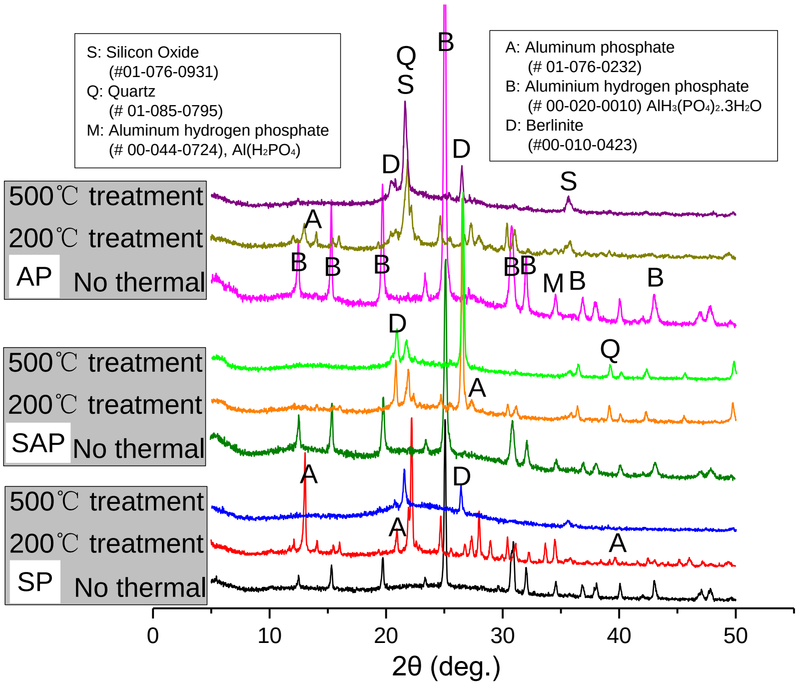

Fig. 4.8 X-ray diffractograms of silico-aluminophosphate geopolymer subjected to elevated temperatures of 200 and 500 ℃

4.3.4 Inference of chemical process

Based on above results and analyses, formation processes of silico-aluminophosphate geopolymer can be derived as follows:

First, the raw materials (e.g., SF, MK, MAP and water) produced a crystalline phase, $AlH_3(PO_4)_2 \cdot 3H_2O$ (detected by the XRD), and an amorphous structure containing Si, Al and P. Also, according to the results of SEM-EDXS (shown in Figs. 4.4-4.6), it was found that the molar ratio of Si, Al and P was identified as about 1:1:1, which further confirmed the amorphous Al-Si-P ternary structure. Similarly, the EDXS-based elementary analysis (i.e., Al/P ratio) supports the existence of $AlH_3(PO_4)_2 \cdot 3H_2O$. Therefore, the first chemical reactions can be derived as Eq. 4.1:

$$\mathrm{SiO_{2(SF)} + Al_2O_3 \cdot 2SiO_{2(MK)} + Al(H_2PO_4)_{3(MAP)} \xrightarrow{geopolymerization} Al_2O_3 \cdot 2SiO_2 \cdot P_2O_5 .\cdot nH_2O + AlH_3(PO_4)_2 \cdot 3H_2O} \quad (4.1)$$

When the temperature was elevated to 200 ℃ for 1 hour, most of the peaks assigned to $AlH_3(PO_4)_2 \cdot 3H_2O$ disappeared (Fig. 4.8), and aluminum phosphate marginally appeared while quartz peaks became obvious. In addition, a clear endothermic peak was presented at around 200-220 ℃ in TG-DTA curves (Fig. 4.7), which indicates the decomposition of $AlH_3(PO_4)_2 \cdot 3H_2O$. Based on these evidences, the second chemical reactions can be derived as Eq. 4.2:

$$\mathrm{Al_2O_3 \cdot 2SiO_2 \cdot P_2O_5 \cdot\ nH_2O + AlH_3(PO_4)_2 \cdot 3H_2O \xrightarrow{210°C} SiO_{2(quartz)} + AlPO_{4(aluminum\ phosphate)} + mH_2O} \quad (4.2)$$

In case of 500 ℃ for an hour, the peaks for $AlH_3(PO_4)_2 \cdot 3H_2O$ disappeared completely, and the enrichment of peaks for berlinite were highlighted (see Fig. 4.3). Furthermore, in the TG-DTA curves, no mass loss was observed between 500 and 1000 ℃. On the contrary, there was a moderate endothermic peak, especially in the case of SP geopolymer. It may be attributed to the transformation from aluminum phosphate to berlinite (Prado-Herrero, et al., 2010). The third reaction was therefore derived as Eq. 4.3:

$$\mathrm{Al_2O_3 \cdot 2SiO_2 \cdot P_2O_5 .\cdot nH_2O + AlH_3(PO_4)_2 \cdot 3H_2O \xrightarrow{500^\circ C} SiO_{2(quartz)} + AlPO_{4(berlinite)} + mH_2O} \qquad (4.3)$$

Given the molar ratio of Al/P=1, plus a certain molar ratio of Si, the geopolymerization of silico-aluminophosphate geopolymer at room temperature will proceed, producing amorphous structure of aluminosilicophosphate phases and a crystalline form of trihydrate, $AlH_3(PO_4)_2 \cdot 3H_2O$. However, a high temperature over about 210 ℃ decomposes this crystalline phase, and the amorphous organization of aluminosilicophosphate transforms gradually to quartz and polymorphic aluminum phosphate under thermal treatment. Continued heating to higher temperatures, a crystallization of aluminum phosphate, named as berlinite, will be formed and may contribute to high compressive strength at elevated temperatures (Cui et al., 2010).

4.4 Chapter Summary

Silico-aluminophosphate geopolymer was chemically synthetized at room temperature, presenting a moderate compressive strength at 28 day when the Al/P molar ratio was equal to 1. The experimental results showed that the 28-day compressive strength of the hardened geopolymer paste arrived at about 31 MPa at that ratio, which was ensured by the formation of an amorphous structure of $SiO_2 \cdot Al_2O_3 \cdot P_2O_5 \cdot nH_2O$ and a crystalline phase, aluminum hydrogen phosphate ($AlH_3(PO_4)_2 \cdot 3H_2O$). The elevated temperature exposure enabled phase transitions to berlinite ($AlPO_4$) and the rearrangement of silicon-containing phases.

4.5 References

Cui, X. M., Liu, L. P., Zheng, G. J., Wang, R. P., & Lu, J. P. (2010). Characterization of chemosynthetic Al_2O_3-$2SiO_2$ geopolymers. *Journal of Non-Crystalline Solids, 356*(2), 72-76.

Cui, X. M., Liu, L. P., He, Y., Chen, J. Y., & Zhou, J. (2011). A novel aluminosilicate geopolymer material with low dielectric loss. *Materials Chemistry and Physics*, 130(1-2), 1-4.

Finch, T., & Sharp, J. H. (1989). Chemical reactions between magnesia and aluminium orthophosphate to form magnesia-phosphate cements. *Journal of Materials Science*, 24(12), 4379-4386.

Ilić, B. R., Mitrović, A. A., & Miličić, L. R. (2010). Thermal treatment of kaolin clay to obtain metakaolin. *Hemijska Industrija*, 64(4), 351-356.

Komnitsas, K. A. (2011). Potential of geopolymer technology towards green buildings and sustainable cities. *Procedia Engineering*, 21, 1023-1032.

Lemougna, P. N., Wang, K. T., Tang, Q., Melo, U. C., & Cui, X. M. (2016). Recent developments on inorganic polymers synthesis and applications. *Ceramics International*, 42(14), 15142-15159.

Louati, S., Hajjaji, W., Baklouti, S., & Samet, B. (2014). Structure and properties of new eco-material obtained by phosphoric acid attack of natural Tunisian clay. *Applied Clay Science*, 101, 60-67.

Petzet, S., Peplinski, B., Bodkhe, S. Y., & Cornel, P. (2011). Recovery of phosphorus and aluminium from sewage sludge ash by a new wet chemical elution process (SESAL-Phos-recovery process). *Water Science and Technology*, 64(3), 693-699.

Prado-Herrero, P., Garcia-Guinea, J., Crespo-Feo, E., & Correcher, V. (2010). Temperature-induced transformation of metavariscite to berlinite. *Phase Transitions*, 83(6), 440-449.

CHAPTER 5 ALUMINUM-INCORPORATED PHOSPHATE ACTIVATOR FOR SYNTHESIS OF SILICO-ALUMINOPHOSPHATE GEOPOLYMER

The previous chapter has proved that an aluminosilicate precursor can be transformed into a cement-like geopolymer binder via a phosphate activation approach, although the early performance of the formed silico-aluminophosphate geopolymer is unsatisfactory. This chapter identifies the effect of the addition of aluminum species into the phosphate activating solution on the formation of such geopolymers, from the fresh to the hardened state. Activating solutions with Al/P molar ratios of 0, 0.1, and 0.3 were prepared by blending monoaluminum phosphate and orthophosphoric acid. The rheological properties, fluidity, and setting times of the fresh geopolymer pastes and the compressive strength of the hardened geopolymer matrices were studied. Liquid-state ^{27}Al and ^{31}P nuclear magnetic resonance measurements for the chemical environments of Al and P, and spectroscopic, thermal, and microscopic analyses revealed that the soluble aluminum in the phosphate activating solution played an important role during the geopolymerization process.

5.1 Introduction

Previous investigations on silico-aluminophosphate geopolymers (Gualtieri et al., 2015; Douiri et al., 2016; He et al., 2016) indicated that thermal curing (e.g., under sealed conditions at 60 ℃ or 80 ℃) was usually needed to achieve fast setting and high early strength. This curing method can be accepted for precast geopolymer products but may impose difficulty in on-site operations, especially for larger-scale engineering applications (Liu et al., 2018). Thermal curing also consumes a significant amount of energy. To obtain an ambient-temperature hardening mechanism in alkali-activated geopolymers, soluble silicate is generally introduced in the alkaline activating solution because a high concentration of dissolved silicate can facilitate a rapid sol/gel transition that leads to the development of a compact matrix with useful early strength (Duxson et al., 2005; Jansson et al., 2015). The addition of a small dose of $NaAlO_2$ into an alkaline activating solution was also reported to improve the workability of the paste and accelerate the growth of the network structure of the formed geopolymer matrix (Benavent et al., 2016).

Following these findings for alkaline systems, this chapter explores the potential to use a corresponding mechanism to improve the early-age characteristics of acidic geopolymers. A second aluminate source, in addition to the aluminosilicate source, is explored in this study as an additive to the phosphate activating solution. It is expected that the aluminum phosphate oligomers which form in a low-pH environment can modify the properties of fresh silico-aluminophosphate geopolymer paste and its hardened matrix. Aluminum and phosphorus generally exist in the free state at a pH of less than 3, and form aluminophosphate phases when the pH is increased (Petzet et al., 2011). Therefore, the addition of soluble aluminum may accelerate geopolymerization in the early stage of reaction to achieve an applicable setting time and early strength. A conceptual scheme for the reaction of an aluminosilicate source activated by alkali and phosphate to synthesize alkali-aluminosilicate and silico-aluminophosphate geopolymers, respectively, is displayed in Fig. 5.1, which illustrates the activating solution-accelerated formation processes from an aluminosilicate source to a geopolymer.

To assess the effectiveness of the addition of soluble aluminum species into a phosphate activating solution for synthesizing geopolymers, various contents of soluble aluminum source were introduced, with the aim of modifying the rheological properties, macroscopic fluidity and setting time of the fresh geopolymer pastes at room temperature. The effects of the soluble aluminum species on the molecular structure of the resulting fresh and hardened geopolymer pastes were elaborated by liquid-state nuclear magnetic resonance spectroscopy, other spectroscopic and thermal analyses. Microstructural features of the hardened geopolymer pastes as a function of aluminum addition were also explored by scanning electron microscopy and mercury intrusion porosimetry .

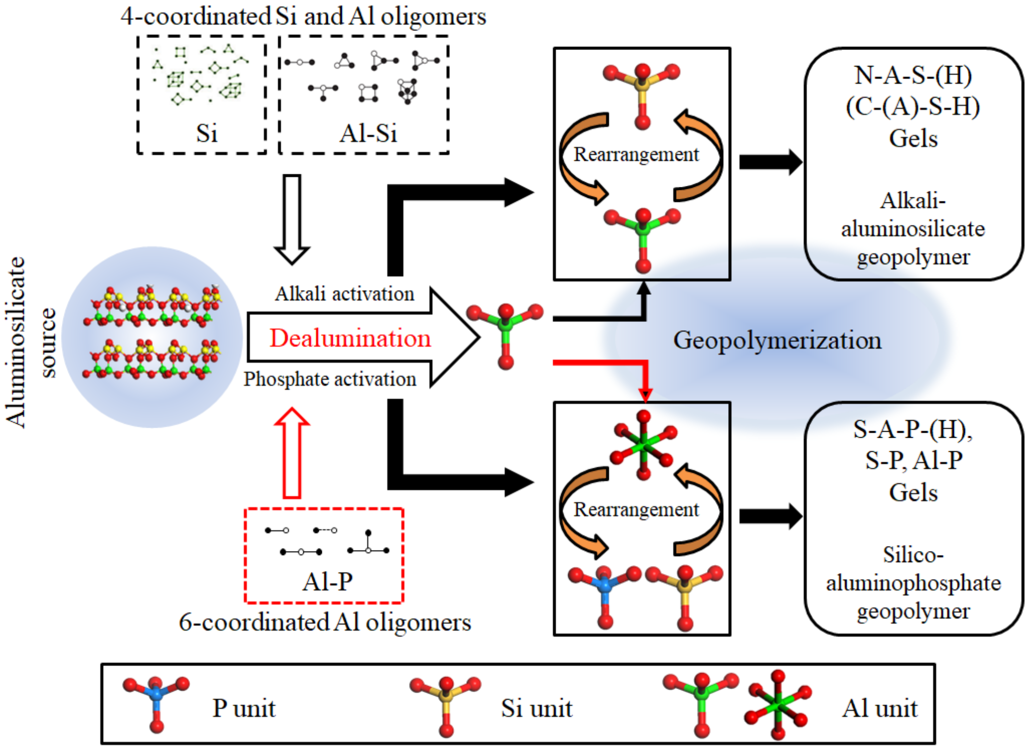

Fig. 5.1 Conceptual scheme for an activating solution-accelerated formation process from an aluminosilicate source to a geopolymer. The aluminosilicate source activated by alkali and phosphate synthesizes the respective alkali-aluminosilicate and silico-aluminophosphate geopolymers.

5.2 Experimental Program

5.2.1 Materials, mix proportions and sample preparation

The silico-aluminophosphate geopolymer pastes were formulated to achieve designed molar ratios of silicon, aluminum and phosphorus. Metakaolin was used as the aluminosilicate source. The phosphate activating solution was prepared using commercial orthophosphoric acid H_3PO_4 (OPA, 85 wt.% in H_2O), liquid monoaluminum phosphate (MAP, $Al(H_2PO_4)_3$, 61.3 wt.% in H_2O) and deionized water. Three soluble aluminum contents (i.e., Al/P molar ratios of 0, 0.1, and 0.3) in the activating solutions were designed to represent control, low-content aluminum and high-content aluminum groups. The MAP supplied the soluble aluminum species in the activating solution, and had little influence on the initial pH value (as shown in Table 1). Silico-aluminophosphate geopolymers with a constant H_2O/MK mass ratio of 0.40 and a fixed Si/P molar ratio of 2.75 were produced by mixing the activating solution with the MK particles. As listed in Table 5.1, six different mix proportions were used, although the mixes C-0.5, GA1-0.5, and GA3-0.5 were used only for tests of rheological properties.

Table 5.1 Mix proportions of phosphate activating solution and silico-aluminophosphate geopolymer

No.	Raw materials by weight ratio					Geopolymer paste	
	Aluminosilicate source	Activating solution					
	MK	OPA	MAP	Water	Initial pH	Soluble Al species (Al/P)	Si/P molar ratio
GA0	10	3.60	0	3.46	1.62	0	2.75
GA1	10	2.51	1.98	2.86	1.64	0.1	2.75
GA3	10	0.36	5.94	1.65	1.69	0.3	2.75
GA0-0.5[a]	10	3.60	0	4.46	1.63	0	2.75
GA1-0.5[a]	10	2.51	1.98	3.86	1.66	0.1	2.75
GA3-0.5[a]	10	0.36	5.94	2.65	1.69	0.3	2.75

a. These mixing proportions were provided only for tests of rheological properties. GA0-0.5 means the geopolymer A0 is prepared with a H_2O/MK mass ratio of 0.5. GA1-0.5 and GA3-0.5 are similarly defined.

The OPA, MAP, and deionized water were fully blended in the specified proportions and cooled down to room temperature for use as the activating solutions, which were then mechanically homogenized with the MK particles for

5 min to form fresh geopolymer pastes. Before casting into 40 × 40 × 40 mm plastic molds, the respective rheological and flow properties of the fresh geopolymer pastes and their initial and final setting times were measured. The hardened geopolymer pastes were demolded 48 hour after casting, and cured in moist conditions (95% to 100% relative humidity) at room temperature for specified periods.

5.2.2 Test methods

The characterization of the fresh geopolymer pastes was performed as follows:

1) A rotational and oscillatory rheometer (Anton Paar MC302) equipped with a parallel-plate measuring system (maximum torque, 200 mN m) was applied to measure the rheological properties of the fresh geopolymer pastes at a temperature of 25 °C by monitoring the evolution of shear stress (Pa) and viscosity (Pa s) under shear rates ranging from 0.01 to 100 s^{-1}. The solid volume fractions of the geopolymer pastes with the two H_2O/MK ratios (0.4 and 0.5) were about 0.78 and 0.70, respectively, to ensure that the paste displayed a yield stress (Roussel et al., 2010).
2) The macroscopic fluidity of the fresh geopolymer pastes was determined by a mini-cone slump flow test setup (Dai et al., 2013) with an upper diameter of 36 mm, lower diameter of 60 mm, and height of 60 mm.
3) The initial and final setting times of the geopolymers were determined using a Vicat apparatus according to BS EN 196-3: 2005.
4) The liquid-state ^{31}P and ^{27}Al NMR spectra for the MAP and activating solutions were obtained using a Bruker 400 spectrometer at ambient temperature. The spectrometer frequencies for ^{31}P and ^{27}Al nuclei were 202.47 and 130.33 MHz, respectively. The corresponding recycle delays applied were 6 and 5 s, with 90º pulse durations of 8 and 2 μs, respectively. The chemical shifts of ^{31}P were expressed in ppm relative to the OPA, and the ^{27}Al resonances were referenced to a 1.0 mol/L $AlCl_3$ solution.

The compressive strength of the hardened geopolymer pastes was assessed before the spectroscopic, thermal, and microstructural analyses:

1) The compressive strength of the 40-mm geopolymer paste cubes was measured after 3, 7, 14, and 28 day of curing by a mechanical testing instrument (Testometric CXM 500-50 kN) with a loading rate of 0.8 kN/s (about 0.5 MPa/s) following the guidance of ASTM C109/C109M-16a for load application.
2) The crushed samples were then manually ground for crystalline phase analysis by X-ray diffractometry with a 9 kW Cu-Kα radiation source (λ=1.5406 Å) and a scanning step of 0.02° (2θ).
3) Simultaneous thermal analysis under an argon atmosphere was performed to analyze the thermal decomposition and phase transition behaviors of the hardened pastes, at a heating rate of 10 ℃ min^{-1}.
4) The microstructural features were characterized by scanning electron microscopy with energy-dispersive X-ray spectroscopy detector. An acceleration voltage of 20 kV was applied. Before the microscopic measurement, the samples were desiccated (60 °C for 24 h) and surface was coated with gold sputter.
5) The pore size distribution of the samples was assessed by mercury intrusion porosimetry.

5.3 Results and Discussion

5.3.1 Rheological properties of fresh silico-aluminophosphate geopolymer

The Bingham model (Eq. 5.1) is often used to approximate the rheological behavior of a hydraulic or geopolymer cement paste in terms of the shear stress-shear rate relationship over a specific range (Favier et al., 2013; Favier et al., 2014):

$$\tau = \tau_0 + \eta_0\gamma \tag{5.1}$$

where τ (Pa) is the shear stress, γ (s^{-1}) is the shear rate, and τ_0 (Pa) and η_0 (Pa s) are the yield stress and plastic viscosity, respectively.

In particulate pastes, the viscosity and yield stress are controlled by colloidal interactions due to electrostatic and van der Waals forces between particles (the MK particles in this case), viscous forces in the interstitial liquid between particles (the activating solution in this case), and direct contact forces (Roussel et al., 2010).

Figure 5.2 plots the evolution of the rheological characteristics of the fresh geopolymer pastes, measured as a function of shear rate from 0.01 to 100 s^{-1}. The data shows that the Bingham model provides a reasonable – although not perfect – description of the rheological characteristics of these pastes. There is some deviation from Bingham behavior at the very beginning of the test, which may be related to thixotropic behavior as the MK particles are far from spherical and can thus cause complexities in time-dependent as well as shear-dependent rheology. Comparing between the various samples, it is seen that the presence of more Al species can promote a lower yield stress in the fresh silico-aluminophosphate geopolymer paste with a H_2O/MK ratio of 0.4 (i.e., GA1-0.4 and GA3-0.4). The geopolymer paste prepared using the Al-free activating solution at low water content (i.e., GA0-0.4) was beyond the measurement range of the rheometer because of its high stickiness. The yield stress of the GA1-0.4 and GA3-0.4 pastes as estimated using the Bingham model reached 500 (±150) and 800 (±200) Pa, respectively, where the quoted error bounds on the yield stress values reflect the uncertainty introduced by the use of different sections of the flow curves to determine the yield stress via Eq. 5.1. The addition of a higher dose of aluminum species to the activating solution (GA3-0.4) gave a lower yield stress, and according to the Bingham model fitting results (i.e., the slope of fitting curves), the geopolymer paste with an Al/P molar ratio of 0.3 has a lower viscosity compared to GA1-0.4 geopolymer paste. The aluminum species in the activating solution acted to some extent as a ‘plasticizer’, enabling the geopolymer paste to obtain improved workability, which was favorable for producing a compact and dense matrix with high early strength.

When the H_2O/MK ratio was increased to 0.5, the three geopolymer pastes all displayed improved workability, with yield stress values of 100 to 200 Pa for all pastes at this water content. Similarly to the H_2O/MK=0.4 series, the geopolymer paste with the most Al species in its activating solution (GA3-0.5) had the lowest yield stress. However, for this set of samples at high water content, the addition of Al to the activator can evidently lower the yield stress of the fresh geopolymer paste while maintaining the viscosity, as seen by the fact that the flow curves for all three -0.5 series samples in Figure 5.2 are parallel at moderate to high shear rate.

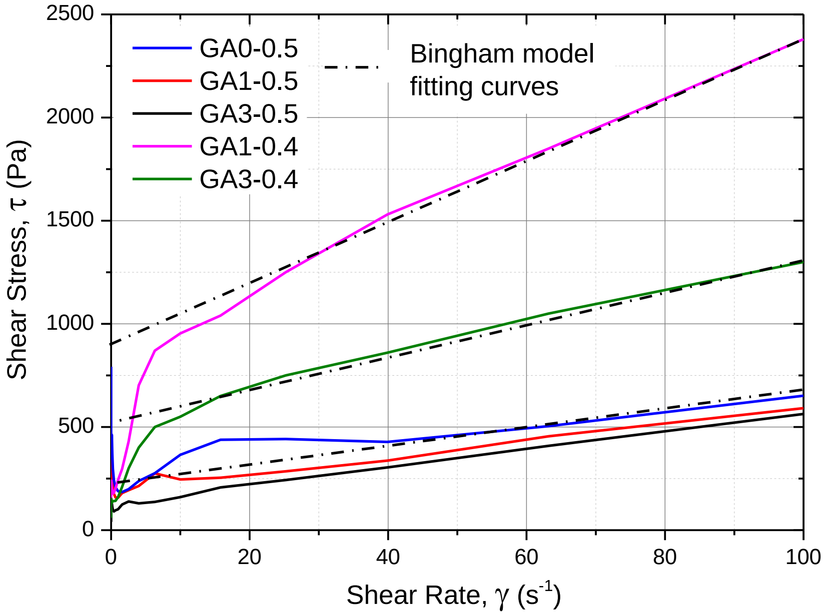

Fig. 5.2 Rheological flow curves of the fresh geopolymer pastes with different contents of soluble aluminum species in their respective activators. The suffix -0.4 or -0.5 in the sample ID indicates the H_2O/MK ratio (0.4 or 0.5). The geopolymer paste prepared using the Al-free activating solution at low water content (i.e., GA0-0.4) was outside the measurement range of the rheometer.

5.3.2 Macroscopic fluidity and setting time of fresh silico-aluminophosphate geopolymer

It is well known that the fluidity of cement paste is mainly influenced by water usage (i.e., the water-to-cement ratio in conventional cements). Figure 5.3a compares the flows (in terms of the diameter spread on a glass plate in a mini slump test) of the geopolymer pastes with varying aluminum contents, at a fixed H_2O/MK ratio of 0.4. The flow increased significantly with the Al/P ratio in the activating solutions. An Al/P ratio of 0.3 led to an increase of the flow diameter by 50% (106 mm) as compared to the reference case of Al/P=0, whose flow diameter was just 78 mm in 60 s. Dividing the flow more specifically into faster and slower processes (i.e., distinguishing yield stress control from viscosity control), the fluidity in the first period between 0 and 30 s dominated in the flow test, consistent with the moderate yield stress but relatively low plastic viscosity observed in Figure 5.2 for each of these pastes. The flow diameter of paste GA3 reached about 92 mm, whereas that reached by paste GA0 during this period was only 58 mm. However, an opposite trend was observed from 30 to 60 s, whereby the flow diameter for GA0 further increased by 19 mm and that for GA3 increased by 14 mm. These results indicate that the involvement of aluminum species greatly improved the macroscopic fluidity of the fresh silico-aluminophosphate geopolymer pastes.

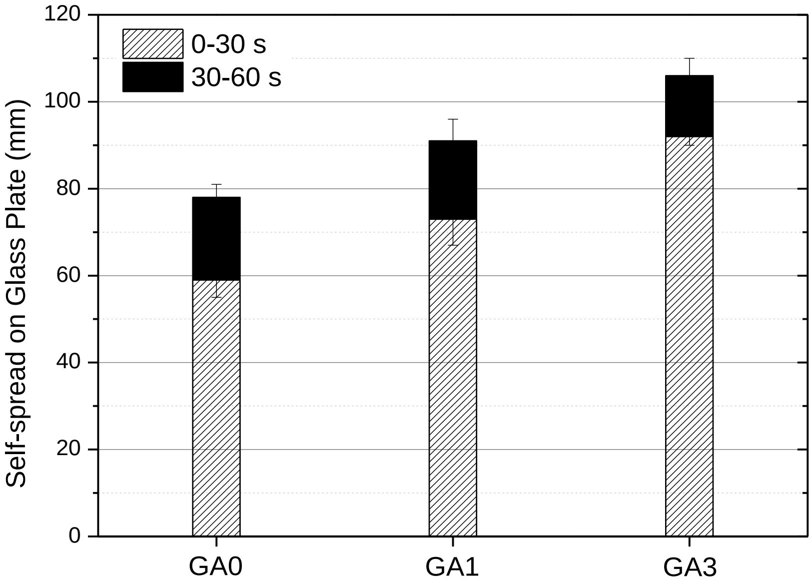

(a) Macroscopic fluidity

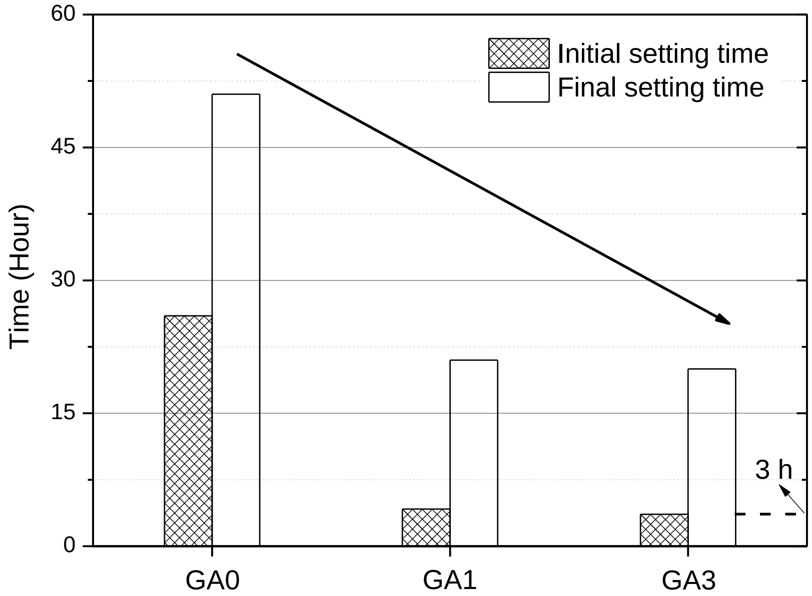

(b) Initial and final setting times

Fig. 5.3 Macroscopic fluidity and setting times of the silico-aluminophosphate geopolymer pastes with different contents of soluble Al species

Achieving a reasonable setting time is critical to engineering applications of any cement to be used at ambient temperature. The setting results shown in Fig. 5.3b demonstrate the difference between the geopolymers with and without the added aluminum species. In the early period, slow dealumination from the MK particles occurred when encountering the activating solution to form an inter-grain gel

(Favier et al., 2013). The initial setting of the geopolymer pastes stemmed from the free aluminum species combining with phosphate to form an aluminophosphate gel (Benavent et al., 2016). Therefore, the long initial setting time in geopolymer GA0 might be a result of the release of aluminum into solution from the solid aluminosilicate source (i.e., the dealumination reaction) delaying its hardening, whereas feeding aluminum directly in the activating solution could provide the necessary aluminum in the early stages of reaction without the need to wait for the solid precursor to dissolve to such an extent. Thus, as shown in the results for mixes GA1 and GA3 (Fig. 5.3b), the free aluminum species in the activating solution could drive a rapid sol/gel transition due to the supplementation of the free Al in the aqueous phase providing the opportunity for near-immediate gel formation. The initial setting times reached a range suitable for engineering applications, although the initial setting time was still rather long (about 3 h). Nevertheless, the free aluminum species, whether supplied from either the activating solution or the solid aluminosilicate source, controlled the reaction rate and affected the setting time of the geopolymer pastes.

5.3.3 Liquid-state ^{31}P and ^{27}Al NMR analysis for phosphate activating solutions

Figures 5.4a and b show the liquid-state ^{31}P and ^{27}Al NMR spectra, respectively, of the MAP solution and the two activating solutions mixed with different Al contents, to further explain the experimental results for the fresh geopolymer pastes. From the ^{31}P spectra for all three solutions (Fig. 5.4a), three distinct bands at 0 to -1.5 ppm, -8 to -9 ppm, and -12 to -14 ppm were detected, and attributed to Q^0, Q^1 and Q^2 phosphate structural units, respectively (Chavda et al., 2015). The orthophosphate group (i.e., phosphoric acid molecules and ions) (Samadi-Maybodi et al., 2009) generates the phosphorus environment of Q^0, while the two clear signals resonated between -5 to -24 ppm are due to polyphosphates – either sites with P-O-P linkages (-7~-9 ppm), or Al complexed to phosphate-containing ligands (-12~-14 ppm) (Abdi et al., 2014; Liu et al., 2014; Samadi-Maybodi et al., 2009). The band assigned to P-O-P linkages is caused by the species $[Al(L)]^{m+}$ (where L is H-bonded polymeric OPA, such as $H_6P_2O_8$), while the band centered at a chemical shift of around -13 ppm is associated to the species of $[Al(H_2O)_5(H_2PO_4)]^{2+}$ and trans-$[Al(H_2O)_4(H_2PO_4)_2]^{+}$ as a result of ionic bonding between Al and P (Samadi-Maybodi et al., 1993). Since the GA1 solution was prepared by using small dosage of the MAP solution to dilute the OPA for a resulting Al/P molar ratio of 0.1, the spectrum of the GA1 solution in Fig. 5.4a is embodied by a sharp resonance peak at -0.5 ppm and two small resonances at -8 and -13 ppm. This indicates that the Q^0 phosphate structural unit is dominated in the A1 activating solution with marginal Q^1 and Q^2 phosphate structural units. Similarly, the GA3 activating solution prepared by a higher ratio of MAP/OPA (Al/P molar ratio is 0.3) contains more Q^0 and Q^2 phosphate structural units but little Q^1 phosphate structural unit. However, the addition of Al to adjust the Al/P ratio did not change the chemical environmental of phosphorus when the molar ratio of aluminum to phosphorus was less than 1.0 (Samadi-Maybodi et al., 2009). However, an increase in the intensity of the band at -8 ppm with decreasing Al content is observed. The resonances assigned to aluminophosphate oligomers (i.e., -12 ~-14 ppm) are intensified (enriched and broadened) with increasing Al content in phosphate activators, which is the result of chemical exchanges between Al and P. This chemistry can break the long phosphate chains (P-O-P linkages) and decrease the polymerization degree. The oligomers formed as a result of the chain breakage benefit the workability of the geopolymer paste, as measured via yield stress and viscosity (in Fig. 5.2) and fluidity (in Fig. 5.3a).

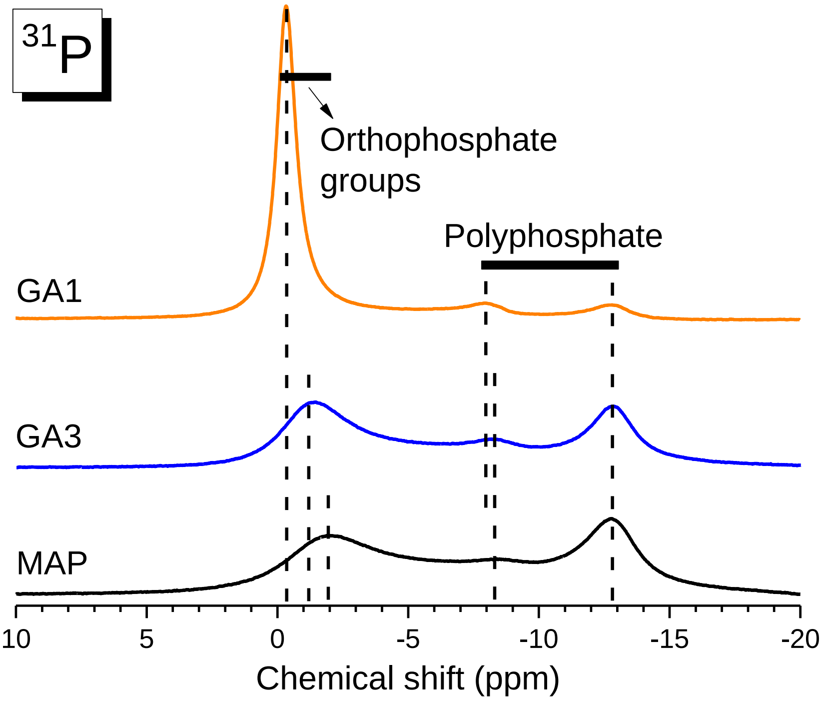

(a) ^{31}P NMR spectrum

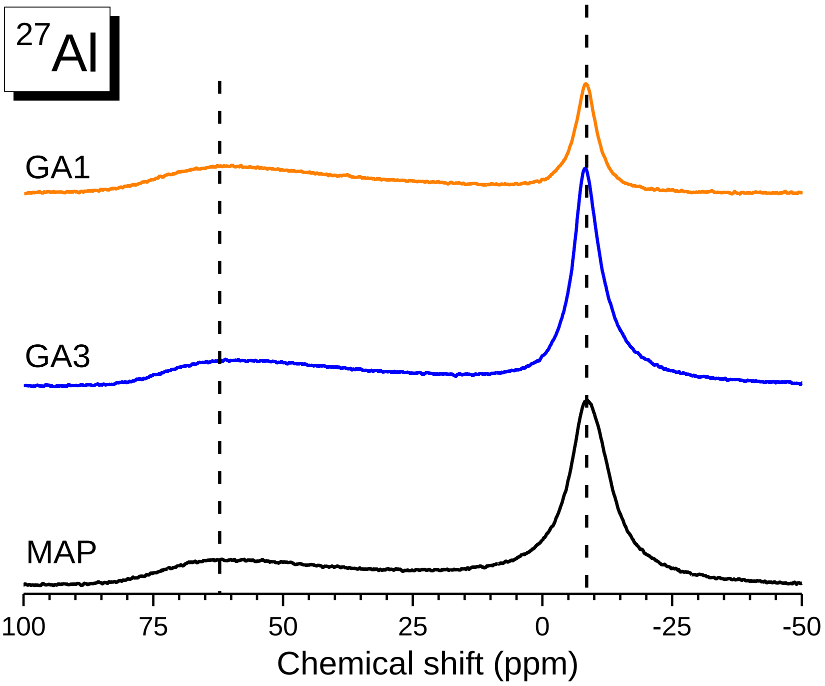

(b) ^{27}Al NMR spectrum

Fig. 5.4 Liquid-state NMR spectra for the GA1 and GA3 activating solutions and the MAP solution

The resonances that are evident in the ^{27}Al spectra at around -8 ppm, and between 80 to 65 ppm, were due to the aluminum species in MAP, in which a clear hexa-coordinated environment of aluminum (i.e., -1 to -9 ppm) was identified (Fig. 5.4b) (Samadi-Maybodi et al., 2009; Haouas et al., 2016). It has previously been reported that the hexa-coordinated aluminum species is the main form of Al in a hardened phosphate-activated geopolymer (Perera et al., 2008). This is consistent with the addition of aluminum to the activating solution accelerating the early stage of the geopolymerization process (formation of aluminate and phosphate oligomers) under an acidic phosphate environment, thus leading to a shortened setting time. A weak and broad resonance at 80 to 65 ppm can be attributed to a small quantity of tetrahedral aluminum present under these conditions (Mueller et al., 1981). These results indicated that in this pH range (i.e., below 2.0, see Table 5.1) the OPA did not change the hexa-coordinated Al environment seeded by the MAP solution. However, as observed in the ^{31}P NMR spectra, the intensity and breadth of the bands resonating at 0 to -20 ppm increase with Al contents in the phosphate activators, which can be attributed to the chemical bonding between Al and P species to form low polymeric units.

5.3.4 Compressive strength of hardened silico-aluminophosphate geopolymer

As displayed in Fig. 5.5, the hardened geopolymer pastes prepared with varying Al/P ratios showed significant differences in strength development from 3 to 28 d. In the early stage at 3 and 7 d, the existence of soluble aluminum species in the activating solution caused significant enhancement of the compressive strength. Compared with mix GA0 (Al/P=0), mix GA2 (Al/P=0.3) showed strengths that were higher by 14.1 MPa and 15.1 MPa at 3 and 7 d, respectively. Geopolymer GA3 remained almost the same strength from 7 d up to 28 d. In comparison, the most significant increase in the compressive strength was achieved in geopolymer GA0 (with no aluminum species in the activating solution), which evolved from 22.1 MPa at 7 d to 51.3 MPa at 28 d. The strength of the geopolymer GA1 (Al/P=0.1) was moderately improved at both 3 and 7 d, but the strength growth thereafter was inferior to that of geopolymer GA0. It seems that the hardening during the early period caused by the addition of free aluminum species in the activating solution can compromise or hinder the ongoing reaction of MK (involving dealumination and delamination to provide nutrients for gel growth) in the latter period. Therefore, a tradeoff was found between the early-state strength and the long-term strength, depending on the aluminum content contained in the activating solution.

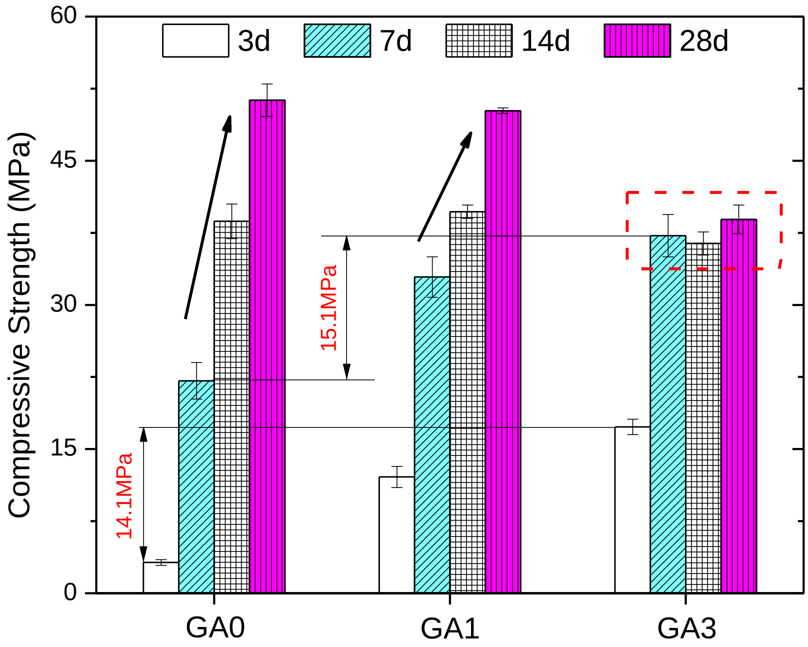

Fig. 5.5 Compressive strength development from 3 to 28 day, of the hardened geopolymer pastes with varying contents of soluble Al species

5.3.5 Crystalline and amorphous phase analysis of hardened silico-aluminophosphate geopolymer

The XRD patterns of the 28 d hardened geopolymers shown in Fig. 5.6 indicate that no new crystalline phase was generated in this reaction process. The only distinct peak in any of the diffractograms is assigned to the quartz that was already present in the unreacted MK particles. The geopolymerization of aluminosilicates, regardless of the activation approach (either by alkali or phosphate activation), involves the dissolution and reconstruction of aluminates and silicates to form disordered gels (Provis et al., 2005; Douiri et al., 2014). In Fig. 5.6a, a visible difference between the geopolymers and the MK is the change in the broad diffuse peak at 15º to 30º (2θ), whose enlarged view is shown in Fig. 5.6b. It can be seen that the diffuse peak partially disappears and shifts after the reaction, especially for geopolymer GA0. For geopolymers GA1 and GA3, the diffuse peak is weakened and shows much less intensity in the range 22 ° to 26 ° (2θ) compared with that of the MK particles. Similar findings were reported by Cui et al., 2011; Douiri et al., 2014 and Louati et al., 2014, although they all used H_3PO_4 without additional aluminum species to activate the aluminosilicate precursors for synthesis of silico-aluminophosphate geopolymers. These spectral changes can be attributed to the effect of phosphate activation on the MK particles. Considering the XRD pattern of MK as a reference, a larger diffuse peak change (at 18 to 28º, 2θ) in geopolymer GA0 than that in the other geopolymers indicates that the degree of reaction of the MK particles in geopolymer GA0 was higher than that of the others at 28 d, consistent with the compressive strength data and confirming that the addition of free aluminum species into geopolymers GA1 and GA3 may, to some extent, hinder the ongoing reaction of MK in the latter period of curing.

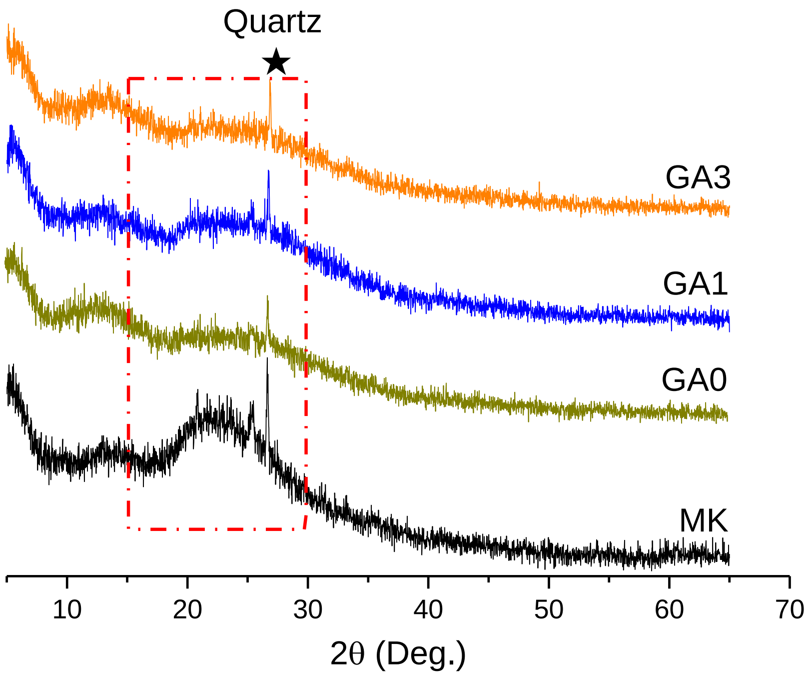

(a) 5 °to 65 °

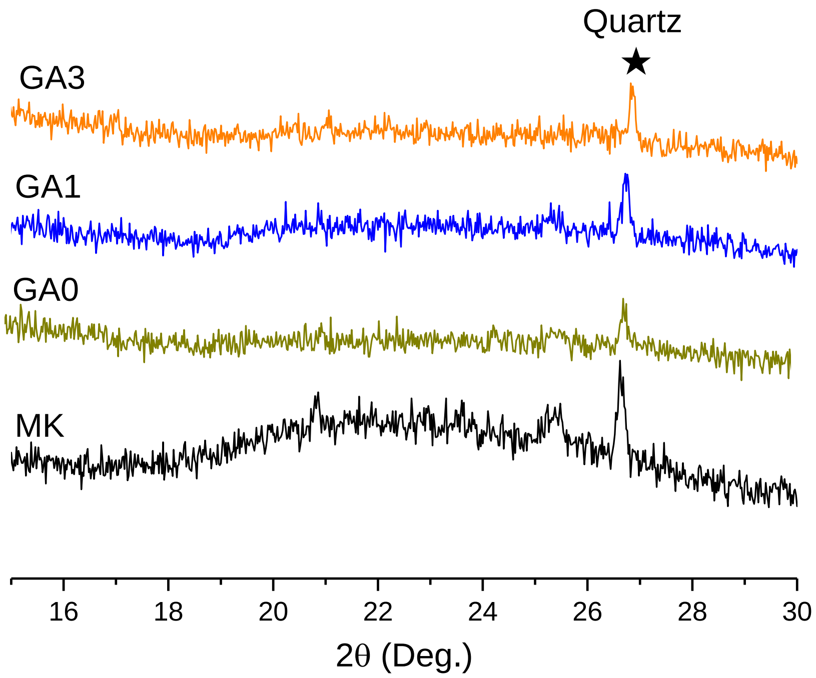

(b) Enlarged from 15 °to 30 °

Fig. 5.6 XRD patterns of the MK precursor and 28 d cured geopolymers prepared with three different Al/P molar ratios in the activating solution

5.3.6 Thermal properties of hardened silico-aluminophosphate geopolymer

The thermogravimetric/differential thermal analysis (TG-DTA) thermograms for the hardened geopolymer pastes, normalized to the basis of constant mass of MK, are shown in Fig. 5.7. For all geopolymers, four distinct groups of decomposition or phase transition peaks are observed in the DTA curve: one is located between 100 and 150 ℃, and the others are located in the ranges of 160 to 230 ℃, 800 to 840 ℃, and 980 to 1010 ℃.

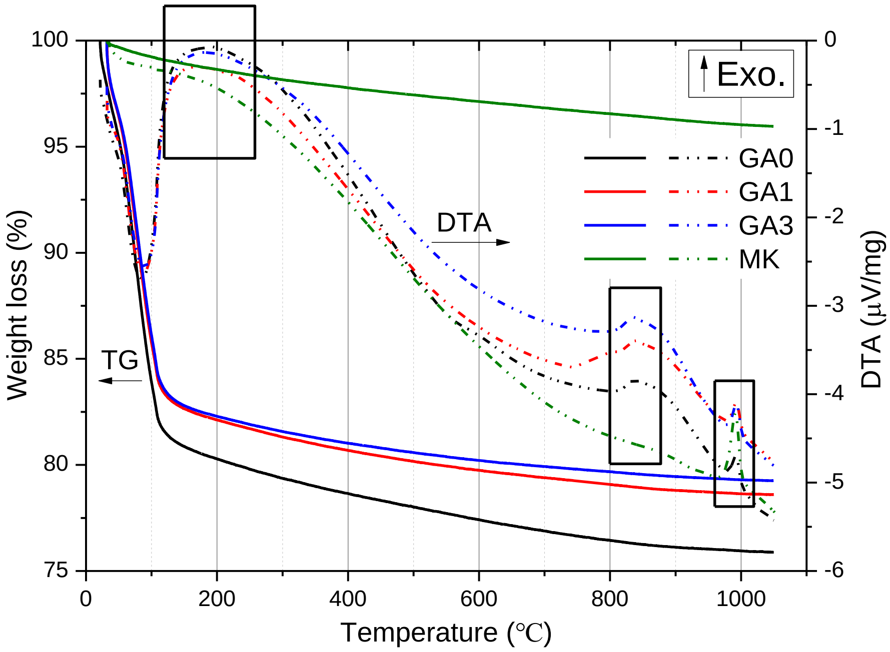

Fig. 5.7 TG-DTA thermograms for the 28 d cured geopolymers with varying Al/P molar ratios. The thermogram of MK is referred.

The weight loss at 100 to 150 ℃, accompanied by a sharp endothermic peak in the DTA curves, is attributed to the removal of physically adsorbed water and the dehydration of some of the water-containing gels (loss of loosely chemically bonded water), which accounted for more than 80% of the total weight loss. The subsequent weight loss from 150 to 1050 ℃ is marginal in each geopolymer, and largely parallels the TGA curve of the MK; this is attributed mainly to dehydration and dehydroxylation of remnant MK particles within the hardened binder, with a potential minor contribution from any remaining chemically bound water in the reaction product gels.

The features at 160 to 230 ℃ and 800 to 870 ℃, respectively, show exotherms in the DTA data but no notable corresponding mass loss, and so are likely to relate to phase transitions in the newly formed binder gel. These may be assigned to the amorphous aluminum phosphate phase transforming into trigonal (α-$AlPO_4$) and tetragonal (β-$AlPO_4$) berlinite at elevated temperature (Prado-Herrero et al., 2010), which is an exothermic process. These two peaks were not detected in the MK particles. The last phase transition was the formation of mullite from residual, fully dehydroxylated MK particles at 980 to 1010 ℃ (White et al., 2010), and is especially prominent in the raw MK particles. For all geopolymer samples, such a peak is less significant, indicating that the raw MK particles had reacted with the phosphate activating solution to synthesize new gels: silicate-aluminate-phosphate gel (Liu et al., 2010) and amorphous or semi-crystalline aluminum phosphate compounds (Cui et al., 2011; Louati et al., 2016). The presence of similar peaks representing thermally induced processes in all of the geopolymers reveals that there were similar reaction products regardless of the Al/P ratio of the activating solutions. In other words, the compositions of the resulting gels were not strongly influenced by changes in the activating solution with different Al/P ratios.

5.3.7 Microstructure analysis: pore structure and morphologies

However, the pore structures of the geopolymer products did exhibit notable differences when the level of soluble aluminum species was varied (Fig. 5.8). The MIP results indicate that the porosity of the geopolymer pastes cured for 28 d increased with the Al/P ratio of the activating solutions used, from 17.1% in geopolymer GA0 to 18.9% in geopolymer GA1 and 21.5% in geopolymer GA3 (Fig. 5.8a). This porosity result is in agreement with the trend in their strength behaviors (i.e., a higher-strength matrix showed lower porosity). The pore diameters accessible to mercury were mainly concentrated between 5 and 1000 nm (Fig. 5.8b), and can be divided into gel pores (less than 10 nm), small capillary pores (10 to 50 nm), medium capillary pores (50 to 100 nm) and large capillary pores (100 to 10 μm) (Ma et al., 2015; Wang and Dai, 2017; Zeng et al., 2012). Fig. 5.8c shows the differential pore diameter distributions and the diameter range between 10 and 1000 nm is enlarged in Fig. 5.8d. It can be seen for all geopolymers that the capillary pores (small, medium, and large) contributed more than 90% of the porosity. However, the incorporation of aluminum species in the activating solution changed the distribution characteristics of the capillary pores. An increase in the aluminum content of the activating solution led to a shift to larger capillary pores. The pore size distribution of the geopolymer with the most soluble aluminum (i.e., GA3 with an Al/P ratio of 0.3) exhibited a sharp maximum at around 90 nm. The other geopolymer samples (GA0 and GA1) showed similar differential porosity distributions to each other, with peak values at 60 nm and 73 nm, respectively. These different distributions of the capillary pores will eventually govern the strength and transport properties of the geopolymer matrix. A delayed or compromised dealumination reaction of the metakaolin particles is more likely to produce discontinuous gels that generate inter-gel spaces which form medium and large capillary pores.

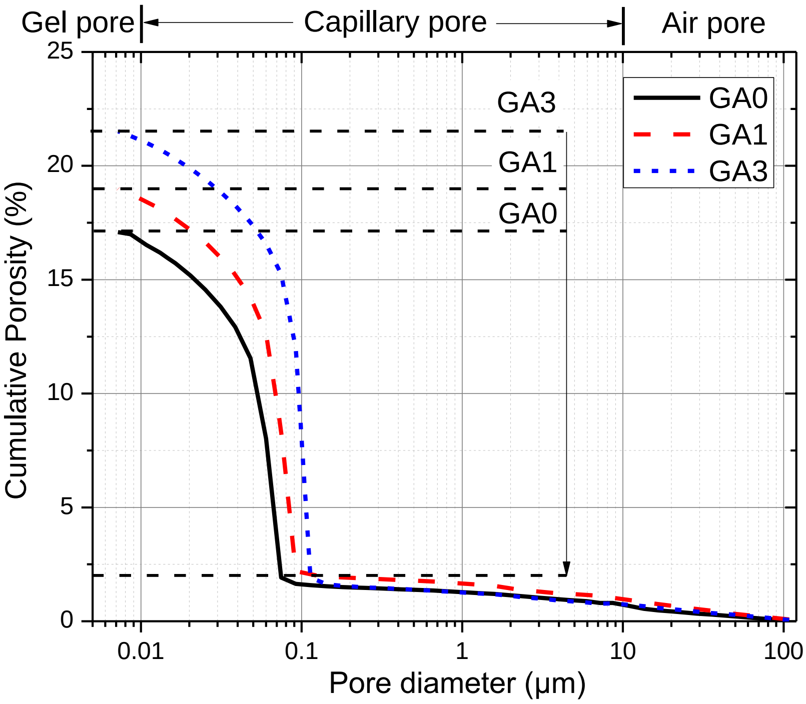

(a)

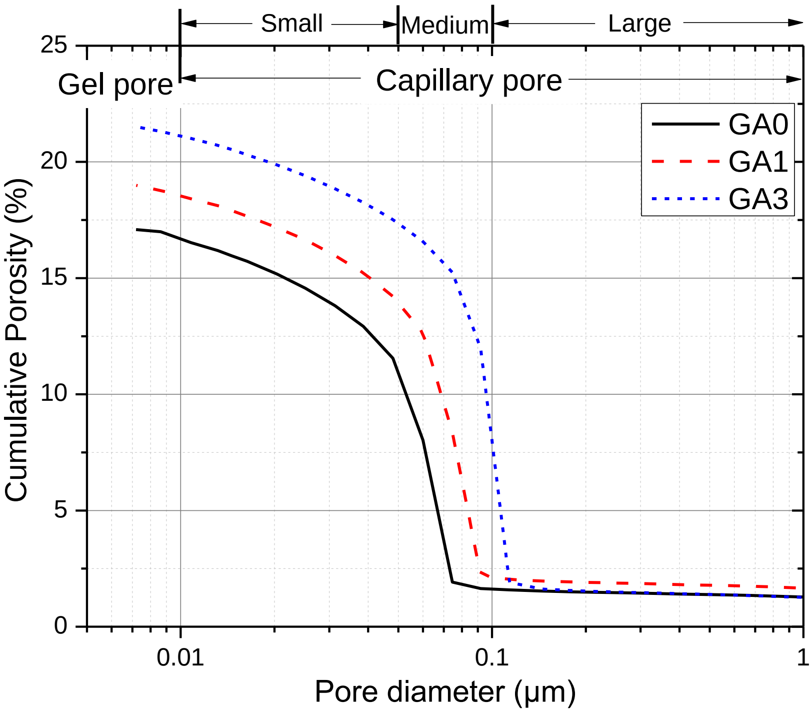
Small
Medium
Large
Gel pore
Capillary pore
GA0
GA1
GA3
Cumulative Porosity (%)
25
20
15
10
5
0
0.01
0.1
1
Pore diameter (μm)

(b)

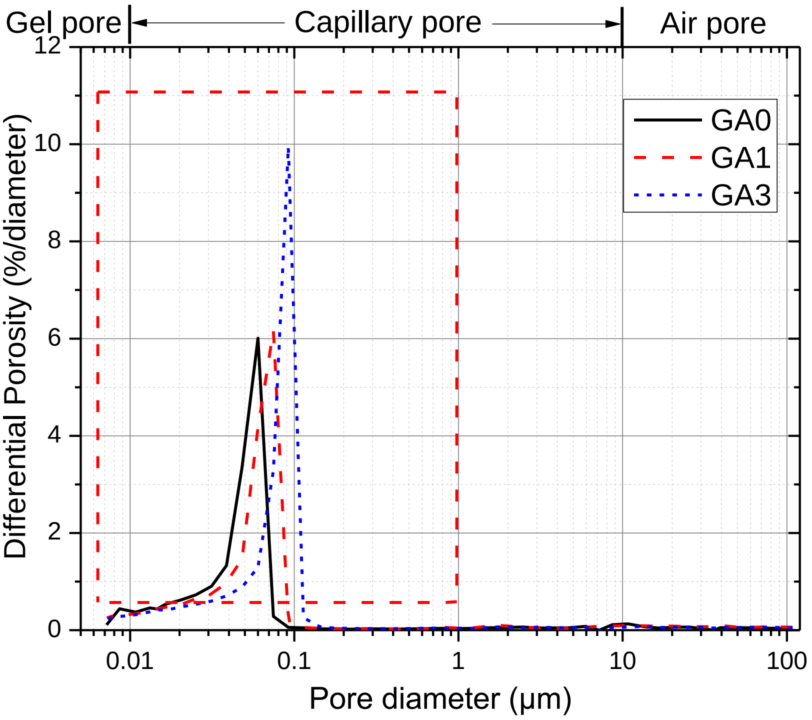
Gel pore
Capillary pore
Air pore
GA0
GA1
GA3
Differential Porosity (%/diameter)
12
10
8
6
4
2
0
0.01
0.1
1
10
100
Pore diameter (μm)

(c)

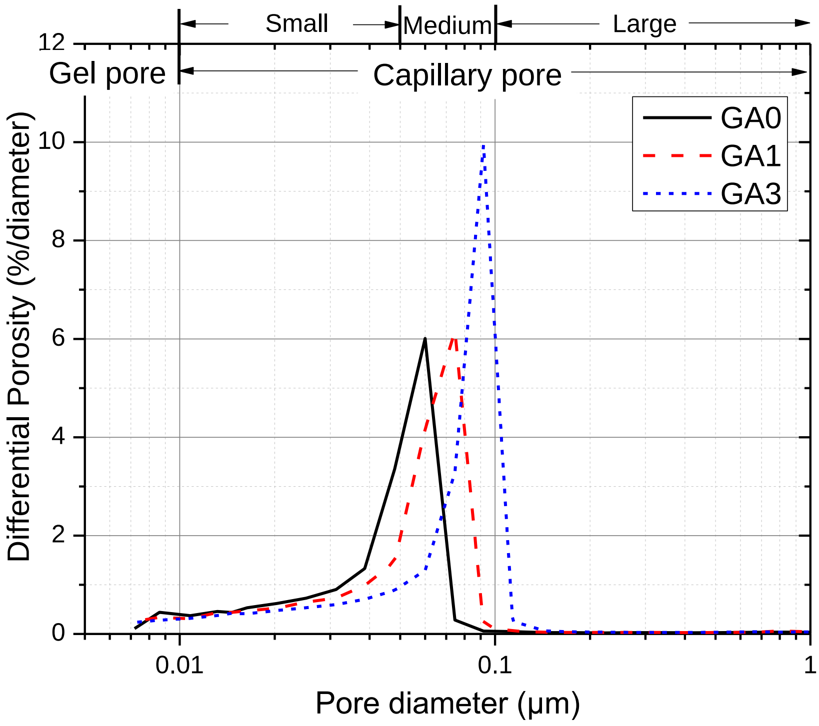

(d)

Fig. 5.8 Pore diameter distributions determined by MIP analysis of the three hardened geopolymer pastes at 28 d. (a) and (b) Cumulative distribution; (c) and (d) Differential distribution.

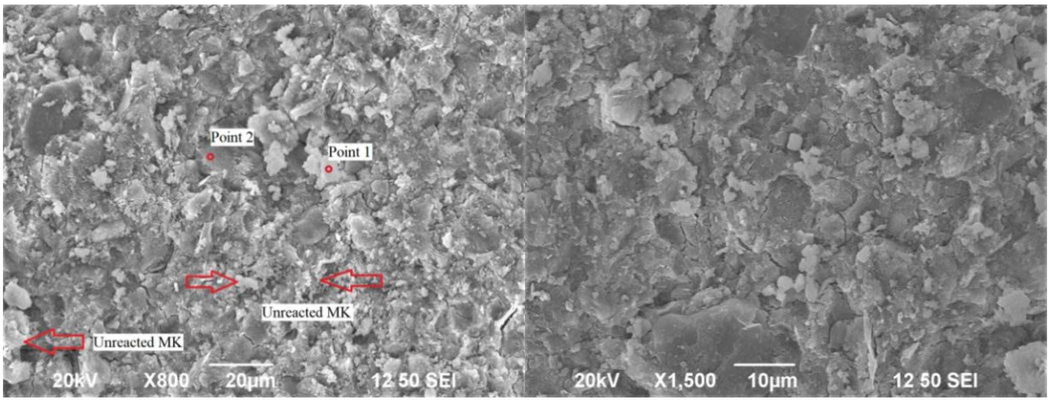

(a) x800

(b) x1500

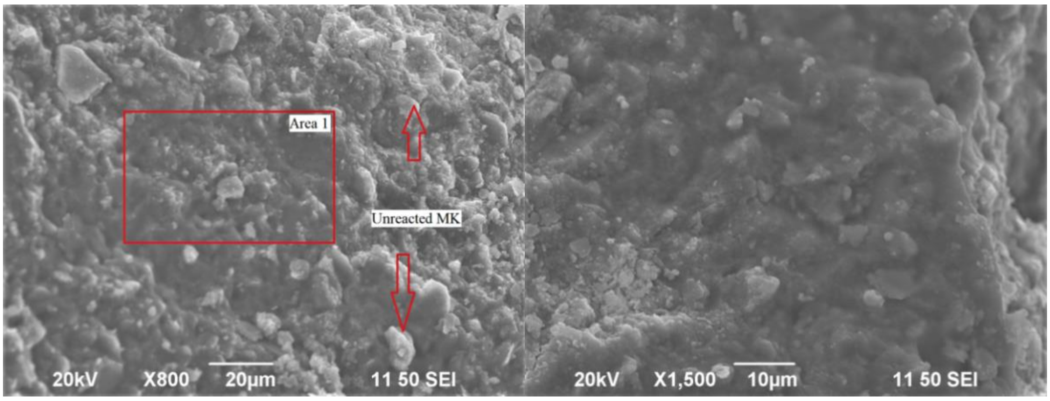

(c) x800 (d) x1500

Fig. 5.9 SEM results of the hardened geopolymer pastes cured at 3 d. (a) and (b) GA0 geopolymer; (c) and (d) GA3 geopolymer.

The features identified through this analysis of pore structure are supported by the morphologies and elemental analysis obtained by SEM and EDS. Fig. 5.9 shows SEM results for the hardened geopolymer pastes cured at 3 d. As shown in Fig. 5.9a, the GA0 matrix consisted of many isolated particles intermixed with gel-like lumps. In the image with higher magnification (Fig. 5.9b), some discontinuous phases and microcracks are found, implying a weak reaction between MK and Al-free activators at the early period. The EDS analysis (Fig. 5.10) indicates the presence of different Al:Si:P ratios at different locations. For instance, points 1 and 2 corresponded to the unreacted MK particles (aluminosilicates without P) and the newly-formed S-A-P gels (reaction products), respectively. As a comparison, the presence of soluble aluminum species in the phosphate activator led to a more compact matrix after the 3 d curing process (in Fig. 5.9c), although such curing was insufficient for geopolymerization between the MK particles and the activating solution. The enlarged image of the GA3 geopolymer cured at 3 d (Fig. 5.9d) shows a high-continuity texture without isolated phases and microcracks. The EDS analysis for the compact area (i.e., area 1 in Fig. 5.9c and Fig. 5.10) reveals the presence of Si, Al and P, which is very likely to be the result of S-A-P gel formation. However, compared to the EDS spectrum of point 2, a lower silicon content in this gel indicates that the presence of soluble Al and P species may form aluminophosphate gels for early strength improvement (Fig. 5.5).

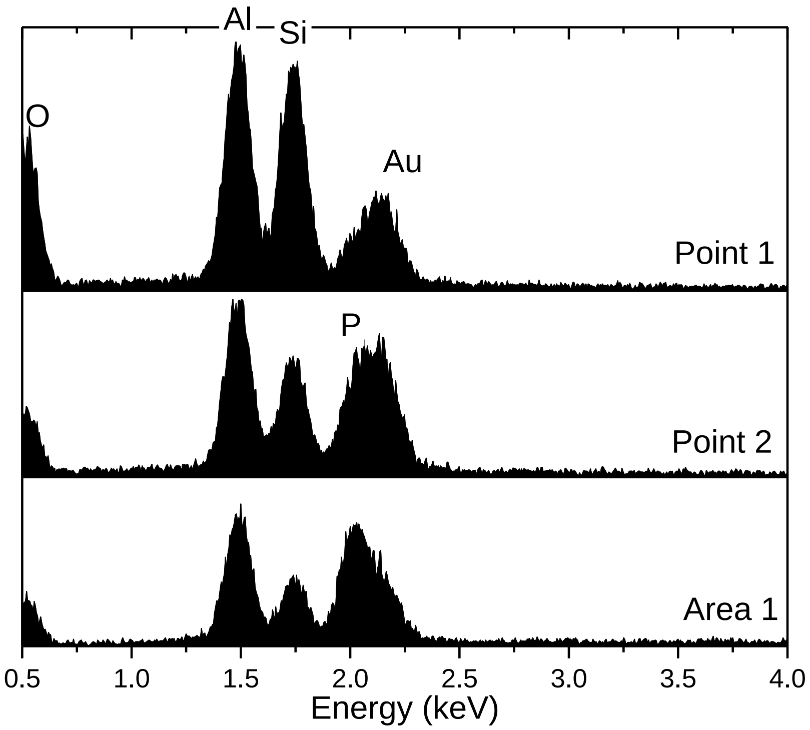

Fig. 5. 10 EDS results of the hardened geopolymer pastes at 3 d. The point 1 point 2 and area 1 can be found in Figs. 5.9a and 5.9b.

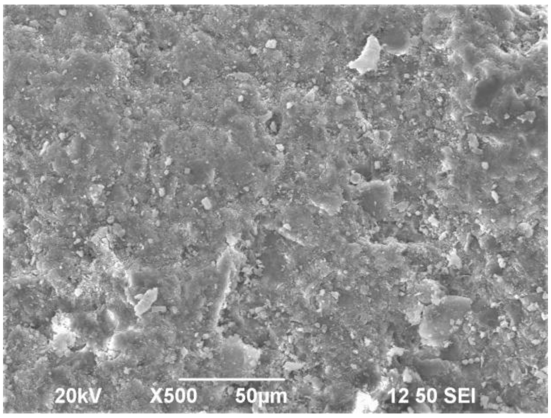

(a)

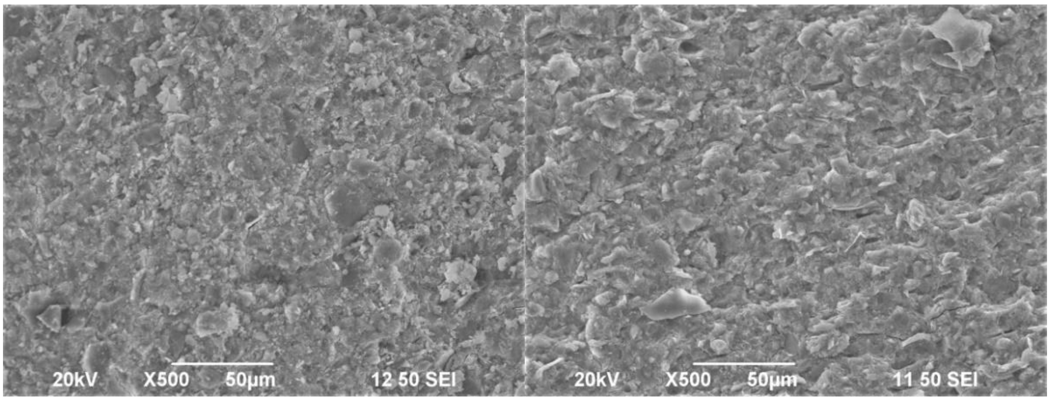

(b) (c)

Fig. 5. 11 SEM results of the hardened geopolymer pastes cured at 28 d. (a) GA0 geopolymer; (b) GA1 geopolymer; and (c) GA3 geopolymer.

The morphologies of the three geopolymer samples imaged at 28 d revealed that the use of excessive aluminum species (GA2, shown in Fig. 5.11c) was unfavorable due to the production of discontinuous gels as compared with GA0 (Fig. 5.11a). Geopolymer GA1, with a moderate content of soluble aluminum species (Fig. 5.11b), seemed to present an intermediate state between GA0 and GA3. These microstructural observations coincided well with the strength variation and development of the three geopolymer matrices as discussed above, where the longer-term strength evolution of GA3 beyond 7 days was negligible while GA0 continued to gain more strength.

5.4 Chapter Summary

The effects of the addition of soluble aluminum species into a phosphate activating solution for geopolymer synthesis on fresh and hardened properties were investigated in terms of workability, compressive strength, and microstructure.

The incorporation of aluminum species into the phosphate activating solution allowed a rapid sol/gel transition in the early state due to the supplementation of the free Al (in six-coordination). As a result, the fresh geopolymer paste achieved good workability. The role of aluminum species was similar to that of a plasticizer, lowering the yield stress of the fresh geopolymer paste while keeping the viscosity unchanged. As a result, a compact and dense matrix was obtained with a high early strength of up to 37 MPa at 7 d of curing.

However, the use of soluble aluminum species may also lead to relatively poor strength development in the latter stage depending on the added dose. A geopolymer with an excessive amount of aluminum species may exhibit significant inter-gel spaces (medium capillary pores) due to the formation of discontinuous gels and inability to close and refine these pores at later age, because the accelerated hardening and gel formation blocks the unreacted MK particles and hinders their dealumination reaction.

5.5 **References**

Abdi, D., Cade-Menun, B. J., Ziadi, N., & Parent, L. É. (2014). Long-term impact of tillage practices and phosphorus fertilization on soil phosphorus forms as determined by ^{31}P nuclear magnetic resonance spectroscopy. *Journal of Environmental Quality*, 43(4), 1431-1441.

Benavent, V., Steins, P., Sobrados, I., Sanz, J., Lambertin, D., Frizon, F., Rossignol, S., & Poulesquen, A. (2016). Impact of aluminum on the structure of geopolymers from the early stages to consolidated material. *Cement and Concrete Research*, 90, 27-35.

Chavda, M. A., Bernal, S. A., Apperley, D. C., Kinoshita, H., & Provis, J. L. (2015). Identification of the hydrate gel phases present in phosphate-modified calcium aluminate binders. *Cement and Concrete Research*, 70, 21-28.

Dai, J. G., Munir, S., & Ding, Z. (2013). Comparative study of different cement-based inorganic pastes towards the development of FRIP strengthening technology. *Journal of Composites for Construction*, 18(3), A4013011.

Douiri, H., Kaddoussi, I., Baklouti, S., Arous, M., & Fakhfakh, Z. (2016). Water molecular dynamics of metakaolin and phosphoric acid-based geopolymers investigated by impedance spectroscopy and DSC/TGA. *Journal of Non-Crystalline Solids*, 445, 95-101.

Duxson, P., Provis, J. L., Lukey, G. C., Mallicoat, S. W., Kriven, W. M., & van Deventer, J. S. J. (2005). Understanding the relationship between geopolymer composition, microstructure and mechanical properties. *Colloids and Surfaces A: Physicochemical and Engineering Aspects*, 269(1-3), 47-58.

Favier, A., Habert, G., d'Espinose de Lacaillerie, J. D., & Roussel, N. (2013). Mechanical properties and compositional heterogeneities of fresh geopolymer pastes. *Cement and Concrete Research*, 48, 9-16.

Favier, A., Hot, J., Habert, G., Roussel, N., & d'Espinose de Lacaillerie, J. B. (2014). Flow properties of MK-based geopolymer pastes. A comparative study with standard Portland cement pastes. *Soft Matter*, 10(8), 1134-1141.

Gualtieri, M. L., Romagnoli, M., Pollastri, S., & Gualtieri, A. F. (2015). Inorganic polymers from laterite using activation with phosphoric acid and alkaline sodium silicate solution: mechanical and microstructural properties. *Cement and Concrete Research*, 67, 259-270.

Haouas, M., Taulelle, F., & Martineau, C. (2016). Recent advances in application of ^{27}Al NMR spectroscopy to materials science. *Progress in Nuclear Magnetic Resonance Spectroscopy*, 94, 11-36.

He, Y., Liu, L., He, L., & Cui, X. (2016). Characterization of chemosynthetic H_3PO_4–Al_2O_3–$2SiO_2$ geopolymers. *Ceramics International*, 42(9), 10908-10912.

Jansson, H., Bernin, D., & Ramser, K. (2015). Silicate species of water glass and insights for alkali-activated green cement. *AIP Advances*, 5(6), 067167.

Liu, J., Yang, J., Liang, X., Zhao, Y., Cade-Menun, B. J., & Hu, Y. (2014). Molecular speciation of phosphorus present in readily dispersible colloids from agricultural soils. *Soil Science Society of America Journal*, 78(1), 47-53.

Liu, Y. L., Wang, Y. S., Fang, G., Alrefaei, Y., Dong, B., & Xing, F. (2018). A preliminary study on capsule-based self-healing grouting materials for grouted splice sleeve connection. *Construction and Building Materials*, 170, 418-423.

Ma, H., Hou, D., & Li, Z. (2015). Two-scale modeling of transport properties of cement paste: Formation factor, electrical conductivity and chloride diffusivity. *Computational Materials Science*, 110, 270-280.

Mueller, D., Hoebbel, D., & Gessner, W. (1981). 27Al NMR studies of aluminosilicate solutions. Influences of the second coordination sphere on the shielding of aluminium. *Chemical Physics Letters*, 84(1), 25-29.

Perera, D. S., Hanna, J. V., Davis, J., Blackford, M. G., Latella, B. A., Sasaki, Y., & Vance, E. R. (2008). Relative strengths of phosphoric acid-reacted and alkali-reacted metakaolin materials. *Journal of Materials Science*, 43(19), 6562-6566.

Petzet, S., Peplinski, B., Bodkhe, S. Y., & Cornel, P. (2011). Recovery of phosphorus and aluminium from sewage sludge ash by a new wet chemical elution process (SESAL-Phos-recovery process). *Water Science and Technology*, 64(3), 693-699.

Prado-Herrero, P., Garcia-Guinea, J., Crespo-Feo, E., & Correcher, V. (2010). Temperature-induced transformation of metavariscite to berlinite. *Phase Transitions*, 83(6), 440-449.

Provis, J. L., Lukey, G. C., & van Deventer, J. S. J. (2005). Do geopolymers actually contain nanocrystalline zeolites? A reexamination of existing results. *Chemistry of Materials*, 17(12), 3075-3085.

Roussel, N., Lema îre, A., Flatt, R. J., & Coussot, P. (2010). Steady state flow of cement suspensions: a micromechanical state of the art. *Cement and Concrete Research*, 40(1), 77-84.

Samadi-Maybodi, R. F., Bell, A. T., & Radke, C. J. (1993). Phosphorus-31 and aluminum-27 NMR investigations of highly acidic, aqueous solutions containing aluminum and phosphorus. *Journal of Physical Chemistry*, ***97***(3), 767-774.

Samadi-Maybodi, A., Nejad-Darzi, S. K. H., & Bijanzadeh, H. (2009). ^{31}P and ^{27}Al NMR studies of aqueous (2-hydroxyethyl) trimethylammonium solutions containing aluminum and phosphorus. *Spectrochimica Acta Part A: Molecular and Biomolecular Spectroscopy*, 72(2), 382-389.

Wang, Y. S., & Dai, J. G. (2017). X-ray computed tomography for pore-related characterization and simulation of cement mortar matrix. *NDT & E International*, 86, 28-35.

White, C. E., Provis, J. L., Proffen, T., Riley, D. P., & van Deventer, J. S. J. (2010). Density functional modeling of the local structure of kaolinite subjected to thermal dehydroxylation. *Journal of Physical Chemistry A*, 114(14), 4988-4996.

Zeng, Q., Li, K., Fen-Chong, T., & Dangla, P. (2012). Pore structure characterization of cement pastes blended with high-volume fly-ash. *Cement and Concrete Research*, 42(1), 194-204.

This page is intentionally left blank

CHAPTER 6 SILICO-ALUMINOPHOSPHATE GEOPOLYMER IMPROVED BY DEAD-BURNT MAGNESIA

In this chapter, an acid-base reaction induced by dead-burnt magnesia and phosphate activating solution is proposed to improve the early properties of the DBM-doped silico-aluminophosphate geopolymer. Reaction mechanisms between the DBM and the monoaluminum phosphate (MAP) in an aqueous solution were investigated at four different Mg/Al ratios. Conductivity and pH evolutions of the solution systems, in addition to X-ray diffraction and scanning electron microscopy results of the final precipitations, indicated that the crystalline phase (i.e., newberyite) started to precipitate at a pH of around 3. Besides, the reaction between DBM and MAP produced an amorphous aluminum magnesium phosphate ($Al_2O_3 \cdot 3MgO \cdot 2P_2O_5$) phase. The DBM/MAP ratios may govern the reaction rate in the solution system. Setting times and early strength of DBM-doped silico-aluminophosphate geopolymer pastes with four different DBM contents were evaluated to confirm the acceleration effect of DBM-induced acid-base reaction.

6.1 Introduction

The studies in Chapter 4 on the silico-aluminophosphate geopolymer indicated that the phosphate activation of the aluminosilicate precursors (i.e., the reaction rate) was extremely slow at ambient temperature (e.g., the final setting time more than 48 hour). The reaction rate is directly related to the properties of the solid aluminosilicate precursor (e.g., reactivity) and the activating solution (e.g., pH, concentration and ion types). In addition to thermal curing (e.g., 60-100 ℃) in the laboratory experiment (Gualtieri et al., 2015; Douiri et al., 2016; He et al., 2016), modifying the activating solution by adding the aluminum species is considered as an effective method to enhance the early performance of the geopolymers at ambient temperature. It was reported that adding small dosage of $NaAlO_2$ in the alkali activating solution improved the workability of the paste and accelerated the network structure growth of the alkali-aluminosilicate geopolymer matrix (Benavent et al., 2016). In the silico-aluminophosphate geopolymer, the research in the previous chapter (i.e., Chapter 5) also indicated that the incorporation of aluminum species in activating solution allowed a rapid sol/gel transition in the early stage, resulting in a fresh geopolymer paste with good workability, fast setting and high early strength.

This chapter provides another strategy, which is to blend an alkali metal source with the aluminosilicates to introduce an acid-base reaction during the geopolymerization process. The phosphate activating solution usually has a strong acidity (e.g., initial pH of about 1.7) (see Chapter 3), and reacts with the alkali metal sources to form crystalline phases (Wilson and Nicholson, 2005). For example, the acid-base reaction induced by magnesium/calcium sources and phosphates generates the crystalline magnesium phosphates, e.g., newberyite (Mesíková et al., 2007; Frost et al., 2011), Struvite (Martí et al., 2017; Wang and Dai, 2017; Wang et al., 2018) and Bobierrite (Takagi et al., 1986; Shih et al., 2017), or calcium phosphates, e.g., brushite and apatite (Zhang et al., 2014; Tamimi et al., 2012), as the main products depending on the environmental pH and Mg/Ca-to-P ratio. Sometimes, the hydrolysis reaction is also accompanied in the acid-base reaction (Ding et al., 2012; Zhang et al., 2014). Since such reactions are usually rapid and violent (Mestres and Ginebra, 2011), it is expected that the reaction starter promotes the setting time and mechanical properties of the silico-aluminophosphate geopolymer in the early stage.

In this chapter, the silico-aluminophosphate geopolymer is synthesized using dead-burnt magnesia (DBM)-doped aluminosilicates and phosphate activating solution. The formation process is designed as follows:

1) The acid-base reaction between DBM and phosphate solution produces the crystalline newberyite and amorphous phosphates to ensure the early strength and setting time of the silico-aluminophosphate geopolymer;
2) The aluminosilicate precursors are then activated by the residual phosphate to form the S-A-P gels in the following period, supporting the long-term working properties of the silico-aluminophosphate geopolymer.

The acid-base reaction products and mechanisms were investigated in aqueous solutions which depend on raw materials ratio and pH variance (i.e., controlling the DBM-to-MAP ratio).The optimal recipes were used to prepare the DBM-accelerated silico-aluminophosphate geopolymer paste to confirm its early properties.

6.2 Experimental Program

6.2.1 Experimental design

The study conducted in aqueous solution aims to investigate the optimum DBM-to-MAP ratio for the generation and growth of newberyite. The conductivity and pH value evolutions of the DBM/MAP solution systems with varying magnesium-to-aluminum (Mg/Al) molar ratios were continuously recorded for 120 min (Xu et al., 2018). The reaction endpoint was set as 24 h. For the solid precipitations, the centrifugal separation, washing, freeze drying and grinding were carried out step-by-step for the microscopic, spectroscopic and thermodynamic observation and analysis.

The DBM-accelerated phosphate-based geopolymer pastes were prepared with four DBM-to-MK weight ratios. The early performance of the geopolymer pastes (e.g., setting time and early compressive strength) was characterized to confirm the effect of acid-base reaction on the silico-aluminophosphate geopolymer. The initial and final setting times of the fresh geopolymer pastes were determined by Vicat apparatus in accordance with ASTM C191, while the compressive strength of the hardened geopolymer pastes were measured after 1-3d curing by a hydraulic pressure testing machine with a loading rate of 0.2 MPa/s in compliance with ASTM C109.

6.2.2 Raw materials

Industrial grade dead-burnt magnesia (DBM) powder with fine granularity was obtained from Jimei Refractory Co. Ltd., China. The median particle diameter and specific surface area of the DBM powder were 5.55 μm and 0.69 m^2/g, respectively. The monoaluminum phosphate (MAP) liquid was synthesized by hydrothermal reaction between the powdered aluminum hydroxide and the liquid orthophosphoric acid resulting in an activating solution with P/Al molar ratio and mass concentration of 3.0 and 62.0%, respectively. The aluminosilicate precursor used for producing DBM-accelerated silico-aluminophosphate geopolymer pastes was metakaolin (MK) with median particle diameter and specific surface area of 2.12 μm and 0.76 m^2/g, respectively. Deionized water was used throughout this study.

6.2.3 Aqueous solution system

The effect of the DBM-to-MAP ratio (i.e., Mg/Al ratio of 1, 2, 4, 8) on the generation and growth of newberyite was investigated in the DBM/MAP solution. The mix proportions of the DBM/MAP solutions are shown in Table 6.1. As soon as the weighted DBM was added into 500 mL MAP solution (Al^{3+} concentration of 0.396 mol/L), the conductivity and pH value of the solution system were monitored every minute at 25°C. Magnetic stirring was applied on the solution systems till the end of 24 hour. The resulting precipitations were separated from the solution for further analysis.

Table 6.1 Mix design in DBM/MAP aqueous solution system with varying DBM-to-MAP ratios

No.	Mg/Al [a]	DBM [b] (g)	MAP [c] (g)	Volume (mL)	Total magnesium (mol)
MA01	1	8.67	100	500	0.193
MA02	2	17.35	100	500	0.396
MA04	4	34.70	100	500	0.772
MA08	8	69.40	100	500	1.544

a. Mg/Al means the molar ratio in the magnesia/MPA solution system;

b. Chemical component determined by X-ray fluorescence: MgO (~89.0%), SiO_2 (~4.2%), Fe_2O_3 (~3.2%), CaO (~2.4%) and Al_2O_3 (~0.5%);

c. Mass concentration of MAP is 61.3% with a P/Al molar ratio of 2.99.

6.2.4 Geopolymer paste preparation

Four DBM-accelerated silico-aluminophosphate geopolymer pastes were prepared with DBM-to-MK weight ratios of 0, 5%, 10% and 20%, which are donated as G0, G05, G10 and G20, respectively. All mix proportions are shown in Table 6.2. The dosage of MAP in G0 was benchmarked, and the MAP was increased in the following series while maintaining DBM/MAP (i.e., Mg/Al) molar ratio of 4.0. The solid materials (i.e., MK and DBM) were dry-mixed for 5 min, and further homogenized with the cooled activating solutions for another 3 min. The resulting fresh geopolymer pastes were cast into 50 mm cube molds, and compacted using a mechanical vibration table. All the specimens were demolded after 24 h and cured in an environmental chamber with a temperature of 25℃ and a relative humidity of 90%.

Table 6.2 Mix proportions (by weight ratio) of the DBM-accelerated silico-aluminophosphate geopolymer paste with different DBM contents

No.	DBM-doped aluminosilicate		Activating solution		Geopolymer paste		
	MK	DBM	MAP	Water	Si/P [a]	Mg/P [a]	*w/s*
G0	10	0	7.62	2.05	2.00	0	0.50
G05	10	0.5	9.05	1.75	1.68	0.21	0.50
G10	10	1.0	10.47	1.45	1.45	0.37	0.50
G20	10	2.0	13.33	0.84	1.14	0.58	0.50

a. Si/P and Mg/P mean the total molar ratio of silicon-to-phosphorus and magnesium-to-phosphors in geopolymer paste;

6.2.5 Analysis techniques

The crystalline compositions of the solid precipitations and hardened geopolymer pastes were determined by a high resolution X-ray diffractometer with a scanning step of 0.02. A simultaneous thermal analysis under an argon atmosphere was employed to analyze the thermal decomposition and phase transition behaviors of the solid precipitations at a heating rate of 10 ℃/min. The micromorphology features were characterized by scanning electron microscopy with energy dispersive X-ray spectroscopy detector. An acceleration voltage of 20 kV was applied, and all the samples were desiccated (60 °C for 24 h) and coated with gold sputter (90 seconds) before the microscopic measurement.

6.3 **Results and Discussion**

6.3.1 Conductivity and pH evolution of DBM/MAP solution system

The evolutions of pH and conductivity of the DBM/MAP aqueous solution systems with four Mg/Al molar ratios are shown in Fig. 6.1. Before DBM was added, the MAP solution was considered as an acidic media (pH = 1.67) as it contains Al^{3+} (aq) and some phosphate anions (e.g., $H_2PO_4^-$, HPO_4^{2-} and PO_4^{3-}) generated by the chemical equilibrium reactions (Eqs. 6.1 to 6.3).

$$Al(H_2PO_4)_3 \leftrightarrow Al^{3+}(\text{aq}) + 3H_2PO_4^- \qquad (6.1)$$

$$H_2PO_4^- \leftrightarrow H^+ + HPO_4^{2-} \qquad (6.2)$$

$$HPO_4^{2-} \leftrightarrow H^+ + PO_4^{3-} \qquad (6.3)$$

As shown in Fig. 6.1, the pH and conductivity of all the DBM/MAP solution systems underwent several similar fluctuations until reaching steady states at 100 min, after which the reaction between DBM and MAP was in a dynamic equilibrium. The pH and conductivity of the solution systems at reaction endpoint (i.e., 24 h) were stabilized. During this period, characteristic points and trends are noticeable on the pH and conductivity curves.

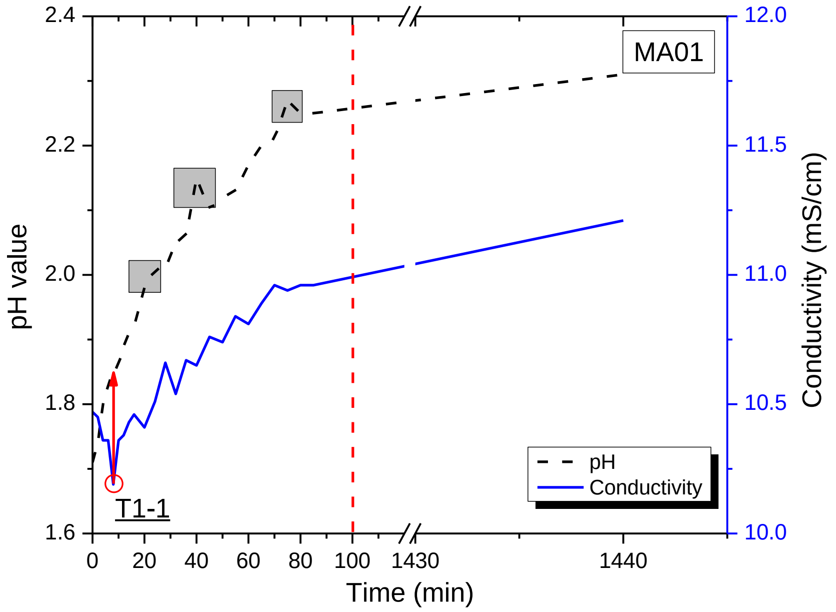
MA01
pH value
2.4
2.2
2.0
1.8
1.6
Conductivity (mS/cm)
12.0
11.5
11.0
10.5
10.0
0
20
40
60
80
100
1430
1440
Time (min)
T1-1
pH
Conductivity

(a) MA01

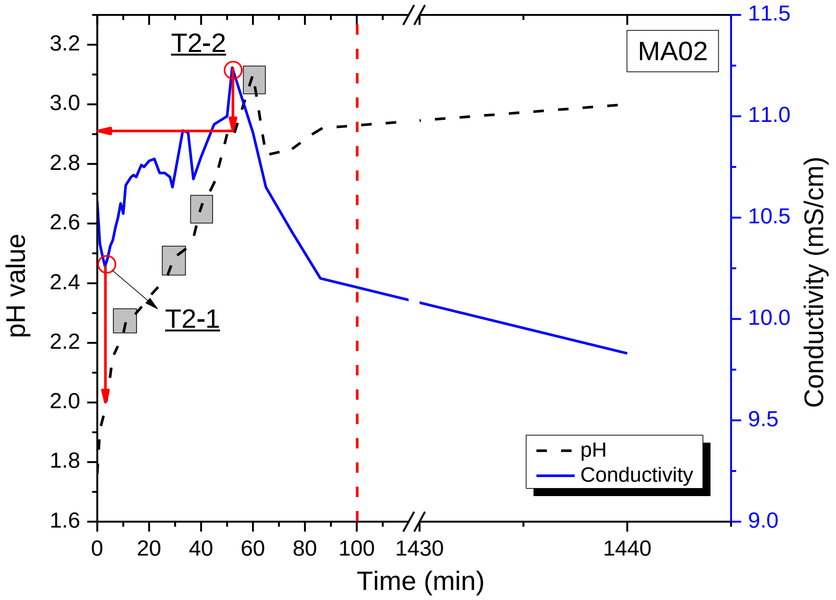
MA02
T2-2
T2-1
pH value
3.2
3.0
2.8
2.6
2.4
2.2
2.0
1.8
1.6
Conductivity (mS/cm)
11.5
11.0
10.5
10.0
9.5
9.0
0
20
40
60
80
100
1430
1440
Time (min)
pH
Conductivity

(b) MA02

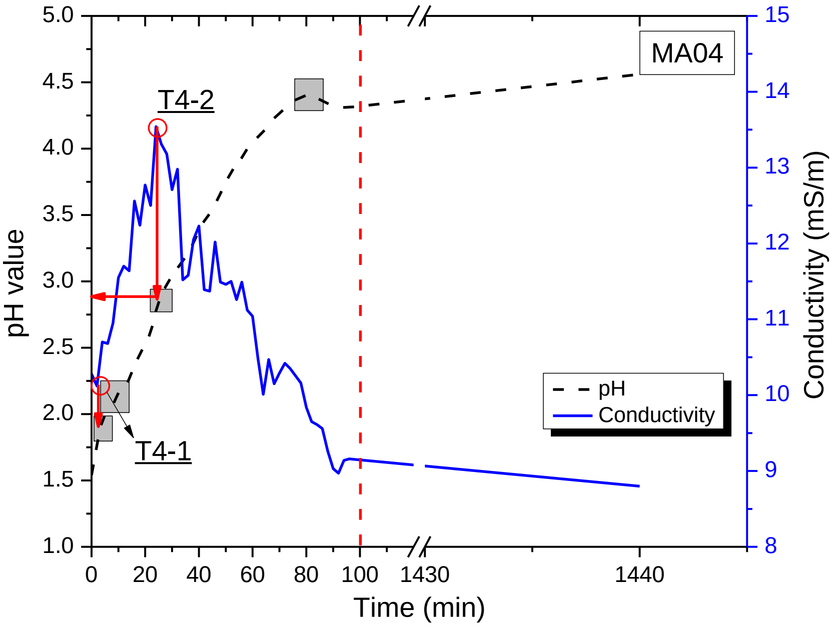

(c) MA04

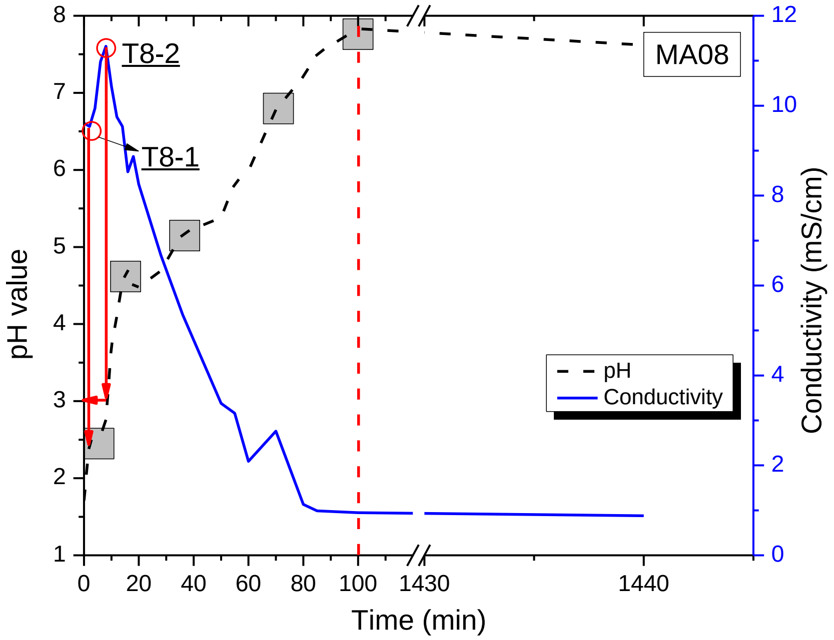

(d) MA08

Fig. 6.1 pH and conductivity evolutions of DBM/MAP aqueous system with different Mg/Al ratios

Clearly, the incorporation of DBM in MAP solution increases the pH value of the system. This is caused by the DBM dissolution (hydrolysis reaction) which continuously releases OH^- as stated in Eq. 6.4. The resulting solution systems, depending on the given DBM contents, arrived at plateaus with pH values of 2.3, 3.0, 4.6 and 7.6 for MA01, MA02, MA04 and MA08, respectively. Some marginally sudden changes in the pH curves (labelled in checkers) were observed which demonstrates the buffer and combining capacity of (hydro)phosphate ions (e.g., $H_2PO_4^-$, HPO_4^{2-} and PO_4^{3-}) to DBM (Wagh, 2016).

$$MgO + H_2O \rightarrow Mg(OH)_2 \rightarrow Mg^{2+} + 2OH^- \tag{6.4}$$

Concerning the conductivity variation, three main features can be highlighted as follows:

1) The sharp decrease of the conductivity at the early stage (e.g., 0-5 min for MA02 solution system) implies a precipitation reaction. The formed phase is mainly magnesium dihydrogen phosphate ($Mg(H_2PO_4)_2 \cdot nH_2O$) (Wilson and Nicholson, 2005), and the chemical process is described in Eq. 6.5.

$$Mg^{2+} + 2H_2PO_4^- + nH_2O \rightarrow Mg(H_2PO_4)_2 \cdot nH_2O \tag{6.5}$$

2) Since magnesium dihydrogen phosphate is instable and may be ionized in water, the conductivity of the DBM/MAP solution system was minimum at the Tx-1 points presented in Fig. 6.1 (x means the Mg/Al ratio, e.g., T2-1 for MA02 solution system). After Tx-1 points, the conductivity of the systems is gradually elevated. The pH at Tx-1 points is around 2 where the ionization effect rather than hydrolysis effect in terms of $H_2PO_4^-$ is dominated. After that, the continuous dissolution of DBM and magnesium dihydrogen phosphate (Eqs. 6.4 and 6.6) augments the ions concentration and conductivity of the solution system.

$$Mg(H_2PO_4)_2 \cdot nH_2O \rightarrow Mg^{2+} + 2H_2PO_4^- + nH_2O \rightarrow Mg^{2+} + 2H^+ + 2HPO_4^{2-} + nH_2O \tag{6.6}$$

3) The conductivity of the DBM/MAP solution systems reaches the maximum at the inflection point of Tx-2 (x means the Mg/Al ratio, e.g., T4-2 for MA04 solution system), at which the pH values is approximately 3. Subsequently, the rapid decrease in conductivity indicates the beginning of newberyite precipitation as shown in Eq. 6.7.

$$Mg^{2+} + HPO_4^{2-} + 3H_2O \rightarrow MgHPO_4 \cdot 3H_2O \tag{6.7}$$

These pH and conductivity results revealed that the formation of newberyite in DBM/MAP solution system is pH dependent. The occurrence of newberyite is initiated at pH=3 regardless of the DBM/MAP ratios, where an instable magnesium dihydrogen phosphate precipitation seems to appear as an intermediate reaction product. The points of maximum conductivity shown in Fig. 6.1 (i.e., T2-2 [52 min], T4-2 [25 min] and T8-2 [10 min]) indicate that the DBM/MAP ratios may govern the reaction rate in the solution system, i.e., a larger ratio leads to a more rapid reaction rate.

6.3.2 Crystalline phase identification

Figure 6.2 displays the XRD patterns of the final precipitations in DBM/MAP aqueous system with different Mg/Al ratios, identifying the crystalline phases. The peaks (e.g., near 37 ° and 43 °) assigned to Periclase (#00-002-1207) exist in all the precipitated assemblages regardless of the mix proportion, which confirms the inert phase in DBM. As shown in Fig. 6.2, no new crystalline phases were detected when the DBM-to-MAP ratio was 1 (i.e., MA01). A few weak reflections of newberyite (#00-020-0153) were identified in the sediment produced by MA02 solution system as the stoichiometric ratio of DBM/MAP can be partially met (Finch and Sharp, 1989). When the DBM-to-MAP ratio was 4 and 8, the enrichment of XRD peaks of newberyite was further intensified. It is worth noting that the Al-containing crystalline phase was not observed in all XRD patterns. A broad diffuse scattering hump from 25 ° to 35 ° (2 Theta) may correspond to some newly-formed amorphous aluminate phases.

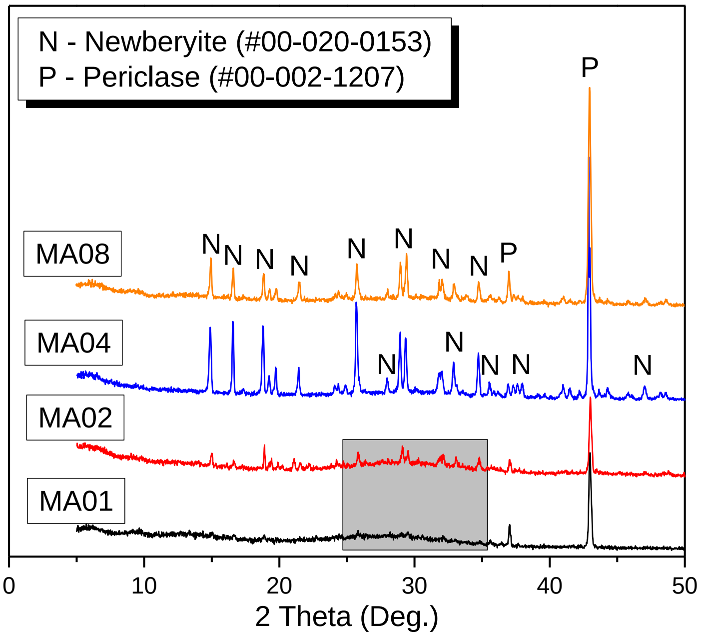

Fig. 6.2 X-ray diffraction patterns of the final precipitations in DBM/MAP aqueous system with different Mg/Al ratios

SEM images of the separated precipitations in DBM/MAP aqueous solutions after 24 h reaction are shown in Fig. 6.3, where the reaction products in DBM/MAP systems with four initial Mg/Al ratios are identified. In Fig. 6.3a, numerous lump phases and irregular agglomerations are observed in MA01, while Fig. 6.3b shows some prism-shaped particles embraced with lump phases in MA02. However, the prismatic particles in MA04 and MA08 precipitations, as shown in Figs. 6.3c and 6.3d, are more available and clearly identifiable than that generated at lower Mg/Al ratios (e.g., 1 and 2) which are most likely to be crystalline newberyite. The formed newberyite shows the different crystal habits, i.e., the height of the prisms in MA08 is larger than that in MA04. It is also found that crystal imperfections were more pronounced in MA08-generated newberyite relative to MA04-generated one. The crystal habits and perfection of newberyite formed in different Mg/Al ratios may be due to exorbitant pH environment caused by dissolution of DBM (Su et al., 2014). These micro-morphological features are in consistence with their XRD results shown in Fig. 6.2, in which the peaks assigned to newberyite in the MA08 are slightly weaker than that in the MA04.

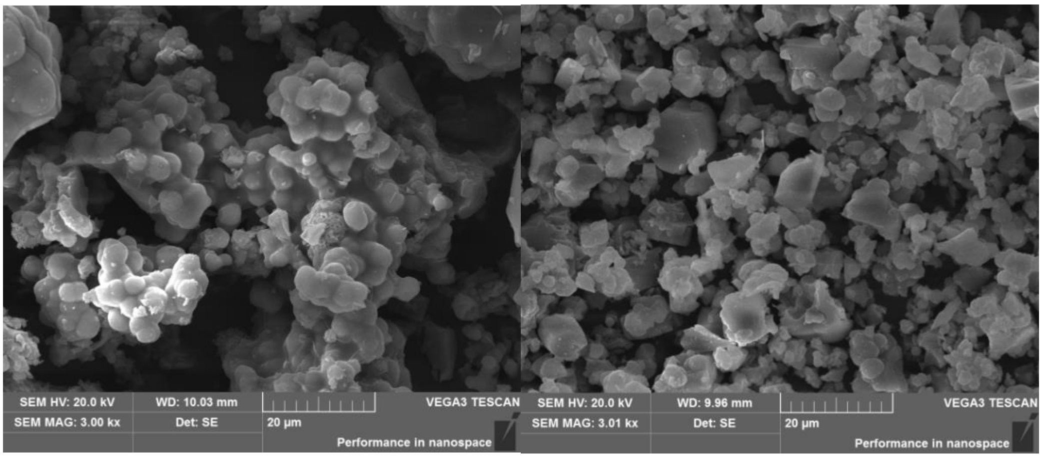

(a) MA01 (b) MA02

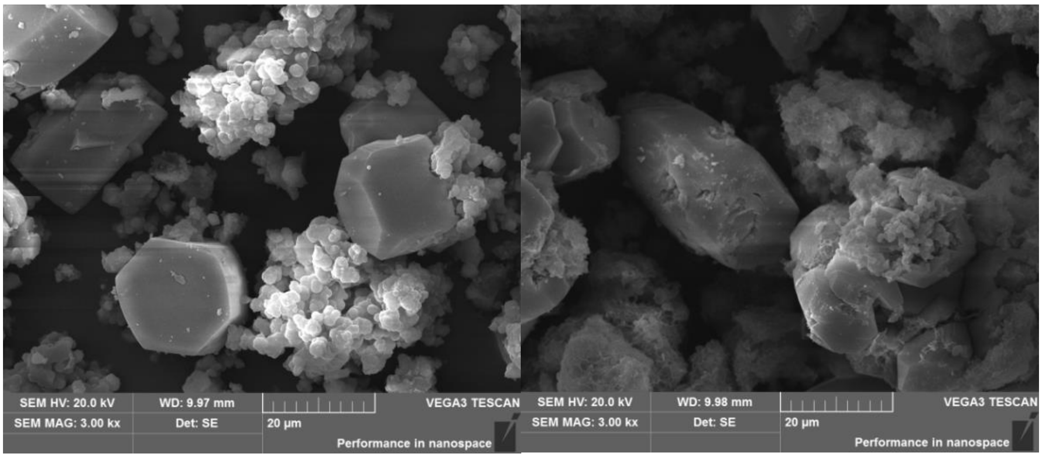

(c) MA04 (d) MA08

Fig. 6.3 SEM images of the final precipitations in DBM/MAP aqueous solution systems with four Mg/Al ratios

Figure 6.4 displays the growing crystalline and lump phase morphologies in addition to EDXS-captured element composition. As shown in Fig. 6.4a, the forming prism-shaped newberyite contains crystalline parts with ‘smooth’ surface (near spectrum 1) and gel-like parts with ‘network’ surface (near spectrum 2). The EDXS results, shown in Fig 6.4b, demonstrate the existence of magnesium and phosphorus in both parts. The Mg/P ratio of 0.88 in the crystalline part presents a marginal deviation from the theoretical value of newberyite (i.e., 1), while the gel-like part with a low Mg/P ratio (0.57) indicates that excessive phosphates are unfavorable to crystalline newberyite growth. Increasing pH value caused by DBM can facilitate the ionization of the dihydric phosphate anion (largely exists in a lower pH environment, e.g., pH < 3) to be hydrogen phosphate ion (Eq. 6.2) which is suitable for newberyite formation (Eq. 6.7). Wafer shapes are agglomerated to form the lump phases (Figs. 4a and c), and the EDXS and XRD results state that they may be amorphous aluminum phosphate phase with an Al/P ratio approaching 1 (e.g., 0.87 and 0.86 in spectrums 3 and 4, respectively). Thus, according to the XRD and SEM-EDXS analysis, the total reaction between MAP and DBM can be described in Eq. 6.8 (Finch and Sharp, 1989; Luz et al., 2015).

$$Al(H_2PO_4)_3 + 2MgO + 4H_2O \rightarrow 2MgHPO_4 \cdot 3H_2O + AlPO_{4(amorphous)} \quad (6.8)$$

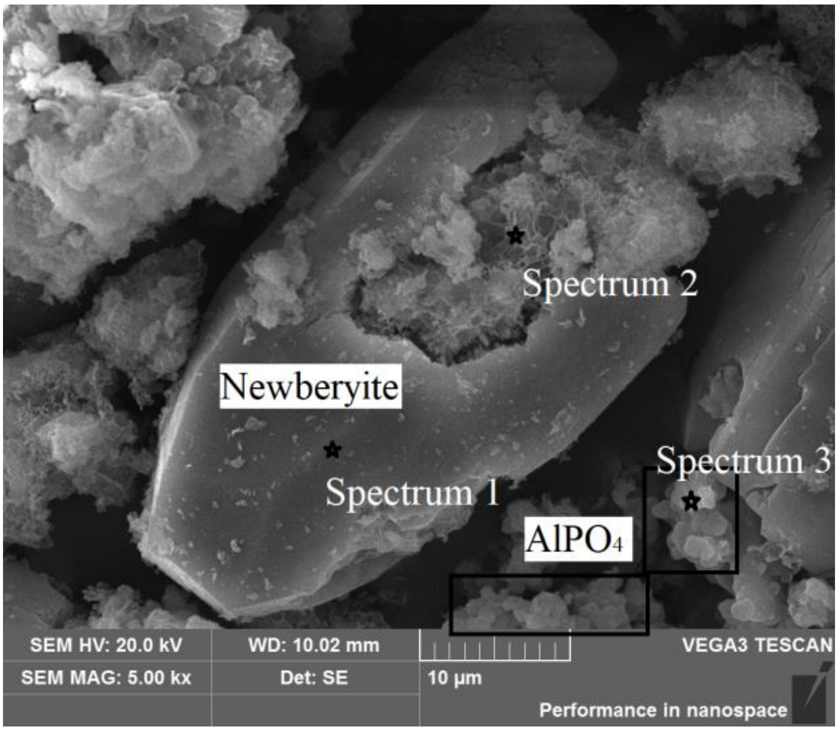

(a) SEM image of prism-shaped newberyite

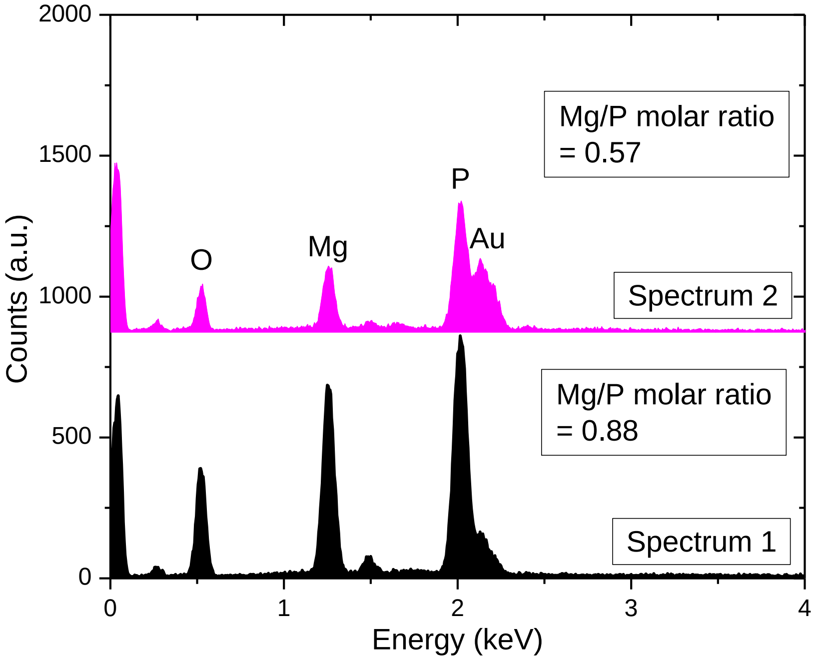

(b) EDXS results prism-shaped newberyite

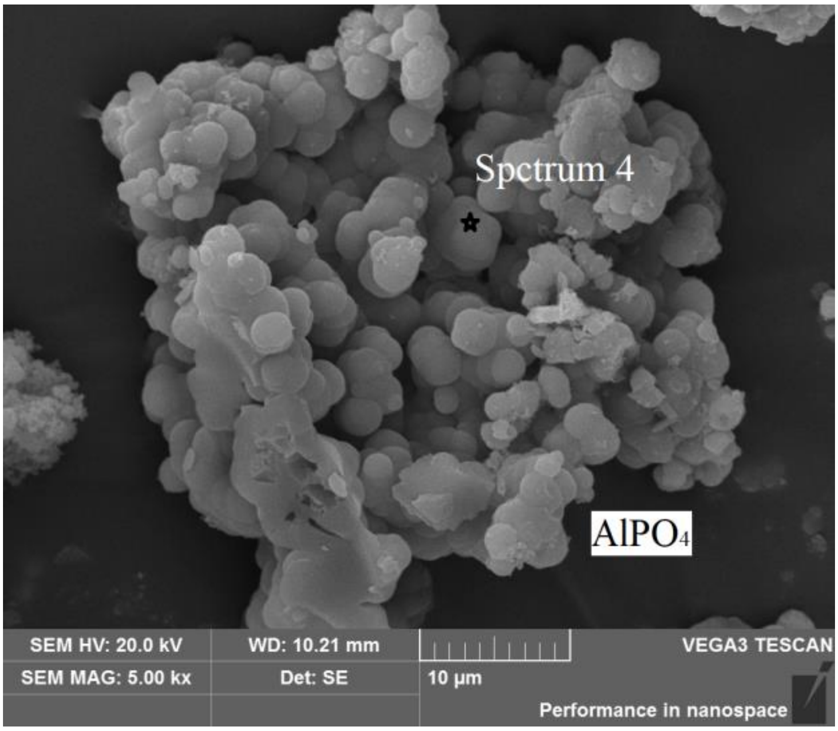

(c) SEM image of lump phases

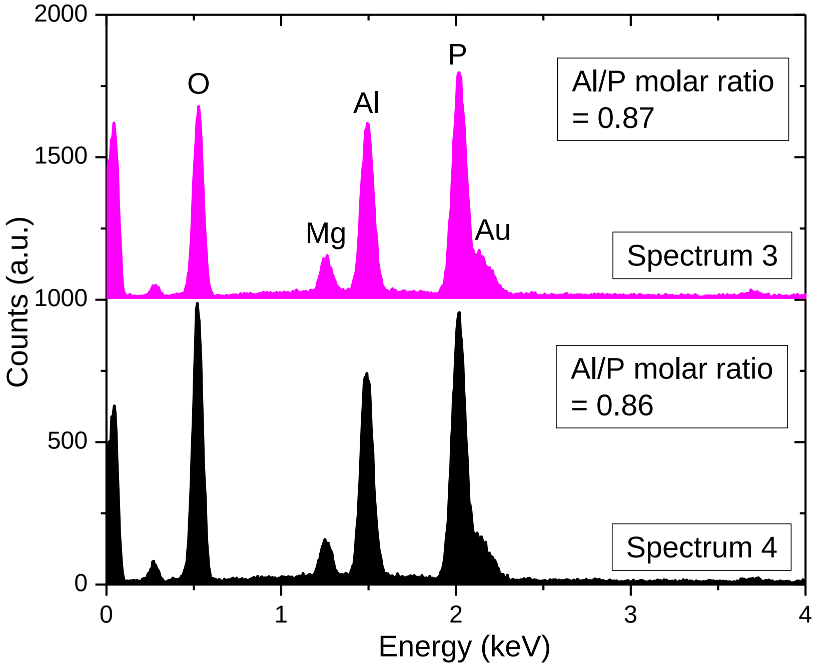

(d) EDXS results of lump phases

Fig. 6.4 SEM-EDXS results of the growing newberyite and lump phases: the precipitation in MA08 system

Figure 6.5 shows the TG-DTA thermograms of the precipitations after 24h reaction for the purpose of analyzing the thermal decomposition and phase transition behaviors at elevated temperatures (20-1000 ℃). As shown in Fig. 6.5, the physically and chemically bound water is lost before 200 ℃ for all the precipitations, which are represented by two endothermic peaks in DTA curves. The weight loss at around 80 ℃ is attributable to the removal of free water in samples, while the second endothermic peak located at 130-180 ℃ is caused by the decomposition of newberyite as stated in Eq. 6.9. The relatively larger weight loss during this period in the MA08 and MA04 compared to MA01 and MA02 revealed that the well-crystalized newberyite existed in MA08 and MA04 is considerably outnumbers that in MA01 and MA02. The elevated temperature may decompose the structural hydroxyl groups of the residual MAP to be aluminum metaphosphate ($Al(PO_3)_3$) when the local P/Al ratio is 3 (Eq. 6.10) (Palacios et al., 2013), which presents a small endothermic peak at 188 ℃. Aluminum phosphates can also be obtained from MAP at local P/Al ratio of 1 (Palacios et al., 2013).

$$MgHPO_4 \cdot 3H_2O \xrightarrow{Heat} MgHPO_4 + 3H_2O \tag{6.9}$$

$$Al(H_2PO_4)_3 \xrightarrow{Heat} Al(PO_3)_3 + 3H_2O \tag{6.10}$$

During 200-600 ℃, the gradual transition from $MgHPO_4$ to $Mg_2P_2O_7$ (shown in Eq. 6.11) gives rise to slight weight loss due to dehydroxylation of $MgHPO_4$ (Frost et al., 2011). The DTA curves except MA01 also exhibit an exothermic peak around 690 ℃ without weight loss, which is due to in-situ phase transition such as the crystallization of the amorphous aluminum phosphate according to Eq. 6.12 (Prado-Herrero et al., 2010).

$$2MgHPO_4 \xrightarrow{Heat} Mg_2P_2O_7 + H_2O \tag{6.11}$$

$$AlPO_{4(amorphous)} \xrightarrow{Heat} AlPO_{4(crystalline)} \tag{6.12}$$

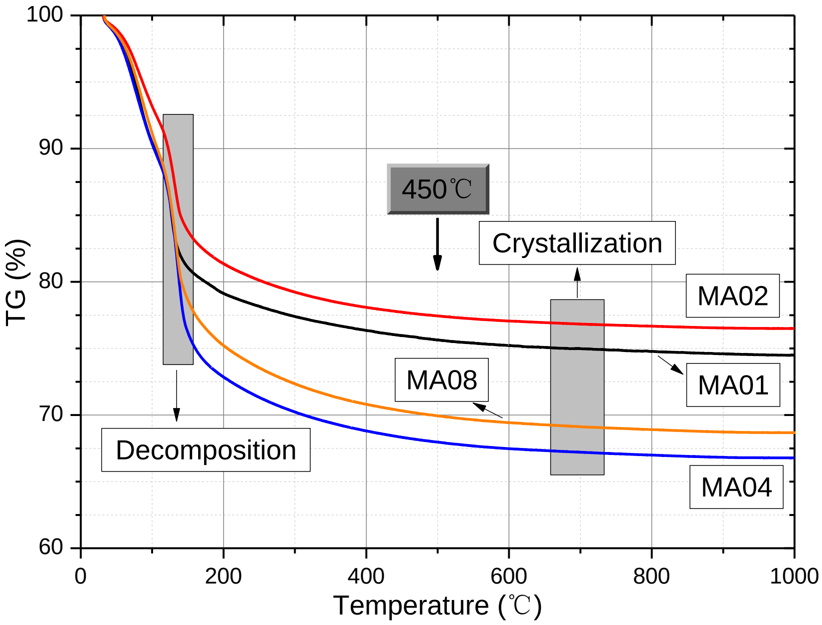

(a) TG thermogram

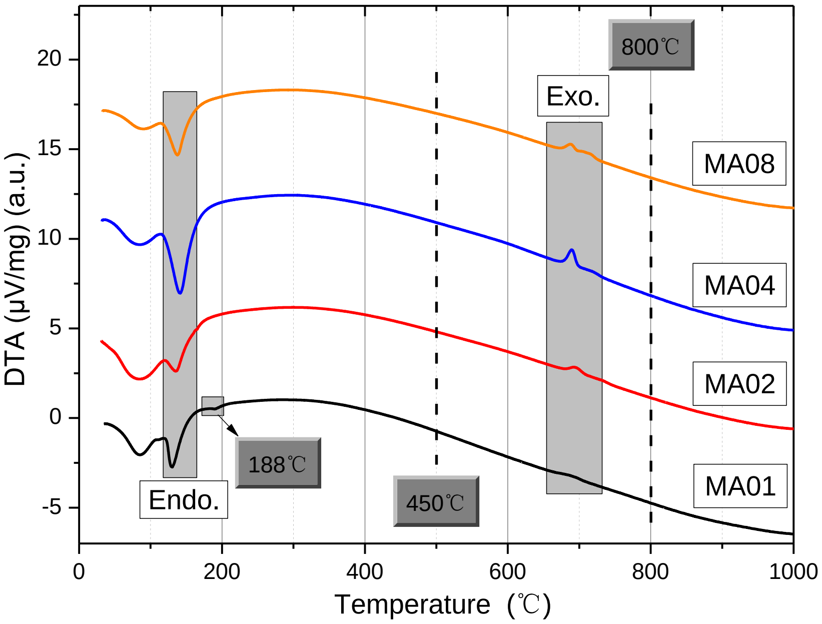

(b) DTA thermogram

Fig. 6.5 Thermogravimetric analysis for thermal decomposition and phase transition behaviors of the final precipitations produced in DBM/MAP systems with different Mg/Al ratios

6.3.3 Amorphous phase identification

The XRD measurements of the precipitations thermally treated at 450 °C and 800 °C are displayed in Figs. 6.6a and 6.6b, respectively, in order to confirm the amorphous phase analyzed by the thermogravimetric results. As shown in Fig. 6.6a, the peaks assigned to newberyite disappeared when the precipitations were heated under a temperature of 450 °C for 2h. The unavailability of phosphate-containing crystalline peaks in MA02, MA04 and MA08 suggests that the generated amorphous aluminum phosphate (Eq. 6.8) is chemically thermostable at 450 °C. The SEM images of all the precipitations in Figs. 6.7a-6.7d show some agglomerates and lumps, which may be amorphous aluminum phosphates and decomposed newberyite, respectively. Besides, the residual MAP in MA01 system led to the generation of aluminum metaphosphate (#00-013-0430) and aluminum phosphate (#00-048-0652) (Fig. 6.6a) after thermal treatment. The chemical composition of these phosphates is statistically analyzed according to the EDXS points marked in Fig. 6.8a. The obtained atomic ratio correlation plot, i.e., Mg/Al ratio *vs.* Mg/P ratio, is shown in Fig. 6.8b. The investigated points with low magnesium content (e.g., Mg/Al and Mg/P ratios less than 0.2) and P/Al ratio of 1-3 (i.e., #1 in Fig. 6.8b) clarify the existence of crystalline aluminum phosphate phases. The P/Al ratio of the amorphous aluminum phosphate phase ranged from 1 to 1.54 (i.e., #2 in Fig. 6.8b) which is larger than the theoretical value (P/Al = 1 for $AlPO_4$). The involvement of magnesium (e.g., Mg/Al ratio of 0.3-0.53 and Mg/P ratio of 0.25-0.4) indicates that the reaction between DBM and MAP in MA01 system produces the amorphous aluminum magnesium phosphate ($Al_2O_3 \cdot 3MgO \cdot 2P_2O_5$) phase instead of crystalline newberyite (Finch and Sharp, 1989).

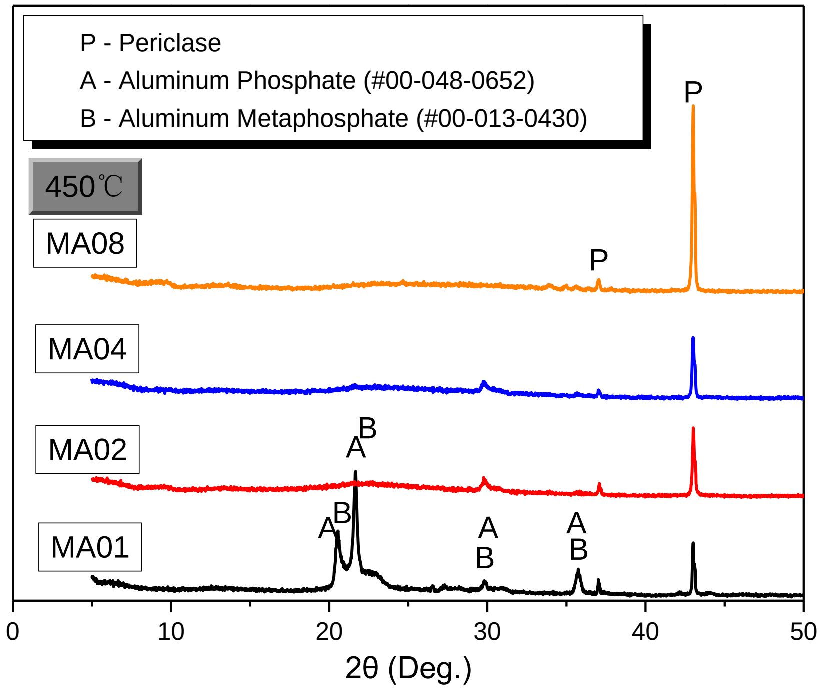

(a) Aged at 450 °C

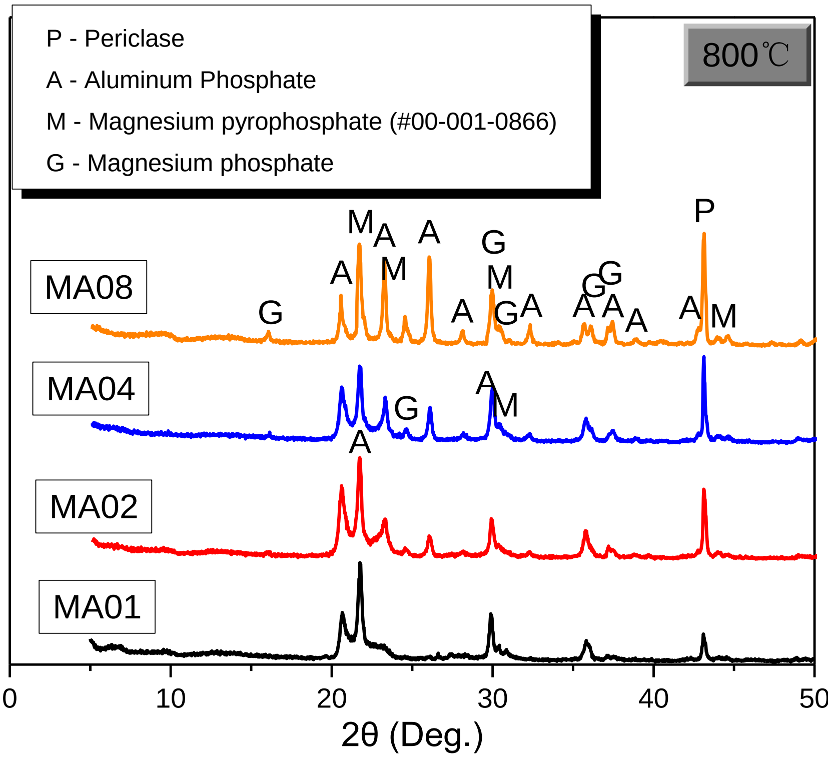

(b) Aged at 800 °C

Fig. 6.6 X-ray diffraction patterns of the four types of precipitations aged at elevated temperatures

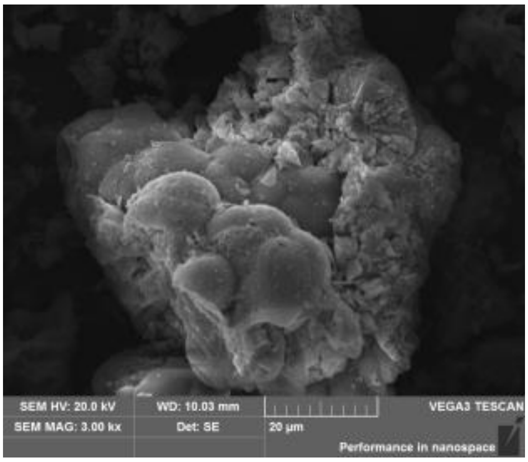

(a) MA01 at 450℃

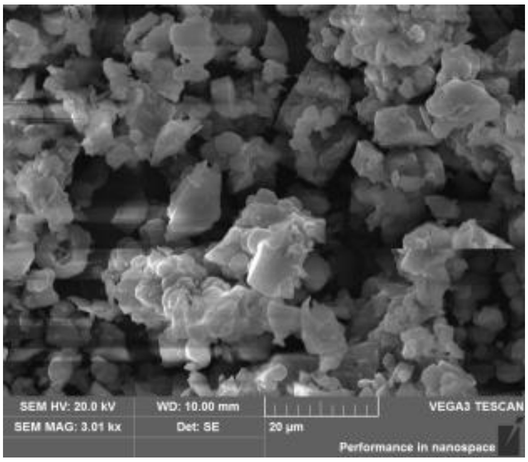

(b) MA02 at 450℃

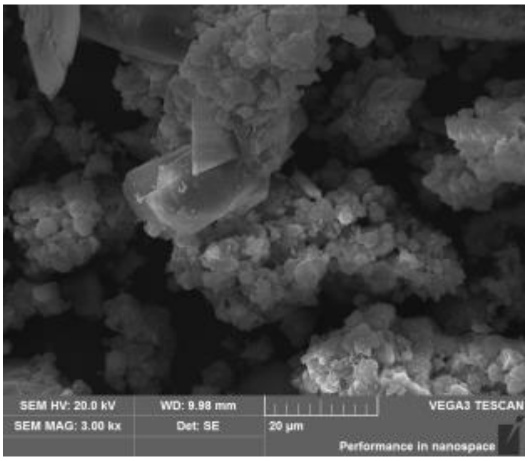

(c) MA04 at 450℃

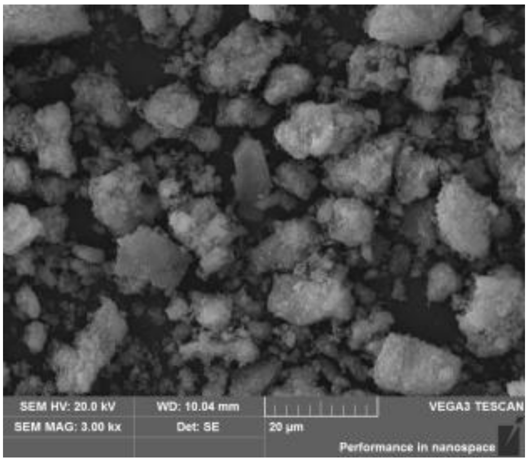

(d) MA08 at 450℃

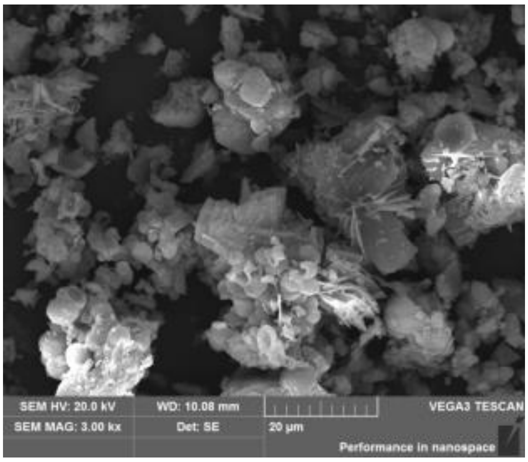

(e) MA01 at 800℃

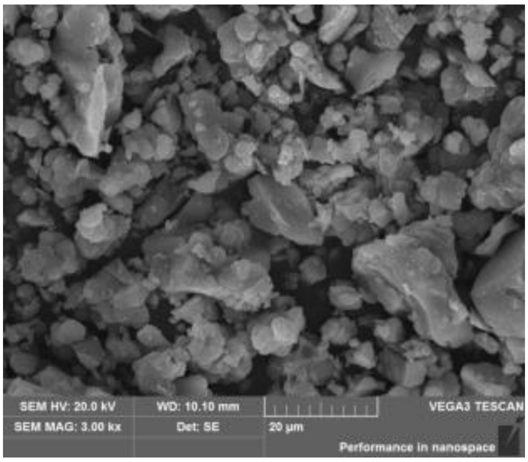

(f) MA02 at 800℃

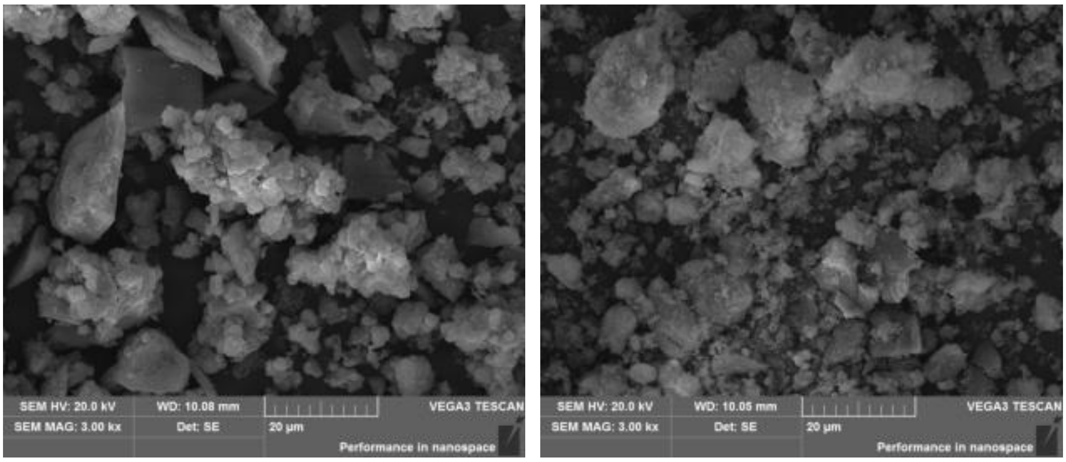

(g) MA04 at 800℃ (h) MA08 at 800℃

Fig. 6.7 SEM images of the four types of precipitations aged at elevated temperatures

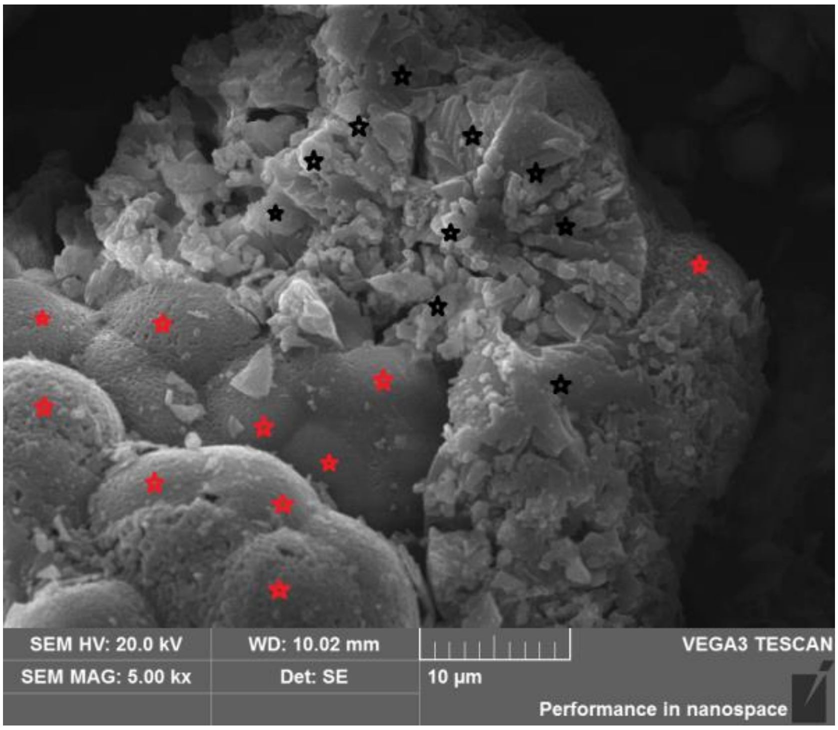

(a) 450 ℃ aged precipitations in MA01

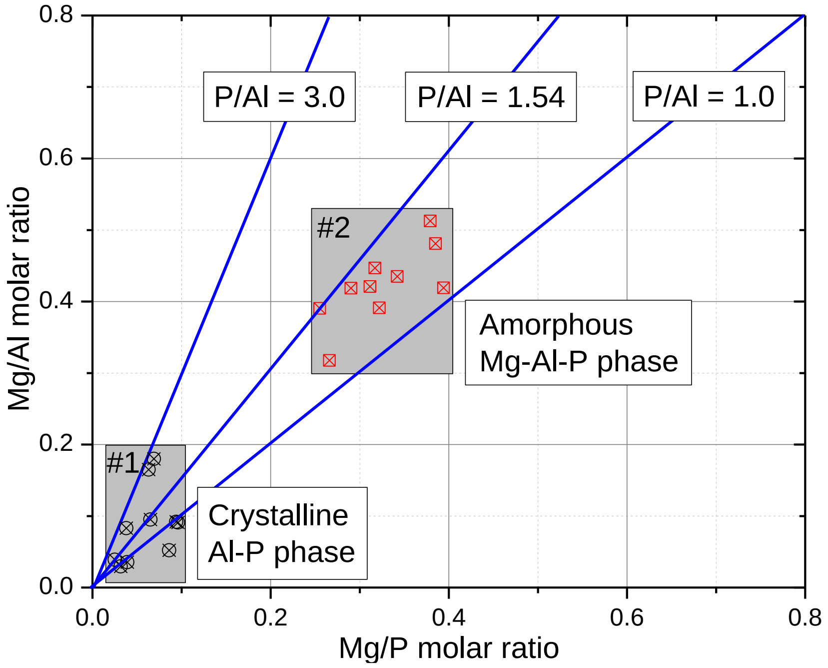

(b) EDXS statistical data of MA01

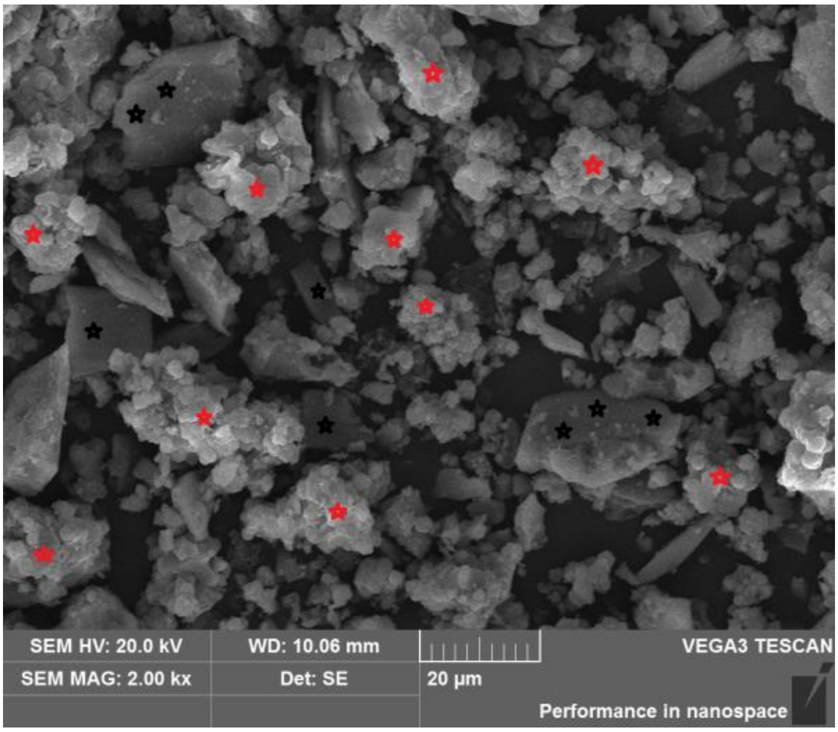

(c) 800 °C aged precipitations in MA04

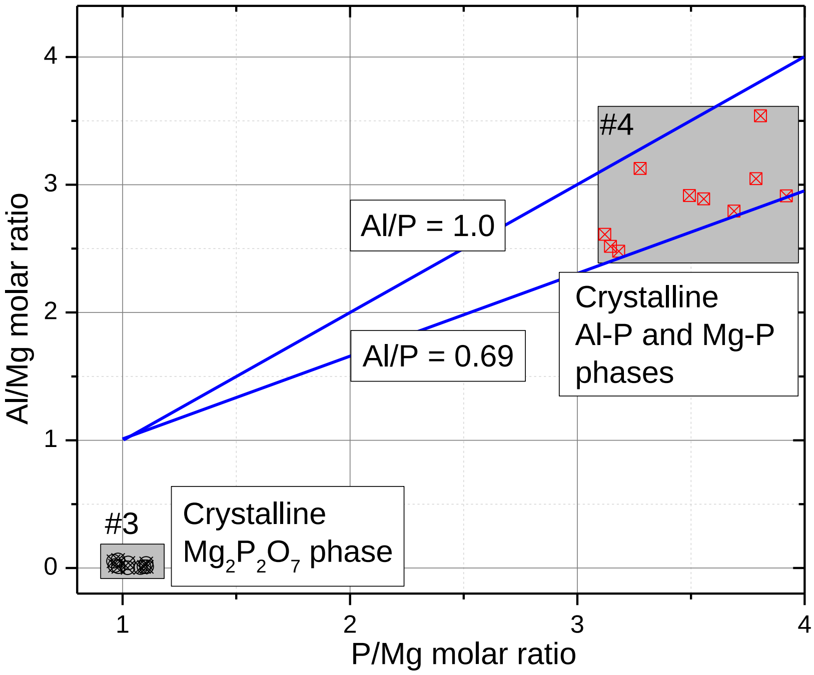

(d) EDXS statistical data of MA04

Fig. 6.8 SEM-EDXS results of the aluminum phosphate and magnesium phosphate phases after high temperature aging. Typical MA01 precipitations at 450 °C and MA04 precipitations 800 °C are selected for analysis

The XRD patterns of the thermal aging precipitations after 800 °C treatment for 2h are shown Fig. 6.6b. , The results revealed the crystalline magnesium pyrophosphate (#00-001-0866), aluminum phosphate (#00-048-0652) and magnesium phosphate, which confirms the phase transitions of $MgHPO_4$ to $Mg_2P_2O_7$ and the amorphous Al_2O_3 ·3MgO ·2P_2O_5 crystallization. Figs. 6.7e-6.7h show the morphologies of the 800°C-aged precipitations which reveal that the lumps are further differentiated from the agglomerates compared to the 450°C-aged ones. The labelled points in Fig. 6.8c (800 °C aged precipitations in MA04) have two concentrated zones. As shown in the zone of #3 in Fig. 6.8d, P/Mg ratio of 0.9-1.2 but with little aluminum can be mainly considered as the crystalline magnesium pyrophosphate whose theoretical P/Mg ratio is 1.0. The EDXS results located in 3.2-4.0 P/Mg and 2.3-3.6 Al/Mg ratios (i.e., #4 in Fig. 6.8d) confirm the blends of aluminum phosphate and magnesium phosphate. The calculated Al/P ratio between 1.0 and 0.69 could be related to the phase transitions of amorphous $Al_2O_3 \cdot 3MgO \cdot 2P_2O_5$ at 800 ℃ forming magnesium phosphate (Luz et al., 2015).

6.3.4 DBM-doped silico-aluminophosphate geopolymer paste

Based on the above mentioned results and analyses, the chemical reaction between MAP and DBM can generate a crystalline phase (newberyite) and some amorphous phosphate phases containing aluminum phosphate and magnesium phosphate, which can be described in Eq. 6.13:

$$2Al(H_2PO_4)_3 + 5MgO + (n+1)H_2O \rightarrow 2MgHPO_4 \cdot 3H_2O + 3MgO \cdot Al_2O_3 \cdot 2P_2O_5 \cdot nH_2O \quad (6.13)$$

Introducing such chemistry in the silico-aluminophosphate geopolymer is expected to enhance its early age performance. The setting times and early compressive strength of the silico-aluminophosphate geopolymer are evaluated in this section.

Figure 6.9 shows the setting time results of the geopolymer pastes which are embedded into pH and conductivity evolution curves of the MA04 aqueous solution system. That is because the increment of MAP used in DBM-doped phosphate-based geopolymer is in proportion to the DBM following a DBM/MAP (i.e., Mg/Al) molar ratio of 4.0. As shown in Fig. 6.9a, it is clearly found that the incorporation of DBM greatly speeded up the setting of the fresh geopolymer pastes. The initial setting time ranges from 152 min for G0 (i.e., without DBM) to 8 min for G20 (i.e., 20% DBM), while more remarkable improvement in final setting time (823, 266, 83 and 33 min for G0, G05, G10 and G20 geopolymer paste, respectively) is observed. The increase of the total Mg/P ratio in geopolymer paste (see Table 6.2) rapidly facilitates the reach to suitable pH environment, in which the newly-formed phosphates initially harden the geopolymer paste (as shown in Eq. 6.13) (Finch and Sharp, 1989). After that, the increase of the mechanical strength of the geopolymer paste can be gradually achieved due to the crystalline phase growth and accumulation, as well as the formation of $Al_2O_3 \cdot 3MgO \cdot 2P_2O_5$ phase and S-A-P gels.

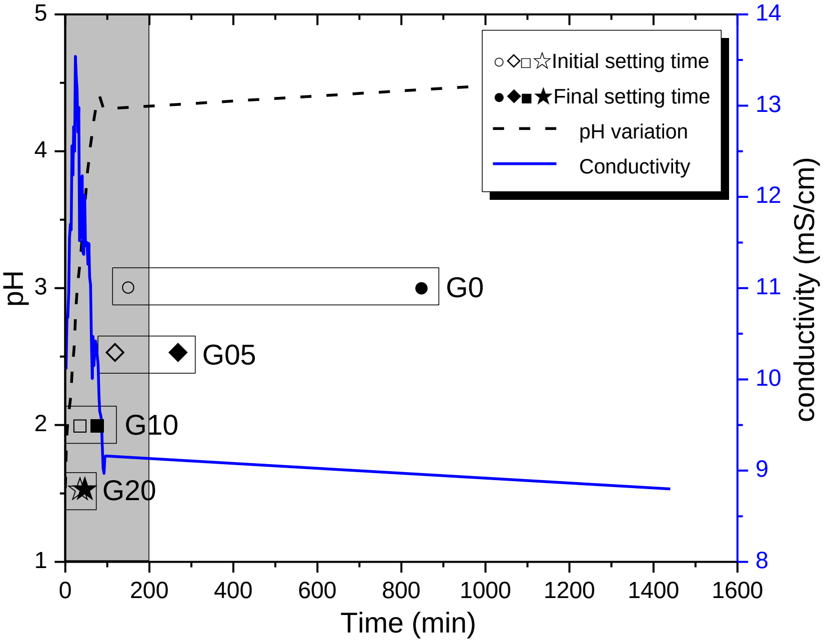

(a) Setting times of four DMB-doped geopolymer pastes

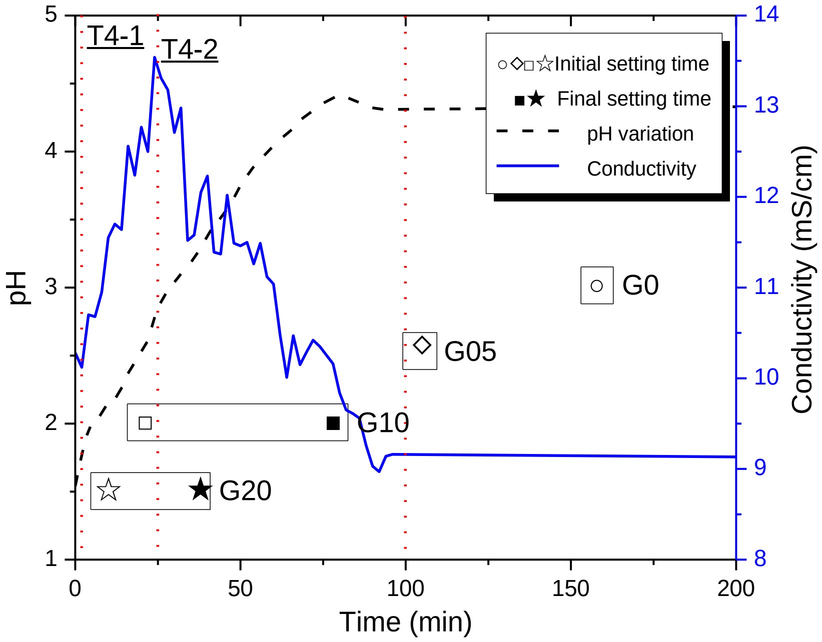

(b) Relationship between pH and conductivity evolution and setting time of geopolymer pastes

Fig. 6.9 Initial and final setting times of the silico-aluminophosphate geopolymer pastes with four different contents of DBM. (The results were embedded into pH and conductivity variation *v.s.* time curves of MA04 aqueous solution system.)

Figure 6.9b presents further details of 0-200 min results. The pH and conductivity evolution of the MA04 aqueous solution system indicates that the precipitation of newberyite starts at T4-2 (around 25 min), which is earlier than the initial setting of G05 and later than that of G10 and G20. The small dosage of DBM diluted by the MK in G05 shows a weak effect on setting acceleration compared to G10 and G20. The DBM-induced acid-base reaction with different DBM-to-MK ratios in silico-aluminophosphate geopolymer could play a crucial role in governing its setting times.

Figure 6.10 plots the early compressive strength development of the DBM-doped geopolymer matrix from 1d to 3d. The G20 paste showed the highest compressive strength at all the ages, reaching 8.3 MPa at 1d and 13.6 MPa at 3d. In contrast, G05 and G10 indicated the worse strength behaviors. This suggests that lower DBM content may barely generate sufficient strength-giving phases (e.g., lower volume ratio of newberyite/matrix) to meet the early strength of geopolymer matrix. Due to the absence of acid-base reaction, the geopolymer without DBM (i.e., G0) behaves with the worst early strength.

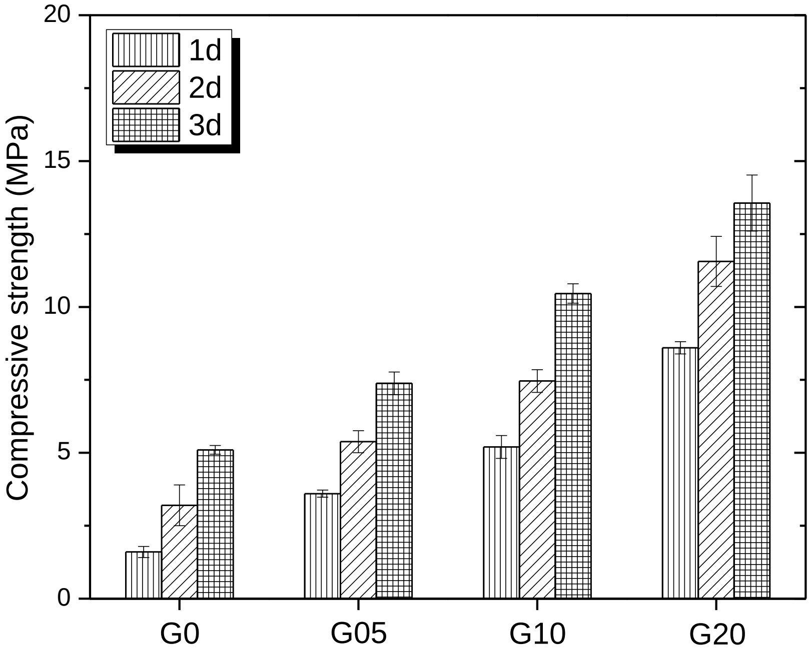

Fig. 6.10 Early compressive strength of the hardened silico-aluminophosphate geopolymer pastes improved by different contents of DBM

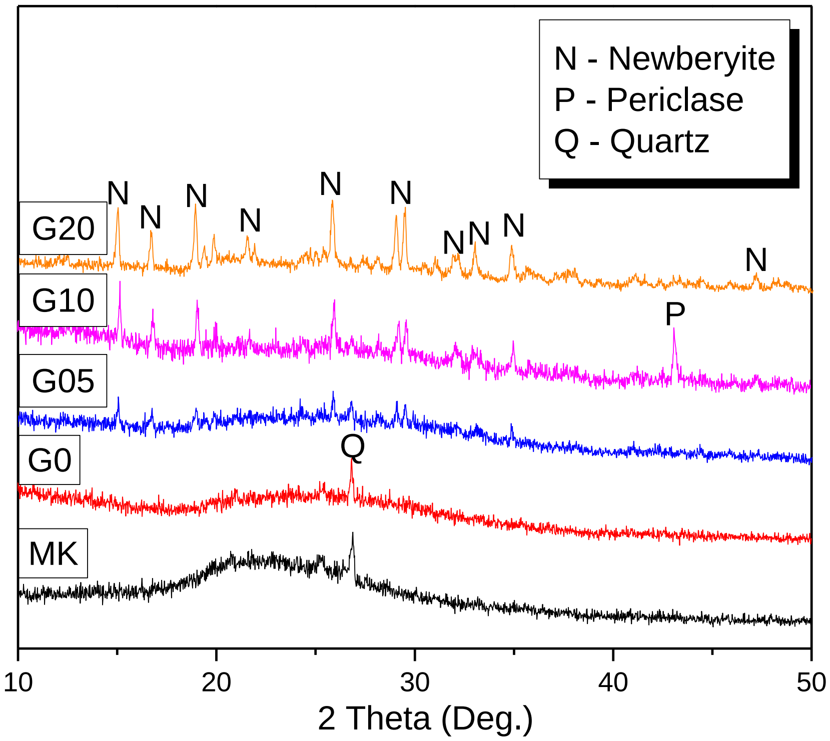

Fig. 6.11 X-ray diffraction patterns of the 3d-cured geopolymer pastes (MK as a reference) blended with four contents of DBM

The observed setting and strength properties can be supported by the X-ray diffraction results shown in Fig. 6.11. It was noticed that the abundant peaks assigned to newberyite appear after 3d curing. Further, the enrichment of XRD peaks increases with the DBM contents. The diffuse peak of the geopolymer at 20-30 ° (2 Theta) slightly shifts from 22 ° to 26 ° relative to the raw MK which is due to the geopolymerization of MK. This is in good agreement with the previous research findings related to silico-aluminophosphate geopolymer (Cui et al., 2011; Douiri et al., 2014; Louati et al., 2014; Louati et al., 2016). As shown in Fig. 6.12, phosphorrösslerite (#00-046-1267) is detected in 1d-cured geopolymer paste but disappears after 3d curing. Such an intermediate reaction product may contribute to the fast setting (Fig. 6.9) and to relatively high early strength (Fig. 6.10).

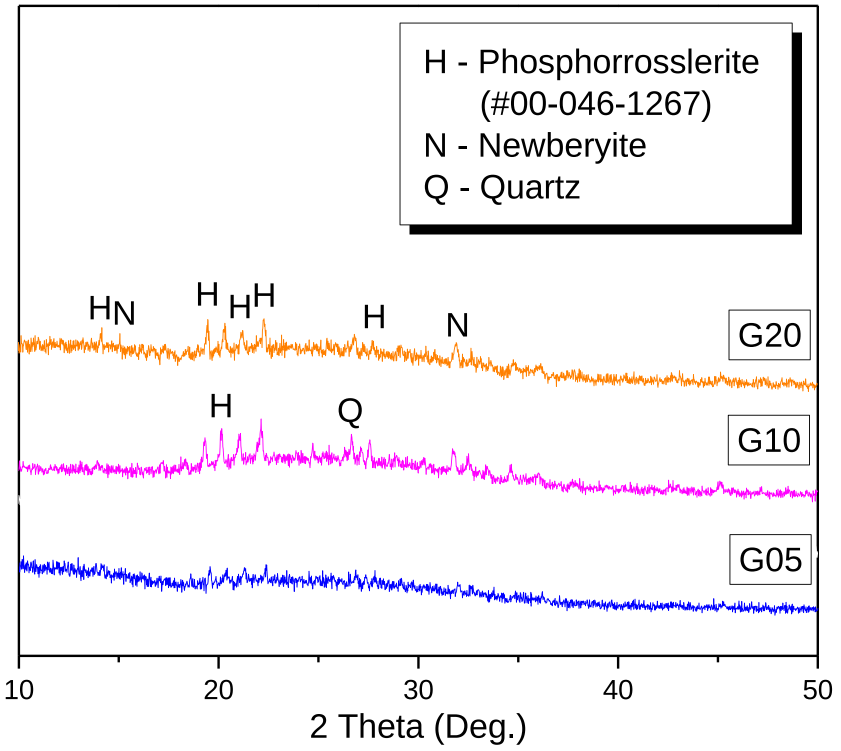

Fig. 6.12 X-ray diffraction patterns of the 1d-cured DBM-doped silico-aluminophosphate geopolymer pastes

6.4 Chapter Summary

This chapter proposes an acid-base reaction with the intention of improving the setting time and early strength of the silico-aluminophosphate geopolymer. The reaction mechanisms between DBM and MAP were elaborated in aqueous solution, following characterizations of early properties of the DBM-doped silico-aluminophosphate geopolymer. Based on the experimental investigations in this chapter, the following conclusions can be drawn:

1) The acid-base reaction between DBM and MAP can yield a crystalline newberyite and an amorphous aluminum magnesium phosphate ($Al_2O_3 \cdot 3MgO \cdot 2P_2O_5$) phase. During this process, magnesium dihydrogen

phosphate appeared at pH of around 2 as an instable intermediate product, and transformed to newberyite at pH of around 3.

2) After the thermal treatment of the reaction products, the magnesium pyrophosphate was generated due to the dehydration and dehydroxylation of newberyite, while the amorphous aluminum magnesium phosphate ($Al_2O_3 \cdot 3MgO \cdot 2P_2O_5$) phase was crystalized to be aluminum phosphate and magnesium phosphate.
3) The DBM/MAP ratios may govern the reaction rate, which can be used to improve the setting time and early strength of the DBM-doped silico-aluminophosphate geopolymer at ambient temperature.
4) The silico-aluminophosphate geopolymer doped with 20% DBM incorporation held an initial setting time of 8 min and 1d compressive strength of 8.3 MPa. Lower dosage of DBM diluted by the aluminosilicates presented a weak effect on setting and strength improvement of the geopolymer.

6.5 References

Benavent, V., Steins, P., Sobrados, I., Sanz, J., Lambertin, D., Frizon, F., Rossignol, S., & Poulesquen, A. (2016). Impact of aluminum on the structure of geopolymers from the early stages to consolidated material. *Cement and Concrete Research*, 90, 27-35.

Ding, Z., Dong, B., Xing, F., Han, N., & Li, Z. (2012). Cementing mechanism of potassium phosphate based magnesium phosphate cement. *Ceramics International*, 38, 6281-6288.

Douiri, H., Kaddoussi, I., Baklouti, S., Arous, M., & Fakhfakh, Z. (2016). Water molecular dynamics of metakaolin and phosphoric acid-based geopolymers investigated by impedance spectroscopy and DSC/TGA. *Journal of Non-Crystalline Solids*, 445, 95-101.

Finch, T., & Sharp, J. H. (1989). Chemical reactions between magnesia and aluminium orthophosphate to form magnesia-phosphate cements. *Journal of Materials Science*, 24, 4379-4386.

Frost, R. L., Palmer, S. J., & Pogson, R. E. (2011). Thermal stability of newberyite Mg (PO3OH) · 3H2O: a cave mineral from Skipton Lava Tubes, Victoria, Australia. *Journal of Thermal Analysis and Calorimetry*, 107, 1143-1146.

Gualtieri, M. L., Romagnoli, M., Pollastri, S., & Gualtieri, A. F. (2015). Inorganic polymers from laterite using activation with phosphoric acid and alkaline sodium silicate solution: mechanical and microstructural properties. *Cement and Concrete Research*, 67, 259-270.

He, Y., Liu, L., He, L., & Cui, X. (2016). Characterization of chemosynthetic H_3PO_4–Al_2O_3–$2SiO_2$ geopolymers. *Ceramics International*, 42, 10908-10912.

Luz, A. P., Gomes, D. T., & Pandolfelli, V. C. (2015). High-alumina phosphate-bonded refractory castables: $Al(OH)_3$ sources and their effects. *Ceramics International*, 41, 9041-9050.

Martí, N., Barat, R., Seco, A., Pastor, L., & Bouzas, A. (2017). Sludge management modeling to enhance P-recovery as struvite in wastewater treatment plants. *Journal of Environmental Management*, 196, 340-346.

Mesíková, Ž., Šulcová, P., & Trojan, M. (2007). Synthesis and characterization of newberyite. *Journal of Thermal Analysis and Calorimetry*, 88, 103-106.

Mestres, G., & Ginebra, M. P. (2011). Novel magnesium phosphate cements with high early strength and antibacterial properties. *Acta Biomaterialia*, 7, 1853-1861.

Palacios, E., Leret, P., María, J., Fernández, J. F., Antonio, H., & Rodríguez, M. A. (2013). Influence of the pH and ageing time on the acid aluminum phosphate synthesized by precipitation. *CrystEngComm*, 15, 3359-3365.

Prado-Herrero, P., Garcia-Guinea, J., Crespo-Feo, E., & Correcher, V. (2010). Temperature-induced transformation of metavariscite to berlinite. *Phase Transitions*, 83, 440-449.

Shih, Y. J., Abarca, R. R. M., de Luna, M. D. G., Huang, Y. H., & Lu, M. C. (2017). Recovery of phosphorus from synthetic wastewaters by struvite crystallization in a fluidized-bed reactor: Effects of pH, phosphate concentration and coexisting ions. *Chemosphere*, 173, 466-473.

Su, C. C., Dulfo, L. D., Dalida, M. L. P., & Lu, M. C. (2014). Magnesium phosphate crystallization in a fluidized-bed reactor: effects of pH, Mg: P molar ratio and seed. *Separation and Purification Technology*, 125, 90-96.

Takagi, S., Mathew, M., Brown, W. E. (1986). Crystal structures of bobierrite and synthetic $Mg_3(PO_4)_2 \cdot 8H_2O$. *American Mineralogist*, 71, 1229-1233.

Tamimi, F., Sheikh, Z., & Barralet, J. (2012). Dicalcium phosphate cements: brushite and monetite. *Acta Biomaterialia*, 8, 474-487.

Wagh, A. S. (2016). Chemically bonded phosphate ceramics. Chapter 4, Elsevier Science.

Wang, Y. S., & Dai, J. G. (2017). Use of magnesia sand for optimal design of high performance magnesium potassium phosphate cement mortar. *Construction and Building Materials*, 153, 385-392.

Wang, Y. S., Dai, J. G., Wang, L., Tsang, D. C., & Poon, C. S. (2018). Influence of lead on stabilization/solidification by ordinary Portland cement and magnesium phosphate cement. *Chemosphere*, 190, 90-96.

Wilson, A. D. & Nicholson, J. W. (2005) Acid-base cements: their biomedical and industrial applications. Cambridge University Press.

Xu, B., Lothenbach, B., Leemann, A., & Winnefeld, F. (2018). Reaction mechanism of magnesium potassium phosphate cement with high magnesium-to-phosphate ratio. *Cement and Concrete Research*, 108, 140-151.

Zhang, J., Liu, W., Schnitzler, V., Tancret, F., & Bouler, J. M. (2014). Calcium phosphate cements for bone substitution: chemistry, handling and mechanical properties. *Acta Biomaterialia*, 10, 1035-1049.

This page is intentionally left blank

CHAPTER 7 SILICO-ALUMINOPHOSPHATE GEOPOLYMER IMPROVED BY COAL FLY ASH

The synthesis of alkali-aluminosilicate geopolymer using high calcium coal fly ash (CFA) at ambient temperature was marked as a great challenge. In this chapter, partial replacement of aluminosilicate precursor by high-calcium CFA can seed the calcium source into silico-aluminophosphate geopolymer, which enhances the properties of the geopolymer due to the physical and chemical actions of CFA particles. Introducing such CFAs physically improves the workability of the fresh silico-aluminophosphate geopolymer cement. In the meantime, acid-base or/and hydrolysis reaction between the alkaline calcium species in CFA and the acidic phosphate species in the activator is also induced. This chemical process produces calcium phosphate compounds, e.g., brushite and monetite. Since the acid-base or/and hydrolysis reaction is generally fast, the silico-aluminophosphate geopolymer can achieve good setting time and early mechanical performance when the high-calcium CFA is blended with aluminosilicate precursors. This study validates the proposed effects of the CFA in silico-aluminophosphate geopolymer paste.

7.1 Introduction

One of the major aluminosilicate precursors for preparing geopolymer cement is the coal fly ash (CFA), which is a largely available byproduct of coal combustion in thermal power plants. However, the upstream raw materials (e.g., coal type), quenching process (e.g., combustion temperature) and place of origin (e.g., local temperature and moisture) usually generate CFA sources with inherent heterogeneity and variance (Yao et al., 2015). Thus, the chemical and physical complexities of the CFA discourage the CFA-based geopolymer cement in in-situ engineering applications, as the performance of the geopolymer product is hardly predictable and designable.

The CFA produced by pulverized coal combustion (PCC) technology usually has high pozzolanic activity and alkali activation reactivity (Fernández-Jiménez and Palomo, 2003), which is suitable for Portland cement replacement (as supplementary cementitious material) and geopolymer cement preparation (as host material). The high calorific value coal (e.g., bitumite and anthracite) used in PPC-equipped power plant can generate high temperatures (1300-1700 ℃), which facilitates the yielding of spherical CFA particles with high content of glassy or vitreous aluminosilicate phases and low content of impurities (e.g., calcium and sulfur) (Seames, 2003; Chindaprasirt and Rattanasak, 2010). Such low-calcium CFA, i.e., Class F type according to ASTM C618, is most widely used in geopolymer synthesis (Duxson and Provis, 2008). However, the use of lignite-mixed bitumite or anthracite in the non-peak period of power consumption also produces such types of CFA with high calcium content (Ma et al., 2016).

On the other hand, circulating fluidized bed combustion (CFBC) unit can digest low-grade fuels (e.g., lignite or subbituminous coal) at a combustion temperature of 800-900 ℃ while still meeting strict air emission requirements (Basu, 1999). CFBC is an advanced coal-combustion technology for high-efficiency energy utilization, which is considered green and clean from the view of gas and dust emission reduction. Therefore, this technology is being widely popularized all over the world. During this combustion process, the desulfurizer (e.g., lime) is usually mixed with the coal in order to reduce sulfide discharge (Srivastava et al., 2004). Thus, such CFA particles contain high contents of calcium and sulfur compounds, which requires some treatments and modifications before use in construction, in order to avoid premature distress in concrete (Hulett and Weinberger, 1980; Slavik et al., 2008; Chindaprasirt, 2010). Numerous studies have revealed that in alkaline environment the sulfur contained in CFBC-produced CFA easily reacts with the activated calcium and alumina in cement to form anhydrites and delayed ettringite crystals (Taylor et al, 2001), whose apparent solid volume expands by around 62% and 125%, respectively. Regarding the delayed formation and growth of needle-like ettringite (Eq. 7.1), the hardened matrix is substantially imposed on internal stresses, resulting in localized cracking, swelling, and even integral failure (Chindaprasirt et al., 2013). The chemical unsoundness may deteriorate the Portland cement (Collepardi, 2003; Kunther et al., 2015) and alkali-activated cement (Chindaprasirt et al., 2014) products when this type of CFA is used.

$$6Ca^{2+} + Al(OH)_4^- + 4OH^- + 3SO_4^{2-} + 26H_2O \rightarrow Ca_6[Al(OH)_6]_2 \cdot (SO_4)_2 \cdot 26H_2O \quad (7.1)$$

Besides, generating equal electricity capacity in coal-fired power station, the amount of CFBC-produced CFA double outnumbers that produced by PCC technology (Chindaprasirt and Rattanasak, 2010). In Hong Kong, for example, the output of CFA is 0.7 million tons per year (Sustainable Development Report, 2013). Around 25% of them (usually contains low calcium source) are classified as direct use in concrete production according to BS3892: Part1: 1997, while the unqualified CFAs (around 75%) need to be further modified by a local cement production industry before use. The reasonable utilization of high-calcium CFA to be a valued resource becomes a serious issue to address.

This chapter proposes to use the high-calcium CFA in silico-aluminophosphate geopolymer. The fresh silico-aluminophosphate geopolymer paste is initiated from the mixing of an acidic phosphate activator (e.g., pH < 2.0) with an aluminosilicate precursor (e.g., metakaolin) to yield isolated aluminate and silicate units through a dealumination reaction of aluminosilicate precursor. The polycondensation of the free-state aluminate, silicate, and phosphate groups facilitates the generation of silico-aluminophosphate geopolymer, where the silicate-aluminate-phosphate gels as the main binding phases are interlinked by Si-O-Al bonds, Al-O-P bonds and/or Si-O-P bonds. Here, partial replacement of aluminosilicate precursor using high-calcium CFA can seed the calcium source in silico-aluminophosphate geopolymer. Possible physical and chemical actions of these CFA particles are described as below:

1) The spherical CFA particles are usually entitled as rheological agents in Portland cement (Erdoğdu and Türker, 1998) and alkali-aluminosilicate geopolymer cement (Rashad, 2014) due to the ball-bearing effect. Introducing such CFAs may physically improve the workability of the fresh silico-aluminophosphate geopolymer cement.
2) An acid-base or/and hydrolysis reaction between the calcium species in CFA and the phosphate species in activator may be also induced. This chemical process is similar to the formation of calcium phosphate cement (CPC), which is widely used for bone substitution and dental restoration in biomedical engineering (Zhang et al., 2014; Zhang et al., 2016). The chemical process between the calcium and phosphate takes place through entanglement of the crystalline calcium phosphate, such as brushite (dicalcium phosphate dihydrate [DCPD], $CaHPO_4 \cdot 2H_2O$), apatite (e.g., $Ca_5(PO_4)_3OH$, hydroxyapatite [HA]) and/or β-tricalcium phosphate (β-TCP, $\beta\text{-}Ca_3(PO_4)_2$). The fast acid-base or/and hydrolysis reaction easily fabricates a CFA-blended 'hybrid' silico-aluminophosphate geopolymer with rapid setting time and mechanical strength development.

The experimental program in this sub-study is designed to validate the proposed effects of the high-calcium CFA in silico-aluminophosphate geopolymer paste. The setting times, workability, and compressive strength of the silico-aluminophosphate geopolymer influenced by high-calcium CFA are investigated. The high-calcium CFA chemistry and phosphate activation are discussed, covering the aluminosilicate and phosphate reaction kinetics and calcium-containing products evolution.

7.2 Experimental Program

7.2.1 Raw materials

The aluminosilicate precursor used for silico-aluminophosphate geopolymer preparation is metakaolin (MK). Two types of CFAs are used as calcium donor and partial replacement of aluminosilicate precursor. The low-calcium series CFA (donated as LCFA) is defined as directly-used ash in concrete production in accordance to BS3892: Part1: 1997. The high-calcium series CFA (donated as HCFA) is reprocessed in Green Island Cement Co. Ltd. The chemical compositions (as oxides), bulk density, loss on ignition (LOI) and granularity information (average particle size and D_{50} particle size) of the three solid powders are displayed in Table 3.1 (Chapter 3).

The phosphate activator was pre-prepared solution formulated using the powdered aluminum hydroxide and the liquid orthophosphoric acid through hydrothermal reaction, as described in Chapter 3. The final phosphate activator has a P/Al molar ratio of 5.0, a mass concentration of 53.4 % and a pH value of 1.83. The final solution was cooled down to room temperature before use. The deionized water was used throughout.

7.2.2 Experimental design

Seven series of silico-aluminophosphate geopolymer pastes were formulated using the phosphate activator and the MK. The MK was replaced by two types of CFA (low-calcium and high calcium series) with different contents, referred to as C, L10, L20, L30, H10, H20 and H30, respectively. The water-to-solid (*w/s*) of all the geopolymer pastes was kept as 0.35. Their mix proportions are summarized in Table 7.1. The high-calcium CFA-blended geopolymers (i.e., H10, H20 and H30) have theoretical calcium/phosphorus (Ca/P) molar ratios of 1.17, 2.34 and 3.51 are used for geopolymer preparation, while low-calcium CFA-blended geopolymers (i.e., L10, L20 and L30) have lower Ca/P molar ratios equal to 0.46, 0.92 and 1.38.

As specified recipe, the silico-aluminophosphate geopolymer pastes were prepared by homogenizing the MK, CFA and phosphate activator by a mechanical mini-mixer. Before adding phosphate activator, an intensive mixing for 10 min was performed on the MK and CFA powders. The fresh pastes were cast into 50 mm plastic cubic molds and compacted using mechanical vibration table. After being demolded at 1 day, the hardened pastes were cured in a water tank with a constant temperature of 25 ℃ for further analysis at specified periods.

Table 7.1 Mix proportions of the silico-aluminophosphate geopolymer pastes blended with two types of CFAs. The solid aluminosilicate precursors and phosphate activator are in weight ratio

Serial number		Aluminosilicate precursor			Phosphate Activator	Geopolymer paste Ca/P molar ratio
		MK	LCFA	HCFA		
C	Control	10	-	-	7.5	0
L10	10% replacement	9	1	-	7.5	0.46
L20	20% replacement	8	2	-	7.5	0.92
L30	30% replacement	7	3	-	7.5	1.38
H10	10% replacement	9	-	1	7.5	1.17
H20	20% replacement	8	-	2	7.5	2.34
H30	30% replacement	7	-	3	7.5	3.51

Table 7.2 CFA/OPA suspension liquids for phosphate activation test

No.	Suspension liquid (wt. ratio)				Initial pH	1 day pH	28 day pH	Theoretical molar ratio		
	OPA	LCFA	HCFA	Water				Ca/P	Si/P	Al/P
LCFAP	1	10	-	50	1.64	1.71	1.75	1.1	8.5	7.1
HCFAP	1	-	10	50	1.65	1.89	1.95	3.4	7.3	6.0

For better understanding of the CFA chemistry in acidic phosphate environment, CFA/OPA suspension liquids were prepared as tabulated in Table 7.2, with a Ca/P ratio of 1.1 for low-calcium CFA series, and a ratio of 3.4 for high-calcium CFA series. The interaction between two types of CFAs (e.g., calcium and aluminosilicate species) and phosphate was studied by analyzing the corresponding residues after 28 day reactions. The resulting sediments are treated twice by centrifugal separation and deionized water washing.

7.2.3 Testing procedures

1) Fluidity was measured using a mini-cone slump flow test setup in accordance with ASTM C1437-15. The top diameter, bottom diameter and height of the truncated conical mold are 70, 100 and 50 mm, respectively. All the slump tests of the fresh geopolymer pastes were conducted after 2 min of mechanical mixing. Three spread diameters on a glass plate were measured, and the average value was recorded as the final spread diameter for comparison.
2) Initial and final setting times of the geopolymer pastes were determined using a Vicat needle in compliance with ASTM C191-13.
3) Compressive strength of the 50 mm geopolymer paste cubes was measured at 1, 3, and 28 day using mechanical testing instrument (Testometric CXM 500-50 kN). The loading rate was set as 0.6 MPa/s complying with ASTM C109/C109M-16a for load application.

7.2.4 Analytical methods

1) XRD analysis of the hardened geopolymer pastes and sediments in phosphate activation test was carried out by a high-resolution X-ray diffractometer. The measurement was conducted under a 9 kW Cu-Kα radiation source (λ=1.5406 Å), ranging from 5 to 65° (2θ) with a step size of 0.02 °and a count time of 5 s/step.
2) Simultaneous thermal analysis was performed from 30 to 1100℃ under an argon atmosphere with a heating rate of 10 ℃/min. The thermal decomposition and phase transition behaviors of the hardened geopolymer

pastes were analyzed through the mass change over times as the temperature changes.

3) Microstructure features and element compositions were characterized by backscattered electron (BSE) imaging and EDXS analysis. The applied acceleration voltage is 20 kV and the working distance ranges between 10 and 20 mm for higher quality images. After 48 h freeze drying, the geopolymer samples were solidified into transparent epoxy resin, which creates a typical surface treated with carbon sputtering for element mapping. The residual sediments after phosphate activation procedure are sputtered with gold for microscopic measurement.
4) All the MAS-NMR spectra were acquired on a Bruker AVANCE III 400 WB spectrometer (9.4 T) at 297 K. The dried and finely powdered samples were packed in 4 mm zirconia rotors for measurement. For ^{27}Al, X channel was tuned to 104.3 MHz, with a spinning speed of 12 kHz and a pulse duration of 0.9 μs. A total of 2000 scans were recorded with 2s recycle delay for each sample. ^{31}P spectrum was conducted at 161.9 MHz, with a spinning speed of 12 kHz. The ^{31}P NMR measurement was conducted at a contact time of 2 ms. A total of 1000 scans were recorded with 5 s recycle delay for each sample. Chemical shifts of ^{27}Al and ^{31}P are benchmarked by the resonances of aluminum chloride solution (1.0 mol/L) and monoammonium phosphate solution (1.0 mol/L), respectively.

7.3 Results and Discussion

7.3.1 Macroscopic fluidity of CFA-blended geopolymer paste

The macroscopic fluidity is an important index to assess the workability of geopolymer paste. Figure 7.1 shows the flow diameters of the geopolymers spread on a glass plate using a mini-cone slump flow test setup, where the fresh geopolymer pastes with different types and contents of CFA at a fixed *w/s* ratio of 0.35 are compared. The incorporation of low-calcium CFA from 10% to 30% contents (i.e., L10, L20 and L30) resulted in the geopolymers with higher workability relative to the control and high-calcium CFA-blended silico-aluminophosphate geopolymers. The low-calcium CFA particles usually present a spherical shape (Fig. 7.2a) with an average diameter size of 8.58μm (see Table 3.1 in Chapter 3), which may exhibit a ball-bearing effect on the fresh geopolymer pastes. 20% replacement of aluminosilicate precursor substituted by low calcium CFA (i.e., L20 geopolymer) can achieve around 5 cm increment of the flow diameter (increasing 24%) compared to the control group (i.e., net silico-aluminophosphate geopolymer). As a comparison, the high-calcium CFA geopolymer series (i.e., H10, H20 and H30) behaved slightly poorer than the geopolymers with low-calcium CFA, but hold higher levels to the control geopolymer (i.e., C).

Dividing the flowing process into two stage (i.e., 0-15s and 16-60s) can specify this phenomenon, caused by physical action (i.e., yield stress control) and chemical action (i.e., viscous control), respectively. The fluidity between 0 and 15s mainly depends on the physical ball rolling. The 15 s flows of all CFA-blended geopolymers (except H30) outperformed that of the control group, which indicates the good physical effect of CFA on the workability of the silico-aluminophosphate geopolymer. The relatively larger flow diameter of low-calcium CFA-blended geopolymers compared to that of geopolymers with high-calcium CFA may be due to some irregular particles contained in the high-calcium CFAs, as shown in in Fig. 7.2b, which weakens the physical lubrication effect in high-calcium CFA-blended geopolymer pastes.

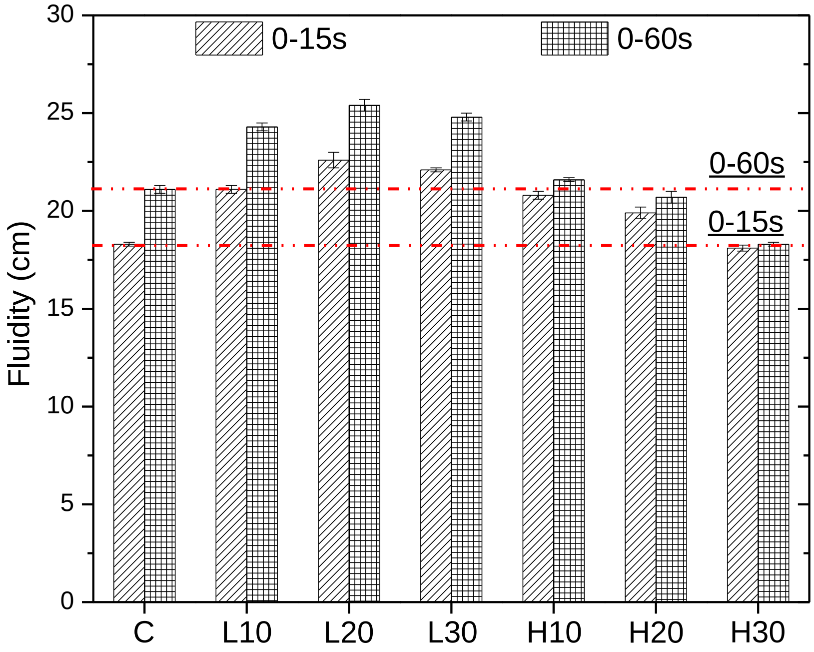

Fig. 7.1 Flows of the silico-aluminophosphate geopolymer with different types and contents of CFA in terms of their diameters spread on a glass plate by a mini-cone slump flow test setup. The results at 15 and 60s are recorded, respectively.

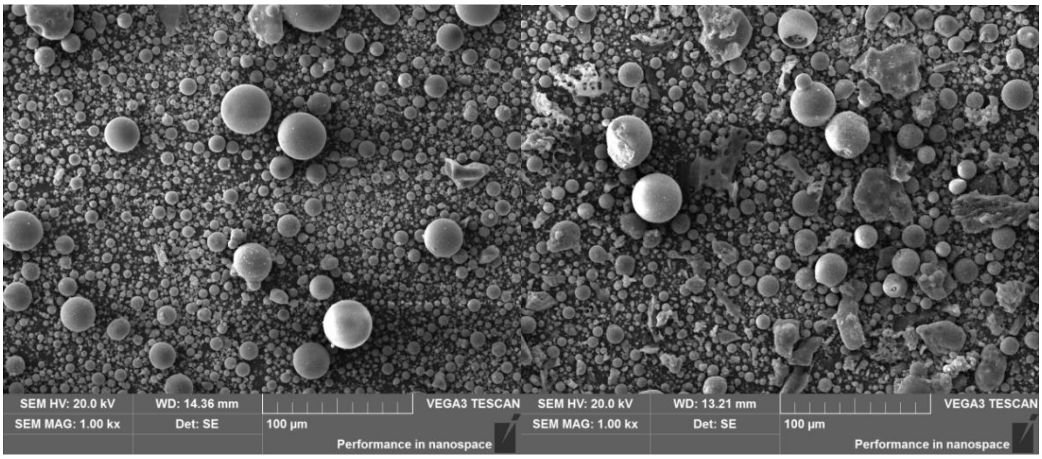

(a) Low-calcium CFA particle (b) High-calcium CFA particle

Fig. 7.2 Microscopic images (×1000) of Low-calcium and high-calcium CFA particles

On the other hand, the active calcium species in high-calcium CFA (alkali metals) may chemically agglutinate with the phosphate activator (acidic solution) through acid-base or hydrolysis reactions, which may influence the workability of the high-calcium CFA-blended geopolymers. Therefore, their flow diameters from 15 to 60s all present marginal increase (no more than 1cm), while the flow diameters of other groups (i.e., C, L10, L20 and L30) all extend by approximately 5 cm during that period. These results indicate that the partial replacement of CFA particles can physically improve the macroscopic fluidity of the silico-aluminophosphate geopolymers. Chemical actions between calcium and phosphate species may partially take the edge off their workability in later period.

7.3.2 Setting time of CFA-blended geopolymer paste

Figure 7.3 plots the initial and final setting times of the silico-aluminophosphate geopolymers influenced by the different types and contents of CFA. Before initial setting, the phosphate activating solution and CFA-blended aluminosilicate precursors form homogenous slurries, where the increasing concentrations of oligomers lead to the initial setting of the fresh geopolymers. In control group, the initial setting of the geopolymer pastes stemmed from the free aluminum species (either dealumination of aluminosilicate precursors or aluminum donor in phosphate activators) combining with phosphate to form an aluminophosphate gel (more explanations in Chapter 4)(Benavent et al., 2016). However, introducting calcium species (e.g., CFA in this study) can substantially speed up this process because of the fast reaction between active calcium in aluminosilicate precursor and acidic phosphate species in activators. Thus, the geopolymers incorporated with high-calcium CFAs, especially higher contents (e.g., H20 and H30 geopolymers with initial setting times of 46 and 18 min, respectively), show very short initial setting times compared to the low-calcium CFA-blended and net geopolymers, whose initial setting times range from 156 to 192 min.

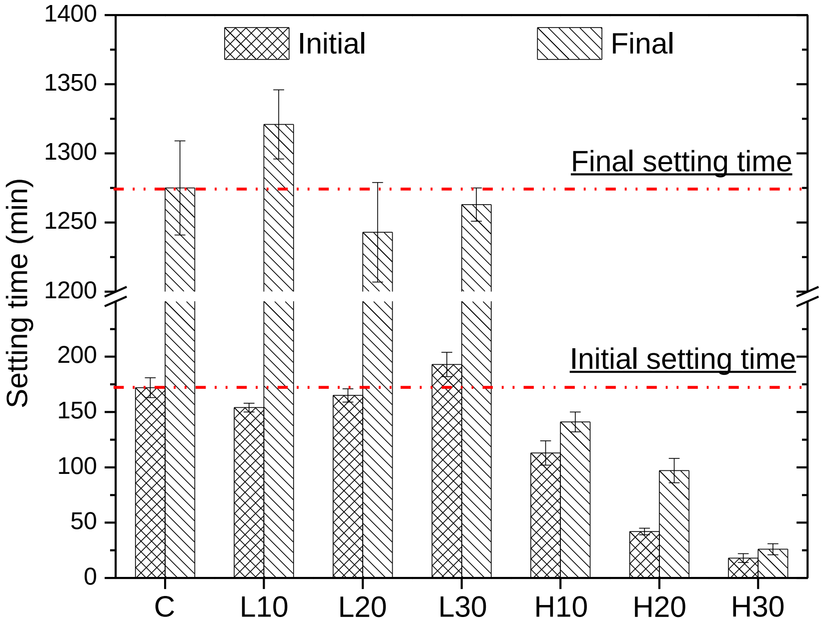

Fig. 7.3 Initial and final setting time of the silico-aluminophosphate geopolymer with different types and contents of CFA

The generation and growth of the formed oligomers contribute to the final setting time of the fresh geopolymers and strength development as a function of curing time. The nucleation of calcium phosphate enhances the initial mechanical strength of the calcium-containing geopolymers in a short period of time. The final setting times of the high-calcium CFA-blended silico-aluminophosphate geopolymer were 141, 101 and 29 min for H10, H20 and H30, respectively. On the contrary, the low-calcium CFA-blended and control geopolymers have longer final setting time at around 21 hour. The low-calcium CFA as a low reactive aluminosilicate precursor retards the dealumination reaction during hardening process of the geopolymer (e.g., L10), while adding higher volume low-calcium CFA can introduce some calcium species that marginally promote setting of the geopolymer (e.g., L20 and L30).

7.3.3 Compressive strength development of CFA-blended geopolymer paste

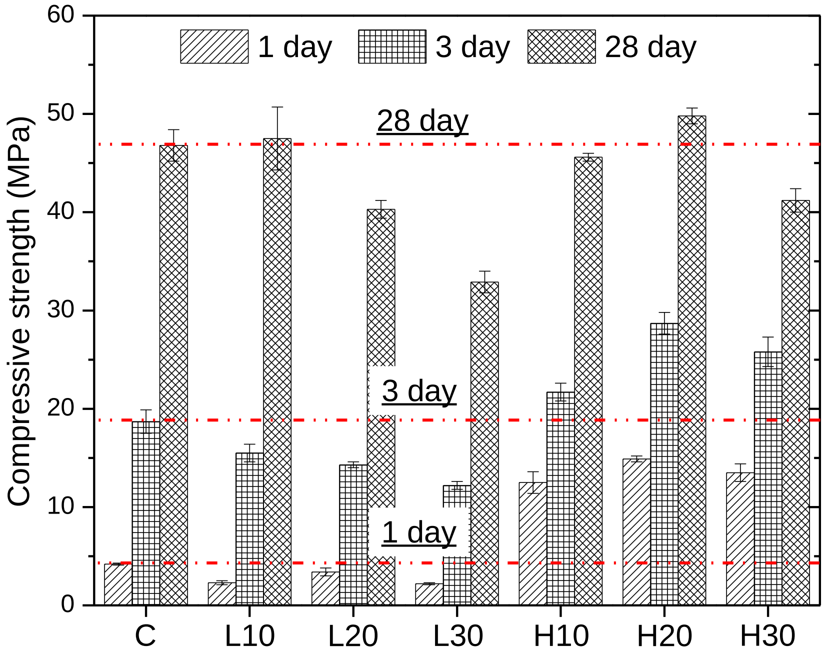

Fig. 7.4 Compressive strength of the CFA-blended silico-aluminophosphate geopolymer cubes as a function of curing time (1, 3 and 28 day) and CFA type (low-calcium and high-calcium). Net silico-aluminophosphate geopolymer cube as a reference is attached.

The compressive strength development (1, 3 and 28 day curing) and comparison (CFA type and contents) of the CFA-blended silico-aluminophosphate geopolymers are displayed in Fig. 7.4. Gradual geopolymerization and/or acid-base/hydrolysis reaction increases the compressive strength of all geopolymers as a function of curing time. Since high content of calcium introduced by CFA facilitates the reaction with phosphate species (e.g., $H_2PO_4^-$, HPO_4^{2-} and PO_4^{3-}) and the formation of calcium phosphate compounds, the high-calcium CFA-blended silico-aluminophosphate geopolymers achieve higher strength at the curing age of 1 day (13-15 MPa). However, at this curing time the counterparts (e.g., low-calcium CFA-blended and net geopolymers) hold poor early strength, vacillating at 3-5 MPa only. After 3 day curing, the high-calcium CFA-blended geopolymer obtains 9-14 MPa augmentation. The 3 day strength of H20 geopolymer was 29 MPa, which was higher than that of the control geopolymer (18.5 MPa at 3 day) and the low calcium-containing geopolymers

(12-15.5 MPa). At 28 day, the compressive strength of geopolymers were all observed to have 42-47 MPa in addition to that of L20 and L30 geopolymers. The H20 geopolymer obtained the highest 28 day strength (around 51 MPa). Such relatively high strength observed in high-calcium CFA-blended geopolymers could not only be attributed to the calcium phosphate formation as stated above, but also be due to the angular particles in high-calcium CFAs (Fig. 7.2b), which is expected to mechanically interlock with the geopolymer matrix much better than the spherical low-calcium CFAs (Fig. 7.2a). Besides, it is found that the incorporation of low-calcium CFA adversely affects the strength development in silico-aluminophosphate geopolymer, i.e., higher replacement amount means lower strength behavior. This could be caused by the relatively low reactivity of aluminosilicate phase in CFAs compared to the MK, which slowed down (or dilute) the geopolymerization or gel formation (e.g., dealumination reaction).

7.3.4 Crystalline phase of CFA-blended geopolymer paste

The X-ray diffraction (XRD) patterns of the CFA-blended geopolymers, control geopolymer and raw aluminosilicate precursors, are shown in Fig. 7.5. The only distinct peak in XRD patterns of MK and control geopolymer appears at 26.5 ° (2θ) assigned to the quartz (JCPDS No. 11-0795), while no new crystalline phase in control geopolymer is generated after 28 day curing. The geopolymerization of aluminosilicates activated by phosphate involves the dissolution and reconstruction of silicates, aluminates and phosphates to form disordered silicophosphate (S-P), aluminophosphate (A-P) and/or silicate-aluminate-phosphate (S-A-P) gels, which are usually amorphous phases (Douiri et al., 2014).

In Fig. 7.5a, the mullite (JCPDS No. 15-0776) and quartz were detected in the geopolymers containing low-calcium species (i.e., L10, L20 and L30), which are both inert phases formed during production and collection of the low-calcium CFA. One modest peak assigned to brushite (JCPDS No. 72-0713) was identified in L30 geopolymer only. The slight calcium (5.3% as calcium oxide in Table 3.1, Chapter 3) measured by X-ray fluorescence provides some calcium sources for brushite formation. The stoichiometric Ca/P ratio of brushite ($CaHPO_4 \cdot H_2O$) is 1.0, thus L10 and L20 geopolymers with the respective Ca/P ratios of 0.46 and 0.92 are unlikely to generate brushite.

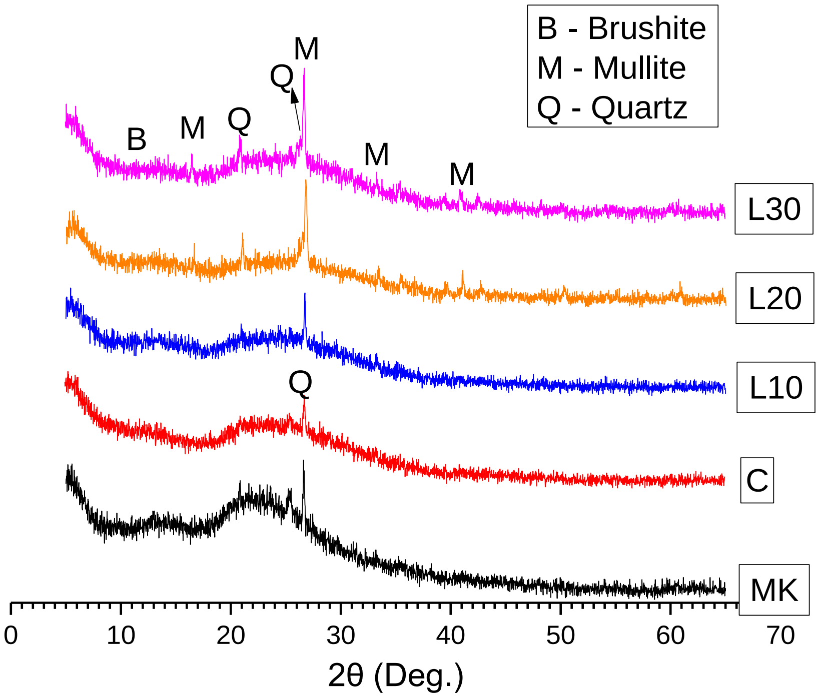

(a) low-calcium CFA-blended geopolymers

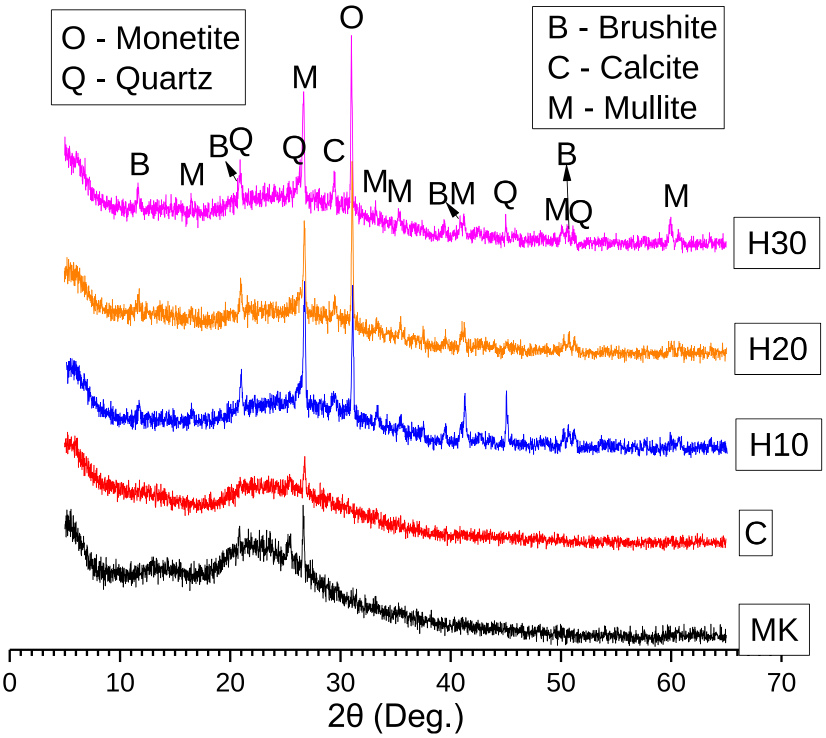

(b) high-calcium CFA-blended geopolymers

Fig. 7.5 X-ray diffractograms of the CFA-blended silico-aluminophosphate geopolymers after 28 day curing. The MK and control geopolymer (i.e., C) as references are attached.

As shown in Fig. 7.5b, the traces of mullite and quartz were also identified in high-calcium CFA-blend geopolymers, as these well-crystallized phases are chemically inert and hardly react with phosphate activators. Contrarily, the characteristic reflections of brushite and monetite (JCPDS No. 70-1425) were observed in all high-calcium CFA-blend geopolymers regardless the contents of CFA. This suggests that the calcium species of such CFA in silico-aluminophosphate geopolymer have formed brushite and monetite. Further, the formation of these crystalline calcium phosphates in the early stage accelerates the fresh high-calcium CFA geopolymer hardening, which is reflected in fast setting times observed (Fig. 7.3). Besides, some weak peaks referring to residual calcite (JCPDS No. 05-0586) in high-calcium CFA-blend geopolymers indicates that the calcium source in this CFA exists in calcite forms.

7.3.5 Thermogravimetric analysis of CFA-blended geopolymer paste

The weight loss and heat flow of the 28 day cured geopolymers as a function of temperature are shown in Fig. 7.6. In the temperature range of 40-500℃, the characteristic weight losses of all the geopolymer during heating are presented as results of two dehydration reactions. The lower temperature at 90-110 ℃ exhibits a primary weight loss, which is accompanied by an endothermic peak in heat flow curves as the result of evaporation of physically-bound water. The other marginal dehydration reaction, located at round 200 ℃, is only observed in high-calcium CFA groups (Fig. 7.6b), which can be attributed to dehydration of chemically-bound water in brushite, as detected in XRD patterns (Fig. 7.5b). In the meantime the brushite (JCPDS No. 72-0713) is transformed to monetite (JCPDS No. 70-1425) due to the removal of crystal water (in Eq. 7.2). A weak endothermic peak at 200℃ states this chemical change, although the weight loss caused by dehydration of brushite is not easily found. Since incorporation of low-calcium CFA cannot provide sufficient active calcium species in geopolymer, there is no weight and heat flow change during 180-220℃.

$$CaHP0_4 \cdot 2H_2O\ (Brushite) \xrightarrow{180-220℃} CaHPO_4(Monetite) + 2H_2O \qquad (7.2)$$

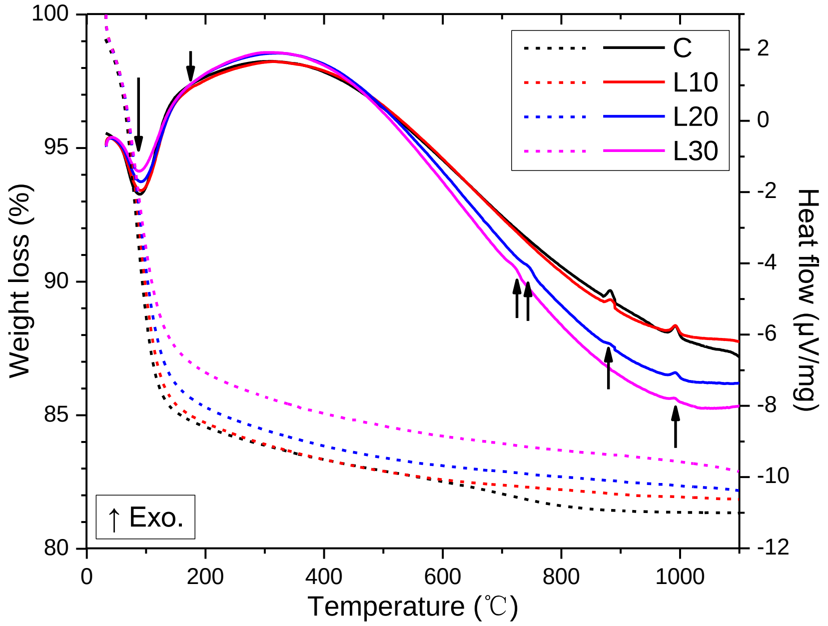

(a) low-calcium CFA-blended geopolymers

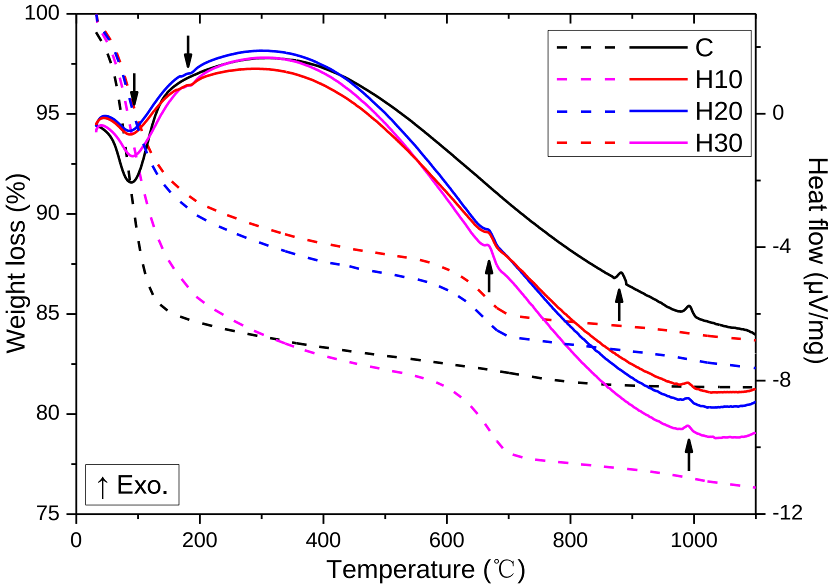

(b) high-calcium CFA-blended geopolymers

Fig. 7.6 Weight loss and heat flow curves of the CFA-blended silico-aluminophosphate geopolymers after 28 day curing

The following heating from 501-1100 °C usually changes the molecular structure of geopolymers through dehydroxylation or phase transition. In low-calcium geopolymers (Fig. 7.6a), three marginal endothermic peaks are observed at 740, 870 and 980 °C, but no favorable mass change is detected. The first change at

740 °C is observed in L20 and L30 geopolymers instead of L10 and C geopolymers, which can be ascribed to the dehydroxylation of monetite (Eq. 7.3), converting into calcium pyrophosphate ($Ca_2P_2O_7$) (Wikholm et al., 1975). The Ca/P ratios in L20 and L30 geopolymers (0.92 and 1.38, respectively) provide the possibility to generate slight monetite, although their XRD patterns (Fig. 7.5a) barely support that. The transformation of amorphous aluminum phosphate phase into crystal trigonal (α-$AlPO_4$) and tetragonal (β-$AlPO_4$) berlinite at around 870 °C (Prado-Herrero et al., 2010), in addition to the dehydroxylation of the MK at 980 °C (White et al., 2010) are main features, which are already reported in Chapter 5.

$$2CaHP0_4 \xrightarrow{600-750℃} Ca_2P_2O_7 + H_2O \tag{7.3}$$

In high-calcium geopolymers (Fig. 7.6b), the endothermic peak of dehydroxylation of monetite (Eq. 7.3) is more intensive, and clear weight losses are detected. This is attributed to the high contents of active calcium in geopolymers (i.e., H10, H20 and H30) which generate more brushite and monetite, thus more phosphate activators are consumed by these calcium species during geopolymerization process. Therefore, the transformation of amorphous aluminum phosphate phase into crystal trigonal (α-$AlPO_4$) and tetragonal (β-$AlPO_4$) berlinite at around 870 °C is barely observed in all high-calcium geopolymers. Due to the same reason, the heat flow of L30 geopolymer has similar trend at around 870 °C (Fig. 7.6a).

7.3.6 Backscattered electron image and elemental mapping of CFA-blended geopolymer paste

The backscattered electron images and elemental mapping results of the high-calcium CFA-blended silico-aluminophosphate geopolymers (H30) after 28 day curing over selected area are shown in Fig. 7.7. It is clearly found that the

CFA particles are embraced by the formed gels in geopolymers. Further, the CFA particles with different chemical reactivity are demonstrated.

A typical section containing a CFA particle with marginal calcium species is shown in Fig. 7.7a, where the CFA particle acts as a fine ‘aggregate’ cemented by the binding phase. The elemental mapping results indicate a homogeneous distribution of Ca, with rare points, throughout the selected area. The CFA particle is rich in Si and Al, while the absence of P reveals that the phosphate activator does not chemically incorporate into the inert aluminosilicate phase in CFA. The bind phase area consists of Al, Si and P, which is in consistent with previous research on silico-aluminophosphate geopolymer. This could be due to the phosphate activator and the aluminosilicate precursor which can form the S-A-P gels to support the geopolymer matrix.

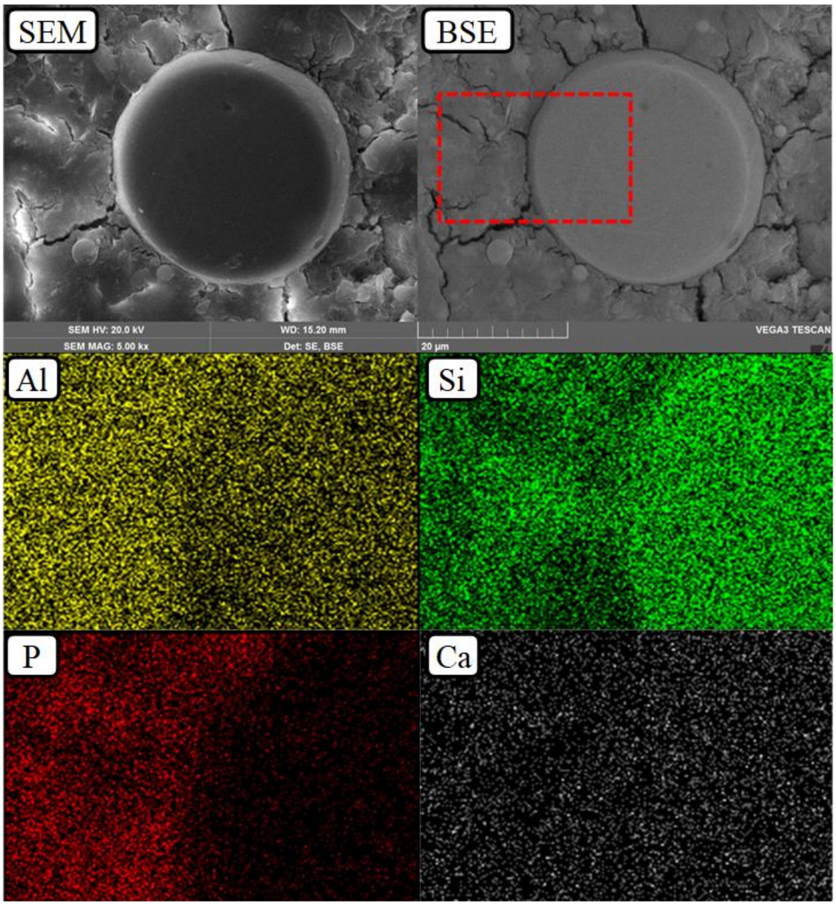

(a) inner high-calcium CFA in geopolymer

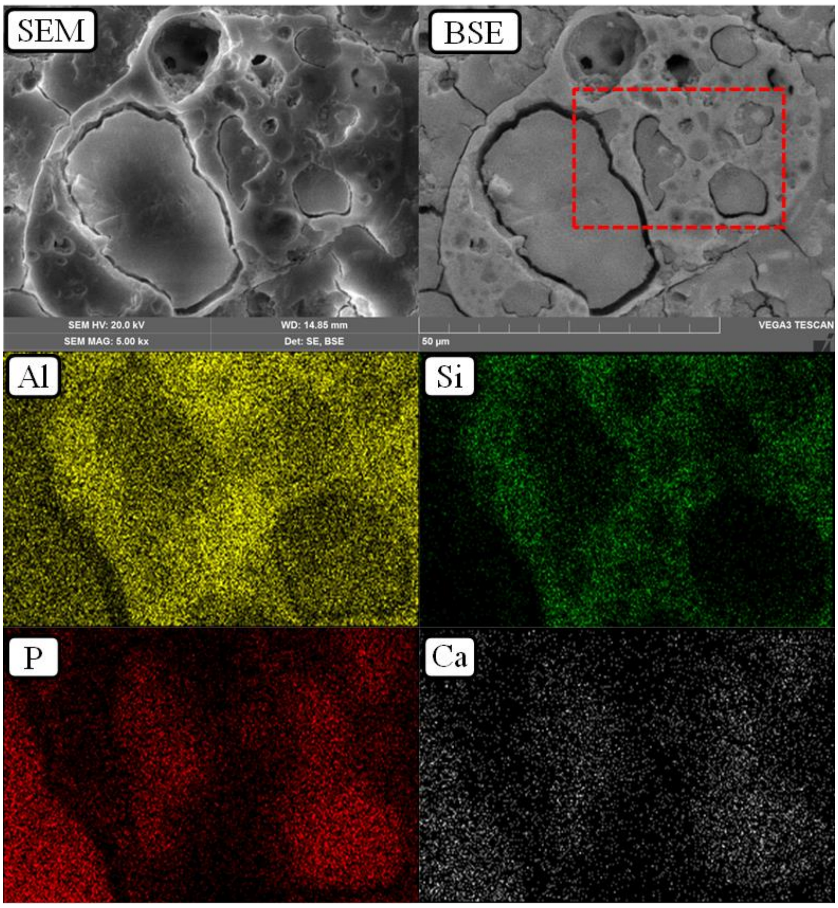

(b) active high-calcium CFA in geopolymer

Fig. 7.7 Typical backscattered electron images and elemental mapping results of the high-calcium CFA-blended silico-aluminophosphate geopolymers after 28 day curing

The CFA particle containing high-content calcium behaves with relateively chemical sensitivity to the phosphate activators. Fig. 7.7b demonstrates the interaction results of calcium and phosphate species in geopolymer containing high-calcium CFA. The same elemental distribution of Ca and P points out the strong evidence that the dissolution of high-calcium CFA due to the reaction between calcium and phosphate has occurred. It was hypothesized that any free Ca in the CFAs could preferentially react with phosphate species to form calcium phosphate phases while co-existing with the S-A-P gels in silico-aluminophosphate geopolymer matrix. The CFA dissolution and subsequent reactions to form the calcium phosphates can explain the improved early strength in high-calcium CFA-blended geopolymers. The rapidly-formed binding phase (e.g., brushite and monetite detected by XRD, Fig. 7.5b) results in a ‘hybrid’ geopolymer with fast setting time and high early strength. The chemical combining capacity of Ca and P has previously been applied in numerous fields, such as the sorbent for phosphate removal or extraction from P-rich wastewater (Agyei et al., 2002) and the formation of calcium phosphate cement for biomedical engineering (Ambard and Mueninghoff, 2006). Besides, the combination of Al and P is also detected in Fig. 7.7b, which indicates the formation of aluminophosphate phase in high-calcium CFA particle.

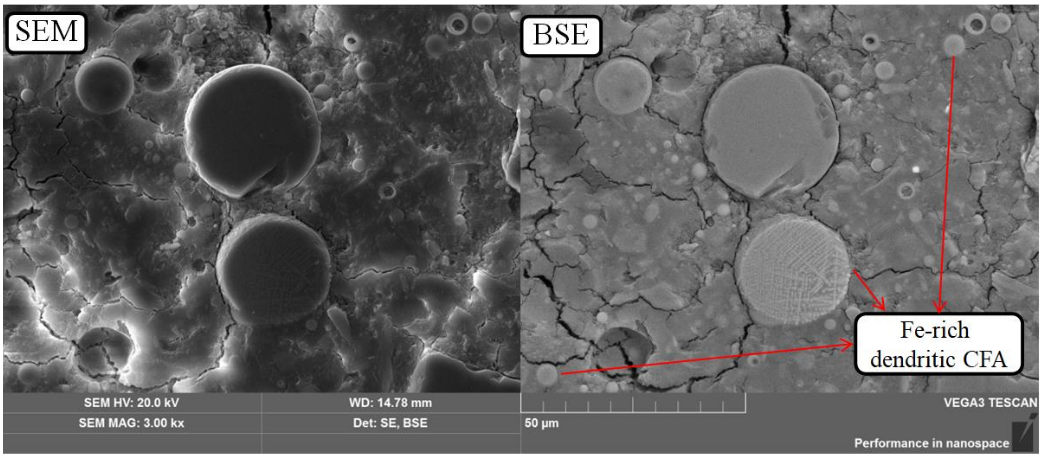

(a) active aluminosilicate phase in low-calcium CFA

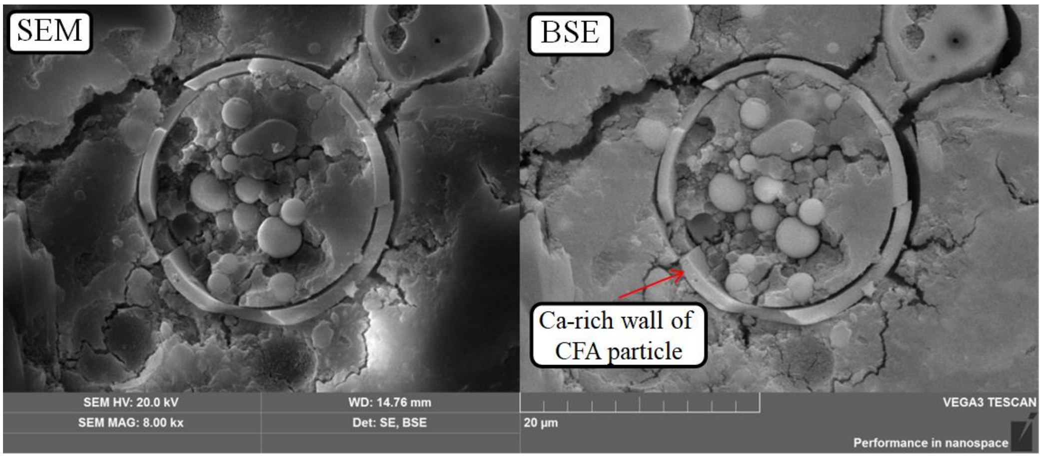

(b) active aluminosilicate phase in low-calcium CFA

Fig. 7.8 Typical backscattered electron images of the low-calcium CFA-blended silico-aluminophosphate geopolymers after 28 day curing

In low-calcium CFA-blended geopolymer, the CFAs mainly donate aluminosilicate phase, thus its chemistry in silico-aluminophosphate geopolymer is different. Figure 7.8 shows the evidence of reaction of such CFA particles in geopolymer. In Fig. 7.8a, several CFA particles with the size of 5-35 μm have undergone partial reaction identified as surface dimpling depending on the variation in CFA reactivity (Fernández-Jiménez and Palomo, 2009; Gardner et al., 2015). It is believed that these detritic textures on the surface are the results of partial reaction or dissolution of active aluminosilicate phase within CFA particle. The dissolution of the aluminosilicate phases could occur in P-rich environment, resulting in the formation of S-A-P gels and leaving dendritic Fe-rich phases. Recent works speculated the chemical action of CFA in phosphate binders (e.g., magnesia potassium phosphate cement), claiming the formation of amorphous Al-P or Si-P phases between CFA and phosphate species (Li and Chen, 2013; Gardner et al., 2015; Xu et al., 2017; Xu et al., 2018) As shown in Fig. 7.8b, the phosphate etching could also chemically ‘open’ the Ca-rich wall of CFA particle to form the phosphate-containing phases within the CFA particles..

7.3.7 CFA chemistry in phosphate: X-ray diffraction

In order to pinpoint the chemistry between CFAs and phosphates, CFA/OPA suspension liquids were prepared with Ca/P ratios of 1.1 (low-calcium CFA) and 3.4 (high-calcium CFA) for 28 day reaction at room temperature.

The XRD patterns of the two types of CFA sediments, along with the corresponding raw CFAs, are shown in Fig. 7.9. The characteristic peaks for crystalline aluminosilicate phase in two types of CFAs are clearly marked. The quartz (JCPDS No. 11-0795) and mullite (JCPDS No. 15-0776) exist in both raw CFAs, and still remain after 28 day reaction with phosphate. This suggests that these phases are chemically stable in acidic phosphate environment, observed in the microscopic images of CFA inert phase in CFA-blended geopolymers (Figs. 7.7 and 7.8)

The XRD pattern of raw high-calcium CFA reveals the crystalline forms of calcium including aragonite (JCPDS No. 41-1475), calcite (JCPDS No. 05-0586) and dolomite (JCPDS No. 79-1346), which they are instable in the acidic phosphate environment. Thus, these calcium-containing peaks are not detected in the sediment (i.e., HCFAP). Besides, the brushite and monetite are not found in XRD patterns of the high-calcium CFA sediments due to unbefitting pH environment. In the phosphate solution with a pH lower than 2, the ionization effect of $H_2PO_4^-$ is dominant. The $H_2PO_4^-$ ion rich environment rather than HPO_4^{2-} is unsuitable to form brushite and monetite (Chow and Eanes, 2001), although sufficient Ca/P ratio is given in the CFA/OPA suspensions. In raw low-calcium CFA, one modest peak at 29° (2θ) is assigned to calcite (JCPDS No. 05-0586), indicating the rare calcium species. Compared to the raw CFAs, the diffuse scattering (15-30°, 2θ) of the sediments is intensified. The phosphate adsorption on the active aluminate phase in CFAs leaves behind isolated silicates (Wilson, 1978), which enriches the hump peak at 15-30° (2θ) (Tanada et al., 2003; Shin et al., 2004).

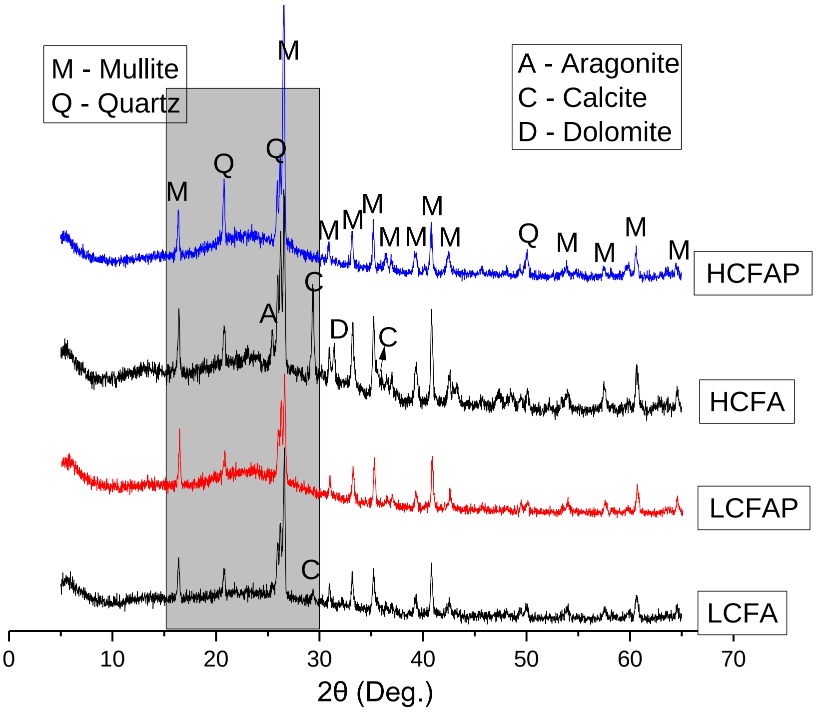

Fig. 7.9 X-ray diffraction patterns of the final sediments treated by centrifugal separation and deionized water washing. The raw CFAs as references are attached.

7.3.8 CFA chemistry in phosphate: microscopic investigation

Fig. 7.10 shows microscopic images of the two types of CFA particles immersed in phosphate solution for 28 day. As shown in Fig. 7.10a, the phosphate species agglomerate the low-calcium CFAs that are previously isolated spherical particles (Fig. 7.2a), which implies that some binding phases are generated through the geopolymerization between CFA and phosphate. The dissolution of glassy aluminosilicate of CFAs allows the precursors to form fibrous gels (e.g., S-P, A-P or S-A-P) in phosphate environment.

Compared to raw high-calcium CFAs (Fig. 7.2b), the phosphate treatment enables the production of inter-particle binding phases, as shown in Fig. 7.10b.

Although their output of the fibrous gels seem to be much less than that of low-calcium CFA, numerous plate-like calcium phosphates appear around CFA particles, which discloses the strong sensitivity of the high-calcium CFA particles to phosphate species. The absence of calcium phosphates peak in XRD pattern (Fig. 7.9) indicates that these phosphates might be amorphous. The unbefitting pH is an unsuitable condition for crystalline generation and growth of brushite. Besides, the formed calcium phosphate grains with lower fineness may be used to fill the micro pores, which compacts the geopolymer matrix for high mechanical strength (Fig. 7.4).

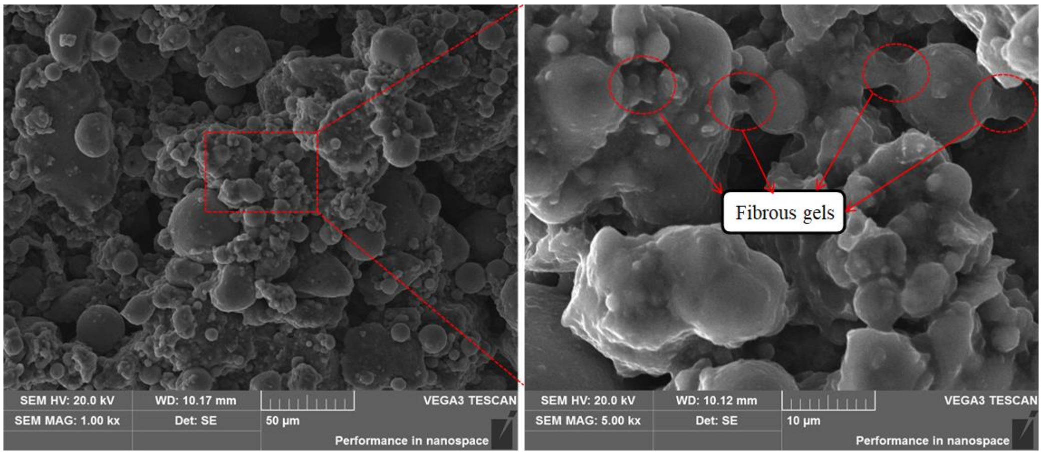

(a) low-calcium CFA sediment

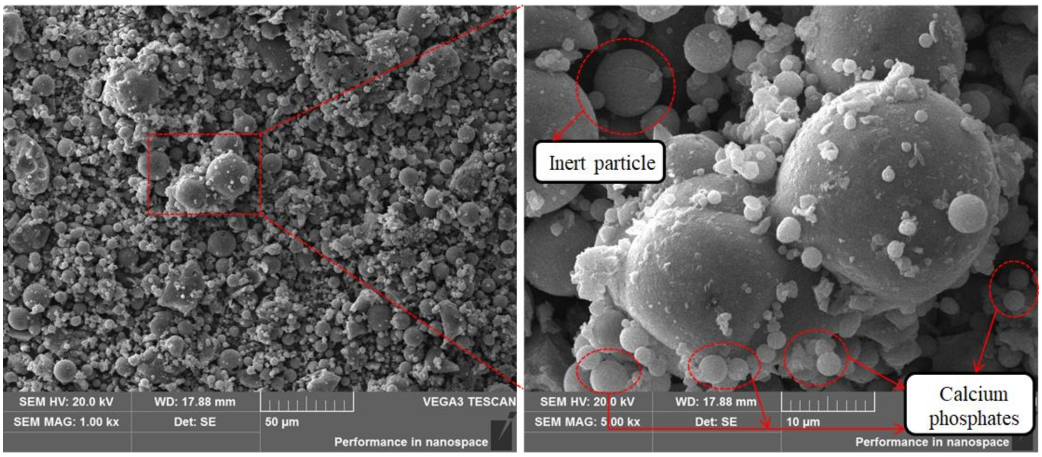

(b) high-calcium CFA sediment

Fig. 7.10 Scanning electron microscopy images of the high-calcium and low-calcium CFA sediments

7.3.9 CFA chemistry in phosphate: ^{31}P and ^{27}Al MAS-NMR

Figure 7.11a shows the ^{31}P NMR spectra of the raw CFAs and sediments, identifying three resonances at -2.6, -6.5 and -13 ppm in both sediments which are attributed to Q^0, Q^1 and Q^2 phosphate structural unites, respectively (Yang et al., 1986; Brow et al., 1993). The chemical shift at 1.2 ppm corresponds to amorphous calcium phosphate (e.g., 1.3 ppm of ^{31}P NMR spectrum for brushite reported by Legrand et al., 2009) (Rothwell et al., 1980; Mudrakovskii et al., 1986). This band appeared in HCFAP rather than LCFAP, despite being partially overlapped by the broad band of Q^0. This may be the resonance of plate-like calcium phosphate observed in Fig. 7.10b.

The noise signals without clear responses in raw CFAs are due to the absence of phosphorus. In sediments, the P environment of Q^0 is from phosphate groups (i.e., phosphoric acid molecules and ions) that are donated by the residual orthophosphate (Samadi-Maybodi et al., 2009; Legrand et al., 2009). The weak signals at -6.5 may be assigned to P-O-P linkage or aluminum-bonded unit due to the formation of polyphosphates or aluminum phosphate (Zhang and Eckert, 2006; Abdi et al., 2014; Liu et al., 2014). The aluminum phosphate mainly resonates at the chemical shift of -13 ppm. The formed aluminum phosphate compounds are presented as outer-sphere, inner-sphere surface complexes and surface precipitates, as reported by Li et al, 2013. The outer-sphere phosphate complexes are embodied as a similar chemical environment to alkaline phosphates, which yields NMR responses at 0-10 ppm. The signals appearing between 0 and -11 ppm could be ascribed to inner-sphere aluminum phosphate complexes. Caused by chemical shielding of Al, the chemical shift for surface precipitates may be similar to those of aluminum phosphate. The ^{31}P resonances for the CFA sediments mainly lie within the regions (-13 ppm) of surface precipitates, which is due to the chemical interaction between glassy aluminosilicate in CFAs and phosphate solution as a result of S-A-P gels formation. A stronger resonance signal intensity in low-calcium CFA than that in high-calcium CFA indicates that the aluminates in low-calcium CFA are more sensitive to phosphate species, which corresponds to more fibrous gels observed in Fig. 7.10a. The structure of the aluminum phosphate can be further explained in ^{27}Al NMR spectra shown in Figs. 7.11b, 7.12 and 7.13.

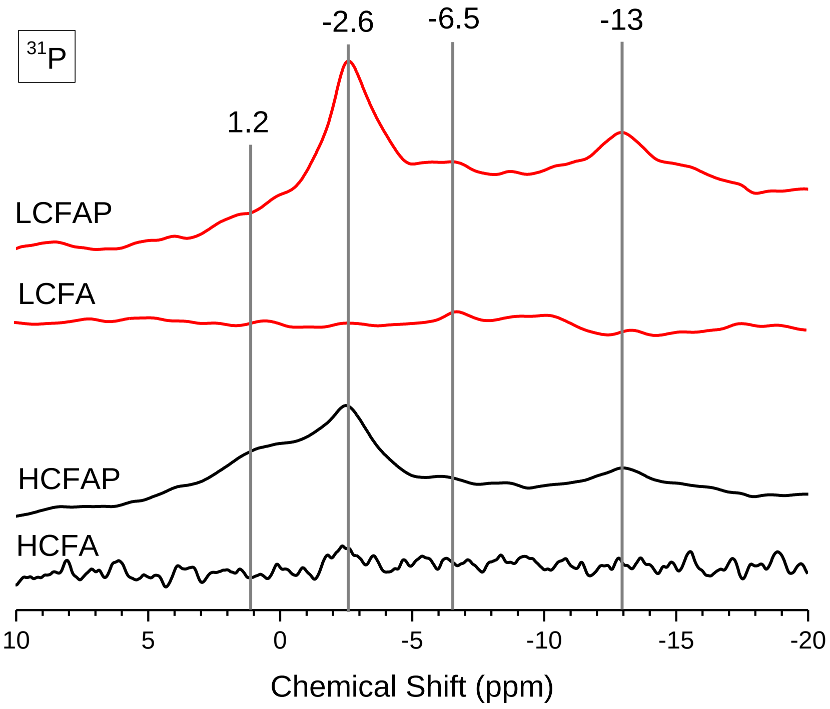

(a) ^{31}P

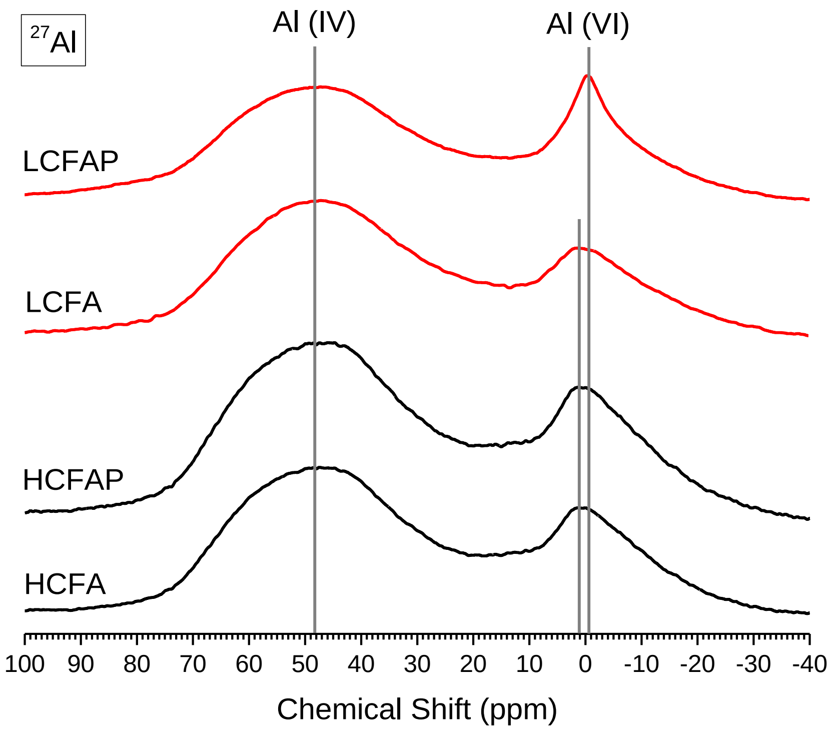

(b) ^{27}Al

Fig. 7.11 ^{31}P and ^{27}Al MAS-NMR spectra of raw CFAs and sediments

The ^{27}Al NMR spectra of the two types of raw CFAs (LCFA and HCFA) and corresponding sediments (i.e., LCFAP and HCFAP) are show in Fig. 7.11b. Two main Al environments were found in both raw CFAs including Al (IV) at around 48 ppm and Al(VI) at around 0 ppm. The bands concentrated at 48 and 0 ppm are assigned to the tetrahedral and octahedral resonance of Al in mullite, respectively (Merwin et al., 1991; Jaymes et al., 1994; Rehak et al., 1998; He et al., 2004). As identified by XRD (Fig. 7.9), the mullite exists in all raw CFAs and sediments. Besides, the broad band from 75 to 25 ppm contains the glassy aluminosilicate components with high cross-linkage, which is expressed as the tetrahedral resonance as well. The difference of the raw CFA and sediments is further distinguished by the deconvolution of NMR spectrum lineshape, which can refine the chemical structure and ordering of the sediments. The Gaussian-based deconvolutions of the ^{27}Al NMR spectra were conducted with an assumption that the all reactions between CFA and phosphate proceed congruently. The deconvoluted curves are shown in Figs. 7.12 and 7.13.

As shown in Fig. 7.12, the Al(VI) region of the sediment (Fig. 7.12b) is strongly sharpened compared to the raw CFAs (Fig. 7.12a), due to the formation of fibrous gels (Fig. 7.10a), which may transform the glassy aluminosilicates [Al (IV)] into S-A-P or A-P gels [Al (VI)] through dealumination reaction of CFAs (see Chapter 5). Thus, the six-coordinated Al species are accumulated, while the four-coordinated Al species are consumed. The inert aluminum-containing phase (e.g., mullite) kept unchanged throughout. The similar change in high-calcium CFA (Fig. 7.13) is unconspicuous, which suggests that the interaction between aluminosilicate phase in high-calcium CFA and phosphate is relatively weaker. That is because the phosphate species is mainly combined with calcium species in high-calcium CFA as observed in Fig.7. 10b.

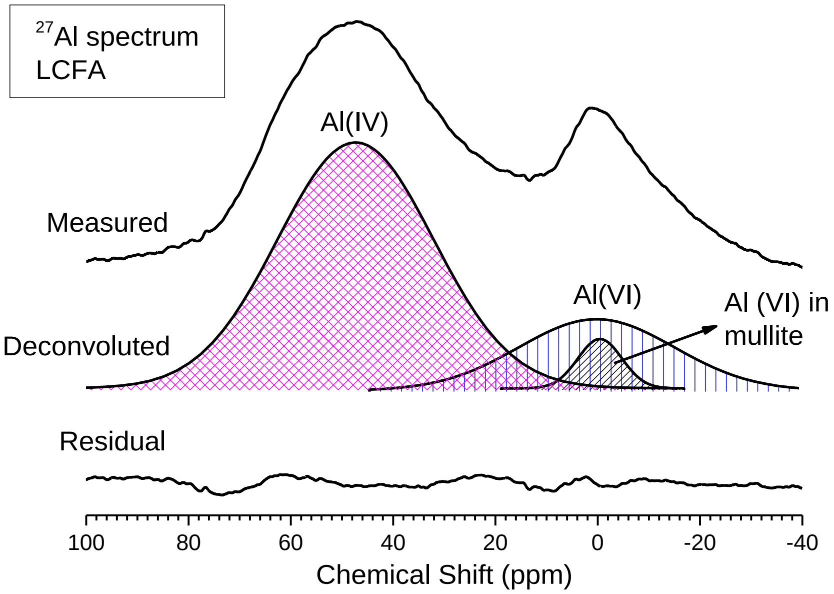

(a) raw low-calcium CFA

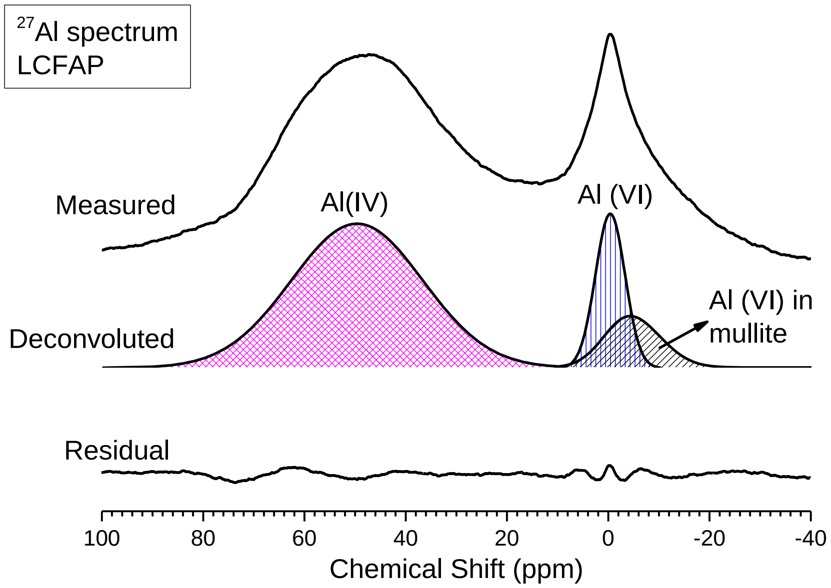

(b) low-calcium sediment

Fig. 7.12 Deconvolution of ^{27}Al MAS-NMR spectra for raw low-calcium CFA and its sediment

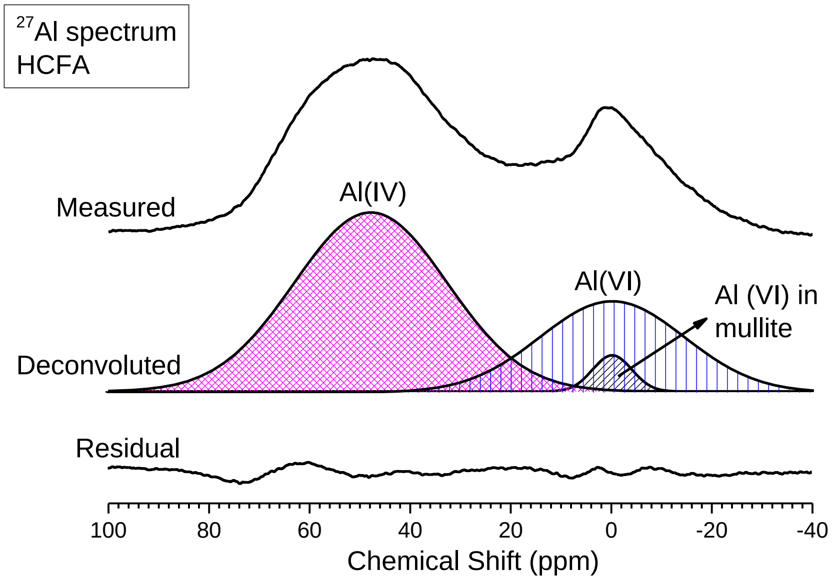

(a) raw high-calcium CFA

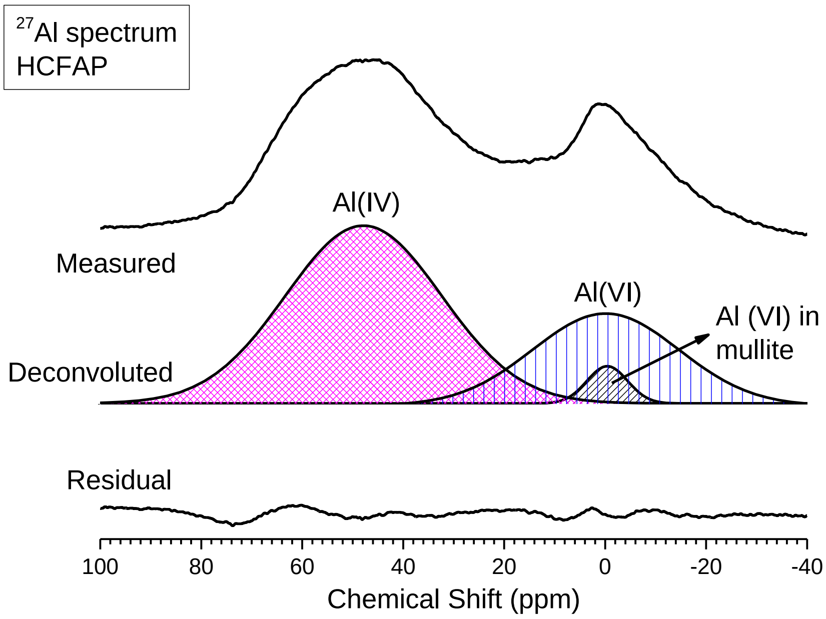

(b) high-calcium CFA sediment

Fig. 7.13 Deconvolution of ^{27}Al MAS-NMR spectra for raw high-calcium CFA and its sediment

7.4 **Chapter Summary**

This chapter proposes the use of CFA in silico-aluminophosphate geopolymer paste. Its effects in terms of setting times, workability, and compressive strength in the high-calcium CFA-blended silico-aluminophosphate geopolymer were experimentally studied and analyzed. Introducing the high-calcium CFA into aluminosilicate precursor aims to seed the calcium species. In addition to some workability enhancement due to ball-bearing action of spherical CFAs, the fast acid-base or/and hydrolysis reaction between the alkaline calcium source in CFA and the acidic phosphate source in the activator is induced. The fine calcium phosphate products (e.g., brushite and monetite) as binding phase and pore filler enable the improvement of the early strength of the high-calcium CFA-blended silico-aluminophosphate geopolymer. For the low-calcium CFA-blended geopolymers, more significant improvement in workability was observed. This CFA mainly acts as aluminosilicate precursors for geopolymerization, and its contribution degree of strength in the low-calcium CFA-blended geopolymer is closely associated with the glassy aluminosilicate.

7.5 **References**

Abdi, D., Cade-Menun, B. J., Ziadi, N., & Parent, L. É. (2014). Long-term impact of tillage practices and phosphorus fertilization on soil phosphorus forms as determined by ^{31}P nuclear magnetic resonance spectroscopy. *Journal of Environmental Quality*, 43(4), 1431-1441.

Agyei, N. M., Strydom, C. A., & Potgieter, J. H. (2002). The removal of phosphate ions from aqueous solution by fly ash, slag, ordinary Portland cement and related blends. *Cement and Concrete Research*, 32(12), 1889-1897.

Ambard, A. J., & Mueninghoff, L. (2006). Calcium phosphate cement: review of mechanical and biological properties. *Journal of Prosthodontics*, 15(5), 321-328.

Basu, P. (1999). Combustion of coal in circulating fluidized-bed boilers: a review. *Chemical Engineering Science*, 54(22), 5547-5557.

Benavent, V., Steins, P., Sobrados, I., Sanz, J., Lambertin, D., Frizon, F., Rossignol, S., & Poulesquen, A. (2016). Impact of aluminum on the structure of geopolymers from the early stages to consolidated material. *Cement and Concrete Research*, 90, 27-35.

Brow, R. K., Kirkpatrick, R. J., & Turner, G. L. (1993). Nature of alumina in phosphate glass: II, structure of sodium alurninophosphate glass. *Journal of the American Ceramic Society*, 76(4), 919-928.

Chindaprasirt, P., & Rattanasak, U. (2010). Utilization of blended fluidized bed combustion (FBC) ash and pulverized coal combustion (PCC) fly ash in geopolymer. *Waste Management*, 30(4), 667-672.

Chindaprasirt, P., Chareerat, T., Hatanaka, S., & Cao, T. (2010). High-strength geopolymer using fine high-calcium fly ash. *Journal of Materials in Civil Engineering*, 23(3), 264-270.

Chindaprasirt, P., Thaiwitcharoen, S., Kaewpirom, S., & Rattanasak, U. (2013). Controlling ettringite formation in FBC fly ash geopolymer concrete. *Cement and Concrete Composites*, 41, 24-28.

Chindaprasirt, P., Paisitsrisawat, P., & Rattanasak, U. (2014). Strength and resistance to sulfate and sulfuric acid of ground fluidized bed combustion fly ash–silica fume alkali-activated composite. *Advanced Powder Technology*, 25(3), 1087-1093.

Chow, L. C., & Eanes, E. D. (Eds.). (2001). *Octacalcium phosphate* (Vol. 18). Karger Medical and Scientific Publishers. pp. 148-163

Collepardi, M. (2003). A state-of-the-art review on delayed ettringite attack on concrete. *Cement and Concrete Composites*, 25(4-5), 401-407.

Douiri, H., Louati, S., Baklouti, S., Arous, M., & Fakhfakh, Z. (2014). Structural, thermal and dielectric properties of phosphoric acid-based geopolymers with different amounts of H_3PO_4. *Materials Letters*, 116, 9-12.

Duxson, P., & Provis, J. L. (2008). Designing precursors for geopolymer cements. *Journal of the American Ceramic Society*, 91(12), 3864-3869.

Erdoğdu, K., & Türker, P. (1998). Effects of fly ash particle size on strength of Portland cement fly ash mortars. *Cement and Concrete Research*, 28, 1217-1222.

Fernández-Jiménez, A., & Palomo, A. (2003). Characterisation of fly ashes. Potential reactivity as alkaline cements. *Fuel*, 82(18), 2259-2265.

Fernández-Jiménez, A., & Palomo, A. (2009). Nanostructure/microstructure of fly ash geopolymers. In Provis, J. L., & van Deventer, J. S. J. (Eds.). (2009). *Geopolymers: structures, processing, properties and industrial applications*. Woodhead, Cambridge, UK,

Gardner, L. J., Bernal, S. A., Walling, S. A., Corkhill, C. L., Provis, J. L., & Hyatt, N. C. (2015). Characterisation of magnesium potassium phosphate cements blended with fly ash and ground granulated blast furnace slag. *Cement and Concrete Research*, 74, 78-87.

He, H., Guo, J., Zhu, J., Yuan, P., & Hu, C. (2004). ^{29}Si and ^{27}Al MAS NMR spectra of mullites from different kaolinites. *Spectrochimica Acta Part A:*

Molecular and Biomolecular Spectroscopy, 60(5), 1061-1064.

Hulett, L. D., & Weinberger, A. J. (1980). Some etching studies of the microstructure and composition of large aluminosilicate particles in fly ash from coal-burning power plants. *Environmental Science & Technology*, 14(8), 965-970.

Jaymes, I., Douy, A., Florian, P., Massiot, D., & Coutures, J. P. (1994). New synthesis of mullite. Structural evolution study by ^{17}O, ^{27}Al and ^{29}Si MAS NMR spectroscopy. *Journal of Sol-Gel Science and Technology*, 2(1-3), 367-370.

Kunther, W., Lothenbach, B., & Skibsted, J. (2015). Influence of the Ca/Si ratio of the C–S–H phase on the interaction with sulfate ions and its impact on the ettringite crystallization pressure. *Cement and Concrete Research*, 69, 37-49.

Legrand, A. P., Sfihi, H., Lequeux, N., & Lemaitre, J. (2009). ^{31}P Solid-State NMR study of the chemical setting process of a dual-paste injectable brushite cements. *Journal of Biomedical Materials Research Part B: Applied Biomaterials*, 91(1), 46-54.

Li, W., Pierre-Louis, A. M., Kwon, K. D., Kubicki, J. D., Strongin, D. R., & Phillips, B. L. (2013). Molecular level investigations of phosphate sorption on corundum (α-Al2O3) by ^{31}P solid state NMR, ATR-FTIR and quantum chemical calculation. *Geochimica et Cosmochimica Acta*, 107, 252-266.

Li, Y., & Chen, B. (2013). Factors that affect the properties of magnesium phosphate cement. *Construction and Building Materials*, 47, 977-983.

Liu, J., Yang, J., Liang, X., Zhao, Y., Cade-Menun, B. J., & Hu, Y. (2014). Molecular speciation of phosphorus present in readily dispersible colloids from agricultural soils. *Soil Science Society of America Journal*, 78(1), 47-53.

Ma, Z., Deng, J., Li, Z., Li, Q., Zhao, P., Wang, L., Sun, Y., Zheng, H., Pan, L., Zhao, S., Jiang, J., Wang, S., & Duan, L. (2016). Characteristics of NOx emission from Chinese coal-fired power plants equipped with new technologies. *Atmospheric Environment*, 131, 164-170.

Merwin, L. H., Sebald, A., Rager, H., & Schneider, H. (1991). ^{29}Si and ^{27}Al MAS NMR spectroscopy of mullite. *Physics and Chemistry of Minerals*, 18(1), 47-52.

Mudrakovskii, I. L., Shmachkova, V. P., Kotsarenko, N. S., & Mastikhin, V. M. (1986). ^{31}P NMR study of I–IV group polycrystalline phosphates. *Journal of Physics and Chemistry of Solids*, *47*(4), 335-339.

Prado-Herrero, P., Garcia-Guinea, J., Crespo-Feo, E., & Correcher, V. (2010). Temperature-induced transformation of metavariscite to berlinite. *Phase Transitions*, 83(6), 440-449.

Rashad, A. M. (2014). A comprehensive overview about the influence of different admixtures and additives on the properties of alkali-activated fly ash. *Materials & Design*, 53, 1005-1025.

Rehak, P., Kunath-Fandrei, G., Losso, P., Jäger, C., Hildmann, B., & Schneider, H. (1998). Study of the Al coordination in mullites with varying Al: Si ratio by ^{27}Al NMR spectroscopy and X-ray diffraction. *American Mineralogist*, 83(12), 1266-1276.

Rothwell, W. P., Waugh, J. S., & Yesinowski, J. P. (1980). High-resolution variable-temperature phosphorus-31 NMR of solid calcium phosphates. *Journal of the American Chemical Society*, *102*(8), 2637-2643.

Samadi-Maybodi, A., Nejad-Darzi, S. K. H., & Bijanzadeh, H. (2009). ^{31}P and ^{27}Al NMR studies of aqueous (2-hydroxyethyl) trimethylammonium solutions containing aluminum and phosphorus. *Spectrochimica Acta Part A: Molecular and Biomolecular Spectroscopy*, 72(2), 382-389.

Seames, W. S. (2003). An initial study of the fine fragmentation fly ash particle mode generated during pulverized coal combustion. *Fuel Processing Technology*, 81(2), 109-125.

Shin, E. W., Han, J. S., Jang, M., Min, S. H., Park, J. K., & Rowell, R. M. (2004). Phosphate adsorption on aluminum-impregnated mesoporous silicates: surface structure and behavior of adsorbents. *Environmental Science & Technology*, 38(3), 912-917.

Slavik, R., Bednarik, V., Vondruska, M., & Nemec, A. (2008). Preparation of geopolymer from fluidized bed combustion bottom ash. *Journal of Materials Processing Technology*, 200(1-3), 265-270.

Srivastava, R. K., Miller, C. A., Erickson, C., & Jambhekar, R. (2004). Emissions of sulfur trioxide from coal-fired power plants. *Journal of the Air & Waste*

Management Association, 54(6), 750-762.

Sustainable Development Report (2013). China Light and Power Co. Ltd.

Tanada, S., Kabayama, M., Kawasaki, N., Sakiyama, T., Nakamura, T., Araki, M., & Tamura, T. (2003). Removal of phosphate by aluminum oxide hydroxide. *Journal of Colloid and Interface Science*, 257(1), 135-140.

Taylor, H. F. W., Famy, C., & Scrivener, K. L. (2001). Delayed ettringite formation. *Cement and Concrete Research*, 31(5), 683-693.

White, C. E., Provis, J. L., Proffen, T., Riley, D. P., & van Deventer, J. S. J. (2010). Density functional modeling of the local structure of kaolinite subjected to thermal dehydroxylation. *Journal of Physical Chemistry A*, 114(14), 4988-4996.

Wikholm, N. W., Beebe, R. A., & Kittelberger, J. S. (1975). Kinetics of the conversion of monetite to calcium pyrophosphate. *The Journal of Physical Chemistry*, 79(8), 853-856.

Wilson, A. D. (1978). The chemistry of dental cements. *Chemical Society Reviews*, 7(2), 265-296.

Xu, B., Ma, H., Shao, H., Li, Z., & Lothenbach, B. (2017). Influence of fly ash on compressive strength and micro-characteristics of magnesium potassium phosphate cement mortars. *Cement and Concrete Research*, 99, 86-94.

Xu, B., Lothenbach, B., & Ma, H. (2018). Properties of fly ash blended magnesium potassium phosphate mortars: Effect of the ratio between fly ash and magnesia. *Cement and Concrete Composites*, 90, 169-177.

Yang, W. H., Kirkpatrick, R. J., & Turner, G. (1986). ^{31}P and ^{29}Si magic-angle sample-spinning NMR Investigation of the structural environment of phosphorus in alkaline-earth silicate glasses. *Journal of the American Ceramic Society*, 69(10).

Yao, Z. T., Ji, X. S., Sarker, P. K., Tang, J. H., Ge, L. Q., Xia, M. S., & Xi, Y. Q. (2015). A comprehensive review on the applications of coal fly ash. *Earth-Science Reviews*, 141, 105-121.

Zhang, L., & Eckert, H. (2006). Short-and medium-range order in sodium aluminophosphate glasses: new insights from high-resolution dipolar solid-state NMR spectroscopy. *The Journal of Physical Chemistry B*, 110(18), 8946-8958.

Zhang, J., Liu, W., Schnitzler, V., Tancret, F., & Bouler, J. M. (2014). Calcium phosphate cements for bone substitution: chemistry, handling and mechanical properties. *Acta Biomaterialia*, 10(3), 1035-1049.

Zhang, L., Weir, M. D., Chow, L. C., Antonucci, J. M., Chen, J., & Xu, H. H. (2016). Novel rechargeable calcium phosphate dental nanocomposite. *Dental Materials*, 32(2), 285-293.

This page is intentionally left blank

CHAPTER 8 CONCLUSIONS AND DIRECTIONS FOR FUTURE WORK

As a necessary supplement to the field of geopolymer, the silico-aluminophosphate geopolymer synthesized by aluminosilicate precursors and phosphate activators is clarified in this thesis. Influences of metal-containing sources, i.e., aluminum species in monoaluminum phosphate, magnesium species in dead-burnt magnesia, and calcium species in coal fly ash, on the microstructural modifications and performance improvements of the silico-aluminophosphate geopolymer are mainly identified. The fresh silico-aluminophosphate geopolymer paste is enhanced through seeding soluble aluminum species into phosphate activators, to obtain improved workability and setting times. The hardened silico-aluminophosphate geopolymer blended with dead-burnt magnesia or coal fly ash further gained an early mechanical performance with fast setting time. A series of experimental investigations, e.g., rheology, thermogravimetry, analytical chemistry and spectroscopies, was conducted for better understanding the mechanisms behind. Thus, notable conclusions and directions for further work can be given as follow:

8.1 Main Conclusions

- Geopolymer terminology. According to activation approach and product composition, the geopolymer can be divided into alkali-aluminosilicate geopolymer (alkaline activation environment) and silico-aluminophosphate geopolymer (acidic activation environment). The silico-aluminophosphate geopolymer is synthesized through geopolymerization between aluminosilicate precursors and phosphate activators, which fills the gap of the geopolymer field.

- Phosphate activator. Three types of phosphate activators proposed in this thesis are applicable in different engineering scenarios. (1) The conjunctive use of solid monoaluminum phosphate and aluminosilicate precursor establishes a feasible foundation to explore the ‘one-part’ or ‘just-add-water’ silico-aluminophosphate geopolymer. (2) Commercial monoaluminum phosphate with industry production as a backup force can fabricate the silico-aluminophosphate geopolymer cement as a larger-scale construction material for rapid rehabilitation, coating and other fields that need acidic binders. (3) Laboratory-prepared monoaluminum phosphate can be arbitrarily tailored to be a phosphate activator with desirable and highly-accurate ion ratios and concentrations, which is suitable for some delicate or exquisite fields (e.g., inorganics-based 3D printing).
- Net silico-aluminophosphate geopolymer. The geopolymers with theoretical, silicate-deficient and aluminate-deficient molecular structures are prepared to investigate their formation process and original properties at room temperature. The deficiency of aluminate in the raw materials can hardly synthesize a useful geopolymer matrix, while the geopolymer with an Al/P molar ratio of 1.0 held better performance, producing an amorphous structure of $SiO_2 \cdot Al_2O_3 \cdot P_2O_5 \cdot nH_2O$ and an aluminum phosphate crystalline phase.
- Aluminum-modified silico-aluminophosphate geopolymer. Six-coordinated aluminum species in phosphate activators facilities the formation of aluminate and phosphate oligomers in addition to rapid transformation into aluminophosphate gels, as a result of the shortened initial setting times of fresh silico-aluminophosphate geopolymer paste. The aluminum species can lower the yield stress of the fresh geopolymer and keep its viscosity unchanged through a ‘plasticizer effect’, which enhances the geopolymer workability. In the meantime, a compact and dense matrix can be obtained

with 7 day strength of up to 37 MPa. However, excessive amount of aluminum species in activator may generate significant inter-gel spaces (medium capillary pores) in geopolymer matrix due to forming discontinuous gels at later curing age.

- Silico-aluminophosphate geopolymer improved by dead-burnt magnesia. Introducing dead-burnt magnesia into aluminosilicate precursors can induce an acid-base reaction that yields a crystalline newberyite and an amorphous aluminum magnesium phosphate ($Al_2O_3 \cdot 3MgO \cdot 2P_2O_5$) phase. The reaction rate of this acid-base reaction governs the setting time and early strength of the silico-aluminophosphate geopolymer. Incorporating 20% dead-burnt magnesia can form a silico-aluminophosphate geopolymer with an initial setting time of 8 min and 1 day compressive strength of 8.3 MPa.
- Silico-aluminophosphate geopolymer improved coal fly ash. In addition to magnesium-induced reaction, blending CFA (especially containing high content of calcium) with aluminosilicate precursor can also function in terms of the geopolymer performance enhancement. In addition to increasing workability due to ball-bearing action of spherical coal fly ashes, the fast acid-base or/and hydrolysis reaction between the alkaline calcium source in coal fly ash and the acidic phosphate species in the activator is induced. The fine calcium phosphate products (e.g., brushite and monetite) as binding phase or pore filler enable the improvement of the early strength of the silico-aluminophosphate geopolymer blended with high-calcium coal fly ash. For the low-calcium coal fly ash-blended geopolymers, more significant improvement in workability is observed. This coal fly ash mainly acts as aluminosilicate precursors for geopolymerization, and its contribution degree of strength in the low-calcium coal fly ash-blended geopolymer is closely associated with the glassy aluminosilicate.

8.2 Directions for Future Work

Although this thesis has pioneered the synthesis of silico-aluminophosphate geopolymer, and modified its microstructures using different metal-containing sources for performance improvement, the research on silico-aluminophosphate geopolymer is just a beginning. Several aspects of refinements and applications are recommended for future work:

- Although the aluminum and phosphorus chemical structures of the S-A-P (silicate-aluminate-phosphate) gels in phosphate activating solutions and silico-aluminophosphate geopolymers were preliminarily studied by NMR spectra, the Si-O-Al, Si-O-P and/or Al-O-P bonds of these gels are far from fully understood, and the chemical details of the mechanisms involved require further investigation. The researches on silicoaluminophosphate molecular sieves can be referred to in the future research (Derouane et al., 1990).
- This thesis aims to develop room-temperature-hardening geopolymers for civil engineering applications where the working environment is usually under ambient temperature. Recent publications (Alizadeh et al., 2016; Abyzov, 2017; Lopes et al., 2017) on aluminum phosphate binders used as refractory castables indicate that the exploration towards refractory matters using the monolithic silico-aluminophosphate geopolymer is a promising research field.
- Acid environment is regarded as an adverse environment to mild steel and traditional concrete. The bonderization of the mild steel (e.g., coating) under ambient temperature can be explored for corrosion protection (Su and Lin, 2014; Ramezanzadeh et al., 2015; Zeng et al., 2017). Phosphate coating materials for concrete (e.g., carbonation and sulfation attack) is another interesting project (Leister et al., 2018; Li et al., 2018).

- Applicable inorganic materials for 3D printing are scarce currently, especially that with designable parameters and properties (Bose et al., 2013). The performance of fresh and hardened silico-aluminophosphate geopolymer material, through different metal ions modification, can be customized in terms of rheology, viscosity, fluidity, hardening time and compressive strength, which is potentially developed to be a ‘full’ inorganic 3D printing material, i.e., the printed products without organic adhesives for inter-particle bonding (Sanchez et al., 2011) or surface treatment post-processing (Mueller, 2012).

8.3 References

Abyzov, V. A. (2017). Refractory cellular concrete based on phosphate binder from waste of production and recycling of aluminum. *Procedia Engineering*, *206*, 783-789.

Alizadeh, S., Shalbafi, A., Monshi, A., & Yazdkhasti, S. (2016). Influence of phosphate binders on the physical and mechanical properties of magnesia carbon monolithics composed of recycled refractory aggregates. *Ironmaking & Steelmaking*, *43*(5), 325-330.

Bose, S., Vahabzadeh, S., & Bandyopadhyay, A. (2013). Bone tissue engineering using 3D printing. *Materials Today*, *16*(12), 496-504.

Derouane, E.G., Fripiat, J.G. and von Ballmoos, R. (1990). Quantum mechanical calculations on molecular sieves. 2. Model cluster investigation of silicoaluminophosphates. *Journal of Physical Chemistry* 94(4): 1687-1692.

Leister, M., Graf, C., & Lippold, K. (2018). *U.S. Patent No. 9,975,809*. Washington, DC: U.S. Patent and Trademark Office.

Li, J., Ji, Y., Huang, G., & Zhang, L. (2018). Microstructure Evolution of a Magnesium Phosphate Protective Layer on Concrete Structures in a Sulfate

Environment. *Coatings*, *8*(4), 140.

Lopes, S. J. S., Luz, A. P., Gomes, D. T., & Pandolfelli, V. C. (2017). Self-flowing high-alumina phosphate-bonded refractory castables. *Ceramics International*, *43*(8), 6239-6249.

Mueller, B. (2012). Additive manufacturing technologies–Rapid prototyping to direct digital manufacturing. *Assembly Automation*, *32*(2).

Ramezanzadeh, B., Vakili, H., & Amini, R. (2015). Improved performance of cerium conversion coatings on steel with zinc phosphate post-treatment. *Journal of Industrial and Engineering Chemistry*, *30*, 225-233.

Sanchez, C., Belleville, P., Popall, M., & Nicole, L. (2011). Applications of advanced hybrid organic–inorganic nanomaterials: from laboratory to market. *Chemical Society Reviews*, *40*(2), 696-753.

Su, H. Y., & Lin, C. S. (2014). Effect of additives on the properties of phosphate conversion coating on electrogalvanized steel sheet. *Corrosion Science*, *83*, 137-146.

Zeng, Y. Z., Wu, T. W., Chiu, L. H., Chen, C. F., & Chiu, S. M. (2017, May). Heat treatment effect on formation of ferrite layer of phosphate coated steels. In *Applied System Innovation (ICASI), 2017 International Conference on* (pp. 1845-1848). IEEE.